Innovative Cold-Formed Steel Nested Tapered Box Section Portal Frames with Bolted-Side Plate Joints

A thesis

submitted in fulfilment

of the requirements for the degree

of

Doctor of Philosophy in Engineering

at

The University of Waikato

By

Bikram Paul

THE UNIVERSITY OF
WAIKATO
Te Whare Wānanga o Waikato

2025

To
my
parents
&
wife

Abstract

Nested tapered box (NTB) portal frames made entirely of cold-formed steel (CFS) are widely used in New Zealand. Shahmohammadi (2019) recently described a full-scale test of such a system. The tested frame had a span of 18.16 meters and a height to the eaves of 4.27 meters. The joints of this NTB portal frame were rigid, constructed with bolted end plates. However, bolted end plate joints can be expensive due to the full penetration butt weld. This thesis proposes an alternative jointing system that uses bolted-side plates. The numerical work conducted in this study yields the following findings:

- A shell finite element (FE) model was developed and validated using previously conducted full-scale portal frame tests. This validated model was then employed to compare the performance of bolted-side plate joints with bolted end-plate joints. The analysis revealed that a portal frame with 10 mm thick bolted side plates could sustain the same load as an NTB portal frame with bolted end-plate joints. Increasing the thickness of the bolted-side plates from 10 mm to 16 mm resulted in a 20% increase in load-carrying capacity. This improvement was due to the confinement effect provided by the side plates, which reduced the slenderness ratio near the eaves joint. However, the NTB portal frame with bolted-side plates exhibited greater apex displacement compared to the frame with bolted end-plate joints.

- FE models were developed for both the eaves and apex joints of the NTB portal frame. A parametric study was then carried out involving 1,000 FE models. Using FE models, design equations are proposed for the moment capacities of the eaves and apex bolted side plates, accounting for both opening and closing moments under partial restraint.

- A parametric study was conducted using the developed design method on eight models, considering a range of spans from 25m to 40m and eaves heights from 5.5m to 6.25m, with a consistent frame spacing of 7.5m. The results showed that portal frames with bolted-side plates can carry on average 7% more load compared to those with bolted end plate joints.

- A methodology was presented to predict the load-carrying capacity of portal frames with back-to-back channel sections. It was shown that the predicted vertical loads from the proposed approach were, on average, within 1% (on an average) of the FEA results for portal frames. The same approach was applied to NTB portal frames through worked examples in Appendix B and C, demonstrating good accuracy.

Preface

This thesis is submitted to the University of Waikato, New Zealand in fulfilment of the requirement for the degree of Doctor of Philosophy. The work contained in this thesis has not been previously submitted for a degree or diploma in any other higher educational institution. To the best of my knowledge and belief, the thesis contains no material previously published or written by another person except where due reference is made.

Publications

Journals

1. Paul, B., Roy, K., Lim, J. B., Fang, Z., McCollum, K., & Bell, D. (2023). Moment-capacity of bolted side-plates for apex joint of nested tapered box beam portal frames. Journal of Building Engineering, 76, 107011. (Published)
2. Paul, B., Roy, K., Shahmohammadi., A., Lim, J. B. Cold-formed steel portal frames with back-to-back section: Behaviour, capacity, design, Journal of Constructional Steel Research. (Submitted)
3. Paul, B., Roy, K., Fang, Z., Shahmohammadi., A., Lim, J. B. Moment-capacity of bolted side-plates for eaves joint of cold-formed nested tapered box beam portal frames. International Journal of steel structure. (Published)
4. Paul, B., Roy, K., Tiwari. S; Lim, J. B. A review on light-weight portal framing system: Tests, numerical modelling, and design, Journal of Constructional Steel Research (Ready for submission)

Acknowledgements

I am deeply grateful to my chief supervisor, Dr. Krishanu Roy, and my co-supervisor, Professor James Lim, for their unwavering support and invaluable guidance throughout my Ph.D. journey. Their expertise and encouragement have been instrumental in shaping this thesis.

I would also like to extend my heartfelt appreciation to Mr. Kerry McCollum and Mr. Jeffre Botanes, head engineers at Donovan Group Ltd., New Zealand. Their generous insights and suggestions significantly enhanced the quality of my research, for which I am truly thankful.

A special acknowledgment goes to Dr Amir Shahmohammadi for his substantial contributions to this endeavour. His expertise played a pivotal role in broadening the scope and depth of this study.

I am sincerely grateful to Dr Arthur Fang, and Dr Leandro Bolzoni for their support and guidance. I would also like to thank my lab mates for their constant encouragement and support throughout my Ph.D. journey. A special thanks to Harsh Birwadkar for his invaluable assistance in proofreading my thesis.

Finally, I wish to express my deepest gratitude to my parents, Mr. Biraj Krishna Paul and Mrs. Rita Paul, as well as my beloved wife, Mrs. Sumana Paul. Their boundless love and encouragement sustained me through the challenges and triumphs of this journey. This thesis stands as a testament to their unwavering support and belief in my abilities.

Table of contents

List of Figures

List of Tables

Notation

a_a	Width of the triangular area of an apex bracket
a_b	Length of bolt-group
a_e	Width of the triangular area of an eaves bracket
a_k	Extended length of bolted-side plate for eaves joint
a_s	Width of the triangular area of bolted side-plate
a_{ab}	The distance from the outline of the bolt group to the edge of bolted side-plate/bracket
a_{sb}	Horizontal side distance of bolted-side plate for eaves joint
a_{sd}	Edge distance of bolted-side plate at eaves joints of NTB portal frame
α'	Load incremental factor
α	Bending moment at the center of rotation of apex joint from beam idealization for 1kN load applied in total on the frame
B	Breadth of NTB section
b_a	Edge width of apex bracket
b_b	Bolt distance in top end row
b_c	Bolt distance in bottom end row
b_d	Breadth of bolt-group for brackets /Horizontal bolt distance between two end rows for bolted-side plates
b_e	Edge width of an eaves bracket
b_{eb}	The distance from the outline of the bolt group to the edge of an eaves bracket
b_k	Edge width of bolted-side plate for eaves joint
b_s	Edge width of bolted side-plate for apex joint
β'	Reliability index
β	Bending moment at the center of rotation of the eaves joint of either the column or the rafter (whichever is greater) from beam idealization for a total load of 1 kN applied
CFS	Cold formed steel
COV	Co-efficient of variation
D	Depth of NTB section
d	Diameter of bolts
$d_{minor_{M16}}$	Minor diameter of M16 bolt
$d_{minor_{M20}}$	Minor diameter of M20 bolt
d_i	Distance from the bolt hole to the rotational center of the bolt group
DDM	Direct design method

DSM	Direct strength method
d_s	Depth of stiffener of bolted-side plate / bracket
E	Modulus of elasticity
EA	Flexural rigidity of column and rafter members
EI	Axial rigidity of column and rafter members
FE	Finite element
F_{beam}	Predicted gravity load from beam idealization
F_{beam}^{EP}	Predicted gravity load from beam idealization for NTB portal frame with bolted end plate system
F_{beam}^{BS}	Predicted gravity load from beam idealization for NTB portal frame with bolted-side plate system
FEA	Finite element analysis
F_U^{FEA}	Ultimate load capacity of portal frame from FEA
F_i	Bolt forces
F_U^{EXP}	Ultimate load capacity of portal frame from experimental test
$F_U^{FEA_{BS}}$	Ultimate load capacity of NTB portal frame with bolted-side plate joint from FEA
F_{FEA}	Predicted gravity load from FEA
f_y	Yield stress
f_u	Ultimate strength
G	Shear modulus
γ_i	Load factors
HAZ	Heat affected zone
h	Eaves height of portal frame
I_w	Wrapping constant
J	Torsional constant
K	Rotational of stiffness of the joint
k_b	Bolt-hole elongation stiffness
k_{AT}	Bolt-hole elongation stiffness of a plate under double shear using thread bolts from Ahmed and Teh
k_{1b}	Bolt-hole elongation stiffness of one bracket
k_{1c}	Bolt-hole elongation stiffness of one channel
k_{1b1c}	Bolt-hole stiffness of the interconnected plates system for joints comprised one bracket with one channel

k_{2b2c}	Bolt-hole stiffness of the interconnected plates system for joints comprised two brackets with two channels
K_{2b2c}	Rotational stiffness of a typical bolt group
L	Span of the portal frame
LTB	Lateral-torsional buckling
l_1	Length of Part 1 rafter member for NTB portal frame
l_2	Length of Part 2 rafter member for NTB portal frame
l_3	Length of Part 3 rafter member for NTB portal frame
l_k	Length of the bolted-side plate
M	Moment capacity of the member
M^*	Bending moment in the member
M_b	Moment capacity of NTB section
M_{bs}^c	Moment capacity of bolted-side plate at eaves under closing moment
M_{bs}^o	Moment capacity of bolted-side plate at eaves under opening moment
M_U^{FEA}	Moment capacity of apex or eaves bracket from FEA
M_U^{EXP}	Moment capacity of apex or eaves bracket from EXP
M_s^o	Moment capacity of bolted-side plate with top-bottom stiffener for apex joint under opening moment
M_n^o	Moment capacity of bolted-side plate without stiffener for apex joint under opening moment
M_s^c	Moment capacity of bolted-side plate with top-bottom stiffener for apex joint under closing moment
M_n^c	Moment capacity of bolted-side plate without stiffener for apex joint under closing moment
M_{1eb}^{c-t-b}	Moment capacity of partially restrained single eaves bracket with top-bottom stiffener under closing moment
M_{1eb}^{o-t-b}	Moment capacity of partially restrained single eaves bracket with top-bottom stiffener under opening moment
M_{1eb}^{o-b}	Moment capacity of partially restrained single eaves bracket with bottom stiffener under opening moment
M_{2eb}^{c-t-b}	Moment capacity of partially restrained double eaves bracket with top-bottom stiffener under closing moment
M_{2eb}^{o-t-b}	Moment capacity of partially restrained double eaves bracket with top-bottom stiffener under opening moment

M_{2eb}^{o-b}	Moment capacity of partially restrained double eaves bracket with bottom stiffener under opening moment
M_{1ab}^{c}	Moment capacity of partially restrained single apex bracket under closing moment
M_{1ab}^{o}	Moment capacity of partially restrained single apex bracket under opening moment
M_{2ab}^{c}	Moment capacity of partially restrained double apex bracket under closing moment
M_{2ab}^{o}	Moment capacity of partially restrained double apex bracket under opening moment
M_{1ab}^{c}	Moment capacity of full restrained single apex bracket under closing moment
M_{1eb}^{c}	Moment capacity of full restrained single eaves bracket under closing moment
M_{2c}	Moment capacity of back-to-back channel section
M_{2c}^{R}	Reduced moment capacity of channel sections
M_{1ab}	Moment capacity of single apex bracket
M_{2ab}	Moment capacity of back-to-back apex bracket
M_{2ab}^{A}	Moment capacity of back-to-back apex bracket for Frame A
M_{2ab}^{B}	Moment capacity of back-to-back apex bracket for Frame B
MPC	Multi point constraints
M	Poisson's ratio
NTB	Nested tapered box section
ω_{ni}	Nominal loads
P^{*}	Axial force in the member
P	Axial capacity of the member
P_m	Mean
P_{2c}	Axial capacity of back-to-back channel section
$\emptyset$	System resistance factor
R_n	Nominal strength of the system
RHS	Rectangular hollow section
S4R	Standard 4-noded doubly curved thin shell elements
t	Thickness of NTB section
t_b	Thickness of bracket
t_s	Thickness of bolted-side plate
t_c	Thickness of channel section
θ	Pitch of the portal frame

V_{2c}	Ultimate shear capacity of back-to-back channel section
X_c	Centroidal distance from the web for single channel section
X_s	Shear centre distance for single channel section

Chapter 1 Introduction

1.1. Background and problem statement

Cold-formed steel (CFS) sections are increasingly popular in the construction industry due to their numerous advantages, including a high strength-to-weight ratio, durability, and ease of handling, transportation, and fabrication (Jackson et al., 2012). A novel form of construction in New Zealand involves the use of CFS nested tapered box (NTB) portal frames, as depicted in Figure 1-1. These frames are commonly used in structures such as warehouses, sports complexes, and farm sheds (see Figure 1-2). Their popularity stems not only from their structural benefits but also from their aesthetic appeal, bird-proofing system, and vermin resistance (Donovan Group Ltd.; Shahmohammadi, 2019). For these portal frames, the eaves and apex joints (see Figure 1-1) are typically formed using a bolted end plate system. Although this system offers several advantages, it also involves the use of costly full penetration butt welds, as shown in Figure 1-1, which increases construction time and labour costs (Shahmohammadi et al., 2022). Moreover, this system is prone to cracking in the heat-affected zone (HAZ) of the weld under opening moments (Wilkinson and Hancock, 2000).

Figure 1-1 Photograph of cold -formed steel NTB portal framing system and its joints (Donovan Group Ltd.)

(a) Warehouse

(b) Canopy

(c) Industrial

(d) Farm shed

(e) Sport complex

Figure 1-2 Application of NTB portal frames (www. coresteel.co.nz)

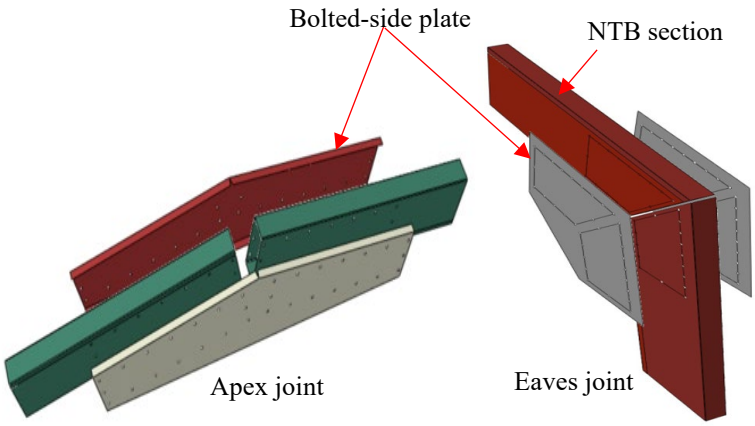

Figure 1-3 Alternative connection system for NTB portal frame with bolted-side plate

As an alternative to the bolted end plate system, a bolted-side plate system (see Figure 1-3) can be used for both the apex and eaves joints in NTB portal framing systems. The strength and stiffness of these portal frames are significantly influenced by the performance of their joints, which mainly depends on the geometric detailing of the joint (Hancock et al., 2001; Rinchen and Rasmussen, 2019a).

Design guidance for CFS members can be found in codes of practice such as AS/NZ 4600 (2018), AISI S-16 (2016), and EN 1993-1-1 (2005). According to AS/NZ 4600 (2018), joints should be strong enough to ensure that failure occurs within the frame members, and the design moment capacity of a joint should meet or exceed the moment it is subjected to. However, no recommended equations exist in the literature or design standards for predicting the strength of bolted-side plates used in eaves and apex joints, although research on brackets can be found.

AS/NZ 4600 (2018) also allows for the use of advanced analysis in the design of steel structures with compact cross-sections, considering geometric and material nonlinear analysis with imperfections. Advanced analysis captures global frame and member instabilities, eliminating the need for separate member checks, unlike the traditional structural design approach, which involves structural analysis followed by individual

member and cross-section examinations (Gardner et al., 2019). Despite extensive research over the past two decades, the application of advanced analysis in the design of CFS structures remains uncommon. Further research is needed on the performance of portal frames before advanced analysis can be widely adopted by engineers.

1.2. Objective of the study:

The objective of this research is to investigate the behaviour of NTB portal frames with a bolted-side plate system under gravity and wind uplift loads using finite element analysis (FEA). The specific objectives of this research project are as follows:

1. To validate the shell finite element (FE) models of NTB portal frames, including apex and eaves joints, against previously reported experimental tests.
2. To develop the shell FE model for the NTB portal frame with bolted-side plates and conduct a feasibility study using this model.
3. To investigate the behaviour of NTB portal frames using FEA and perform parametric studies on apex and eaves joints with the validated shell FE models.
4. To propose unified equations for predicting the moment capacity of bolted-side plates used in practice.
5. To propose simplified design method for predicting the load-carrying capacity of portal frames used in practice.

1.3. Thesis outline

This thesis comprises six chapters, as outlined below:

Chapter 1: Provides an introduction to the research topic, including the problem statement, objectives, and the method of investigation used in the study.

Chapter 2: Presents a literature review of related research. This chapter explores previous studies on portal frames, including apex and eaves joints, primarily under static

loading. It discusses both experimental and numerical investigations conducted by other researchers and describes current design guidelines.

Chapter 3: Investigates the performance of full-scale NTB portal frames using non-linear finite element (FE) models. The chapter begins by validating the non-linear FE model against previously reported full-scale NTB portal frame tests. It then conducts a feasibility study for NTB portal frames with bolted-side plates.

Chapter 4: Focuses on the moment capacity of apex joints in NTB portal frames with bolted-side plates. The chapter validates the FE model for the apex joint using previously reported experimental tests. It concludes by proposing a set of unified design equations for bolted-side plates, considering various geometric parameters consistent with New Zealand practice for both opening and closing moments.

Chapter 5: Examines the moment capacity of eaves joints in NTB portal frames with bolted-side plates. Similar to Chapter 4, this chapter validates the FE model for the eaves joint using previously reported experimental tests. It also proposes a set of unified design equations for bolted-side plates, taking into account different geometric parameters consistent with New Zealand practice for both opening and closing moments.

Chapter 6: This chapter presents the methodology for predicting the load-carrying capacity of portal frames with back-to-back channel sections under gravity loads. The proposed approach is also applied to the frames used in New Zealand and compared with existing equations from the literature.

Chapter 7: Summarizes the research outcomes, provides conclusions, and offers recommendations for further research.

Chapter 2 Literature review

In this chapter, a literature review on various portal framing systems, including their joints (apex, eaves, and knee) and their design, is presented.

2.1. Research on experimental tests

A summary of experimental tests on various portal framing systems, including apex and eaves joints, from the literature is presented in Table 2-1.

Table 2-1 Summary of the previous experimental tests

Experimental tests	Researchers	Load	Cross-Section	Figures
Portal frame	Dowling et al. (1982)	Seismic	I-section	Figure 2-1(a)
	Hwang et al. (1991)	Seismic		Figure 2-1(b)
	Junid (1992)	Static		Figure 2-1(c)
	Li and Li (2002)	Static		Figure 2-1(d)
	Lim and Nethercot (2002a)	Static	Double channel	Figure 2-2
	Dubina (2008)	Seismic		Figure 2-3
	Wrzesien et al. (2015)	Static		Figure 2-4
	Zhang et al. (2016a)	Static		Figure 2-5
	Blum and Rasmussen (2019a)	Static		Figure 2-6
	Rinchen and Rasmussen (2020)	Static	Single channel	Figure 2-7
	Nguyen et al. (2024)	Static	Double channel	Figure 2-8
	Wilkinson and Hancock (1998)	Static	Closed Box	Figure 2-9
	Arrayago et al. (2020a)	Static		Figure 2-10
	Shahmohammadi et al. (2022)	Static and cyclic		Figure 2-11
Apex Joints	Lim (2001)	Static	Double channel	Figure 2-12
	Lim and Nethercot (2003)	Static		Figure 2-13
	Öztürk and Pul (2015)	Static		Figure 2-14 and Figure 2-15
	Zhang 2014	Static		Figure 2-16
	Peng et al. (2018)	Static		Figure 2-17
	Rinchen and Rasmussen (2019b)	Static	Single channel	Figure 2-18 and Figure 2-19
Eaves Joints	Lim and Nethercot (2002b)	Static	Double channel	Figure 2-20
	Zhang et al. (2016a)	Static		Figure 2-21
	Pouladi et al. (2019)	Static	Single channel	Figure 2-22
	Rinchen and Rasmussen (2019b)	Static		Figure 2-23
Knee Joints	Wilkinson and Hancock (2000)	Static	Closed Box	Figure 2-25

2.1.1. Experimental tests on portal frames

In the past, many experimental tests have been conducted on hot-rolled steel portal frames with tapered I-sections under various load cases (see Figure 2-1). Notably, Dowling et al. (1982) and Hwang et al. (1991) carried out experimental tests on portal frames with tapered members under gravity load and horizontal load (shake table test), respectively. The primary cause of failure in these experiments was lateral-torsional buckling (LTB) in the rafter member. Additionally, these studies revealed that fabrication costs could be reduced by up to 30% using tapered sections.

Junid (1992) also conducted experimental tests on tapered I-section portal frames and proposed modified guidelines for BS 5950 regarding the stability of portal frames based on his findings. Similar to the experiments by Dowling et al. (1982). LTB in the rafter member was observed during Junid's tests, as shown in Figure 2-1(c).

Li and Li (2002) tested two portal frames with a span of 9 meters under both vertical and horizontal loads. They found that significant compression combined with insufficient lateral restraints could lead to out-of-plane failure.

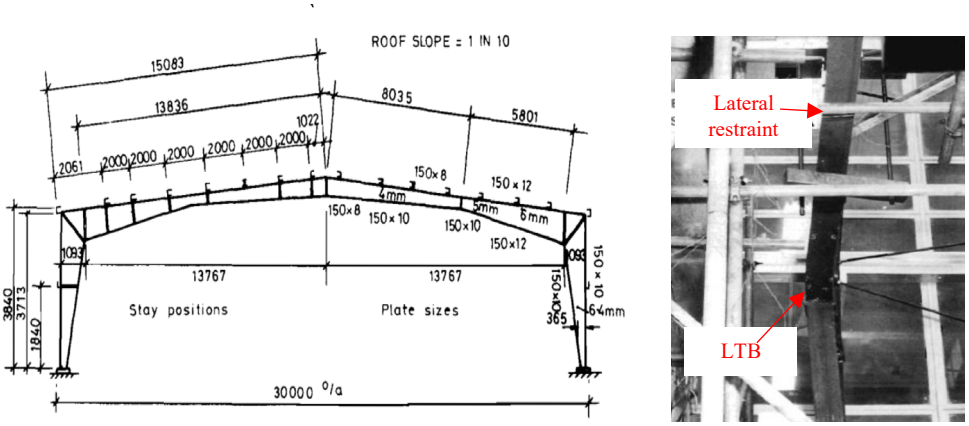

(a) Dowling et al. (1982)

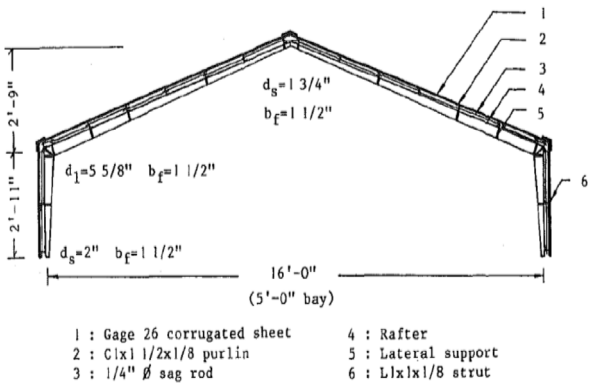

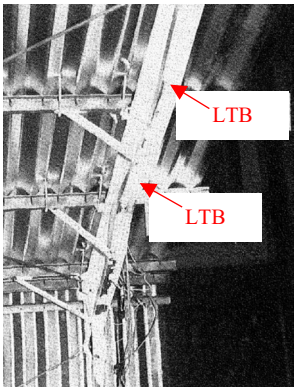

(b) Hwang et al. (1991)

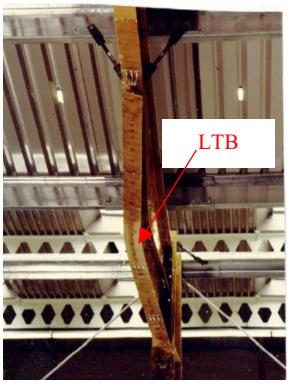

(c) Junid (1992)

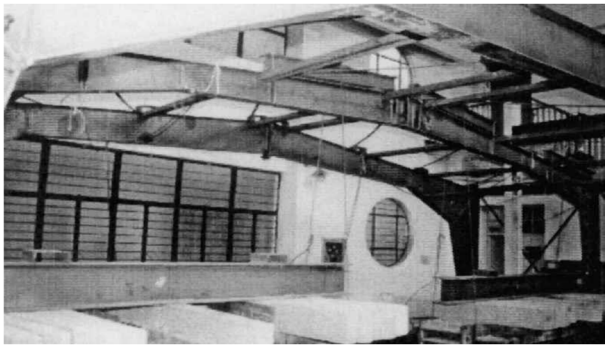

(d) Li and Li (2002)

Figure 2-1 Experimental tests on portal frames with tapered I-section and its failure modes

Lim and Nethercot (2002a) conducted tests on two portal frames (see Figure 2-2): one with smaller brackets and another with comparatively larger brackets. As shown in Figure 2-2(a), columns and rafters were restrained against lateral-torsional buckling at regular intervals. The frames failed due to buckling of the apex brackets. The tests revealed that

failure in the apex brackets was caused by the semi-rigidity of the joints, which led to higher bending moments at the apex joint than those calculated for a rigid joint. This underscores the need for practicing engineers to account for joint flexibility.

In a subsequent study, Lim and Nethercot (2004) demonstrated that the semi-rigidity of bolted moment connections primarily influences the serviceability deflection of the portal frame. Apex deflection can lead to problems such as water leakage, water ponding, and increased construction costs.

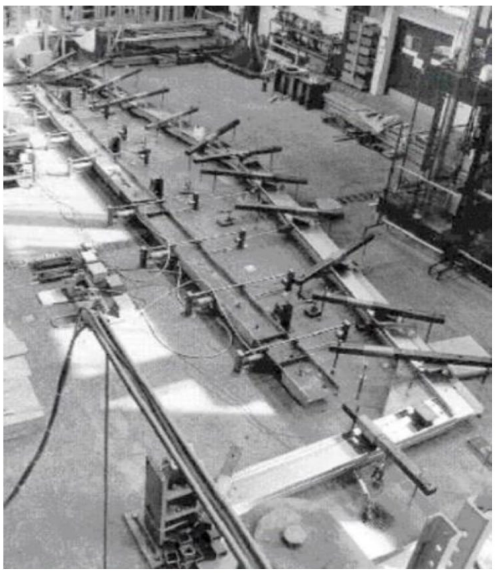

(a) Photograph of test set-up

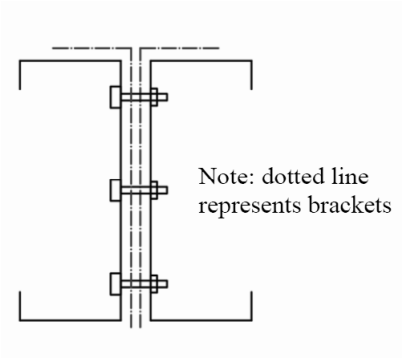

(b) Double shear bolted joint

Figure 2-2 Full scale CFS portal frame test with back-to-back channels after Lim and Nethercot (2002a)

Dubina (2008) investigated the behaviour of CFS pitched-roof back-to-back channel portal frames with bolted joints under horizontal loading (see Figure 2-3). The study involved two experimental tests aimed at evaluating the performance of these pitched-roof CFS portal frames under earthquake loading.

Figure 2-3 Details of experimental test setup for CFS portal frame after Dubina (2008)

Wrzesien et al. (2015) examined the behaviour of CFS portal frames with back-to-back channels, focusing on the effects of stressed-skin diaphragm action and joint flexibility. The test setup, as shown in Figure 2-4, included two gable frames and two integral frames. A total of six tests were conducted: two with gravity loading and four with horizontal loading. The main objective of the study was to achieve an economical design for the portal frame by considering shear forces from the roof sheeting and preventing damage to the fixings.

Figure 2-4 Experimental test setup CFS portal frame with back-to-back channels after Wrzesien et al. (2015)

Zhang et al. (2016a) conducted a full-scale test on a portal frame with back-to-back channels (see Figure 2-5). The aim was to assess the behaviour of the portal frame, particularly when intentionally designed with slender columns to induce failure due to the interaction of local and distortional buckling in the column members (Zhang et al., 2016b). In this study, the joints were designed to ensure that the columns would fail before the joints, using configurations that are not typical in practice.

(a) Test setup

(b) Deformed shape of the column at failure

Figure 2-5 Double channels portal frame test after Zhang et al. (2016a)

Blum and Rasmussen (2019a) focused on portal frames with back-to-back lipped channel sections, including columns, rafters, and knee braces. The joints of these portal frames (eaves and knee joints) were formed by connecting all members (rafters and columns) with back-to-back lipped brackets using bolts. Most tests were conducted on portal frames with unbraced columns (see Figure 2-6a). Failure in these frames was attributed to lateral-torsional buckling of the column member, which was initiated by out-of-plane movement of the knee brace-to-column joint bracket.

In contrast, for portal frames with braced columns (which included girts on the columns), failure occurred due to buckling of the apex bracket (see Figure 2-6b). This buckling caused significant vertical displacements at the apex, leading to frame failure at both the apex joint and the rafter at the knee-brace joint locations.

(a) Test set up (b) Buckling failure of apex bracket

Figure 2-6 CFS portal frame test with back-to-back channel section after Blum and Rasmussen (2019a)

Rinchen and Rasmussen (2020) conducted a series of experimental tests on CFS single-channel portal frames (see Figure 2-7a). As shown in Figure 2-7c, the primary mode of failure was local buckling in the channel section. A notable feature of single-channel section portal frames with sufficient lateral restraints is their ability to withstand significant flexural-torsional deformations from the onset of loading (see Figure 2-7b).

This behaviour is attributed to the non-coincident location of the shear center and centroid of the cross-sections, as well as the non-symmetric arrangement of bolts at the joints.

(a) Experimental test setup

(b) Large displacements due to torsion

(c) Local buckling in the column

Figure 2-7 Experimental test on single channel cold-formed steel portal frame after Rinchen and Rasmussen (2020)

Recently, Nguyen et al. (2024) conducted three tests on unbraced cold-formed aluminium portal frames with back-to-back channel sections, subjected to both gravity and horizontal loads. As shown in Figure 2-8, the main cause of failure was lateral-torsional buckling. Notably, all joints, which were formed using bolted back-to-back aluminium brackets, did not fail during the tests. The critical buckling load was evaluated and compared to the classical buckling theory proposed by Southwell (1932) and Meck (1977).

(a) Photographs of experimental test setup

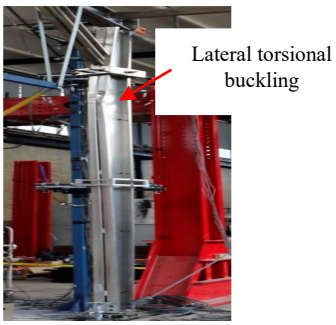

(b) Failure mode

Figure 2-8 Experimental test on back-to-back cold-formed aluminium portal frame conducted by Nguyen et al. 2024

Wilkinson and Hancock (1998) investigated the behaviour of portal frames with rectangular hollow sections (RHS). They conducted three experimental tests on portal frames with a 7-meter span. The primary objectives of these tests were to determine the ultimate load-carrying capacity of RHS portal frames and to assess their failure mechanisms. As shown in Figure 2-9, the main failure mode observed was in-plane buckling.

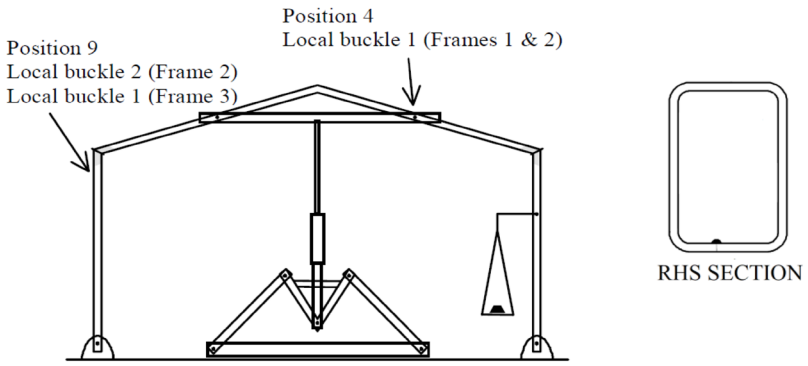

Figure 2-9 Experimental test on RHS portal frame and failure modes after Wilkinson and Hancock (1998)

Arrayago et al. (2020a) conducted experimental tests on cold-formed stainless-steel frames with rectangular hollow sections (RHS) under both horizontal and gravity loads. As shown in Figure 2-10a, lateral restraints were provided at the loading points. Figure 2-10b illustrates that rigid joint, directly welded to the RHS sections, were used in the portal frame. The failure of the frame, also depicted in Figure 2-10b, occurred due to in-plane buckling, which was influenced by the closed-box action of the RHS section. The aim of the research was to investigate the impact of material non-linearity on second-order effects by evaluating compliance with Eurocodes (EN 1993-1-4 and EN 1993-1-1).

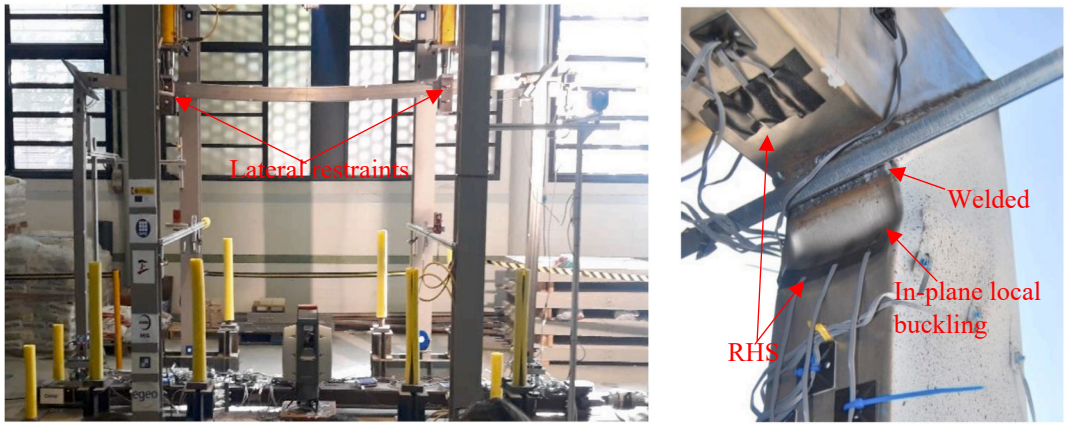

(a) Photograph of the experimental test set-up (b) Rigid joint

Figure 2-10 Details of the experimental tests conducted by Arrayago et al. (2020a)

Recently, Shahmohammadi et al. (2022) conducted full-scale experimental tests on two NTB portal frames under gravity and horizontal loading, respectively. As shown in Figure 2-11, minimal lateral restraints were provided through lateral braces at the column bases and near the apex joint. The tests revealed that the main failure mode for both specimens was in-plane buckling, attributed to the high torsional resistance of the NTB sections. This provides a significant structural advantage over tapered I-section portal frames, which require additional fly bracing to resist flexural-torsional buckling. In addition to the structural benefits, NTB portal frames help maintain health and hygiene by preventing birds from perching, which is advantageous for industries such as agriculture and pharmaceuticals. However, the joints, which use full penetration butt welds, are costly and require more manpower for construction. This suggests the need for further investigation into alternative jointing methods, particularly for eaves and apex joints. More details on this can be found in Chapter 3.

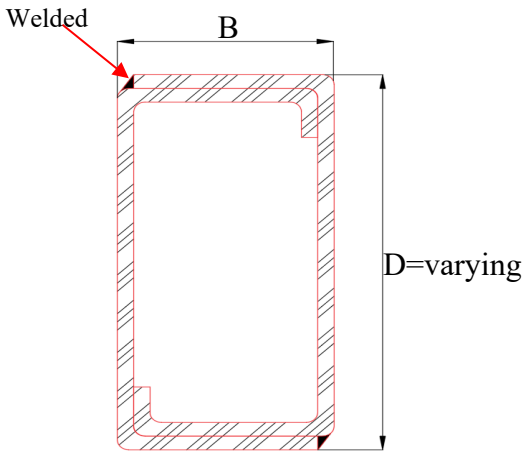

(a) Photograph of experimental test setup (b) NTB section

Figure 2-11 Details of experimental test conducted by Shahmohammadi et al. (2022)

2.1.2. Experimental test on apex joints

As shown in Figure 2-12, Lim (2001) described a test on apex joints where a single bracket was used to connect back-to-back channels. The main objective of the test was to evaluate the moment capacity of the apex bracket. The apex joint was fully restrained on the webs of the channels. However, the apex bracket buckled prematurely, leading to the failure of the joints.

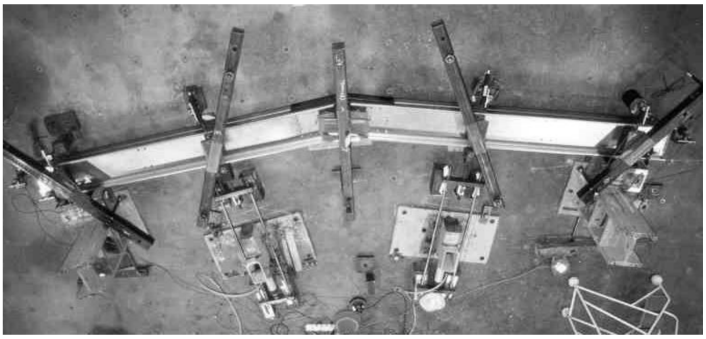

Figure 2-12 Photograph of test setup for apex joint after Lim (2001)

Building on the previous study, Lim and Nethercot (2003) conducted four tests on apex joints using a similar setup. In this study, double brackets were used to form the joint at the apex. As shown in Figure 2-13, the failure of the apex joint was attributed to web buckling of the channels. This failure occurred because the back-to-back brackets provided greater strength compared to the single bracket used in earlier tests.

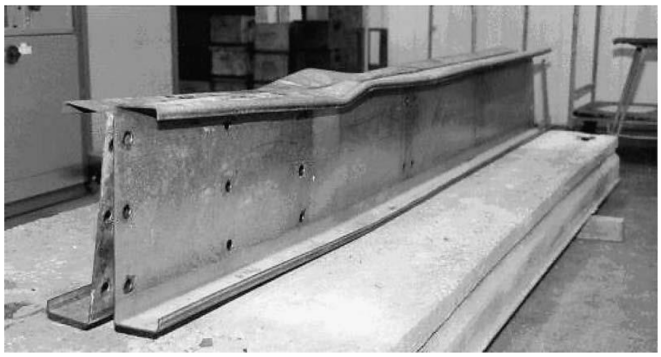

Figure 2-13 Failure of apex joint due to web buckling of channels after Lim and Nethercot (2003)

Öztürk and Pul (2015) conducted experiments on the apex joint of CFS portal frames with back-to-back sigma profile rafters, focusing on practical joint details for the portal frame. As shown in Figure 2-14, two types of apex plates were tested: one with a stiffener and one without. Figure 2-15 confirms that the apex bracket failed due to buckling. Although the stiffener in the apex plate did not significantly affect the overall failure mode, it was effective in restraining local buckling of the apex plate.

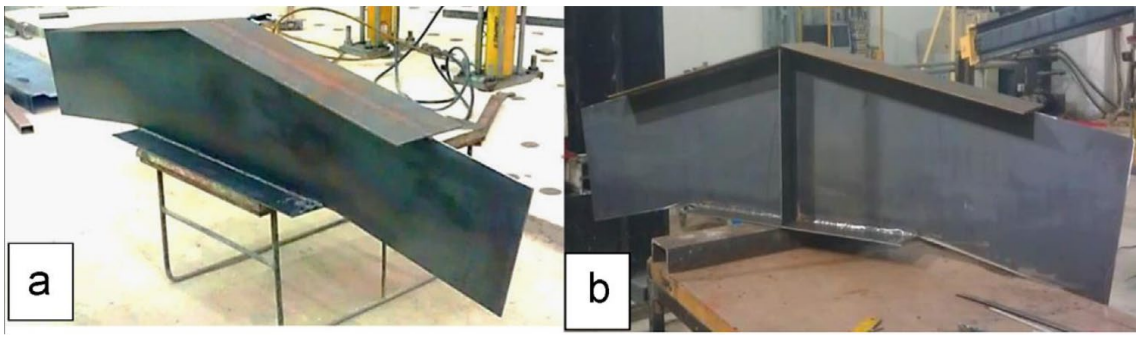

Figure 2-14 Without stiffener (a) and with stiffener(b) apex plates in the apex joint test after Öztürk and Pul (2015*)*

Figure 2-15 Buckling failure of apex brackets after Öztürk and Pul (2015)

As shown in Figure 2-16, apex joint tests using double channel sections were conducted by Zhang (2014) and Zhang et al. (2016a). The focus of these tests was to study the rotational stiffness behaviour of the joints used in portal frames. The results indicated that the bending moment has a more significant impact on the rotational behaviour of the joint compared to axial or shear forces. Additionally, a simplified tri-linear moment-rotation curve was derived from the test results and used to simulate the behaviour of the apex joint in the FE model of the portal frame, as depicted in Figure 2-26b.

Figure 2-16 Details of test setup after Zhang (2014)

Peng et al. (2018) conducted twelve component tests on apex joints with double channels, as shown in Figure 2-17a. The primary objective was to investigate the moment-rotation behaviour of the joints and to quantify their strength and initial stiffness. The tests revealed that the main cause of joint failure was buckling of the apex bracket web (see Figure 2-17b), which occurred irrespective of the channel depth or thickness.

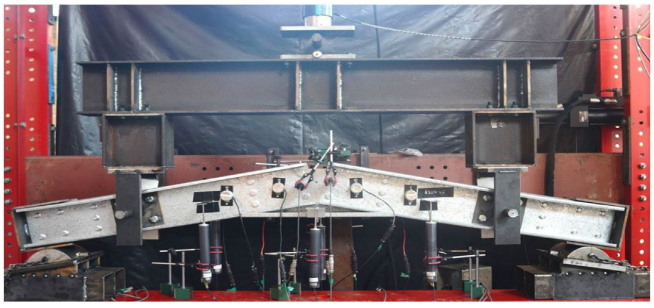

(a) Photograph of test setup

(b) Buckling of apex bracket

Figure 2-17 Details of the experimental test after Peng et al. (2018)

Rinchen and Rasmussen (2019b) conducted a series of tests to study the flexural behaviour of apex joints in single-channel CFS portal frames. Figure 2-18 shows the test setup used for the apex joint tests. As depicted in Figure 2-19, local buckling near the junction of the web and flange led to the failure of the apex joint at its maximum capacity. The failure mode indicates that the strength of the brackets was sufficient to transfer the moment at the apex joint effectively.

Figure 2-18 Photograph of the laboratory test set-up of apex joints Rinchen and Rasmussen (2019b)

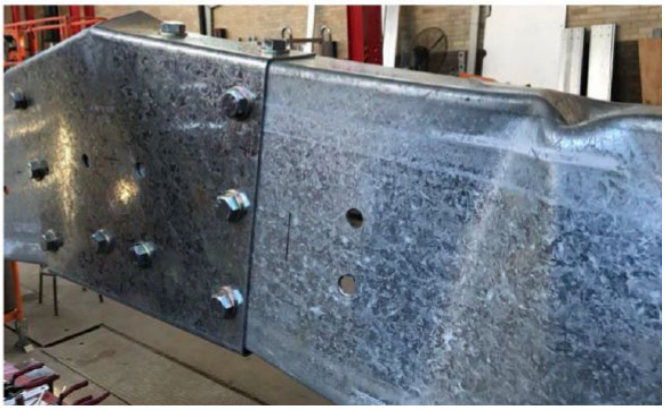

Figure 2-19 Local buckling of flange-web junction in the apex joint test after Rinchen and Rasmussen (2019b)

2.1.3. Experimental tests on eaves joints

Figure 2-20 shows the test setup for eaves joints conducted by Lim and Nethercot (2002b). The tests, which focused on studying the moment capacity of an eaves bracket,

involved a setup where a single eaves bracket was sandwiched between two channel sections. Full lateral restraints were applied to the webs of the channels. The eaves bracket prematurely buckled, leading to the failure of the joints.

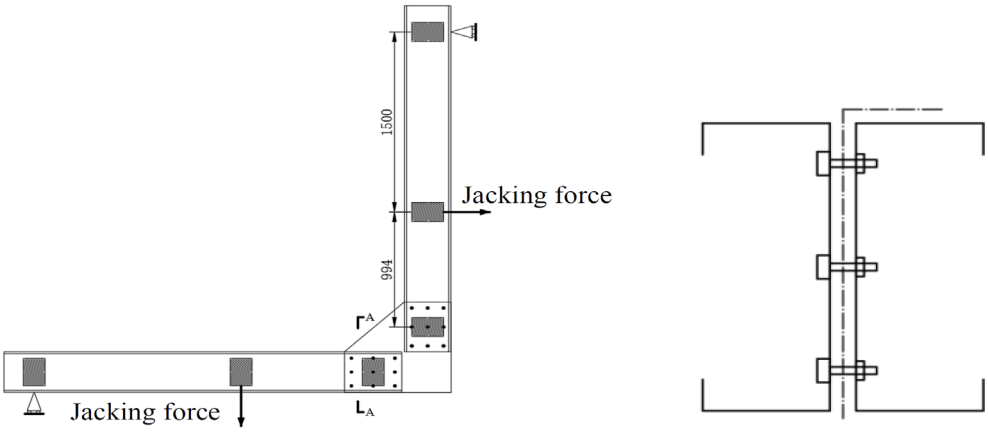

(a) Test setup (b) Singe bracket with double channels

Figure 2-20 Details of the experimental test for eaves joints after Lim and Nethercot (2002b)

Zhang (2014) and Zhang et al. (2016a) conducted experimental tests on eaves joints with back-to-back channels, as shown in Figure 2-23. The main objective of the study was to investigate the behaviour and rotational stiffness of these joints, which was subsequently used to inform the FE model of the portal frame.

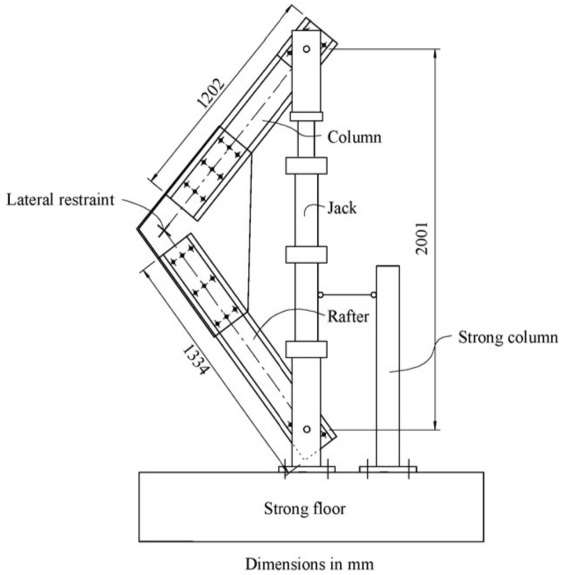

Figure 2-21 Details of test setup for eaves joint after Zhang et al. (2016a)

Pouladi et al. (2019) conducted a test on eaves joints formed with one channel and one bracket, as shown in Figure 2-22a. The experiment revealed shear failure of the screws, followed by twisting of the joint (see Figure 2-22b). After failure, it was observed that the screws were no longer intact with the bracket.

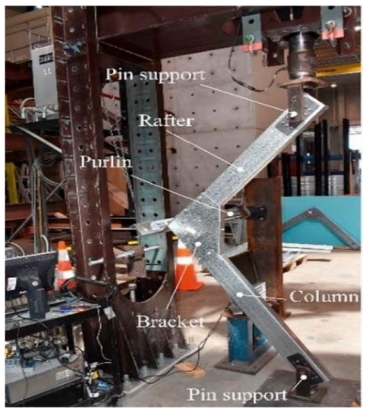

(a) Test setup

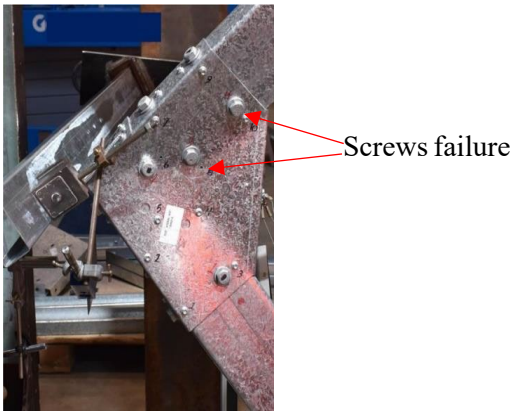

. (b) Failure mode in the eaves joint

Figure 2-22 Details of the test and failure mode at eaves joints after Pouladi et al. (2019)

Rinchen and Rasmussen (2019b) conducted a series of tests on eaves joints of single-channel portal frames using the setup shown in Figure 2-23. In these tests, bolts and screws were used to fabricate the eaves joint, connecting the web and lip of the channel to the bracket plate. As depicted in Figure 2-24, the failure of the eaves joint was attributed to the bending of the eaves brackets, followed by the fracture of the screws.

Figure 2-23 Photograph of the laboratory test set-up of eaves joint after Rinchen and Rasmussen (2019b)

Figure 2-24 Failure modes of eaves joint tests after Rinchen and Rasmussen (2019b) (a) Out-of-plane bending of bracket; (b) Screw fracture in the specimen; (c) Lip tearing in the specimen

Wilkinson and Hancock (2000) investigated the behaviour of five different types of knee joints for CFS portal frames with RHS, using the test setup shown in Figure 2-25. Figures 2-26 and 2-27 show the joint details for the CFS portal frames with RHS sections. The primary objective was to obtain moment-rotation curves for the joints under both closing and opening moments. It was observed that all the joints exceeded the plastic moment capacity of the RHS sections.

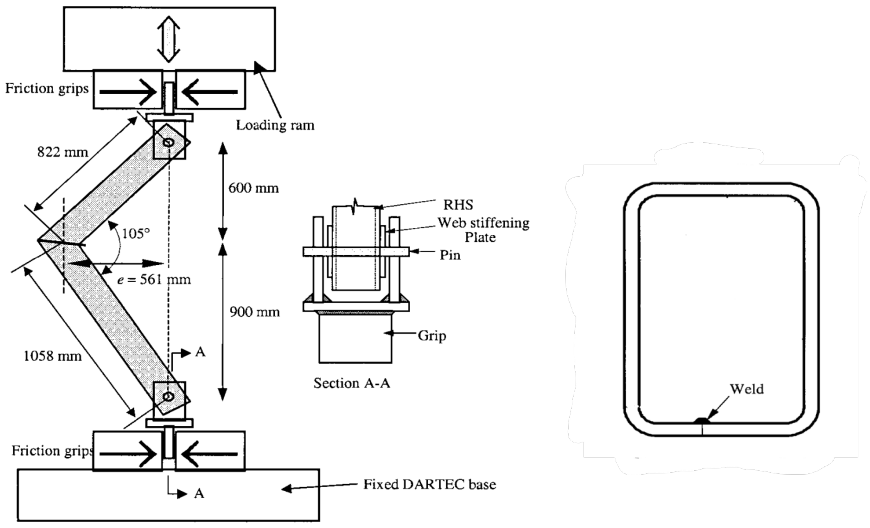

(a) Test setup (b) RHS cross section

Figure 2-25 Details experimental test for knee joints for portal frame and its cross-section after Wilkinson and Hancock (2000)

For welded stiffened and unstiffened joints under closing moments, failure was attributed to local buckling in the RHS sections. In contrast, joints subjected to opening moments failed due to cracks formed in the HAZ of the weld. The welded sleeve joint demonstrated higher stiffness compared to bolted end plate or bolted sleeve joints. Additionally, it facilitated plastic hinge formation in the RHS sections, thereby reducing the likelihood of weld cracks.

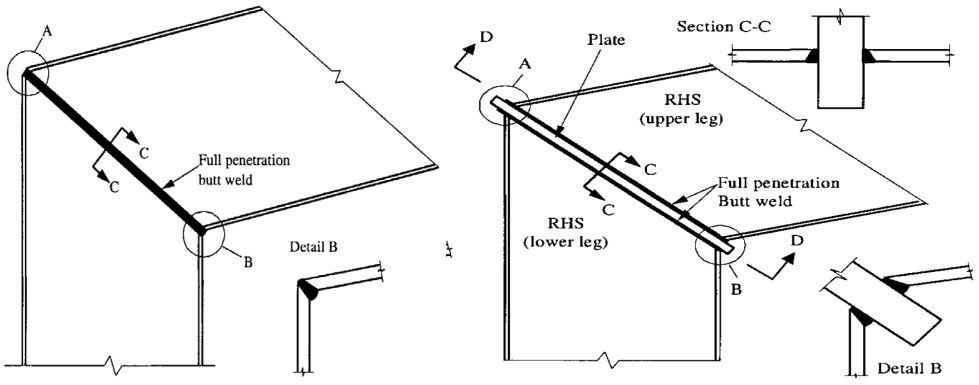

(a) Unstiffened welded joint (b) Stiffened welded joint

Figure 2-26 Details of the welded joints considered for the test after Wilkinson and Hancock (2000)

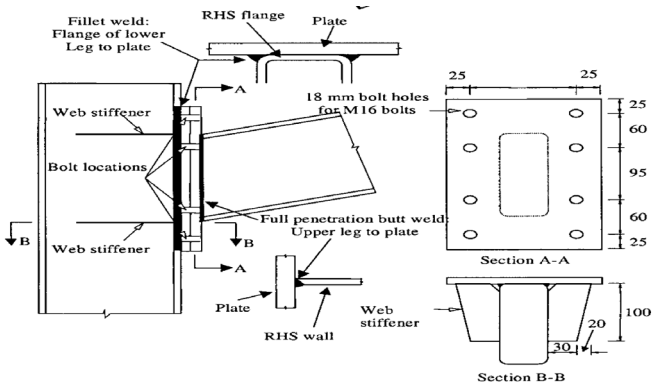

(a) Bolted end plate joint

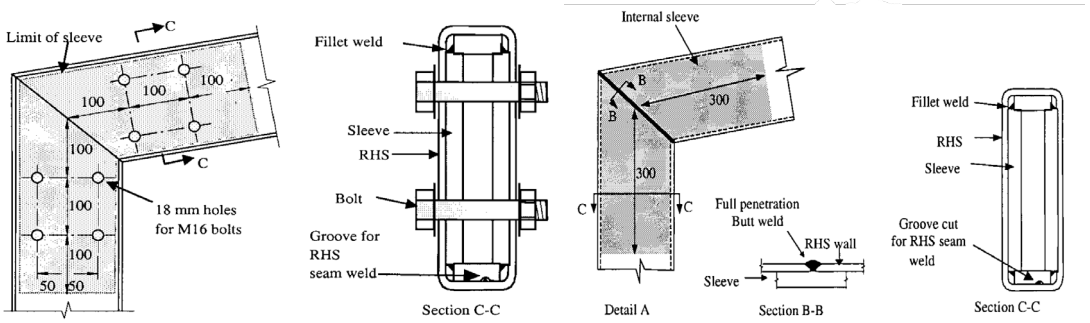

(b) Bolted sleeve joint (c) Welded sleeve joint

Figure 2-27 Details of the bolted end plate and sleeve joint considered for the test after Wilkinson and Hancock (2000)

2.2. Research on FE models

Given that experimental tests on full-scale portal frames, apex joints, and eaves joints are both time-consuming and expensive, it is essential to employ numerical methods to investigate their behaviour.

2.2.1. FEA on portal frames

Lim and Nethercot (2004) investigated a full 3-D linear shell FE model of portal frames to determine the deflection at the apex. To leverage symmetry, only half of the portal frame was modelled, as shown in Figure 2-28. It is important to note that geometric imperfections were not considered in this model.

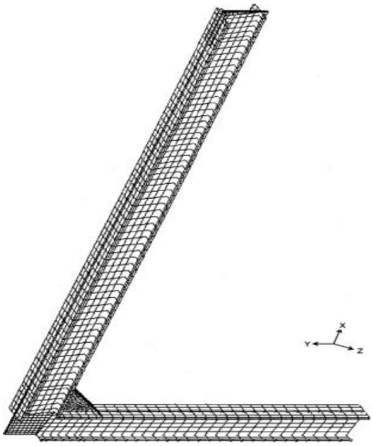

Figure 2-28 FE model developed for portal frame with back-to-back section by Lim and Nethercot (2004)

Dubina et al. (2010) described a FE modelling technique for portal frames, illustrated in Figure 2-29. This model incorporated all types of non-linearity and geometric imperfections and was validated against experimental tests. The aim of the study was to evaluate the effects of imperfections on the ultimate capacity of the portal frame. The results indicated that geometric imperfections did not significantly affect the ultimate capacity of the portal frame.

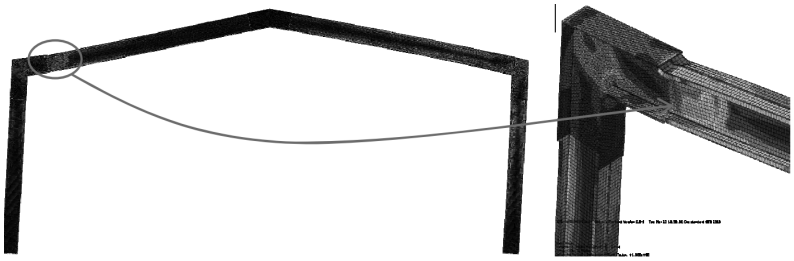

Figure 2-29 FE model for portal frame described by Dubina et al. (2010)

In the shell FE models of pitched roof portal frames with back-to-back channel sections, Zhang et al. (2015) incorporated the semi-rigid behaviour of joints by using spring-like elements at the intersections of the column and rafter centrelines. The bracket was divided into two parts, each connected to a reference node using multi-point restraints (MPC), as shown in Figure 2-30. The bolted joints were not explicitly modelled, and no member imperfections were simulated in the portal frame model.

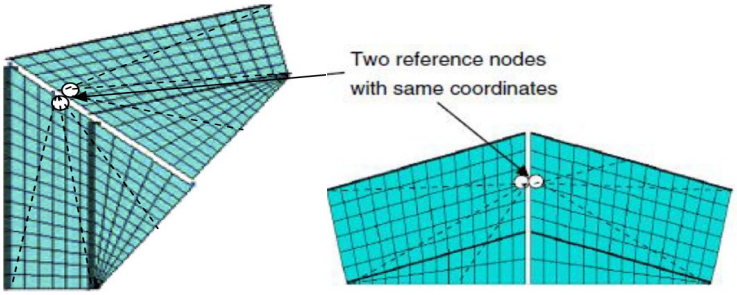

(a) Eaves joints (b) Apex joint

Figure 2-30 FE modelling technique use for portal frame at eaves and apex joints after Zhang et al. (2015)

Blum and Rasmussen (2019b) investigated a shell FE model of long-span cold-formed steel (CFS) single-channel portal frames, as shown in Figure 2-31. The model incorporated the semi-rigidity of bolted joints by using point-based fasteners to represent bolts. FEA results indicated that torsional buckling deformation of the columns is a primary behaviour in single-channel portal frames. To minimize these torsional deformations, bracing the columns with girts was recommended. However, the model did not account for member imperfections.

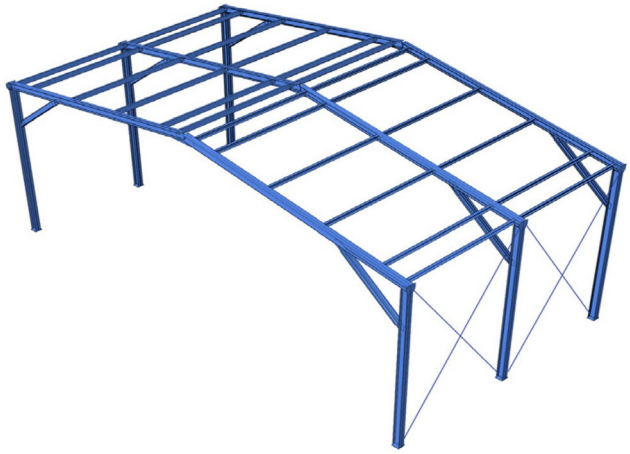

Figure 2-31 FE model developed by Blum and Rasmussen (2019b)

Rinchen and Rasmussen (2019a) investigated a shell FE model of long-span cold-formed steel (CFS) single-channel portal frames, as shown in Figure 2-32. The model incorporated the semi-rigidity of bolted joints by using point-based fasteners to represent

bolts. The FEA results indicated that torsional buckling deformation of the columns is a primary behaviour in single-channel portal frames. To minimize these torsional deformations, bracing the columns with girts was recommended. However, the model did not consider member imperfections.

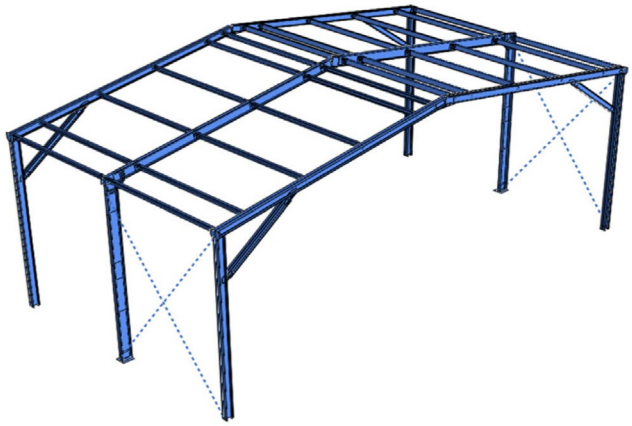

Figure 2-32 FE model developed by Rinchen and Rasmussen (2019a)

Recently, Chen et al., (2021) developed a FE model for portal frames with back-to-back channel sections, as illustrated in Figure 2-33a. This model was validated against the experimental tests described by Lim and Nethercot (2004). In the FE model, bolts connecting the rafters and columns to the brackets were represented using the 'SPRING-2' element, as shown in Figure 2-33b. The main goal of this investigation was to emphasize the importance of precise detailing and design of the brackets to ensure that failure occurs through the members rather than the joints. Notably, the model employed advanced analysis techniques, incorporating all relevant non-linearities, member imperfections, bracket imperfections, and frame imperfections.

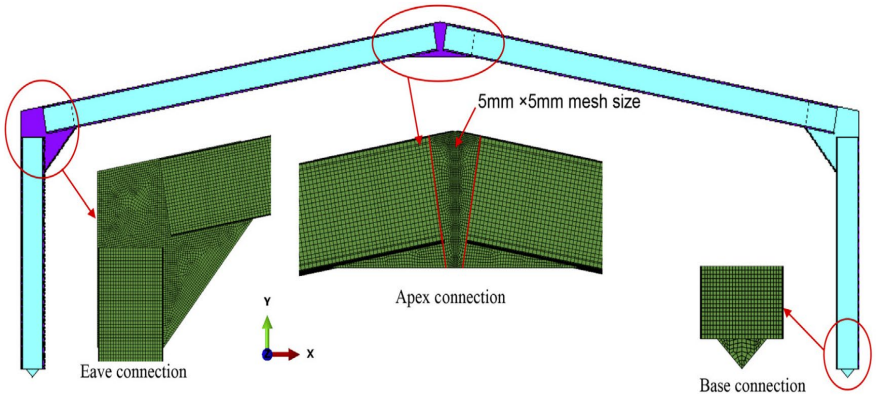

(a) FE model of portal frame

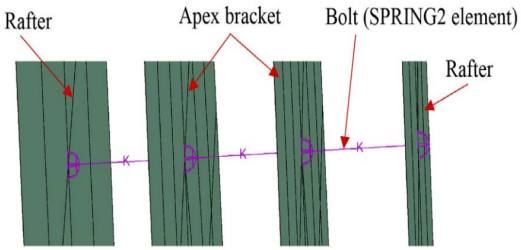

(b) Bolted connection at the joints

Figure 2-33 FE model described by Chen et al. (2021)

2.2.2. FEA on apex joints

Lim and Nethercot (2003) conducted a study using a FE model validated against experimental tests (see Figure 2-13), as illustrated in Figure 2-34, to investigate the ultimate moment capacity of apex joints with back-to-back brackets. The model, depicted in Figure 2-34, included only a single channel and applied pure bending at the end. Since the failure occurred in the channel rather than the brackets, this arrangement effectively and accurately predicts the ultimate moment capacity of the brackets. A parametric study using the validated FE model revealed that the strength of a typical-sized joint could be up to 20% less than that of the CFS sections. Therefore, web buckling, as caused by this discrepancy, must be considered in the design of such connections.

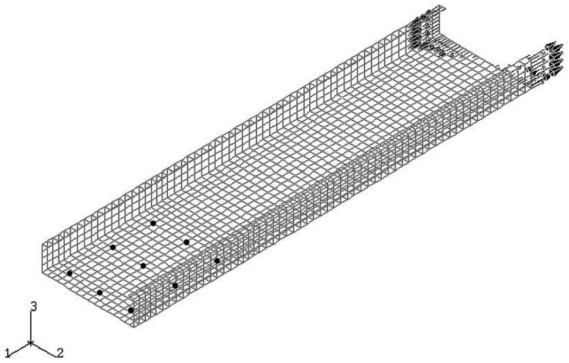

Figure 2-34 FE model of a single channel under pure bending after Lim and Nethercot (2003)

Blum and Li (2019) developed advanced shell FE models using ABAQUS to simulate apex joint tests. In their model, bolts in the connections were represented using "MPC beam" element. The bending moment versus apex rotation behaviour from the FE models (see Figure 2-35) was compared to experimental tests of the apex joints. The comparison revealed that the ultimate bending moment obtained from the FE models varied between 3% and 13% from the experimental results.

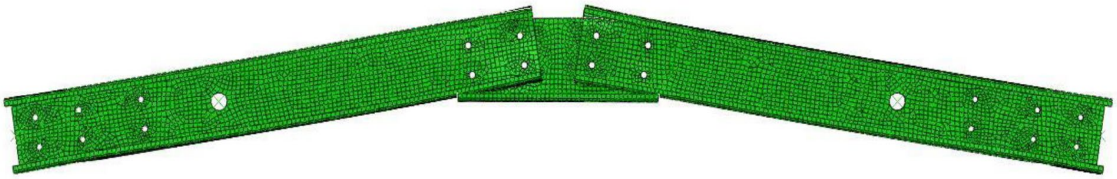

Figure 2-35 FE model of a single channel under pure bending after Blum and Li (2019)

Rinchen and Rasmussen (2019a) investigated the flexural behaviour of apex joints in CFS single-channel portal frames using the FE model depicted in Figure 2-36. This FE model was validated against corresponding experimental tests. The model simulated the behaviour of bolts and screws using fasteners, with reference nodes at the center of the MPC constraints subjected to gravity loads. They derived simplified multi-linear in-plane bending moment-rotation relationships and corresponding flexural stiffness values for the apex joints. These relationships effectively represent the semi-rigidity of the joints.

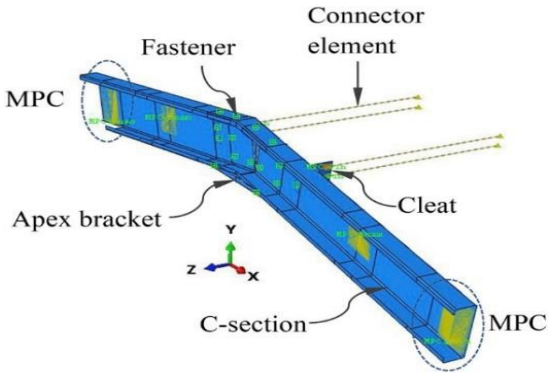

Figure 2-36 FE model of an apex joint after Rinchen and Rasmussen (2019a)

Phan et al. (2020) developed an FE model of the apex joint, as shown in Figure 2-37, which was validated against the experimental tests conducted by Lim and Nethercot (2003). This FE model incorporated material nonlinearity, geometric imperfections, and accurate bolt-bearing behaviour. The validated model was then used to evaluate the accuracy of the analytical approach for predicting the ultimate bending capacity of CFS bolted moment connections, taking into account bimoment effects across a range of cross-sectional dimensions.

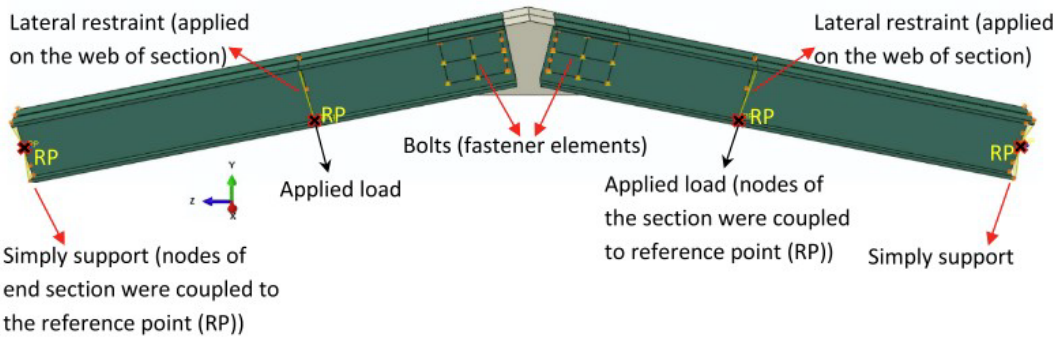

Figure 2-37 FE model of an apex joint after Phan et al. (2020)

Mojtabaei et al. (2020) validated an FE model of apex joints, shown in Figure 2-38, against the experimental tests by Lim and Nethercot (2003). Their study focused on local buckling failure adjacent to moment-resisting bolted joints in CFS back-to-back channels connected to apex brackets through their webs. The sensitivity study revealed that increasing the length of the bolt group and the thickness of the channels reduces the detrimental effects of local

buckling. Conversely, eccentric loading increases the likelihood of local buckling. Based on their findings, a practical design equation was developed for predicting the moment capacity of CFS channels, demonstrating a wide range of applicability.

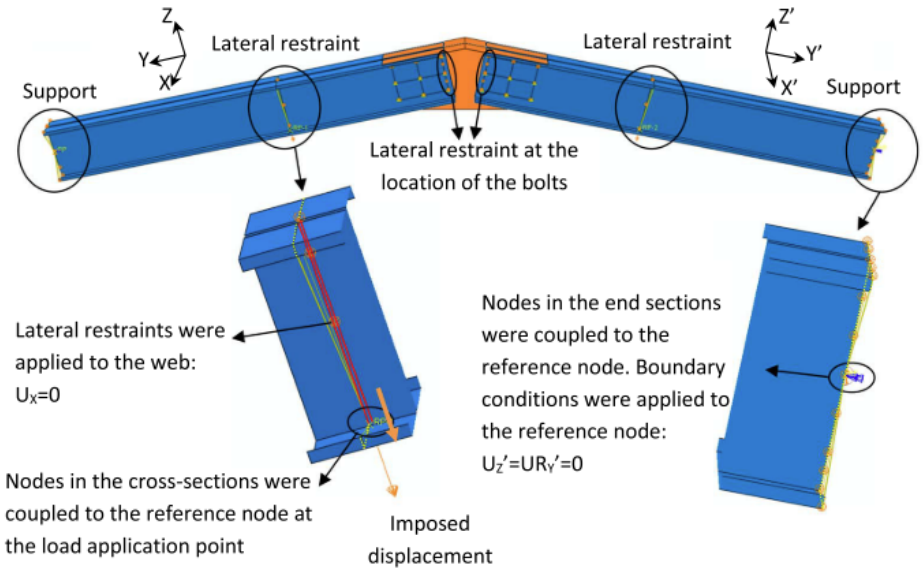

Figure 2-38 FE model of an apex joint after Mojtabaei et al. (2020)

Chen et al. (2021) conducted a numerical study to investigate the importance of bracket details for the apex joint of a portal frame using FE models (see Figure 2-39 and Figure 2-40). Their study, validated against experimental tests by Lim (2001) used a fully restrained FE model that considered only closing moments. The research aimed to highlight the impact of detailed bracket designs on the apex joint's performance.

Chen et al. (2023a) extended their previous work, addressing additional research gaps by considering both closing and opening moments for the partially restrained apex bracket (see Fig. 2-41). This extension aimed to provide a more comprehensive understanding of the joint's behaviour under varied loading conditions.

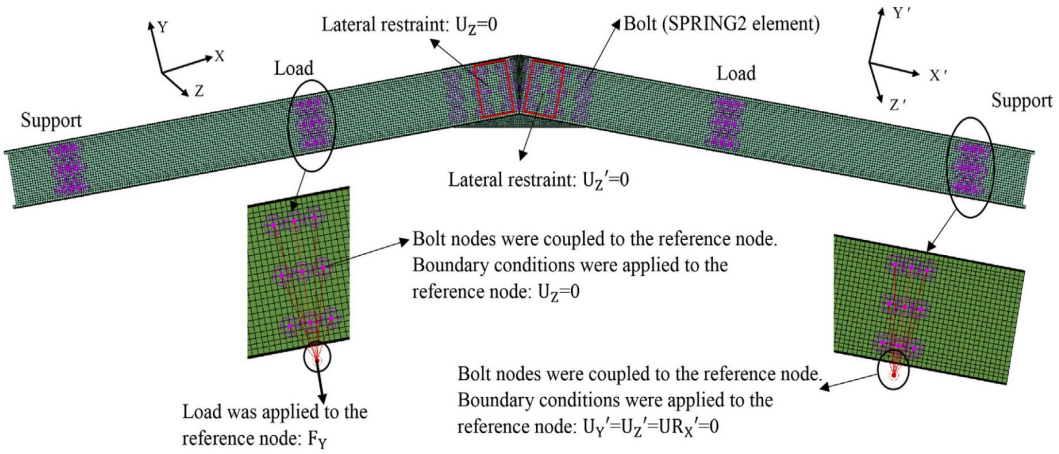

Figure 2-39 FE model developed for apex joint by Chen et al. (2021)

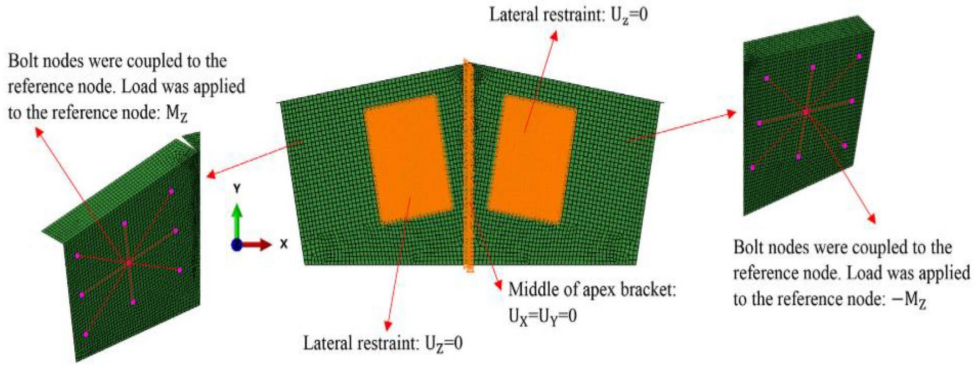

Figure 2-40 FE model of a simplified apex bracket after Chen et al. (2021)

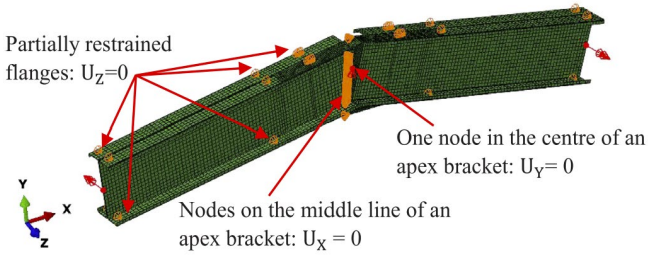

Figure 2-41 FE model described by (Chen et al. 2023a) for partially restrained apex bracket

Paul et al. (2023) developed a FE modelling technique to investigate the behaviour of apex joints formed through bolted-side plates for NTB portal frames. Their study included a sensitivity analysis to identify key parameters affecting the joint's

performance, which was utilized for a comprehensive parametric study. Further details of this investigation can be found in Chapter 4.

2.2.3. FEA on eaves joints

Pouladi et al. (2019) developed a FE modelling technique for eaves joints in single-channel portal frames. The model is capable of estimating both lower and upper bound strengths of the eaves joints, depending on whether screw failure is considered. The FE model uses point-based fasteners to represent bolts and screws, with the stiffness of these fasteners calculated using the equations proposed by Zaharia and Dubina (2006). Details of the loading and boundary conditions for the FE model are provided in Figure 2-42.

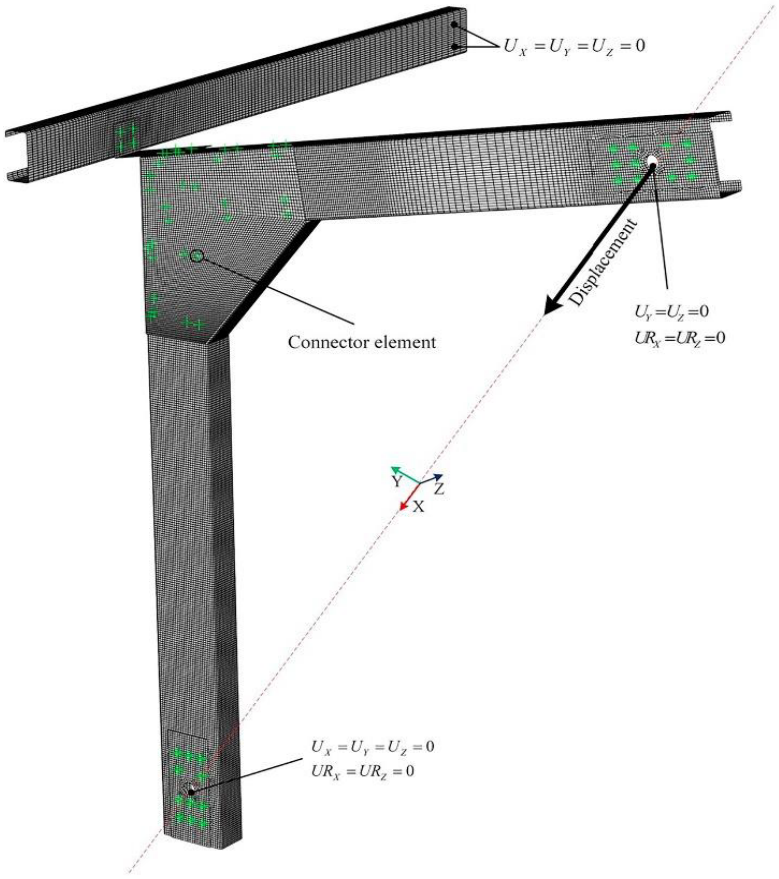

Figure 2-42 FE model of the eave joints after Pouladi et al. (2019)

To study the flexural behaviour of eaves joints, Rinchen and Rasmussen (2019a) developed a FE model validated against experimental tests (see Figure 2-43). The modelling approach was similar to that used by Pouladi et al. (2019), employing point-based fasteners to represent bolts and screws. In this model, horizontal loads were applied to the reference nodes located at the centre of the MPC.

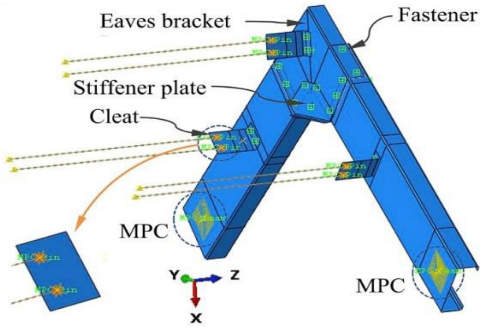

Figure 2-43 FE model of the eave joints after Rinchen and Rasmussen (2019a)

2.3. Research on the design of CFS portal frames

2.3.1. Moment capacity of apex joint

Based on the design of the full-scale frame tests, Lim (2001) conducted component tests on apex joints, each consisting of a single bracket (see Figure 2-12). The results of these tests were utilized to validate a non-linear elasto-plastic FE model. From this model, Lim (2001) proposed an equation to predict the strength of fully restrained apex bracket, denoted as (M_{1fa}^{c}):

$$M_{1ab}^{c} = \frac{f_y b_a^2 t_b}{4}\left[2.88 - 2.88\left(\frac{b_a}{a_a}\right) + 1.26\left(\frac{b_a}{a_a}\right)^2\right] \qquad \text{Closing moment} \qquad 2.1$$

Where a_a and b_a are defined in Figure 2-44. However, this equation is limited, only valid for $0.4 \leq b_a/a_a \leq 1.0$, an apex bracket thickness of 3 mm, an apex bracket yield stress of 280 N/mm^2, and a frame pitch of 10^0.

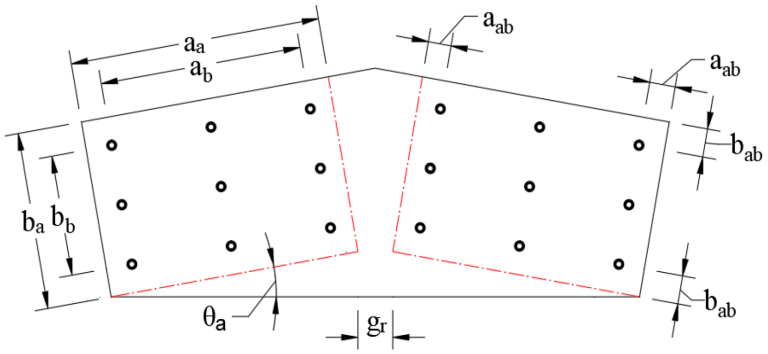

Figure 2-44 Diagram showing the parameter of an apex bracket (the dotted line represents the outline of channels)

Due to the back-to-back arrangement and the observed failure of the apex bracket in the tests conducted by Lim (2001), only the brackets need to be modelled (i.e., no channels were included). The FE idealization shown in Figure 2-44 was validated by Chen et al. (2021) against experimental tests. The validated FE model was then used in a parametric study to develop a design equation for the moment capacity of the apex bracket. However, this design guidance was limited to apex brackets with only a top stiffener and was restricted to cases considering only opening moments and fully restrained brackets.

Chen et al. (2023a) extended this work by considering both single and double apex brackets with partial restrained, consistent with New Zealand practices. They also addressed both opening and closing moments (or gravity and wind uplift loads) on apex joints. This study proposed unified design equations based on a parametric study that included 5,040 finite element models. The unified equations developed from the study cover different types of brackets and load cases.

The proposed equations are as follows:

For partially restrained single bracket

$$M_{1ab}^{c} = 2.1323\, a_a^{0.4162} b_a^{1.1194} f_y^{0.6439} t_b^{1.4669} 10^{-5} \qquad \text{Closing moment} \qquad 2.2$$

$$M_{1ab}^{o} = 5.1645 a_a^{0.5380} b_a^{1.0979} f_y^{0.89} t_b^{0.5124} 10^{-5} \qquad \text{Opening moment} \qquad 2.3$$

For partially restrained double brackets

$$M_{2ab}^{c} = 1.7463\, a_a^{0.4380} b_a^{1.0979} f_y^{0.7678} t_b^{1.6134} 10^{-5}$$ Closing moment 2.4

$$M_{2ab}^{o} = 5.3415 a_a^{0.4652} b_a^{0.9519} f_y^{0.6412} t_b^{1.7447} 10^{-5}$$ Opening moment 2.5

2.3.2. Moment capacity of eaves joint

Lim and Nethercot (2002b) used the FE model shown in Figure 2-45 to determine the moment capacity of the eaves bracket, which is form the eaves joint with one bracket bolted to the back-to-back channels (see Figure 2-17). The design equation for the moment capacity of fully restrained eaves brackets (M_{1eb}) was proposed by the parametric studies.

$$M_{1eb}^{c} = f_y a_e^2 t_b \left[0.0675 + 0.4886 \left(\frac{b_e}{a_e}\right) - 0.1466 \left(\frac{b_e}{a_e}\right)^2\right]$$ Closing moment 2.6

Where a_e and b_e are defined in Figure 2-45. However, this equation is limited, only valid for $0.05 \leq b_e/a_e \leq 0.90$, an eaves bracket thickness of 3 mm, an eaves bracket yield stress of 280 N/mm^2, and a frame pitch of 0°.

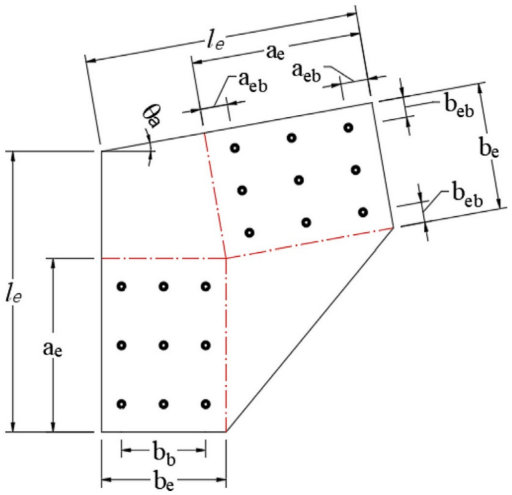

Figure 2-45 Diagram showing the parameter of an eaves bracket (the dotted line represents the outline of channels)

However, Eq-2.6 is limited to eaves joints fully restrained against lateral torsional buckling, for use under a closing moment and an eaves bracket details having a stiffener along its hypotenuses. Chen et al. (2023b) described a finite element study comprising 7,560 models, that addressed all these limitations. Unified equations were proposed that can be used for the

design of eaves brackets in practical partially restrained eaves joints, as found in New Zealand practice, both closing and opening moments, and different arrangements of stiffeners in the detail of the eaves bracket, including both single and back-to-back eaves brackets. The equations are presented as follows:

For partially restrained single bracket

With top-bottom stiffener

$$M_{1eb}^{c-t-b} = 1.0117\ a_e^{0.9364} b_e^{0.3450} f_y^{0.4134} t_b^{1.9766} 10^{-4} \quad \text{Closing moment} \quad 2.7$$

$$M_{1eb}^{o-t-b} = 4.1544\ a_e^{0.8741} b_e^{0.5352} f_y^{0.5929} t_b^{1.6176} 10^{-5} \quad \text{Opening moment} \quad 2.8$$

With bottom stiffener

$$M_{2eb}^{o-b} = 2.2186 a_e^{0.8692} b_e^{0.3078} f_y^{0.4021} t_b^{1.7695} 10^{-4} \quad \text{Opening moment} \quad 2.9$$

For partially restrained double bracket

With top-bottom stiffener

$$M_{2eb}^{c-t-b} = 2.4022\ a_e^{1.2674} b_e^{-0.050} f_y^{0.4401} t_b^{2.1270} 10^{-4} \quad \text{Closing moment} \quad 2.10$$

$$M_{2eb}^{o-t-b} = 4.0847 a_e^{1.1053} b_e^{0.3166} f_y^{0.7} t_b^{1.6985} 10^{-5} \quad \text{Opening moment} \quad 2.11$$

With partially restrained bottom stiffener

$$M_{2eb}^{o-b} = 2.3248\ a_e^{1.1039} b_e^{0.1470} f_y^{0.4332} t_b^{1.8391} 10^{-4} \quad \text{Opening moment} \quad 2.12$$

2.3.3. Rotational stiffness of the joint

In practical applications, the analysis and design of steel framing systems rely on simplified assumptions concerning the behaviour of connections. These connections are typically assumed to be either perfectly pinned or fully rigid (Hayalioglu and Degertekin, 2005). In general, it is more appropriate to classify a joint as semi-rigid, as this designation accounts for behaviour where relative rotations take place while transmitting bending moments between neighbouring members.

CFS portal frames are well-known to have semi-rigid joints. The assumption of pinned or rigid joints may result in an unconservative design; the apex joints may be designed and detailed to carry a smaller bending moment than there would be in practice (due to the re-distribution of the bending moment from the eaves to the apex in portal frames having flexible joints).

Furthermore, the mechanical behaviour of joints plays a crucial role that should not be overlooked during both the analysis and design stage, as well as the safety assessment phase. Unfortunately, in many cases, designers tend to underestimate the actual behaviour of joints within steel buildings. Neglecting the true behaviour of joints can have significant implications for the overall structural integrity and safety of the building. Therefore, it is essential to consider the behaviour of joints to ensure the reliability and safety of steel structures Msabawy and Mohammad (2019).

As described by Lim and Nethercot (2004), Rinchen et al. (2019) deflection and capacity of the portal frame could be obtained by incorporating the rotational stiffness of the semi-rigid joint in the beam model. The rotational stiffness (K) of the typical bolt group (see Figure 2-46) can be predicted by the following equation:

$$K = k_b \sum_{i=1}^{n} d_i^2 \qquad 2.13$$

Where, k_b is the bolt-hole elongation stiffness of the interconnected plates system for joints comprised of two brackets with two channels; d_i is the distance from the bolt hole to the center of rotation of the bolt group. Detailed calculation for bolt-hole elongation stiffness (k_b) can be found Appendix A.

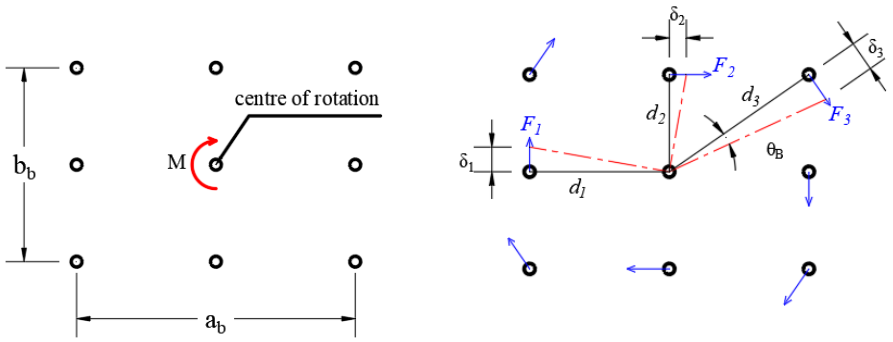

(a) Dimension of the bolt group (b) d_i in the bolt group

Figure 2-46 Diagram showing the 3x3 bolt group

In a CFS portal frame, two types of joints are considered: single-shear and double-shear (see Figure 2-47). In a single-shear joint, the load is transferred through a single-shear plane. The connection typically involves fastening one member to another through fasteners like screws or bolts. In a double-shear joint, the load is distributed and transferred through two shear planes. It is commonly used in the back-to-back channel section bolted with the brackets.

It is very important to estimate the bolt-hole elongation stiffness (k_b), to predict the rotational stiffness of joints in a CFS portal frame. The bolt-hole elongation stiffness for single shear joints can be determined from the study conducted by Zaharia and Dubina (2006). However, detailed calculations for bolt-hole elongation stiffness in double shear joints have been provided by Lim and Nethercot (2004). A comprehensive explanation of the detailed calculation can be found in Figure 2-48.

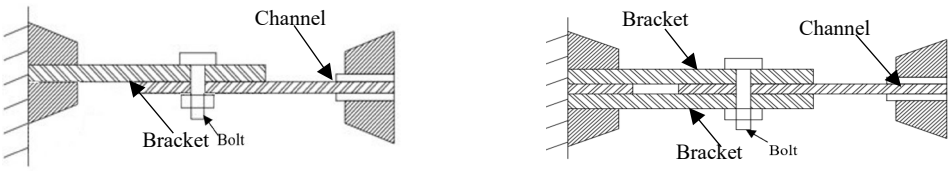

(a) Bolts in single shear (b) Bolts in double shear

Figure 2-47 Typical joints in portal frame

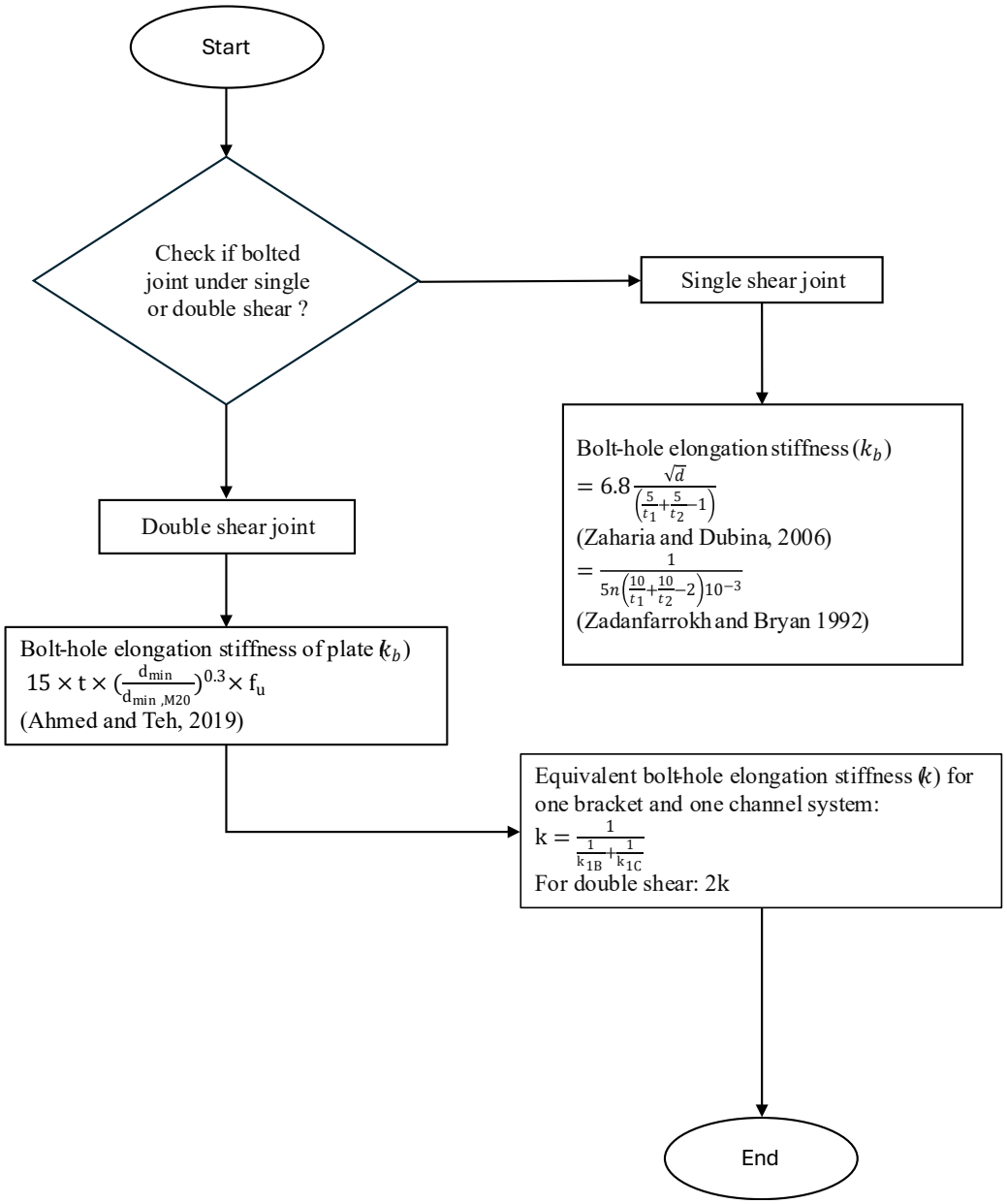

Figure 2-48 A flowchart for calculation process to estimate the bolt-hole elongation stiffness of joints in CFS portal frames

2.3.4. Prediction of capacity for portal frame

In literature, two methods could be found which could be used to predict the capacity of portal frame. Rinchen et al. (2019) described the method in detail. These methods are direct strength method (DSM) and direct design method (DDM), respectively.

DSM based method:

Members in the portal frame must satisfy the following equation:

$$\frac{P^*}{P} + \frac{M^*}{M} \leq 1.0 \qquad 2.14$$

Where P^* and M^* represent the axial compression and bending moment, respectively, which need to be calculated through the analysis of the portal frame. P and M denote the design capacities of the member, which can be calculated using the DSM method specified in AS/NZ 4600 (2018) or AISI S-16 (2016).

DDM based method:

For the system-based design, the limit state criteria requires that the applied factored loads do not exceed the factored nominal resistance of the structure (see Eq-2.15).

$$\emptyset R_n \geq \sum \gamma_i \omega_{ni} \qquad 2.15$$

Where R_n, ω_{ni}, $\gamma_i$and $\emptyset$ are the nominal system strength, nominal loads, load factors and system resistance factor respectively.

The design process involves the application of a load increment factor (α) to the factored nominal loads (i.e. $\alpha \sum \gamma_i \omega_{ni}$) and running an advanced analysis by gradually increasing from 0 to 1, its ultimate value (α), at which the structure reaches its limit state by yielding and/or buckling. In the ultimate limit state, $\alpha \sum \gamma_i \omega_{ni} = R_n$, and realizing that $\emptyset R_n = \sum \gamma_i \omega_{ni}$ in this state, the limit state criterion in terms of the load factor and system resistance factor is obtained as $\alpha' \geq 1/\emptyset$.

2.4. Research gaps

From the comprehensive literature review presented in this chapter, several critical research gaps have been identified.

- While portal frames with tapered I-sections, back-to-back channel section, single channel section, closed box section with end plate connection system have been extensively investigated, research on frames using tapered box sections remains scarce.
- No existing work has explored the structural behaviour of portal frames with tapered box sections where the connections are formed using bolted side-plate joints
- There is currently no robust validated FE modelling approach available to capture the behaviour of NTB portal frames with bolted side-plate connections.
- A simplified method for predicting the load-carrying capacity of portal frames is not available in the existing body of knowledge.

Chapter 3 Shell FE model of portal frame

3.1. Introduction

According to AS/NZ 4600 (2018), advanced analysis for steel structures with compact cross-sections involves geometric and material nonlinear analysis, including imperfections. This approach differs from traditional design methods, which typically involve separate structural analysis and individual member checks. Advanced analysis, on the other hand, captures global frame and member instabilities, reducing the need for additional member checks (Gardner et al., 2019).

Recent research has extensively explored advanced design methods, primarily for structural systems with hot-rolled sections. In conventional FEA for portal frames, beam elements are often used to represent structural members. However, these elements may not accurately capture the semi-rigid behaviour of joints, which can significantly impact the response of CFS portal frames (Gardner et al., 2019). Therefore, it is crucial to use shell FE models that accurately simulate the geometry of joints, members, and the behaviour of fasteners in portal frames.

Chen et al. (2021) investigated the behaviour of CFS portal frames by incorporating geometric imperfections into their FE models. However, their study focused on back-to-back channel sections with bracket connections, rather than box or NTB portal frames. While there is considerable literature on numerical studies of CFS portal frames (Blum and Rasmussen, 2019a; Lim, 2001; Lim and Nethercot, 2004; Lim and Nethercot, 2002a; Rinchen and Rasmussen, 2019a; Zhang et al., 2016a) research on NTB portal frames with bolted-side plate connections is lacking. Existing studies on portal frames with box or NTB sections (Arrayago et al., 2020a, 2020b; Shahmohammadi et al., 2022) have focused

on rigid bolted connections or welded end plate connections rather than bolted-side plate systems.

This chapter presents a FE modelling technique for NTB portal frames with bolted-side plates, validated against experimental tests reported by Shahmohammadi (2019). Details of the experimental tests and the FE modelling approach are discussed in the following sections.

3.2. Details of previously reported portal frame tests

3.2.1. Test conducted by Shahmohammadi (2019)

Shahmohammadi (2019) conducted full-scale test on the NTB portal frame under gravity load, representing the closest test for the NTB portal frame. Figure 3-1 shows photograph for the frame test and minimum no of lateral restraints were employed to take the advantage of the tapered box member. As can be seen, the frame was loaded using the four set water tanks and the pinned supports were at the column bases (See Figure 3-2). The average dimensions of the NTB section used in the tests are shown in Figure 3-3. The average measured material properties of the NTB section are summarised in Table 3-1. This frame had a span of 18.1m, column height of 4.27 m, and pitch of 5°, and joints of this frame is formed through the bolted end plates. Details of the joints is shown in Figure 3-3.

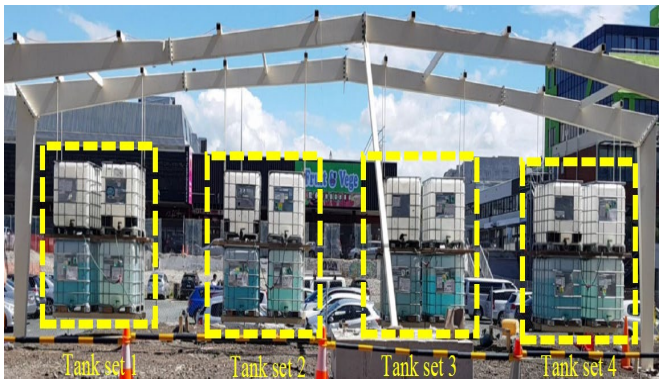

Figure 3-1 Photograph of the NTB portal frame testing under gravity load (Shahmohammadi, 2019)

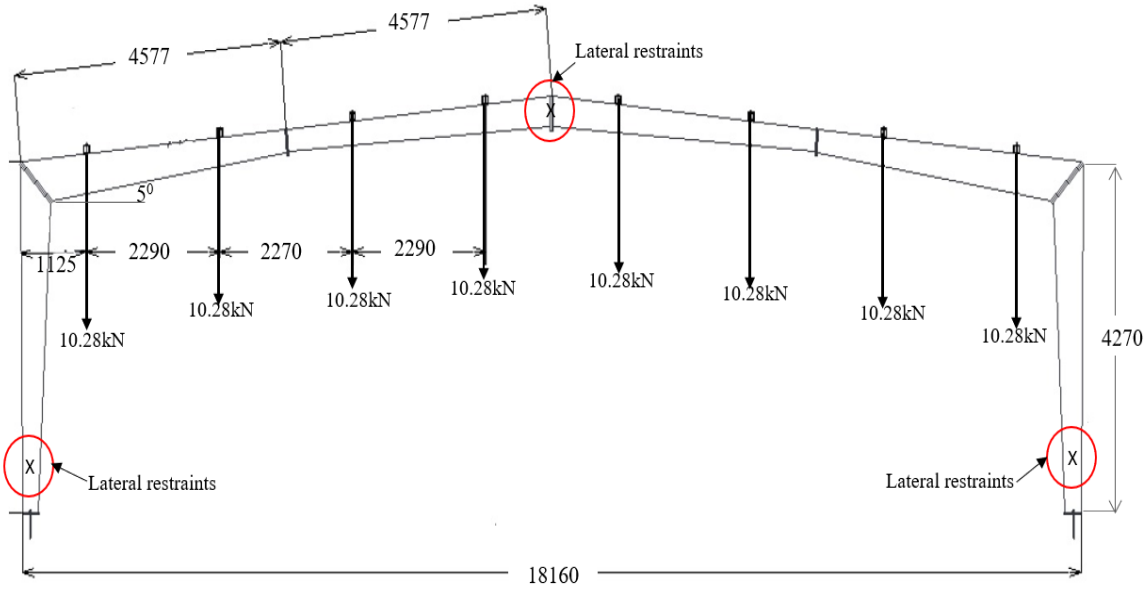

Figure 3-2 Details of dimensions and loadings applied for the test by Shahmohammadi, (2019) (All dimensions are in millimeters)

Table 3-1 Material Properties from the tensile coupon tests conducted by Shahmohammadi (2019)

Test specimen No.	Thickness (t)	Yield stress (f_y)	Ultimate strength (f_u)
	(mm)	(N/mm^2)	(N/mm^2)
1	4.17	256	389
2	4.21	263	388
3	4.29	246	375
4	4.17	266	393
Mean	4.20	258	386

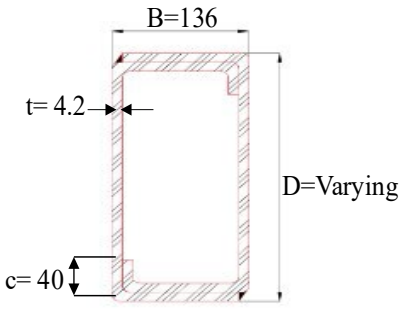

All dimensions are in millimeters

Figure 3-3 Details of cross section after Shahmohammadi, 2019

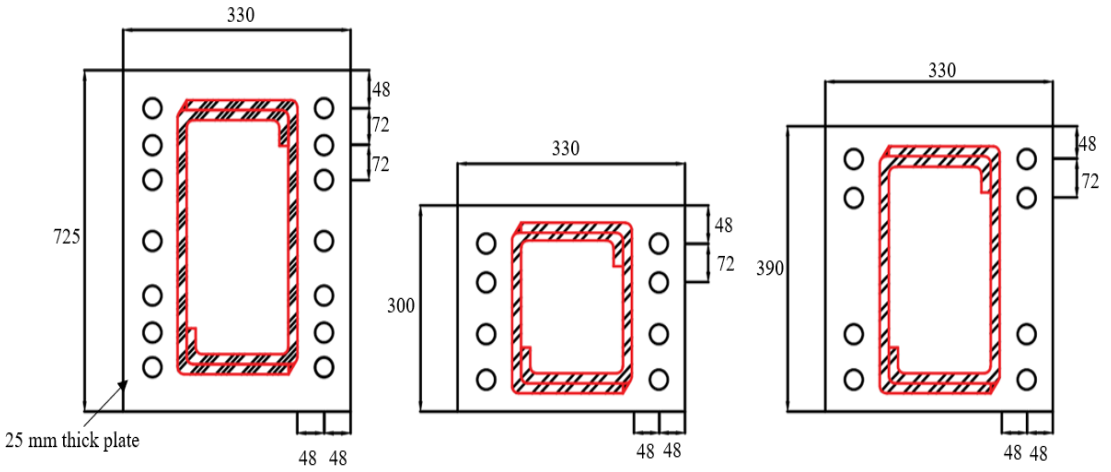

(a) Eaves (b) Mid rafter (c) Apex

Figure 3-4 Connection details at eaves, mid rafter, and apex joint after Shahmohammadi (2019) (All dimensions are in millimeters)

3.2.2. Test conducted by Lim and Nethercot (2004)

Lim and Nethercot (2004) tested two portal frames, designated as Frame A and Frame B, using the setup illustrated in Figure 3-5a. In this setup, the frames were loaded using a rig equipped with eight jacks, and pinned supports were placed at the column bases. To prevent premature lateral buckling of the back-to-back channel sections, lateral restraints were provided at both the loading position (on the rafter) and at the joints (Lim and Nethercot, 2004). The details of the point loads applied to the portal frames are shown in Figure 3-5b.

The channel sections used in the tests are detailed in Figure 3-5c. The average measured material properties for the channel sections and brackets are summarized in Table 3-1. Both frames had a span of 12 meters, a column height of 3 meters, and a pitch of 10°. The primary difference between the two frames was the size of the joints, which were based on two different bolt-group sizes: 315 mm × 230 mm for Frame A and 615 mm × 230 mm for Frame B (see Figures 3-5d and 3-5e).

Table 3-2 Material properties of channel sections and brackets used for frame tests after Lim and Nethercot (2004)

Components	t (mm)	f_y (N/mm^2)	f_u (N/mm^2)
Channel section	2.95	358	425
Brackets	2.98	200	305

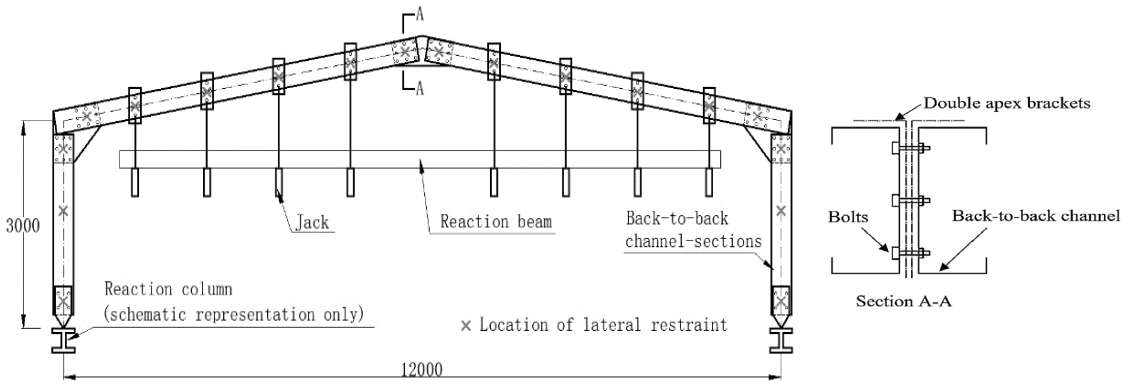

(a) Details of the general arrangement for the frame test

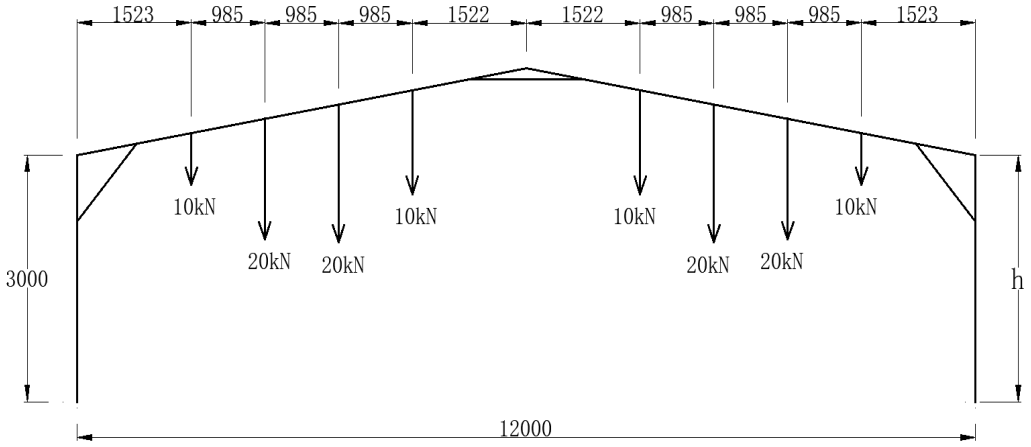

(b) Detail of point loads applied to the test frame (dimensions in millimeters)

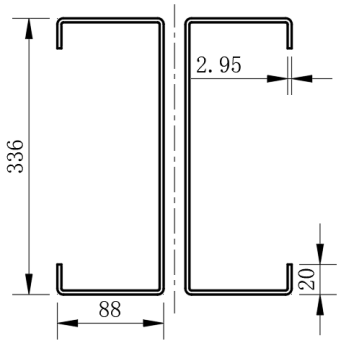

(c) Channel section dimension

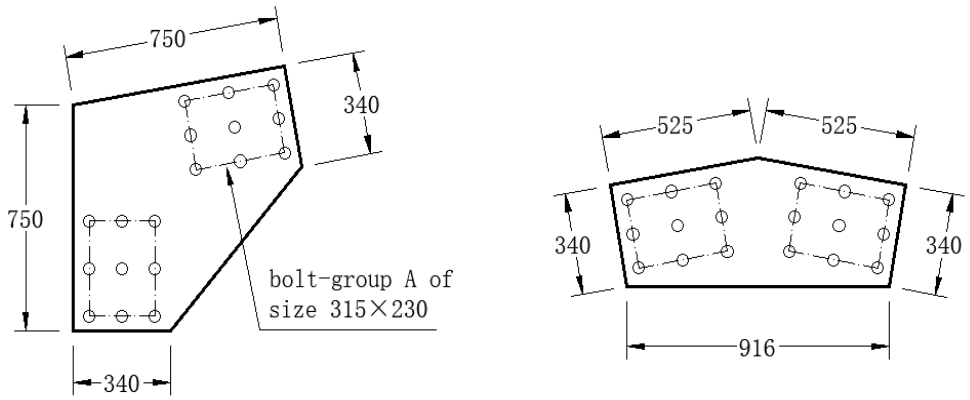

(d) Joints details of Frame A

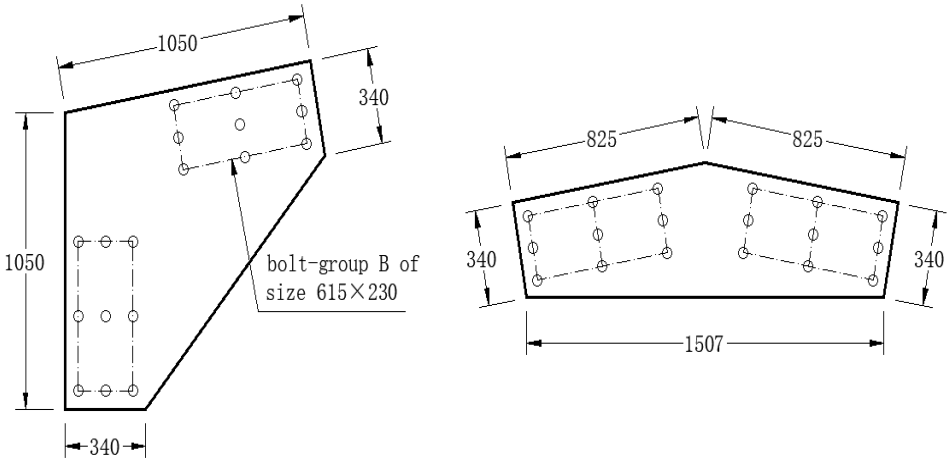

(e) Joints details of Frame B

Figure 3-5 Detail of the general arrangement of the test frame after Lim and Nethercot (2004) (All dimensions are in millimeters)

3.3. Validated shell FE model of NTB portal frames

3.3.1. Geometric modelling

A FE model was developed using ABAQUS (2021) to simulate the behaviour of NTB portal frames. The frame was modelled to match the experimental details outlined in Section 3.2.1, including the overall frame dimensions and the average cross-sectional dimensions. The members (columns and rafters) in the model consist of two tapered G-channels joined along the weld line. The entire frame is divided into six segments, each connected by a plate. The tapering of the members was achieved using the shell lofting option in ABAQUS (2021). The complete FE model of the portal frame is shown in Figure 3-6.

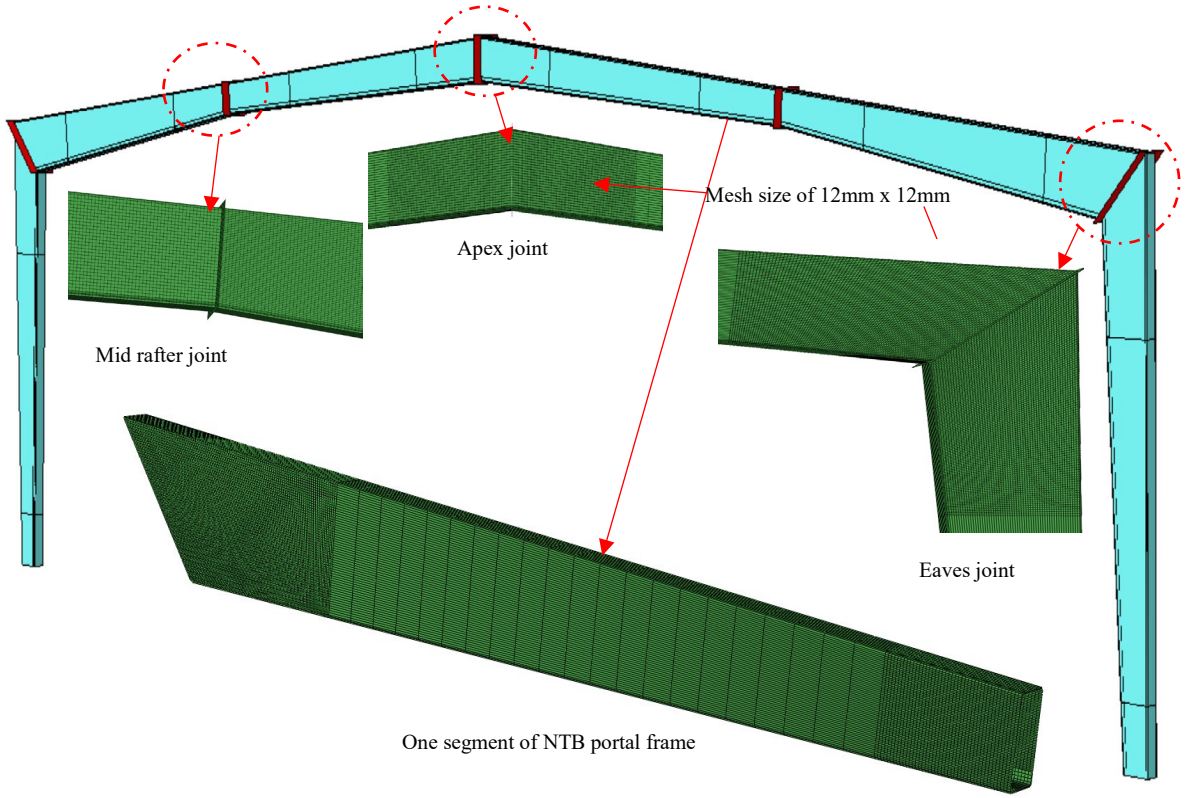

Figure 3-6 FE model of NTB portal frame

3.3.2. Contact and connection modelling

Surface-to-surface contact was used to define the interaction between the webs of the NTB member and the bolted-side plate. Two types of contact behaviour were specified:

normal and tangential. For the normal behaviour, a "Hard" contact approach was employed to manage pressure-overclosure interactions, with non-linear contact stiffness applied. No failure was observed in the seam welds and bolted end plates during the experimental tests. Consequently, the bolted end plates were modelled as elastic, with only one plate represented instead of two, simplifying the model by omitting the bolts. To simulate the interaction between the plate and the NTB member, 'Tie constraints' were used (Paul et al., 2023).

3.3.3. Element type and material properties

All frame members were modelled using standard 4-node doubly curved thin shell elements with linear interpolation, reduced integration, hourglass control, and finite membrane strains (S4R elements) (ABAQUS, 2021). This element type has been effectively used in previous studies of CFS portal frames (Blum and Rasmussen, 2019a; Chen et al., 2021). For the columns and rafters, a fine mesh size of 12 mm × 12 mm (see Figure 3-6) was used near the connections, where higher strain levels are anticipated. The mesh size was coarser in the central portions of the members to reduce analysis time. The same 12 mm × 12 mm mesh size was applied to the plates. Based on the mesh sensitivity analysis, this mesh size was found to provide a good balance between computational efficiency and accuracy of the results.

Material behaviour was modelled using a bilinear stress-strain curve with an elastic modulus (E) of 200 GPa and a Poisson's ratio (μ) of 0.3, followed by piecewise linear segments to represent true plastic stress-strain behaviour. The yield stress and ultimate stress values for the FE model were obtained from coupon tests reported by Shahmohammadi (2019) and are summarized in Table 3-1.

3.3.4. Boundary conditions, lateral restraint, and loading

As described in Section 3.2.1, the pinned column base boundary condition was applied at the bottom of the base plate. This condition constrained all in-plane translations and rotations except for rotation in the x-direction (see Figure 3-7).

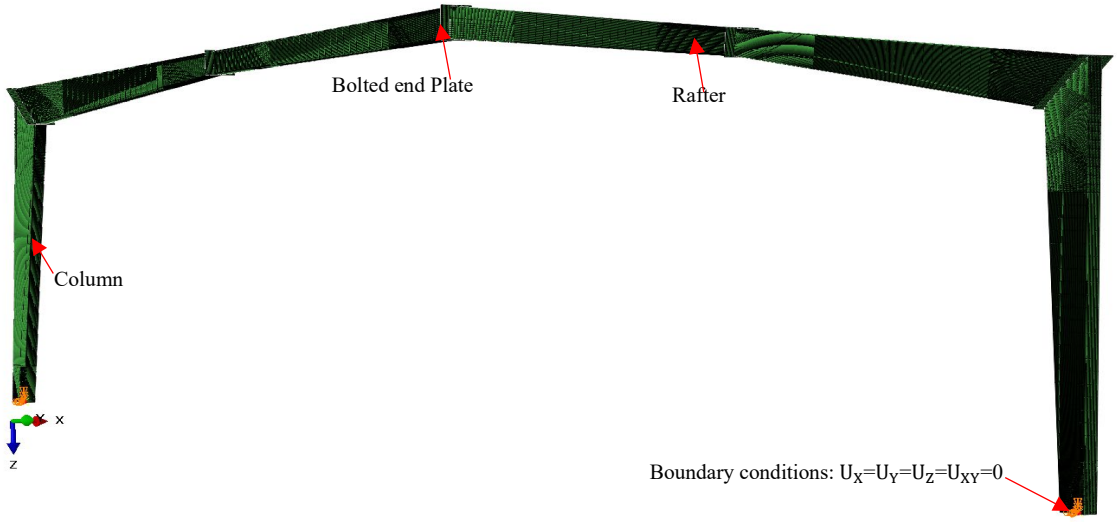

Figure 3-7 Boundary conditions and lateral restraint on the NTB portal frame

In the experiment, eight concentrated loads were applied to the rafter of the NTB portal frame, as shown in Figure 3-1. Accordingly, in the FE model, these loads were directly applied to the nodes on the rafters. All nodes at the column bases were coupled to a reference point. Instead of modelling the base plate, MPC beam-type constraints (Shahmohammadi, 2019) were used at the reference points to simulate the interaction between the base plate and the column base. As illustrated in Figure 3-7, both translational and rotational degrees of freedom at the column bases were fully restrained. However, a spring with a stiffness of 2370 kNm/rad was assigned at the column bases to allow for in-plane rotation, as suggested by Shahmohammadi (2019).

3.3.5. Analysis

A static geometric and material nonlinear analysis was conducted for the test frame model. A single load step was defined, as the frames were subjected only to vertical loads.

The analysis employed the "static general" option with a full Newton-Raphson solution technique to handle the nonlinearities.

3.3.6. Comparison of the experimental test results with FE results

The FEA results were compared with experimental data to validate the accuracy of the modelling approach. Table 3-3 presents the ultimate strengths predicted by the FEA alongside the test results for the NTB portal frame. The ultimate load predicted by the FEA (F_U^{FEA}) closely matches the test result (F_U^{EXP}) with a difference of less than 2%. Several factors contribute to the observed differences, including potential imperfections introduced during frame installation, variations in bolt pretension, and the eccentricity of loading points—factors that are challenging to accurately model numerically.

Figure 3-8 illustrates the comparison of water load (excluding self-weight and other loads, which is 24.4 kN) versus apex deflection curves from both experimental and FEA results. Overall, the FE model demonstrates good agreement with the experimental data.

Table 3-3 Comparison of experimental test by Shahmohammadi (2019) and FEA results of NTB portal frame

NTBB Portal frame	F_U^{EXP} (kN)	F_U^{FEA} (kN)	F_U^{EXP}/F_U^{FEA}
End plate (EP)	143.9	140.9	1.02
Bolted-side plate (BS-8mm thick)	-	107.2	-
Bolted-side plate (BS-10mm thick)	-	140.8	-

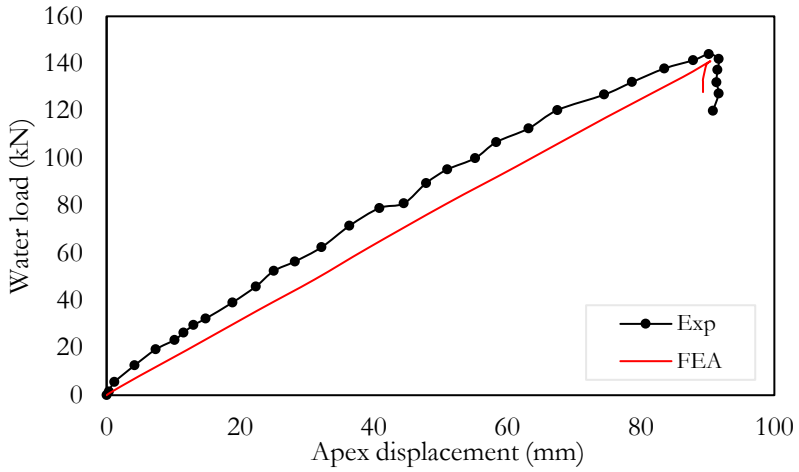

Figure 3-8 Water weight vs. apex deflection curve comparison of experimental and FEA results

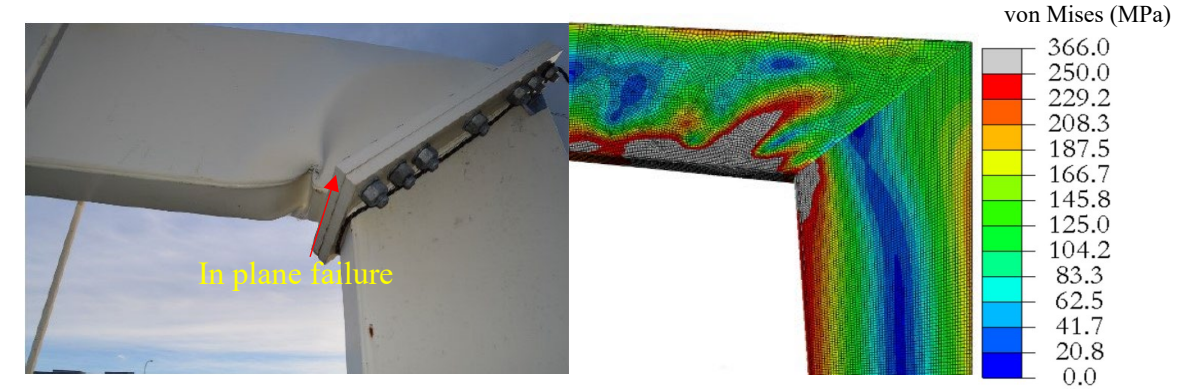

(a)Experimental test after Shahmohammadi (2019) (b) FEA from this study

Figure 3-9 In plane failure at eaves joints of NTB portal frame from tests and FEA

3.4. Validated shell FE model of portal frames with back-to-back channels

Figure 3-10 illustrates the application of a similar modelling technique for a portal frame with back-to-back channels, as detailed in Section 3.3 for the NTB portal frame. In this model, the connections (bolts) between the channels and brackets were simulated using "SPRING 2" elements (ABAQUS, 2021) (see Figure 3-11) to account for joint flexibility. The in-plane stiffness of the springs, connecting a node on the channel with a node on a bracket, was set to 6.21 kN/mm, while the stiffness in normal direction was assumed to be 1000 times greater than the in-plane stiffness.

The S4R element was used to model the rafter, column, and brackets (eaves and apex) of the portal frame. The mesh size was 15 mm × 15 mm for the column and rafter members, and 10 mm × 10 mm for the brackets. A finer mesh of 5 mm × 5 mm was applied to the middle of the apex brackets to more accurately capture the failure observed in the experimental tests described in Section 3.2.2. A pinned boundary condition was used to replicate the test conditions (see Figure 3-12).

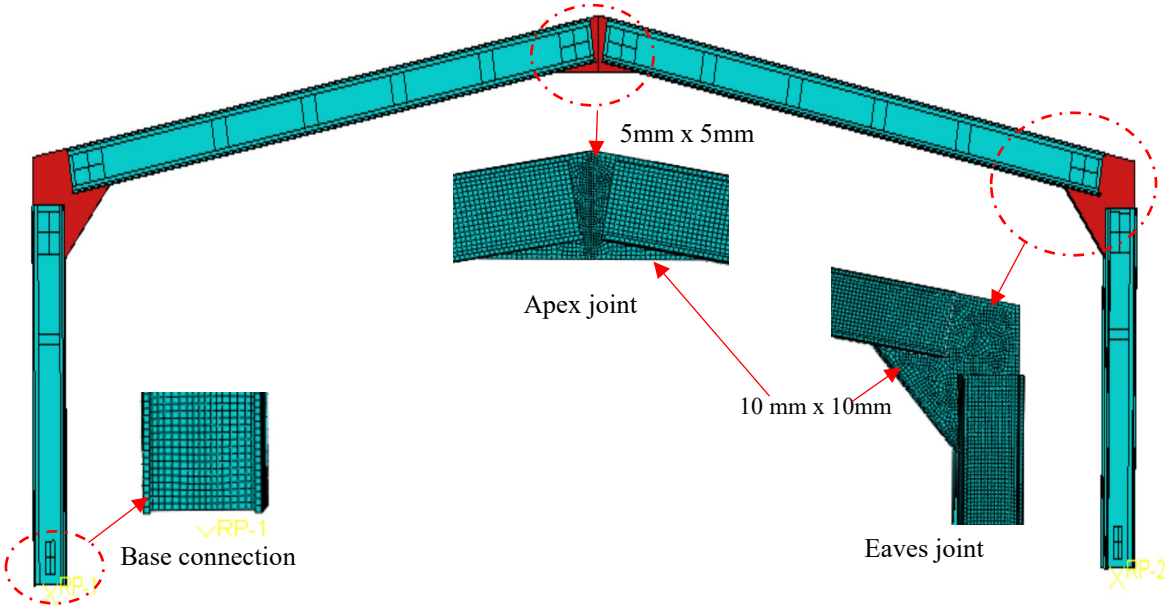

Figure 3-10 Shell FE model frame layout

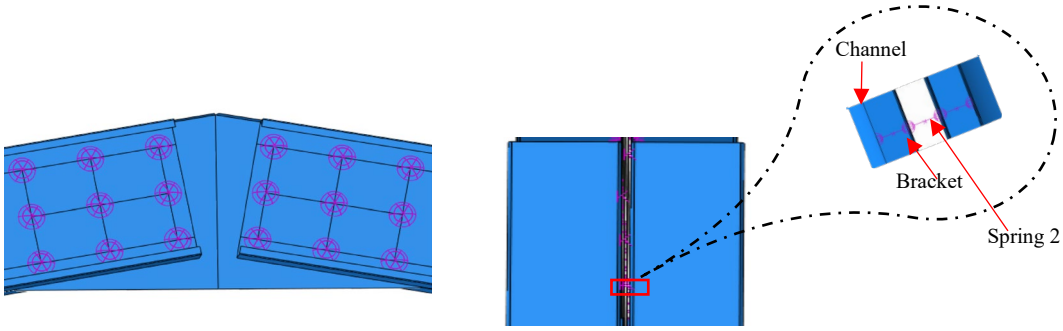

(a) Apex Joint (b) SPRING 2 element

Figure 3-11 FE idealisation of apex joints

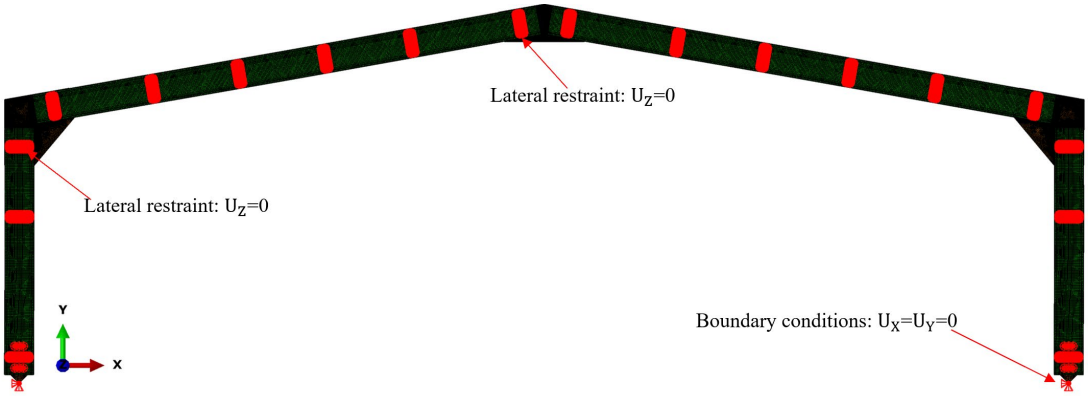

Figure 3-12 Boundary conditions and lateral restraint on the portal frame FE model

3.4.1. Validation of the shell FE model

FEA results were compared with the experimental results to validate the suitability of the modelling method. The ultimate strengths of the experimental test frames (F_u^{EXP}) and the FEA model (F_u^{FEA}) are presented in Table 3-4. As observed, the values of F_u^{FEA} are close to those obtained from the experimental tests and the differences are within 5% for both Frames A and B. Load-displacement curves from the test also closely matched with the curves of shell FE model for both the frames (see Figure 3-13). There are several contributing factors to the differences, including varying degrees of bolt pretension and eccentric location of loading points. These factors are difficult to account for in the numerical model.

Table 3-4 Comparison of experimental (Lim and Nethercot, 2004a) and FEA results form this study

Frame	F_u^{EXP} (kN)	F_u^{FEA} (kN)	F_u^{FEA}/F_u^{EXP}
A	76.7	74.3	0.97
B	106.7	101.7	0.95

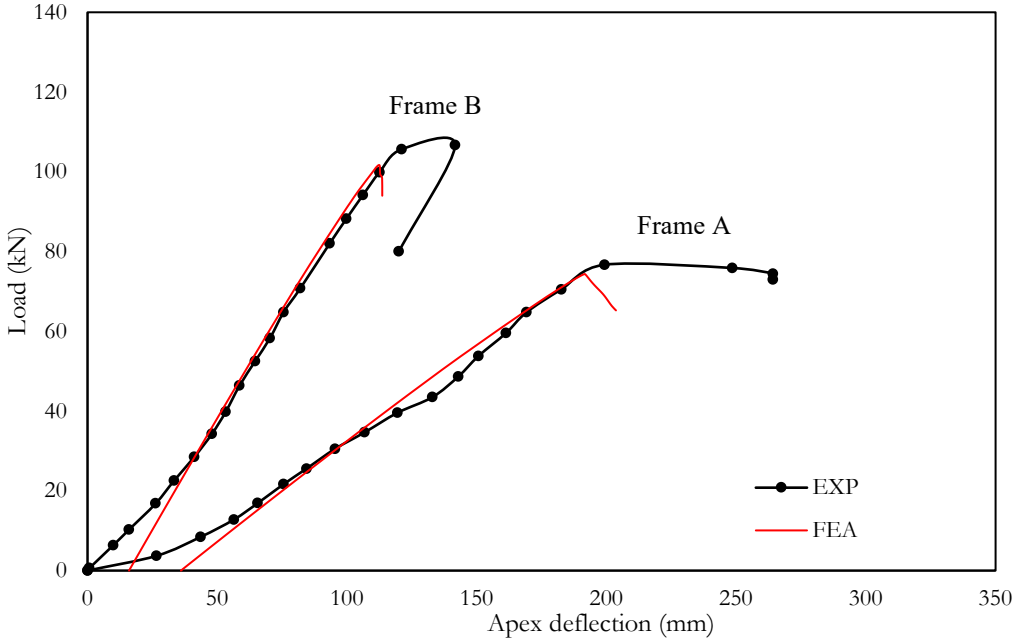

Figure 3-13 Load displacement behaviour of the portal frame from the test (Lim and Nethercot, 2004a) and the shell FE model from this study

3.5. Shell FE model of the NTB portal frame with bolted-side plates

3.5.1. FE Modelling

As can be seen from Figure 3-14, both apex and eaves joints were changed into bolted-side plate connections. The same load and boundary conditions were assigned as discussed in section 3.2.1, with lateral restraint applied consistent with New Zealand practice.

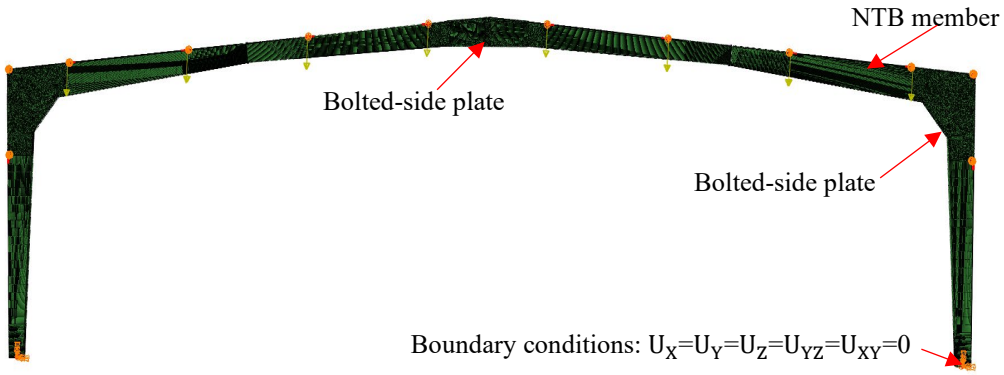

Figure 3-14 Boundary conditions of the NTB portal frame with bolted-side plate

A typical shell element model of the joint used in the portal frame is shown in Figure 3-15. As can be seen, 'SPRING 2' element was used to simulate the behaviour bolts at eaves

joints. In-plane stiffness of the springs connecting one node on the NTB section with one node on a bolted-side plate was 15.5 kN/mm (Y and Z-direction) while in the X-direction, stiffness was assumed to be 1000 times of the other directions.

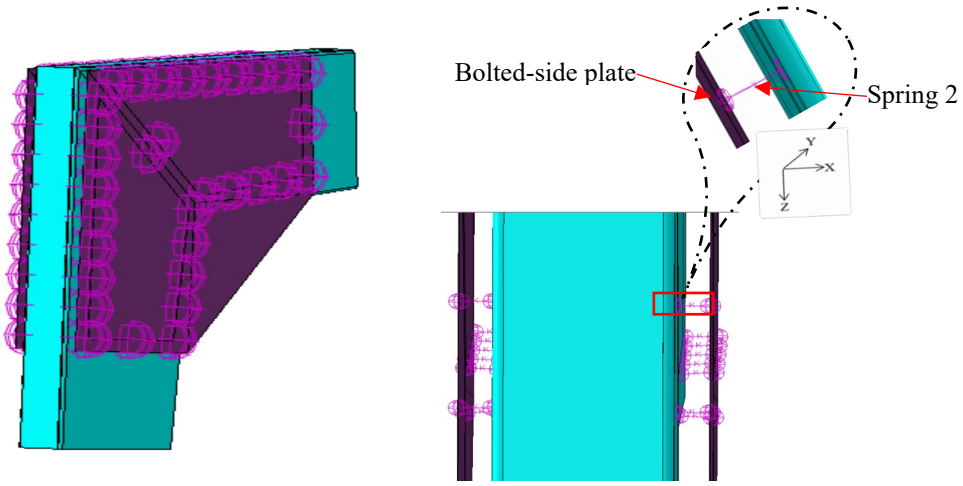

(a) Eaves joints (b) Spring 2 element

Figure 3-15 FE idealization of eaves joints for the NTB portal frame

Figure 3-17 illustrates the stress distribution within the NTB portal frame and indicates that the failure of the NTB portal frame is primarily attributed to the buckling of the bolted-side plate. Geometric details for the bolted-side plates used for this study can be found in Figure 3-16.

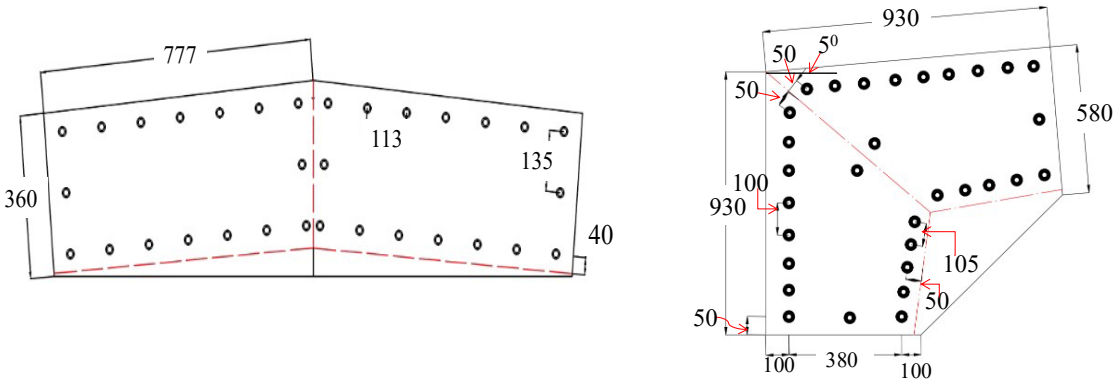

(a) Bolted-side plate for apex joint (b) Bolted-side plate for eaves joint

Figure 3-16 Geometric details for the bolted-side plates for the NTB portal frame (all dimensions are in millimeters)

3.5.2. Effect of the bolted-side plate on the ultimate capacity

To assess the effect of bolted-side plates on the ultimate capacity of NTB portal frames, the thickness of bolted-side plates was varied for eaves joints, and the analysis was rerun. Figure 3-17 shows the von Mises stress contours for the column and rafter for two different failure mode of NTB portal frame; one in the bolted-side plate and other is in rafter and column of NTB portal frame. The red areas indicate where yielding has occurred, and the observed failure mode is the buckling of the column and rafter members near the eaves joint.

The load versus apex deflection curve, indicating failure within the members, is illustrated in Figure 3-18 with a red line and a blue line, while the indigo line represents the failure of the bolted-side plate at the eave joints. As shown in Figure 3-18, increasing the thickness of the bolted-side plate at the eaves joint from 8 mm to 10 mm results in an 18% increase in the ultimate capacity of the NTB portal frame. When the thickness of the bolted-side plate is increased further from 10 mm to 16 mm, the ultimate capacity of the NTB portal frame increases by an additional 20%. More importantly, ultimate capacity of NTB portal frame with bolted-side plates closely aligns the ultimate load capacity of the NTB portal frame with that of bolted end plate joints when the thickness bolted-side plates at eaves was 10mm. This highlights the significant effect of bolted side plate thickness on the frame's ultimate capacity.

The failure mode shown in Figure 3-17 is reasonably accurate, as the bending moment is maximum and the slenderness ratio of the NTB member is minimum at the eaves joint. If the bolted side plates do not have sufficient stiffness (i.e., are too thin), the failure will occur in the bolted-side plates. Conversely, if the bolted side plates are thick, the overall stiffness near the eaves will increase, enhancing the ultimate load capacity of the portal frame. In this case, failure will occur in the NTB members.

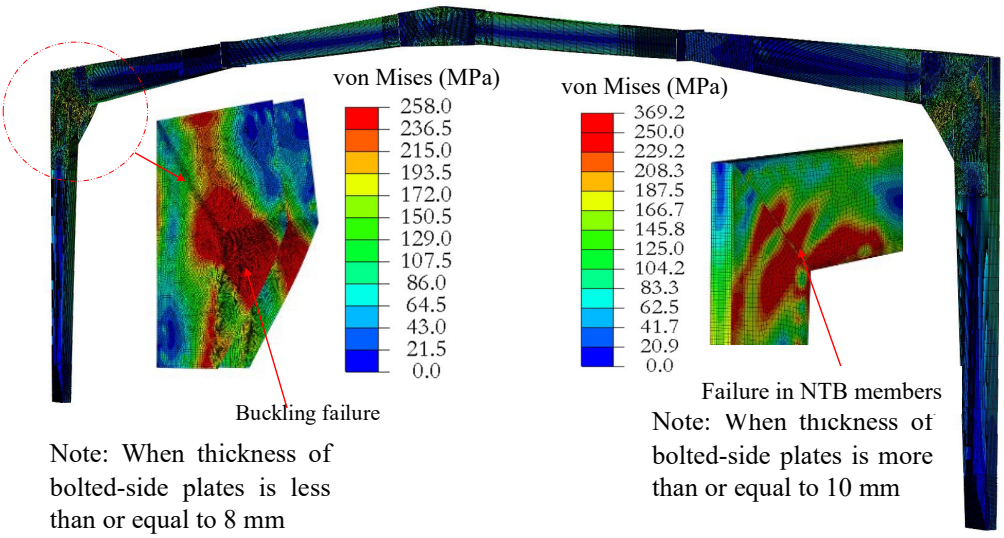

Figure 3-17 Stress contours of the NTB portal frame with bolted-side plate

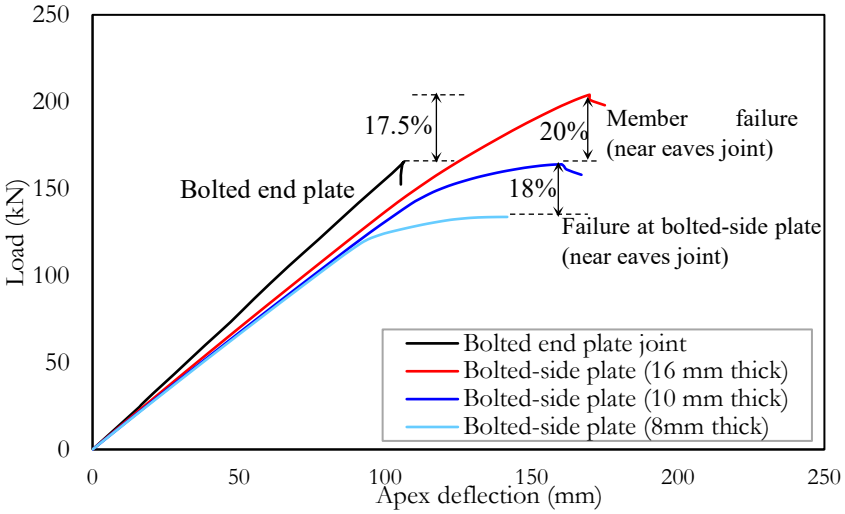

Figure 3-18 Effects of thickness on the ultimate capacity of NTB portal frame

3.6. Parametric study

A parametric study was conducted to compare the ultimate load capacities of NTB portal frames with rigid bolted end plate and bolted-side plate joints. Figures 3-19a and 3-19b illustrate the parameters considered for the NTB portal frame and provide details of the bolted-side plate joints used in this study. The results are summarized in Table 3-5.

As can be seen from Table 3-5, the NTB portal frame with the bolted-side plate system can support 7% more load compared to the rigid bolted end plate system. It is important to note that this parametric study utilized a simplified beam model of the portal frame. Further details on the modelling approach can be found in Appendix B and C.

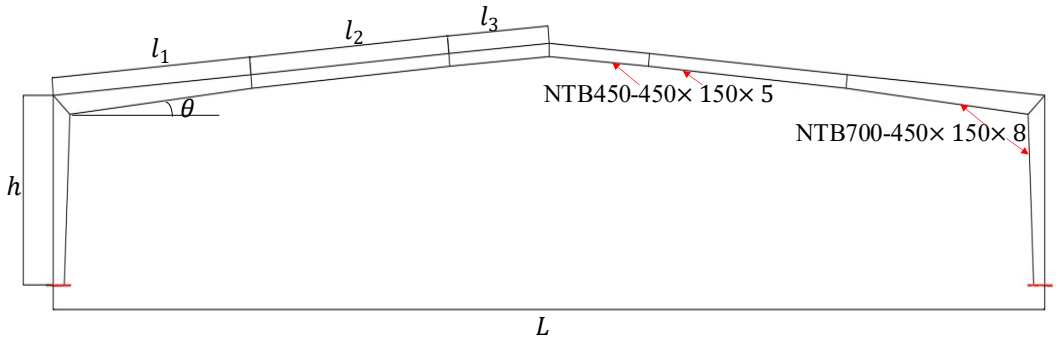

(a) Parameters adopted for the NTB portal frame with bolted-side plate joints

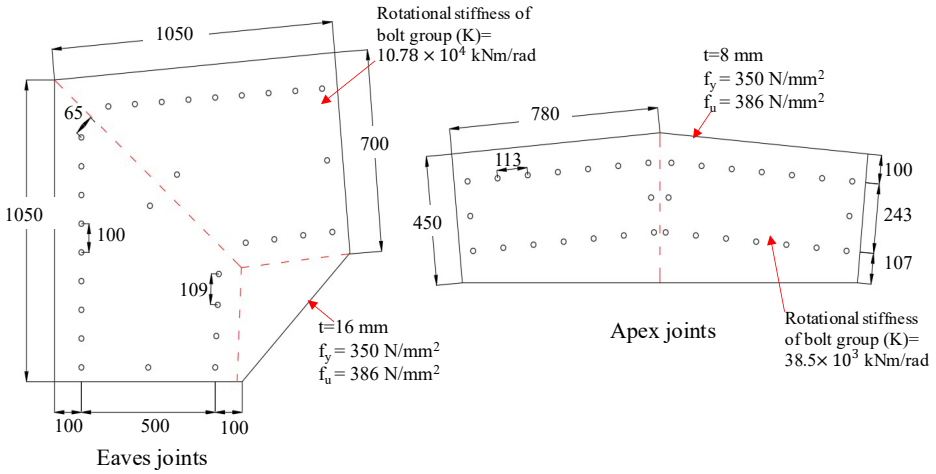

(b) Details of the bolted-side plate joints

Figure 3-19 Parameters for the NTB portal frames with bolted-side plate and details of the bolted-side plate

Table 3-5 Comparison of the ultimate load for NTB portal frame with bolted end plate and bolted-side plate

Sl. No	L	l_1	l_2	l_3	h	θ	F_{beam}^{EP}	F_{beam}^{BS}	$F_{beam}^{BS}/F_{beam}^{EP}$	Failure
	m						kN/m			
1	40	8.0	8.0	4.06	6.25	5^0	7.6	8.13	1.07	Near eaves
2	30	8.0	7.06	-	6.25	5^0	13.0	14.08	1.08	Near apex
3	25	8.0	4.55	-	6.25	5^0	18.46	19.8	1.07	Near apex
4	40	8.0	8.0	4.06	5.5	5^0	7.69	8.16	1.06	Near eaves
								Mean	1.07	
							Co-efficient of variation		0.007	

3.7. Summary

In this chapter, a non-linear FE model for NTB portal frames was developed and validated against experimental tests by Shahmohammadi (2019) and (Lim and Nethercot, 2004a). The study also explored the feasibility of using bolted-side plates in NTB portal frames. The FE analysis revealed that bolted-side plates could increase the ultimate load capacity by 17.5% compared to ultimate capacity of NTB portal frame rigid bolted end plate joint, provided that the thickness of the bolted-side plates is 16mm. This would be due to the confinement of the NTB member at eaves joint with the bolted-side plates which increases the load carrying capacity of the NTB portal frame. It can be concluded that bolted-side plate joint not only increased the load carrying capacity but also improving the ductile behaviour of the NTB portal frame.

Additionally, a parametric study was performed to examine the effects of various geometric parameters, such as the span and height of the NTB portal frame. In this study, a simplified beam model was used for the analysis. The results demonstrated that a portal frame with bolted-side plate joints can carry 7% more load than a frame with bolted end plate joints.

Chapter 4 Moment capacity of bolted-side plate for apex joint

4.1. Introduction

In portal frames, around 30-40% of the cost lie in the fabrication of the joints (SCI_P358, 2014;Toma` et al., 1993). Additionally, the strength and stiffness of the CFS frame is heavily influenced by the detailing of the joints. Following AS/NZ4600 (2018), joints should have adequate strength to ensure the frame fails within the members, and the design moment capacity of a joint should be equal to or exceed the moment to which the joint is subjected, as predicted by the advanced analysis. This chapter considers the strength of the bolted-side plate of the apex joint.

A photograph of NTB portal frame is shown in Figure 4-1 and its joints are formed through the bolted end plate connections, as commonly found in the apex joints of conventional hot-rolled steel portal frames. Such a joint detail, however, may be considered as over-designed for cold-formed steel portal frames, where the clear span is less than that of hot-rolled steel portal frames.

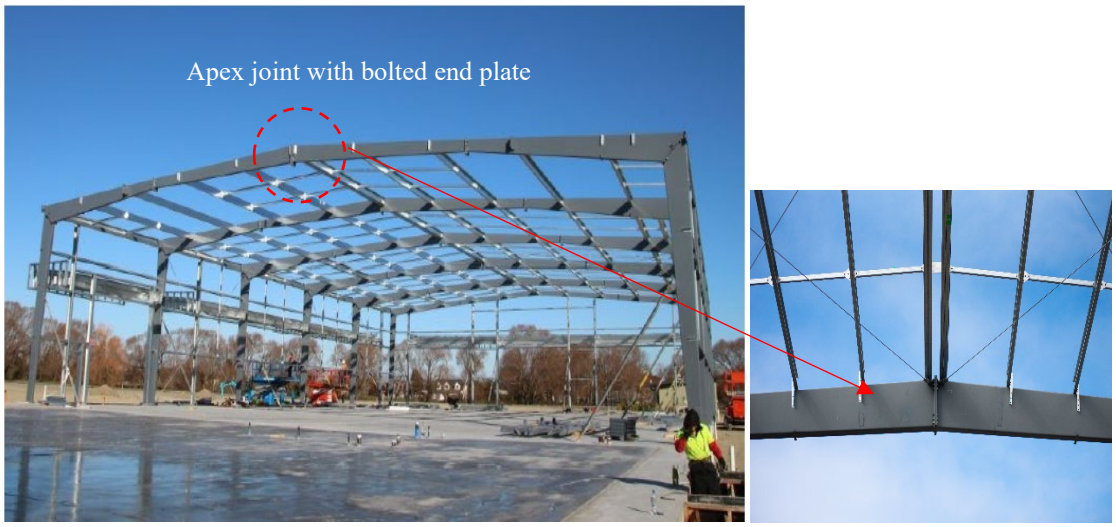

Figure 4-1 Photograph of NTB portal frame with bolted end plate system (Shahmohammadi 2019)

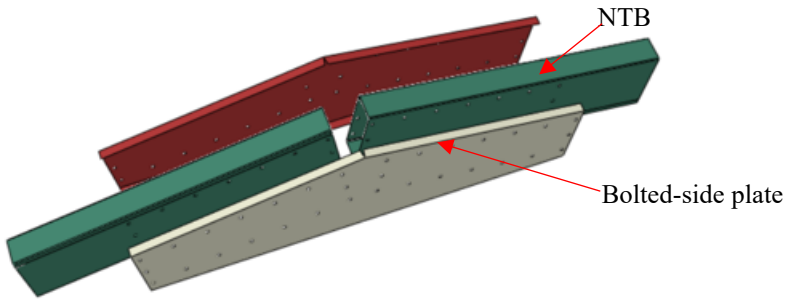

Note: no stiffener is used for plate thicknesses less than 8 mm

Figure 4-2 Schematic diagram of the bolted side-plates bolted to the webs of the NTB section (Note that no stiffener is used for plate thicknesses less than 8 mm)

A simpler apex joint detail comprising bolted-side plates is proposed here, as shown in Figure 4-2. As can be seen, the bolted-side plates are in pairs i.e., one on each side of the NTB section. The bolt size is M16. Thicknesses of plates commonly available in New Zealand are 3 mm, 5 mm, 6 mm, 8 mm, 9 mm, 10 mm, and 12 mm (New Zealand steel Ltd.). From discussions with practitioners, it is well-known that plates with a thickness greater than 8 mm are difficult to fold. Therefore, only plates with a thickness of less than 8 mm can be folded. It is assumed that the yield stress of the steel plate is 350 N/mm^2 (New Zealand steel Ltd.). Figure 4-3 shows the parameters of the bolted-side plate adopted in this paper.

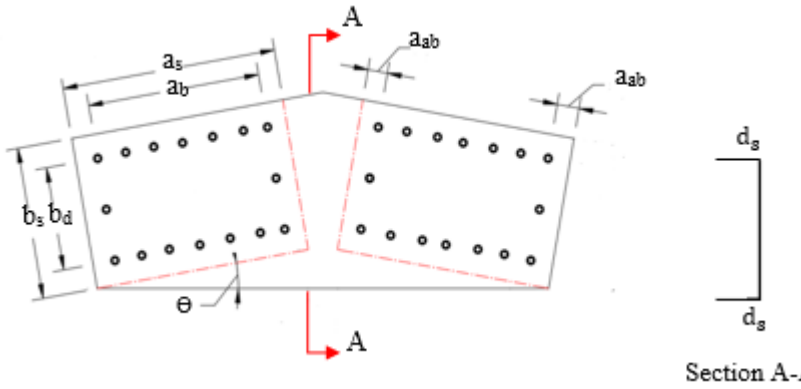

Figure 4-3 Diagram showing the parameter of bolted-side plate for apex joints (dotted lines represent the outline of NTB sections)

As mentioned previously, only plates of thicknesses less than 8 mm can be folded. For such plates a top-bottom stiffener arrangement is adopted i.e. a stiffener is folded at both the top and bottom of the bracket. For plate thicknesses greater than 8 mm, no stiffeners are used i.e. the plate is flat.

In this chapter, both opening moments (due to wind uplift) and closing moments (gravity loading) were considered, as previous studies on portal frame connections were limited to considering only gravity loading, which is equivalent to the closing moments.

In the literature, it was found that most portal framing systems used conventional end plate connections. The use of a bolted side plate connection is an alternative to conventional end-plate connections. As a result, there is no guidance found in the literature on such bolted-side plate connections. Other portal framing systems with hollow rectangular or built-up box sections described in the literature used an end-plate connection system (Shahmohammadi et al. 2022;Wilkinson and Hancock, 1998; Jůza and Jandera, 2022). While innovative beam-column connections have recently been described using box system by other researchers, these were for modular construction and were not related to bolted-side plates (Tekieh et al. 2022; Qin et al. 2022; Lacey et al. 2019).

More general CFS portal framing systems described in the literature tend to use channel-sections (either single or back-to-back) for the column and rafter members (Lim 2001, Blum and Li 2021; Rinchen and Rasmussen 2019a; Öztürk and Pul 2015). From the literature, it is evident that bolted side-plate is used for both single and back-to-back channel sections for apex joints (Blum and Li 2019; Öztürk and Pul 2015; Lim and Nethercot 2003). However, there is limited information available on the use of bolted-side plates for apex joint in box sections. Although design guidance on the strength of

apex brackets has been reported by Chen et al. (2021 and 2023a), it should be noted that these guidelines are applicable only for brackets with thicknesses less than 4 mm and connections formed through channel sections.

This chapter focuses on the moment capacity of bolted-side plate for apex joint when NTB portal frames are under bearing gravity load or wind uplift load. Unified design equations are provided to aid in the design of bolted-side plate with top-bottom stiffeners, and with characteristics depicted in Figure 4-3.

4.2. Summary of experimental tests conducted by Lim (2001)

As stated in Section 1, no experimental tests using bolted side-plates for the apex joint have been reported in the literature. Lim (2001) described apex joint tests using the arrangement depicted in Figure 4-4. This section briefly describes the closest experimental tests to bolted side-plates in the literature, and it will be used to validate the FE modelling.

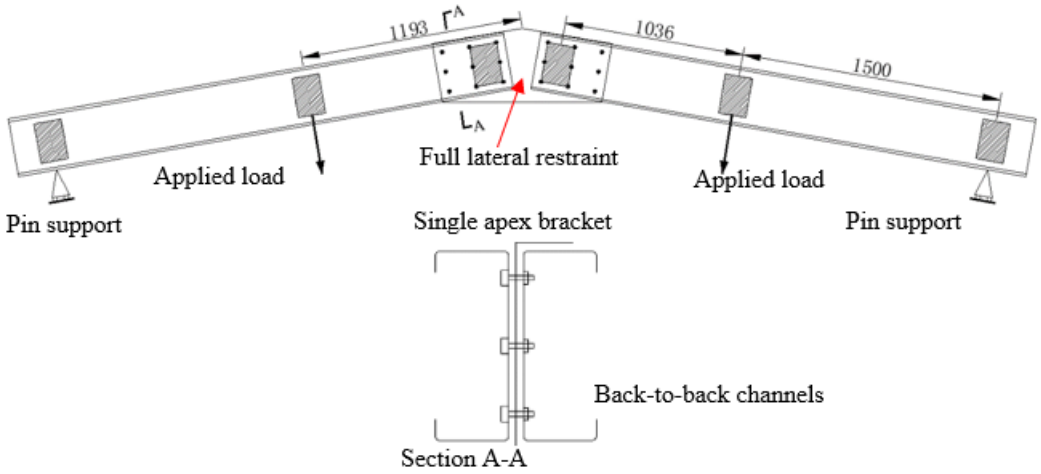

Figure 4-4 Details of apex joint test conducted by Lim (2001) (dimensions in millimeters)

The measured dimension of the channels tested is shown in Figure 4-5, and the details of the apex brackets tested are tabulated in Table 4-1. The average yield stress of the channel, measured from three tensile coupons, was 300 N/mm^2. The yield stress of the apex bracket

was summarized in Table 4-1. The pitch angle θ shown in Figure 4-3 is 10° in the apex joint.

4.3. FE modelling techniques for apex joints

This chapter uses the FE program ABAQUS (2021) to model the apex joint for portal frames using the NTB section. The modelling techniques used in this paper are described in this section.

4.3.1. Geometry

Details of the FE model for apex joint shown in Figure 4-5. As only pure moment load is considered, the full model is not created. Instead, the bolted-side plates and the NTB section with a cantilever length $3\times b_a$ are modelled. A representative of the pure moment is applied at the end of the NTB section.

4.3.2. Contact and connection

To account for the contact between the NTB and the bolted side-plate, surface-to-surface contact is simulated with "hard" normal behaviour and with the allowance for separation after the contact. The "Penalty" friction formulation is considered, and the coefficient of friction is assumed to be 0.2 (Chen et al. 2021). As seen in Figure 4-5a, the linear translational "SPRING2" element (ABAQUS 2021), is used to idealise the behaviour of bolted connections.

The weld between the edges of the G-section was modelled using a "tie constraint." This approach aligns with the method used by Lukačević et al. (2021) in their study, where they employed a "tie constraint" to model welded back-to-back channel sections.

4.3.3. Element and material

The bolted side-plate connection is modelled using the standard 4-noded doubly curved thin shell elements (S4R) (ABAQUS, 2021). The NTB section and the bolted side-plates are modelled with a mesh size of 15 ×15 mm and 10 ×10 mm, respectively (Paul et al. 2023). The simulated material behaviour follows an elastic-perfectly plastic force-displacement relationship. Material property of the NTB section is modelled as a linear elastic material. The initial modulus of elasticity (E) is 200 GPA.

4.3.4. Boundary conditions and loading

Nodes at the end of the NTB are coupled to reference points at the centre of the sections in the simplified FE model. The reference points are subjected to the opening moment. Nodes on the box's middle line are restrained in the X-direction, and one node in the bolted side-plate's center is restrained in the Y-direction. As described in the reported test setup, full lateral restraints are used on the webs of NTB section. Figure 4-5b shows the boundary conditions and loading, which have assigned to the FE model.

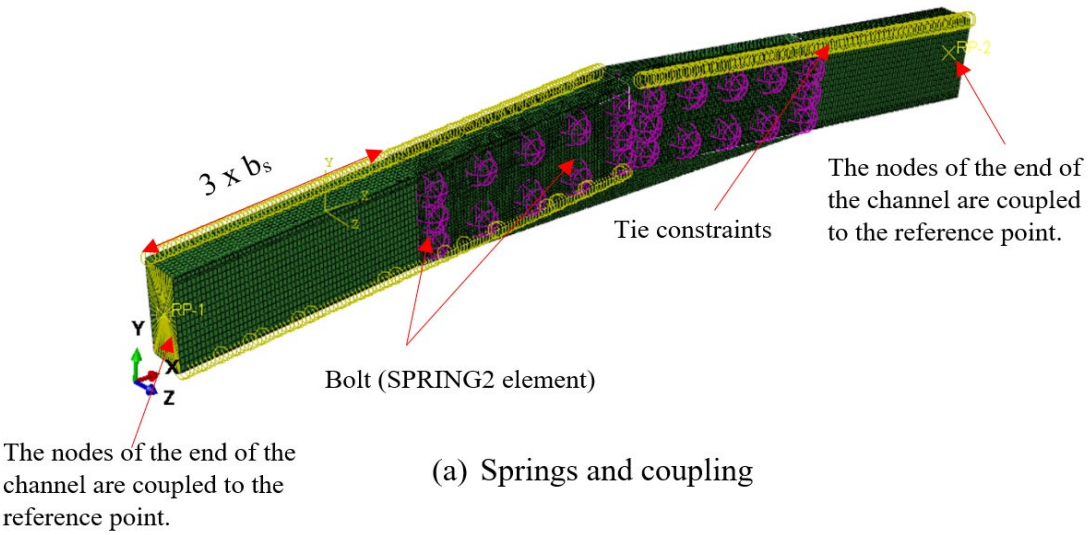

(a) Springs and coupling

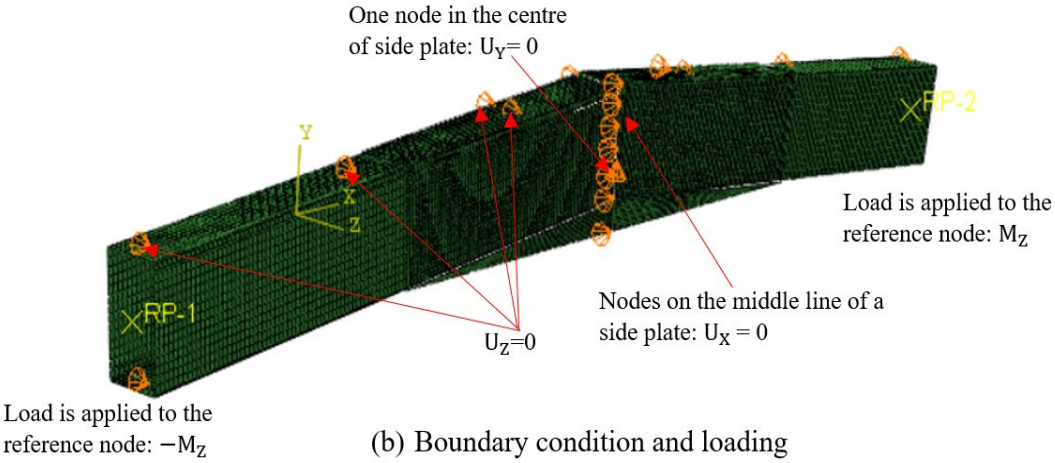

(b) Boundary condition and loading

Figure 4-5 Finite element model for bolted side-plate connection

4.3.5. Validation of the FE model

A static geometric and material nonlinear analysis was performed for the apex joint model. A single load step was defined for the joint subjected to the moment. Table 4-1 summarises the results of nonlinear analysis on the apex joint. The failure load (M_U^{FEA}) agrees well with the experimental results (M_U^{EXP}), with a standard deviation of 0.04 and an average difference of 7%. The buckling failure of the apex bracket in Figure 4-8, matches the experimental results from Lim (2001) suggesting the modelling techniques adopted here can be used for further study. It should be emphasised here again that in the experimental tests described by Lim (2001), the apex was tested under four-point bending, and so here only failure loads are reported.

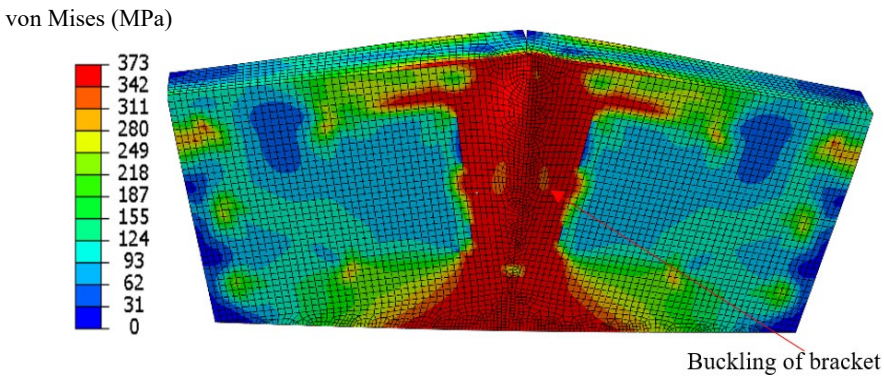

Figure 4-6 Buckling failure of the apex bracket of the fully restrained apex joints

Table 4-1 Comparison of experimental and FEA results of apex joint tests by Lim (2001)

Test	a_a	b_a	d_s	t_b	f_y	M_u^{EXP}	M_u^{FEA}	$\frac{M_u^{FEA}}{M_u^{EXP}}$
	(mm)				(N/mm^2)	(kN. m)		
1	406	340	80	2.99	272	32.5	31.7	0.98
2	700	340	80	2.95	262	35.0	32.3	0.92
3	475	340	65	4.06	305	55.0	51.6	0.94
4	550	340	80	4.09	311	57.5	53.7	0.88
5	700	340	80	3.94	373	75.0	64.7	0.93
Average								0.93
Standard deviation								0.04

4.4. Sensitivity analysis

A sensitivity analysis is used to narrow down the variables for the parametric study. The variability to moment capacity is assessed using the FE model shown in Figure 4-5 by taking into account the changes to the strength of the NTB member, stiffener arrangement, thickness of the bolted-side plates and geometric parameters. The bolted-side plates thickness is assumed to be 6 mm for this analysis, and the yield stress is 350 N/mm^2. The values of a_s and b_s for the bolted-side plates used in this section are 600 mm and 300 mm, respectively.

4.4.1. Yield stress of NTB sections

In practice, NTB behaves like an elasto-plastic material. As shown in Figure 4-9, a sensitivity analysis was performed to investigate the changes in joint capacity for NTB sections with varying yield stresses. Varying the yield stress of the NTB sections from 200 N/mm^2 to 650 N/mm^2 demonstrates that when the yield stress of the NTB section is low, failure may occur as a result of premature web buckling (Lim and Nethercot 2003). As can be seen in Figure 4-7, when the strength of NTB section is sufficient then failure is no longer sensitive to the yield stress of the NTB section and failure occurs in the

bolted-side plate. Figure 4-7 indicates that considering the NTB section as elastic does not affect the moment capacity.

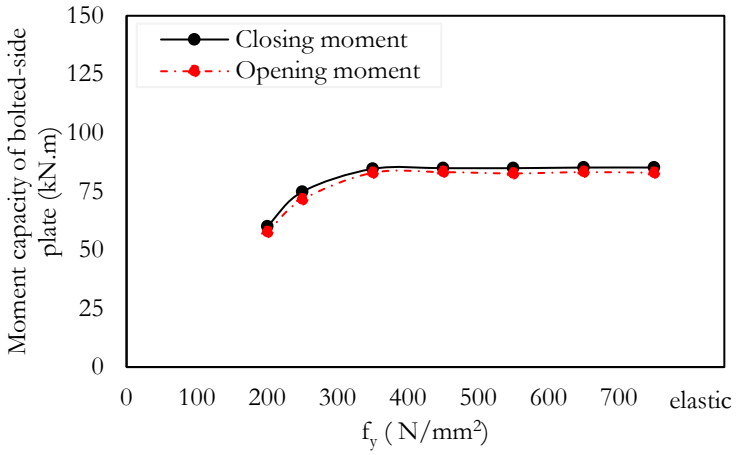

Figure 4-7 Effect of yield stress of NTB (a_s = 600 mm, b_s = 300 mm and t_s =6 mm; θ=5^0)

4.4.2. Bolted side-plates with different stiffener arrangements

Sensitivity analysis is useful for determining the best stiffener configuration to achieve maximum moment capacity. Figure 4-8 illustrates the evaluation of both opening and closing moment capacities for the two previously discussed stiffener arrangements. As expected, the bolted side-plates exhibited the highest moment capacity when stiffeners were applied to the top and bottom of bolted-side plates. Interestingly, there was minimal difference in moment capacity between the scenarios for opening and closing moments, indicating consistent performance of the bolted side-plates.

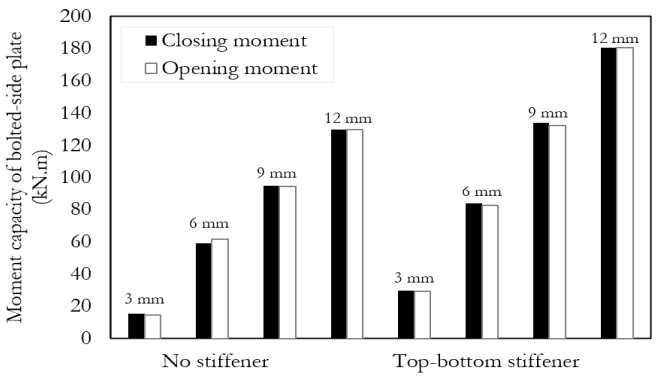

Figure 4-8 Effects of stiffeners arrangements (a_s = 600 mm, b_s = 300 mm and t_s =6 mm; and θ=5^0)

4.4.3. Thickness of side plates

A sensitivity analysis was performed by varying the thickness of the bolted side-plates from 6 mm to 12 mm. For this analysis, the thickness of the NTB section was assumed to be 6 mm, as changes in the NTB section thickness do not influence the moment capacity of the bolted side-plates. As shown in Figure 4-9, the moment capacity of the bolted side-plates increases with greater thickness. Based on these findings, it is recommended to use a thickness range of 6 mm to 12 mm for the parametric study.

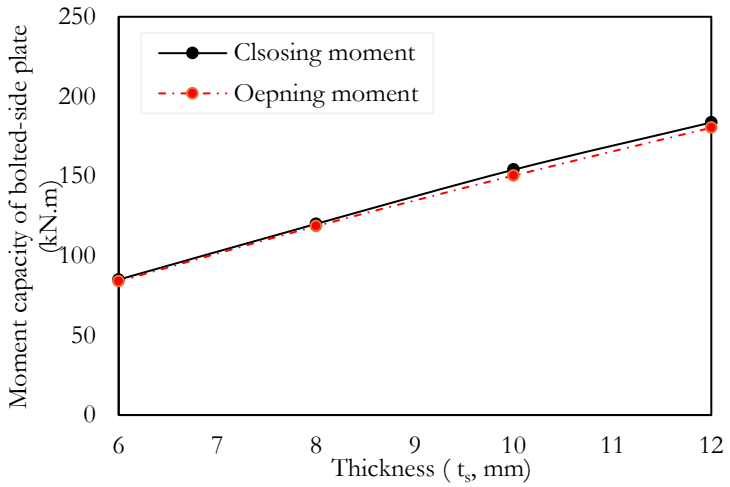

Figure 4-9 Effect bolted-side plates thickness (a_s = 600 mm, b_s = 300 mm; $\theta=5^0$)

4.4.4. Geometric parameter

A sensitivity analysis was conducted on the geometric parameters of bolted-side plate, considering, edge distance (a_{ab}), width of the triangular area to edge width of bolted side-plate (a_s/b_s), bolt distance (b_d), and pitch (θ). As shown in Figure 4-10a, the highest moment capacity for bolted side-plate was observed when the edge distance (a_{ab}) was 30 mm. Therefore, an edge distance of 30 mm is recommended for the parametric study. Figure 4-10b shows that the moment capacity of bolted-side plates increased with an increase in the a_s/b_s ratio, and a ratio between 2.0 to 3.0 is recommended to save material.

Since the moment capacity did not change significantly with bolt distance (b_d), a bolt distance of 120 mm is recommended (see Figure 4-10c).

For both the opening and closing moments, the moment capacity of bolted side-plates increased with an increase in the degree of pitch of the frame (see Figure 4-10d). Since pitches of 5^0 and 10^0 are commonly used for portal frames in practice, these values are recommended for parametric study.

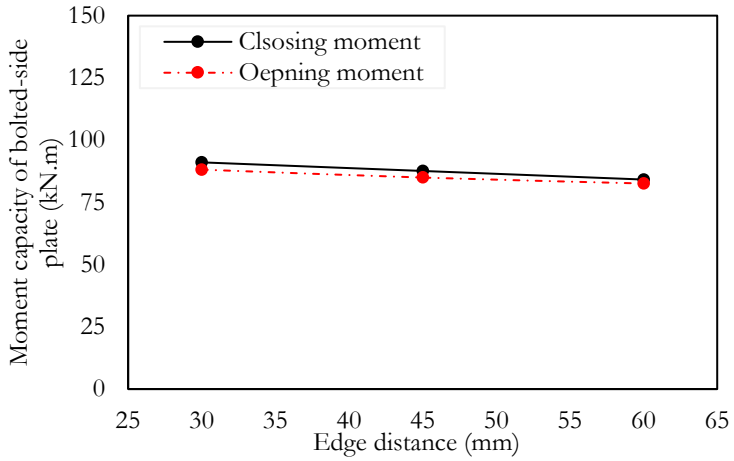

a) Effect of edge distance (a_{ab}) (a_s = 600 mm, b_s = 300 mm and t_s =6 mm; and $\theta=5^0$)

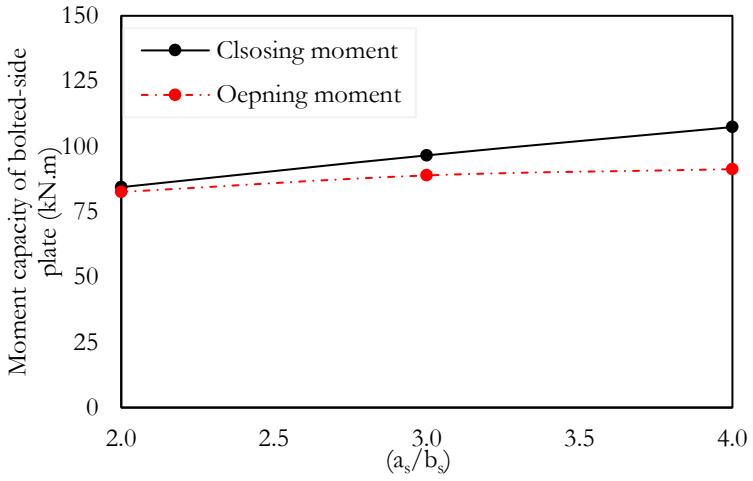

b) Effect of the a_s/b_s ratio (b_s = 300 mm and t_s =6 mm; and $\theta=5^0$)

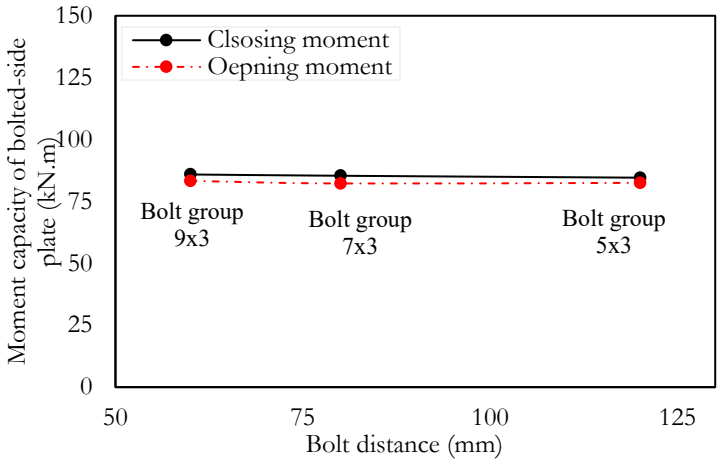

c) Effect of bolt distance (a_s = 600 mm, b_s = 300 mm and t_s =6 mm; and $\theta=5^0$)

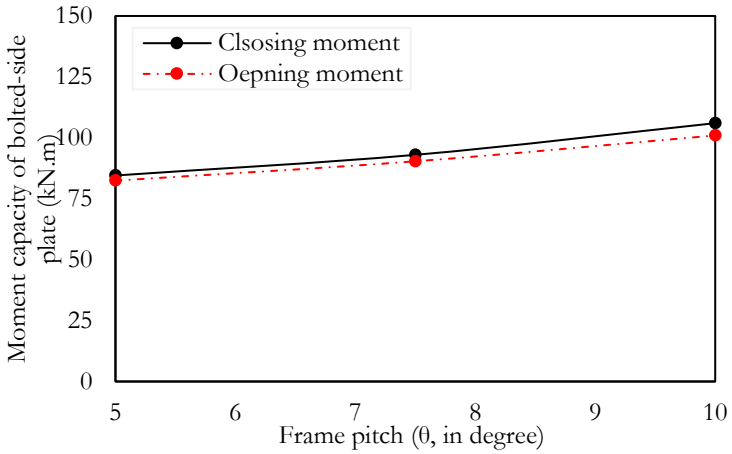

d) Effect of pitch (a_s = 600 mm, b_s = 300 mm and t_s =6 mm)

Figure 4-10 Effect of geometric parameters

4.5. Moment capacity prediction

To investigate the minimum thickness of bolted side-plate, a parametric study is conducted using the FE model shown in Figure 4-5. The first column of Table 4-2 summarises three different NTB cross-sectional geometries, consisting of two G-sections and designated by web size, flange width, and thickness.

Table 4-2 Selected variable for parametric studies

NTB section	b_s (mm)	a_s/b_s	t_s (mm)	θ	Material properties	Unified geometric parametric	Moment capacity of NTB section (M_b) (kN.m)
300 x 150 x 6	300	[2 and 3]	[6 ~ 12]	5^0 and 10^0	E = 200x10^3 N/mm^2 f_y =350 N/mm^2 μ =0.3	a_{sb}= 30 mm d_s= 60 mm, With top-bottom stiffeners. Without stiffener	82.0
400 x 150 x 6	400						492.1
1300 x 220 x 12	1300						753.1

4.5.1. Opening moment

The parametric study first examines the opening moment for the bolted-side plate of NTB section using 170 finite element models, from varying four of the design parameters of a bolted-side plate: b_s, a_s/b_s, t_s, θ. The remaining design parameters outlined in Table 4-2 are held constant during the analysis to match the values normally seen in practice. Each of the varied design parameters covers values typically used in design following AS/NZ 4600 (2018). The edge width (b_s) is increased from 200 mm to 1300 mm, and the ratio a_s/b_s is varied between 2 and 3. Thickness varied from 6 mm to 12 mm in 1 mm increments. θ is 5^0 or 10^0.

Linear regression analysis was used to fit a model with coefficients by minimising the residual sum of squares between observed and predicted data. A linear regression algorithm is used in this study to develop a design equation for the moment capacity. The opening moment of the bolted-side plate with top-bottom stiffener (M_s^o) and without stiffener (M_n^o) of the can be calculated by the following equations:

$$M_s^o = 0.003 \times {a_s}^{0.366} \times {b_s}^{1.364} \times f_y \times (\sin\theta)^{0.478} \times t_s^{1.27} \quad 4.1$$

$$M_n^o = 0.003 \times {a_s}^{0.839} \times {b_s}^{0.794} \times f_y \times (\sin\theta)^{0.684} \times t_s^{1.367} \quad 4.2$$

Where, units of a_s, b_s and t_s are in mm, the unit of f_y is kN/mm^2, and the unit of M_s^o is kNm.

4.5.2. Closing moment

Next, the moment capacity of the closing moment is analysed using the same parametric values as the previously discussed opening moment. These results in 170 FE models subjected to pure moment are evaluated with variations in b_s, a_s/b_s, t_s, θ, corresponding to the range of values shown in Table 4-2. The closing moment capacity follows similar trends to the opening moment capacity.

For closing moment, the minimum thickness of bolted side-plate with top-bottom stiffener (M_s^c) and without stiffener (M_n^c) of the can be calculated by the following equations:

$$M_s^c = 0.002 \times {a_s}^{-0.495} \times {b_s}^{2.197} \times f_y \times (\sin\theta)^{-0.94} \times t_s^{5.692} \quad 4.3$$

$$M_n^c = 0.001 \times {a_s}^{0.006} \times {b_s}^{1.793} \times f_y \times (\sin\theta)^{0.093} \times t_s^{1.201} \quad 4.4$$

Where, units of a_s, b_s and t_s are in mm, the unit of f_y is kN/mm^2, and the unit of M_s^c is kNm.

A reliability study was carried out to evaluate the performance of the proposed design equations. In North American Specification, a target reliability index of 2.5 is recommended as a lower limit for cold-formed steel structural members AISI S-16 (2016). If the reliability index is greater than or equal to 2.5, the design rules are reliable. The reliability indices determined for the proposed equations are shown in Table 4-3 and all are greater than the target reliability index of 2.5 AISI S-16 (2016), both with and without stiffener, indicating that the proposed equations are reliable when predicting the

minimum thickness for bolted-side plates. It should be noted that equations are not applicable for θ is equal to 0^0.

Table 4-3 Reliability analysis of proposed equations for moment capacity of bolted-side plate

Ratio of equations	FEA /Proposed Eq(4.1)	FEA /Proposed Eq(4.2)	FEA /Proposed Eq(4.3)	FEA /Proposed Eq(4.4)
Data number	45	45	45	30
Mean, P_m	1.04	1.05	1.04	1.03
Coefficient of variation, COV	0.08	0.07	0.08	0.08
Reliability index, β'	2.55	2.57	2.55	2.52
Resistance Factor, φ	0.95	0.95	0.95	0.95

4.6. Design recommendation

Table 4-4 shows the design recommendations for the minimum thickness of the bolted-side plates for the case where there is no top-bottom stiffener. (The thickness shown in brackets is for the case where stiffeners are included. As mentioned previously only plates with a thickness of 8 mm or less can be stiffened) The design recommendations cover a frame pitch of 5^0 and 10^0.

As can be seen from Table 5, for NTB 200 x 125 x 5 section, a_s/b_s = 2.0 and θ= 5^0 minimum thickness required for bolted side-plate is 9.0 mm for closing moment, whereas for a_s/b_s = 3.0, thickness required is 7.1 mm. Therefore, minimum thickness for the bolted side-plates requirement is decreased for a particular NTB section with increase in a_s/b_s ratio.

Table 4-4 Minimum thickness of bolted side plate (in millimetres) predicted from equations (Eq-4.1 to 4.4)

a) Frame pitch of 5°

	a_s/b_s			
NTB Section	Opening moment		Closing moment	
	2	3	2	3
200 x 125 x 5	7.2 (6.2)[1]	7.1 (N/A)[1,3]	9.0 (6.2)[1]	7.1 (N/A)[1,3]
400 x 150 x 8	9.5 (8.5)[1]	9.0 (7.6)[1]	N/A[3] (8.6)[1]	10.0 (7.6)[1]
1300 x 220 x 12	11.3 (N/A)[1]	11.2 (N/A)[1]	N/A[3] (10.6)[1]	N/A (9.4)[1]

b) Frame pitch of 10°

	a_s/b_s			
NTB Section	Opening moment		Closing moment	
	2	3	2	3
200 x 125 x 5	6.8 (6.4)[1]	6.7 (N/A)[1,3]	6.8 (N/A)[1,3]	6.7 (N/A)[1,3]
400 x 150 x 8	9.2 (9.0)[1]	9.1 (7.1)[1]	9.2 (6.6)[1]	9.0 (N/A)[1,3]
1300 x 220 x 12	10.6 (N/A)[1,3]	10.6 (9.3)[1]	12.0 (8.2)[1]	9.3 (7.3)[1]

Note:

1. Thickness shown in parentheses indicates the reduced minimum thickness for the case when a top-bottom stiffener is folded (only applicable only for thicknesses of plate less than 8 mm).
2. Not applicable in this case as the thickness of plate would be greater than 8 mm.
3. Not applicable in this case as the equation is beyond the range.

4.7. Summary

In this chapter, apex joint with bolted-side plates for NTB portal frame have been studied using the FEA. A FE model is developed for bolted-side plate connection for NTB section and validated against the experimental test on apex joint with back-to-back channel section after Lim (2001). Using the validated model, a sensitivity analysis is performed by varying the parameters such as yield stress of NTB sections, thickness of bolted-side plates, edge distance of bolts and length to depth ratio of the bolted-side plate. Based on the sensitivity analysis, parameters for the analysis are chosen and analysis results are used to propose the design recommendation, i.e., equations for the minimum thickness of the bolted side-plates for different NTB sections under opening as well as closing moment. A reliability analysis has been conducted to confirm the reliability of the

proposed equations. Reliability index (β') of the proposed equations is greater than 2.5, and hence equations are reliable and can be used for the practical design.

Chapter 5 Moment capacity of bolted-side plate for eaves joint

5.1. Introduction

As stated in AS/NZ4600 (2018), the joints must be strong enough to prevent the frame from collapsing, and the design moment capacity of the joint must match or surpass the joint's moment capacity as calculated using advanced analysis methods.

In NTB portal frames, the eaves joints are commonly formed through bolted end plate systems (See Figure 5-1). As can be seen, the NTB members are welded by full penetration butt weld to the plates and then bolted together to form the joints. However, these joints are prone to cracking in the HAZ of the weld under bearing opening moment (Wilkinson and Hancock, 2000) and are costly in terms of fabrication (Shahmohammadi et al., 2022).

To address the above issue, bolted-side plates can be used in the eaves joints for the NTB portal frame as an alternative (see Figure 5-2). As can be seen, bolted-side plates have no stiffeners, as thicknesses greater than 8mm are difficult to fold in practice.

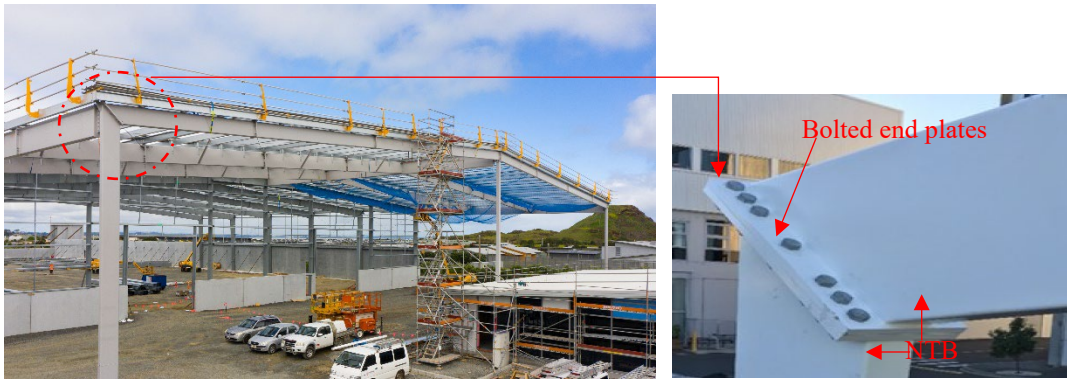

Figure 5-1 A photograph of NTB portal frame and its eaves joints (Donovan Group Ltd.)

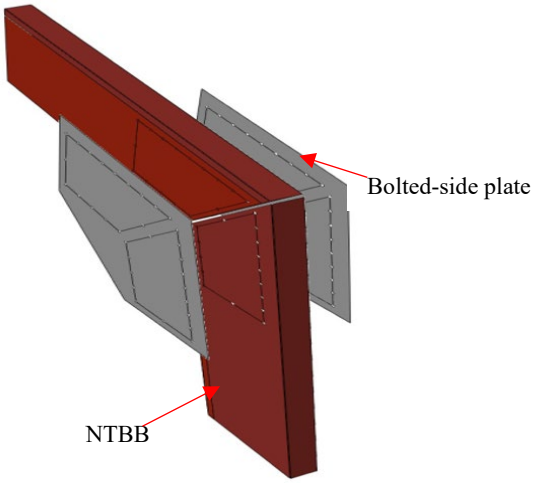

Figure 5-2 Eaves joint with bolted-side plates for NTB portal frame (Note: Plates thickness is greater than 8mm used and M20 bolts are considered)

The overall strength and stiffness of NTB portal frames with bolted-side plates joints are affected by the detailing of the bolted-side plate (i.e. overall dimensions and thickness of the bolted-side plates, number of fasteners, etc.). Guidance in AS/NZ 4600 (2018) is limited to stating that joints should be designed to have adequate strength and ductility to ensure the structure fails within the members, and no guidance is provided on the detailing of the joints.

Bolted-side plates for eaves joints should thus be sized to ideally have sufficient strength such that failure occurs in the NTB members of the portal frame. Proper sizing of the bolted-side plate transfers the load to the member (Lim and Nethercot, 2003; Lim and Young, 2007; Mojtabaei et al., 2020).

In the literature, Dubina et al. (2006); Kwon et al. (2006); Zhang et al. (2016a) described experimental tests on eaves joints. These studies comprise eaves brackets sandwiched between back-to-back channels and consider the rigidity and stiffness of the joint. None of these studies, however, focuses on the prediction of the moment capacity of eaves brackets. Experimental tests by Rinchen and Rasmussen (2019b) and Pouladi et al. (2019) focused on the flexural behaviour and stiffness of eaves joints, without considering the

strength of eaves brackets. Additionally, all the previously described experimental tests limit their considerations to eaves joints under closing moments. Lim and Nethercot (2002b) provided guidance for sizing fully restrained eaves brackets used in CFS portal frames by considering the strength of joints for closing moments. Recently, Chen et al. (2023b) extended the study conducted by Lim and Nethercot (2002b) on eaves brackets by considering eaves joints as partially restrained under both bearing opening and closing moments and proposed a unified equation for predicting the moment capacity for the eaves brackets. However, no information was found related to the design of bolted-side plates for the eaves joint of NTB portal frame.

This chapter thus fills an existing research gap by investigating the closing and opening moment capacities of bolted-side plates of eaves joints for NTB portal frame. Unified design equations are proposed for designing bolted-side plates for eaves joint with parameters illustrated in Figure 5-3, considering both closing and opening moments.

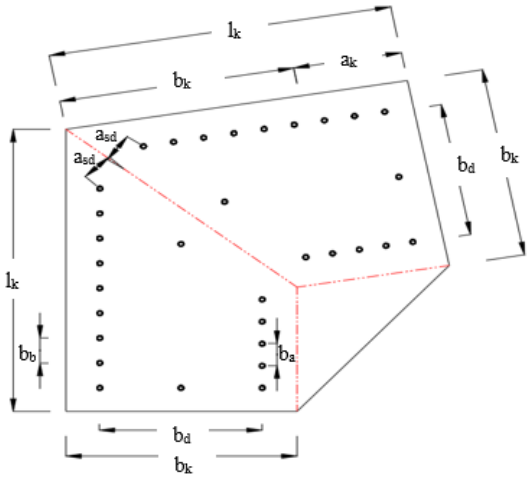

Figure 5-3 Diagram showing the parameter of a bolted-side plates for eaves joints (red dotted line shows the NTB member)

5.2. Summary of experimental tests by Lim and Nethercot (2002b)

The eaves joint tests conducted by Lim and Nethercot (2002b) are the only experimental tests described in the literature specifically designed to assess bracket strength and are the closest tests to bolted-side plate joints. The test set-up details are shown in Figure 5-4a, with idealized pure bending on the eaves bracket. As illustrated, only one eaves bracket was bolted to the back-to-back channels and full lateral restraints were applied to the eaves bracket. The channel dimensions used in the tests are shown in Figure 5-4b. In the tested eaves bracket with only bottom stiffeners, the pitch angle θ is 0°. All joint tests failed due to premature buckling of the eaves bracket. The moment capacity (M_U^{EXP}) was calculated from the failure load and is tabulated in Table 5-1.

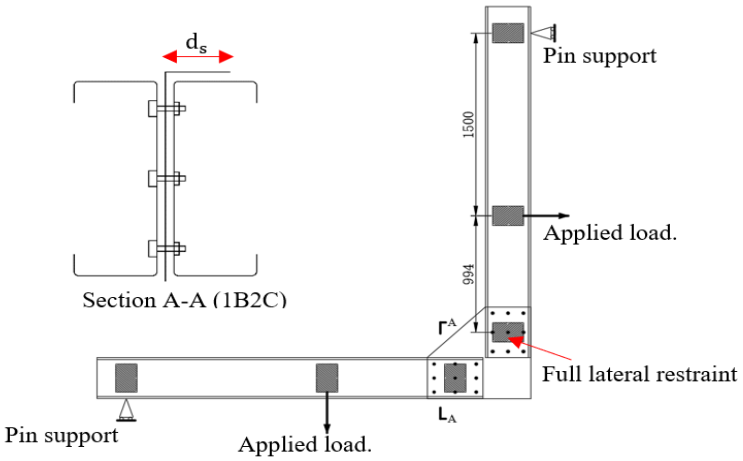

(a) Test set up

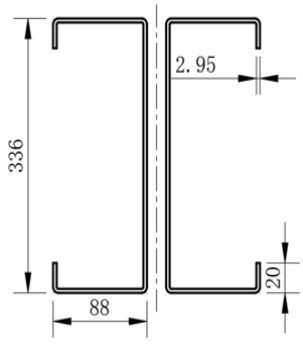

All dimensions are in millimeters

(b) Dimensions of back-to-back channels

Figure 5-4 Details of eaves joint test by Lim and Nethercot (2002b)

5.3. FE modelling techniques for eaves joints

The modelling techniques used in this chapter are validated against the results of the experimental tests described in Section 5.2. The CFS eaves joints are modelled using the FE program ABAQUS (2021).

5.3.1. Geometry

Details of the FE model geometry is shown in Figure 5-5. The bolted-side plates and the NTB member with a cantilever length $3 \times b_e$ are modelled, and as only pure moment load is considered, it is not necessary to model the whole experimental test setup (Paul et al., 2023).

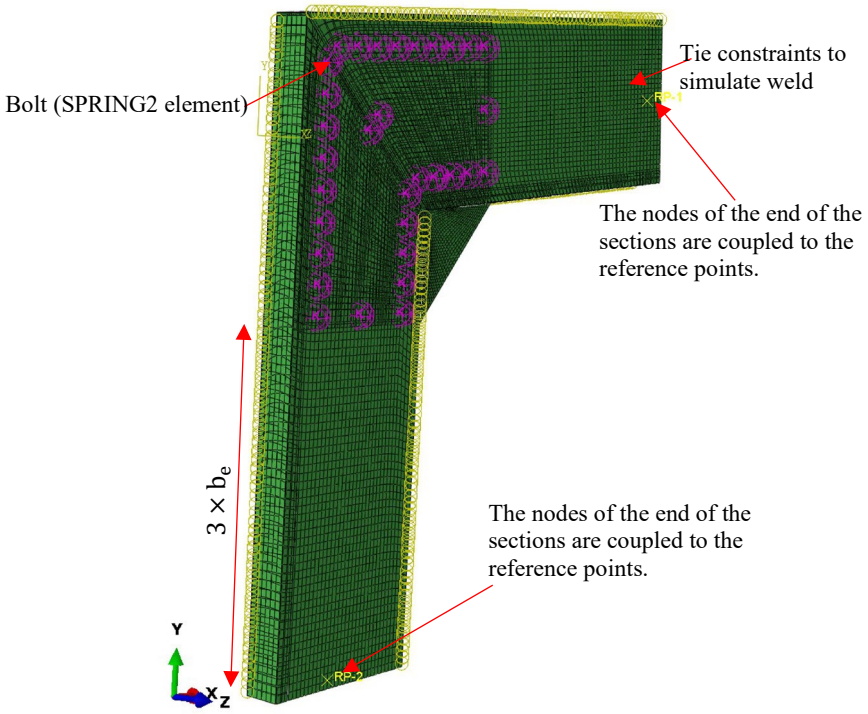

(a) Springs and coupling

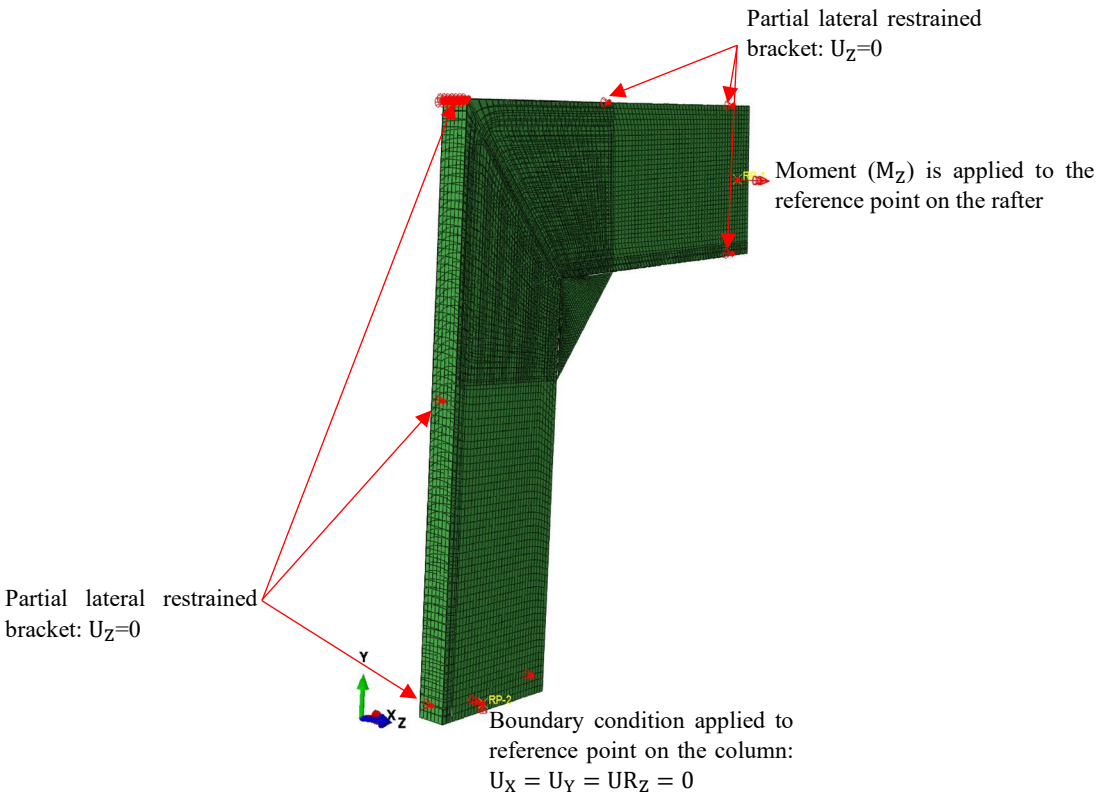

(b) Boundary condition and loading

Figure 5-5 Details of FE model for eaves joint of NTB portal frame

5.3.2. Contact and connection

Surface-to-surface contact between NTB member and bolted-side plates is simulated and the behaviour of bolted connections is modelled using the "SPRING2" element. The details of the contact and connection are the same as in Section 4.3.1.2.

5.3.3. Element and material

Standard 4-noded doubly curved thin shell elements (S4R) in ABAQUS (2021) are used to model the eaves joint. The mesh sizes used to model the NTB members (columns and rafters) and the bolted-side plates are 15 mm × 15 mm and 10 mm × 10 mm, respectively. The simulated material behaviour follows an elastic-perfectly plastic model. The initial elastic modulus (E) used was 200 GPA.

5.3.4. Boundary conditions and loading

In the FE model, reference points are created at the center of the end sections and coupled to the end nodes. The reference point on the rafter bears the closing moment. As shown in Figure 5-5b, the reference point on the column is limited to rotation along the axial Z direction (UR_Z=0) and displaces in-plane (U_X=U_Y=0).

5.3.5. Validation of FE model

Table 5-1 summarizes the outcomes obtained from a static nonlinear analysis conducted on the eaves joint. The calculated failure load (M_U^{FEA}), aligns closely with the experimental results (M_U^{EXP}), exhibiting an average of difference 4.0 % and a small standard deviation of 0.08. The observed buckling failure of the eaves bracket, as shown in Figure 5-6, corresponds to the experimental findings reported by Lim and Nethercot (2002b). Therefore, the aforementioned FE modelling technique can be used for the further investigation in the current research.

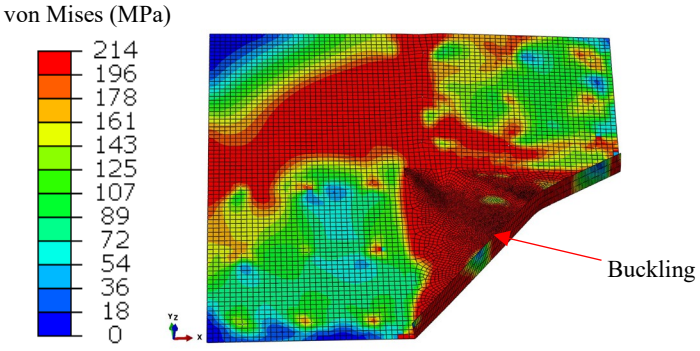

Figure 5-6 Buckling failure of fully restrained eaves bracket

Table 5-1 Comparison of experimental and FEA results of eaves joint tests after Lim and Nethercot (2002b)

Test	a_e	b_e	d_s	t_b	f_y	M_U^{EXP}	M_U^{FEA}	$\frac{M_U^{FEA}}{M_U^{EXP}}$
	(mm)				N/mm^2	(kN.m)		
1	400	344	20.4	2.91	207	33.0	33.87	1.03
2	400	352	31.5	2.98	214	40	40.05	1.00
3	400	346	46.8	2.96	209	45	42.20	0.94
4	400	342	102.6	2.98	213	52	44.32	0.85
Average								0.96
Standard deviation								0.08

5.4. Sensitivity Analysis

The eaves joint FE model shown in Figure 5-5 is used to conduct a sensitivity analysis on the yield stress of NTB member, the thickness, and other geometric parameters of the bolted-side plates. In Section 5.5, the prediction equations consider the variability of the thickness and other geometric properties. However, in this sensitivity study, thickness and yield stress of NTB member are treated as constant and set to be 6 mm and 350 N/mm^2, respectively. The geometric dimensions of the eaves bracket are a_k=750mm, b_k=375 mm, and θ= 0° (see Figure 5-3).

5.4.1. Yield stress of NTB sections

The validated FE model assumes a linear elastic behaviour for the NTB member. However, in real construction, the NTB member material behaves in an elasto-plastic manner. Varying the NTB member yield stress provides further insight into how the moment capacity changes with the strength of NTB member. The sensitivity analysis varies the yield stress of NTB section from 100 N/mm^2 to 700 N/mm^2. The ultimate moment capacities of eaves joints are shown in Figure 5-7. As can be seen, for the given eaves joints, members with inadequate yield strength, (less than 600 N/mm^2), causing the joints to fail in the NTB member. In the parametrical study of Chapter 5.5, to avoid the

failure that occurs on the NTB member, the linear elastic property is assumed for the NTB member.

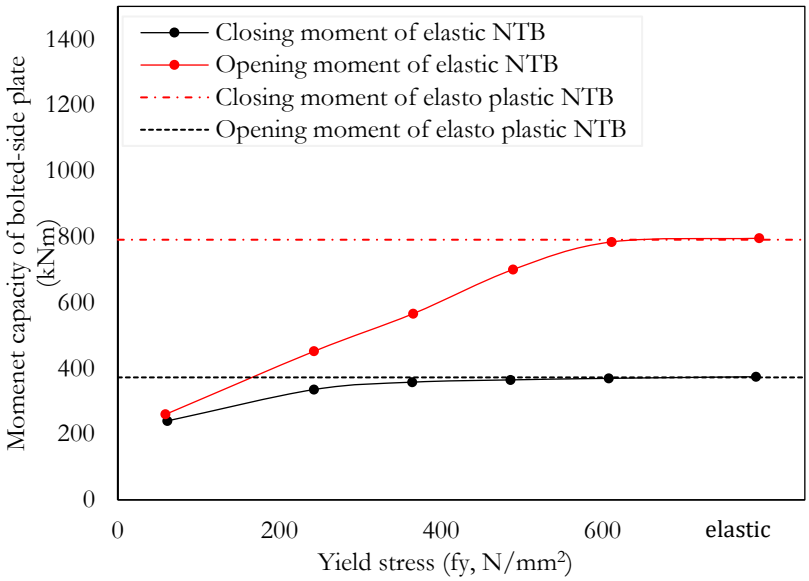

Figure 5-7 Effect of the yield stress (f_y) of the NTB member on the moment capacity (b_k = 750 mm, a_k = 375 mm, and t_s =6 mm; θ=0^0)

5.4.2. Thickness of bolted-side plates

A sensitivity analysis was performed to evaluate the effects of varying thicknesses on the moment capacity of bolted side plates. The thickness was varied from 8 to 16 mm. In contrast, the thickness of the NTB section was held constant at 6 mm for this sensitivity analysis. It was observed that altering the thickness of the NTB section had no significant effect on the moment capacity of the bolted side plates. As can be seen from Figure 5-8, the relationship between the thickness of the bolted side plates and the corresponding increase in moment capacity is almost linear. Based on these findings, it is recommended to consider varying the thickness of the bolted side plates within the range of 8 mm to 16 mm for the parametric study.

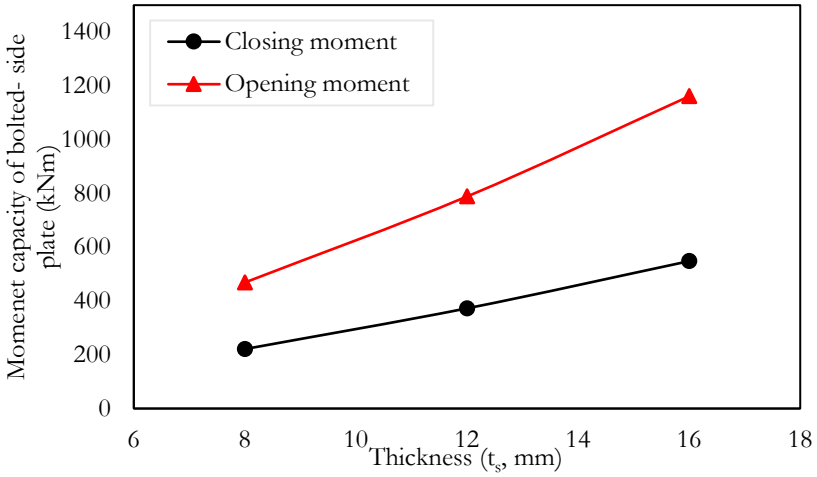

Figure 5-8 The effect of thickness (t_s) on the moment capacity of bolted-side plates (b_k = 750 mm, a_k = 375 mm; θ=0^0)

5.4.3. Effects of bolts-group

The influence of bolt group size on the moment capacity of side plates was also investigated. As illustrated in Figure 5-9, a marginal 1% reduction in moment capacity is observed when the bolt group size increases from 7 ×5 to 9 ×5 for both closing and opening moment capacities. Beyond this point, the moment capacity remains relatively constant. Given that the primary objective of this study is to obtain the moment capacity and bolts group has limited influence on the moment capacity, it is advisable to use the practical bolt group size of 9 × 5.

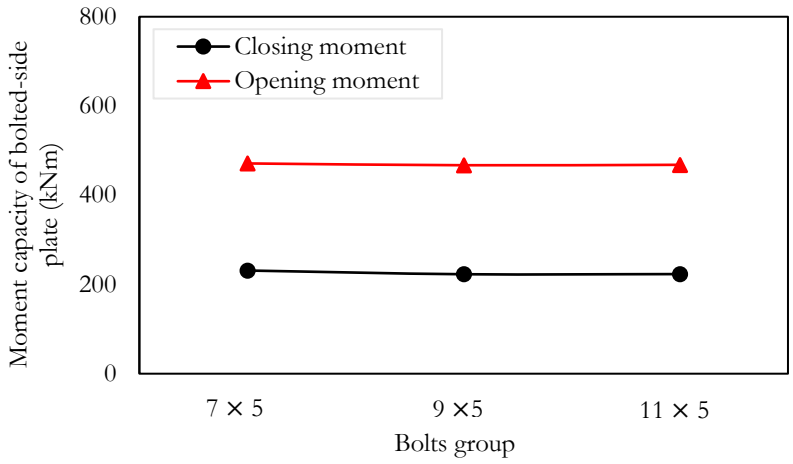

Figure 5-9 Effect of the bolts group size on the moment capacity (b_k = 750 mm, a_k = 375 mm, and t_s =6 mm; θ=0^0)

5.4.4. Geometric parameters

The effects of different geometric parameters of bolted-side plate for eaves joints on the moment capacity are investigated. The parameters investigated were edge distance (a_{sd}), ratio of edge width of bolted-side plate to extended length of bolted-side plate (b_k/a_k), bolt distances (b_b or b_a) and pitch (θ) of the portal frame. The ranges for these parameters were 40 mm to 60 mm, 0.3 to 0.7, 85 mm to 100 mm, and 0° to 10°, respectively.

From Figure 5-10a, it is evident that the bolted-side plate achieved its highest moment capacity with an edge distance (a_{sd}) of 50 mm. Therefore, it is recommended to maintain an edge distance of 50 mm for the subsequent parametric study.

As can be seen from Figure 5-10b, the moment capacity of the side plates increases with the a_k/b_k ratio. To optimize the material usage, a_k/b_k ratio is suggested to be in between 0.3 and 0.5.

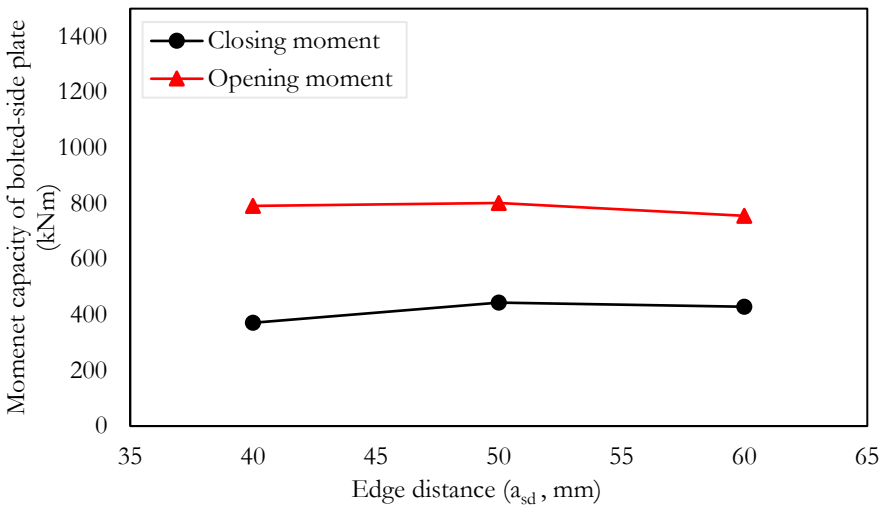

(a) Effects of a_{sd} on the moment capacity

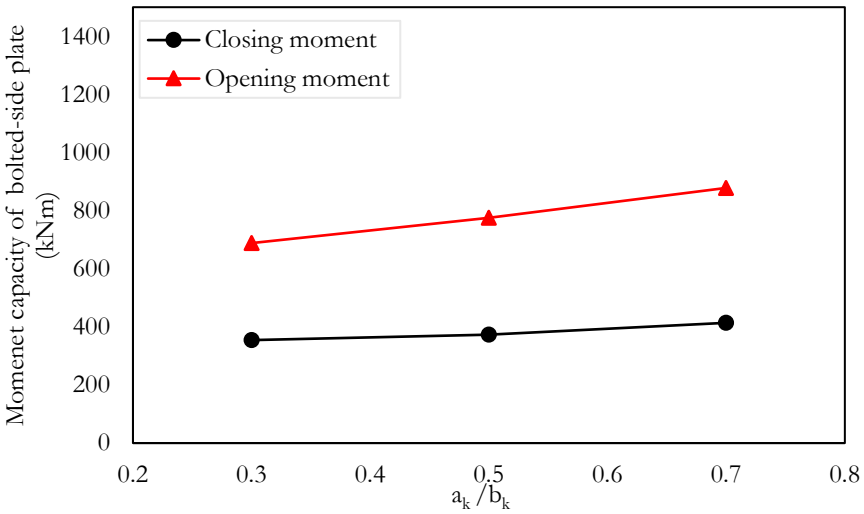

(b) Effects a_k/b_k ratio on the moment capacity

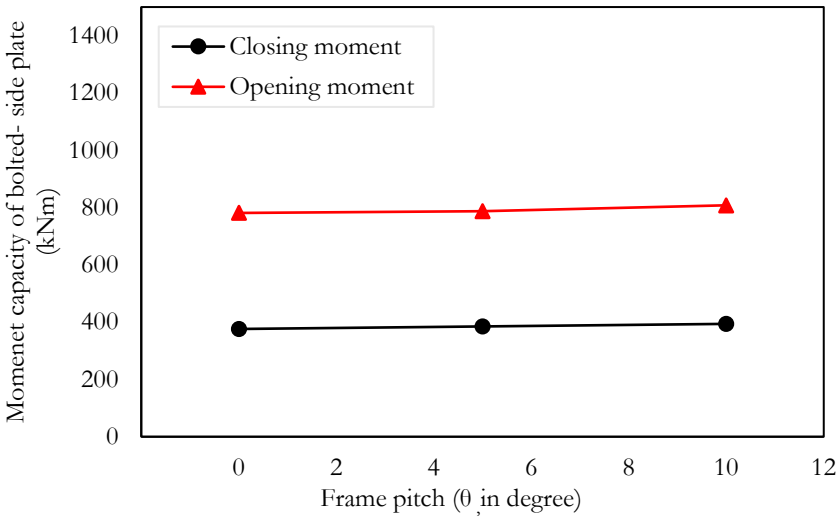

(c) Effects of $'\theta'$ on the moment capacity

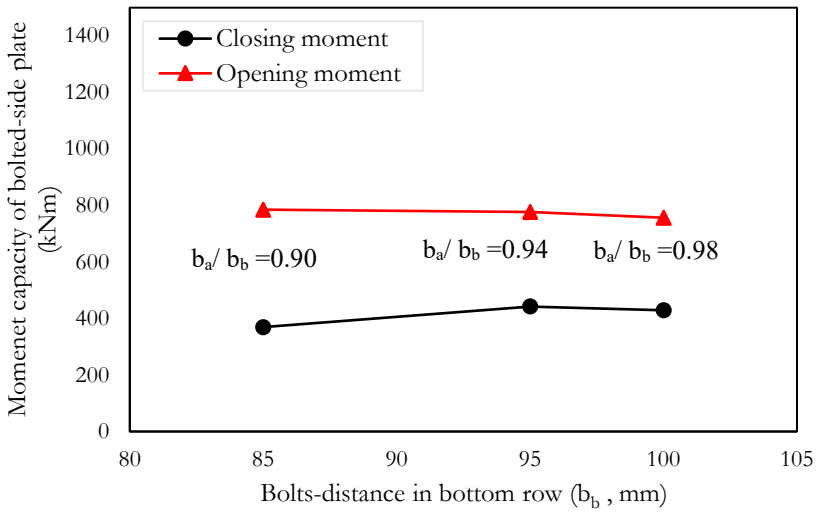

(d) Effects of b_b on the moment capacity

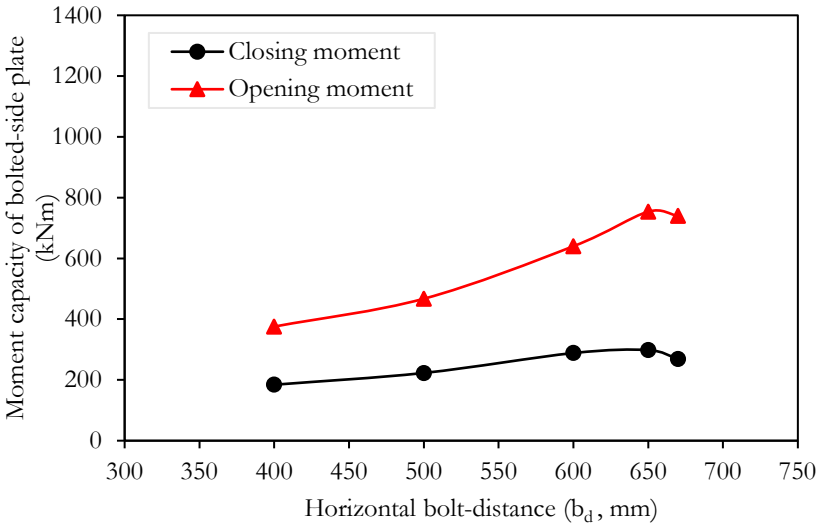

(e) Effects of b_d on the moment capacity

Figure 5-10 Effects of different geometric parameters on the moment capacity (b_k = 750 mm, a_k = 375 mm and t_s =6 mm; θ=0^0)

Figure 5-10c shows that the frame's pitch (θ) has a negligible effect on the moment capacity of the bolted-side plate for both closing and opening moments. In New Zealand, the recommended value for the frame's pitch is 5° to 10°.

Figure 5-10d depicts the effects of horizontal bolt distance in bottom row of bolt group on the moment capacity of the bolted-side plate. As can be seen from Figure 5-10d, the moment capacity of the bolted-side plate in eaves joints is influenced by the horizontal distance between the bolts for both closing and opening moment. In this study, the ratio between the distances of the top and bottom row of bolt group (b_a/b_b ratio) was considered, as these distances were not equal. When the b_a/b_b ratio is approximately 0.94, moment capacity of the bolted-side plate is maximum.

Figure 5-10e depicts the influence of the horizontal bolt-distance, b_d, on the moment capacity of the bolted-side plate. The moment capacity increases as the b_d distance increases and reaching its maximum at 650mm. For b_d =650mm and b_k = 750mm, horizontal side distance ($2*a_{sb}$) should be 100mm. As the moment capacity is maximum

when b_d = 650mm, moment capacity for side plate is also maximum when a_{sb} = 50mm. Therefore, it is advisable to use horizontal side distance of 50mm.

5.5. Moment capacity prediction

The moment capacity of bolted-side plate for eaves joint is further investigated by conducting a parametric study using the validated FE model shown in Figure 5-9, for the partially restrained eaves joint. Three alternative cross-section geometries of the NTB member, identified by web size, are considered as tabulated in Table 5-2. As described in Section 5.4.1, the NTB in the eave's joints are assumed to be linear elastic.

Table 5-2 Selected variable for the parametric study

NTB section	b_k	t_s	a_k/b_k	θ	Material properties	Unified geometric parametric	Moment capacity of NTB section (M_b)
	(mm)						kNm
700 x 125 x 5	700	8-16	0.3 and 0.5	0^0 to 10^0	E = 200 x10^3 N/mm^2 f_y =350 N/mm^2 μ =0.3	a_{sd}= 50 mm, a_{sb}= 50 mm, Bolt distance <=100 mm	409.0
750 x 150 x 6	750						1105.6
800 x 150 x 8	800						4109.0

5.5.1. Closing moment

A parametric study composing 301FE models is conducted to analyse the closing moment of the bolted-side plate. The edge width, b_k, varies from 700 mm to 800 mm, and the ratio a_k/b_k is adjusted between 0.3 and 0.5. The thickness, t_s, varies from 8 mm to 16 mm in steps of 0.5 mm. Frame pitch (θ*),* was varied from 0^0 to 10^0. The remaining design parameters are listed in Table 5-2, following the AS/NZ4600 (2018) design standard.

The parametric study shows variations in the closing moment. The ratio a_k/b_k is directly correlated to the moment capacity, as presented in Figure 5-10b. In this study, unified design equations for the moment capacity are created using a regression analysis. The

closing moment capacity (M_{bs}^{c}) of the bolted-side plate can be predicted using the following equation:

$$M_{bs}^{c} = 2.77 \times {a_k}^{0.47} \times {b_k}^{4.80} \times f_y \times (\cos\theta)^{1.70} \times t_s^{0.761} \times 10^{-13};\ t_s \leq 12.0 \quad 5.1$$

$$M_{bs}^{c} = 2.95 \times {a_k}^{0.415} \times {b_k}^{5.137} \times f_y \times (\cos\theta)^{-0.093} \times t_s^{0.877} \times 10^{-14};\ t_s > 12.0 \quad 5.2$$

Where, units of a_k, b_k, and t_s are in mm, the unit of f_y is $\mathrm{kN/mm^2}$, and the unit of M_{bs}^{c} is kNm.

5.5.2. Opening moment

To predict the opening moment capacity of bolted-side plate for eaves joint, the 301 FE models described in Section 5.5.1.1 are employed. The parametric study shows the opening moment capacity of the bolted-side plate follows similar trends to the closing moment capacity of bolted-side plate. As illustrated in Figure 5-10b, with increasing the ratio of a_k/b_k decreases its opening moment capacity.

The moment capacity for the closing moment was also investigated, employing the same set of parametric values as those used for the previously discussed opening moment. In this analysis, a total of 301 FE models were subjected to pure moment, while varying b_k, b_k/a_k, t_s, and θ within the range of values presented in Table 5-2. The evaluation of the closing moment capacity reveals trends similar to those observed for the opening moment capacity.

To predict the opening moment capacity (M_{bs}^{c}) of the bolted-side plate, the following equations can be used for the calculation:

$$M_{bs}^{o} = 6.15 \times {a_k}^{0.35} \times {b_k}^{3.317} \times f_y \times (\cos\theta)^{5.9} \times t_s^{1.235} \times 10^{-9} \quad 5.3$$

Where, units of a_k, b_k, and t_s are mm, the unit of f_y is $\mathrm{kN/mm^2}$, and the unit of M_{bs}^{o} is kNm.

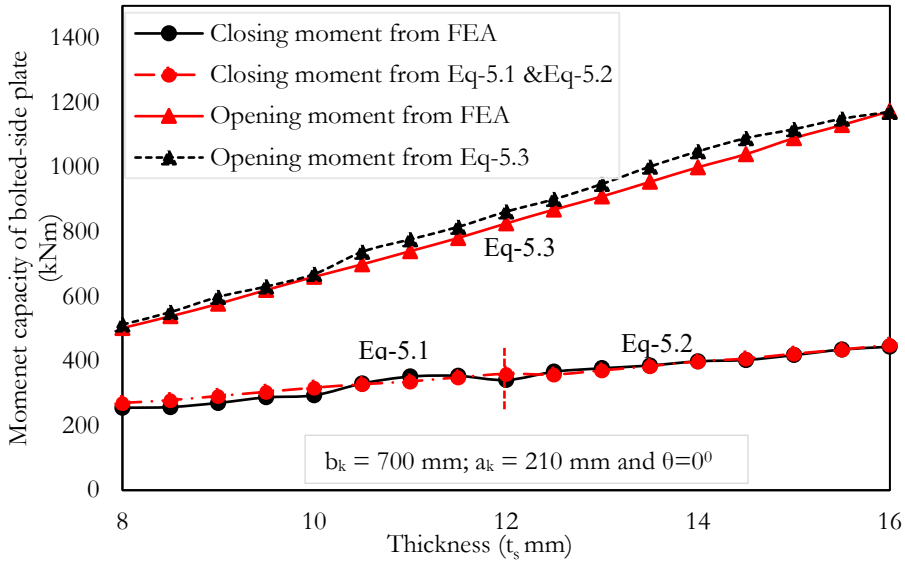

(a) Comparison of FEA data with the data from the equation proposed

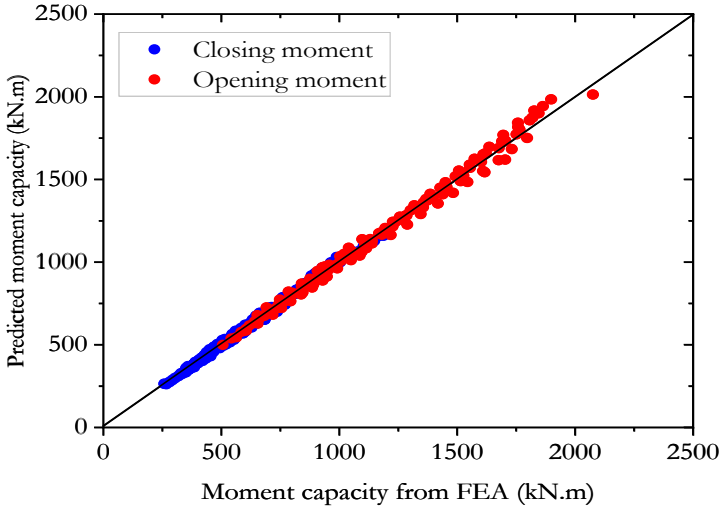

(b) Predicted data points from the proposed equation with FEA data points

Figure 5-11 Comparison of predicted moment capacity from the proposed equations with the FEA results

A reliability analysis was conducted to evaluate the accuracy of the proposed equations. According to AISI S-16 (2016), a target reliability index of greater than 2.5 is recommended for CFS structures. Since the reliability index for the proposed equations exceeds this threshold (as shown in Table 5-3), the equations can be considered reliable. Figure 5-11 illustrates the comparison between the FEA results and those obtained using

the proposed equations, demonstrating a strong correlation. It is important to highlight that these equations are valid within the specified thickness range of 8.0 mm to 16.0 mm. Additionally, the equations can be used to predict the moment capacity of the bolted-side plates within this range.

Table 5-3 Results of the reliability analysis of the proposed design equations

Ratio of equations	FEA /Proposed Eq-1	FEA /Proposed Eq-2 and Eq-3
Data number	186	190
Mean, P_m	1.0	1.0
Coefficient of variation, COV	0.03	0.03
Reliability index, β'	2.52	2.50
Resistance Factor, φ	0.95	0.95

5.6. Design recommendation for the bolted-side plate

As illustrated in Figure 5-3, the dimension of the bolted-side plate is dependent on the total length of the edge width (b_k) and the extended length (a_k) of bolted-side plate, respectively. For calculating the length of the bolted-side plate (l_k), it was assumed that the bolted-side plate should resist the moment capacity of NTB members (see Table 5-2).

Table 5-4 shows the calculated minimum length of the bolted side plate (l_k) using equations 5.1 to 5.3. For the NTB cross-section with dimensions 750 x 150 x 6, where b_k is 750 mm, θ is 0^0, and t_s is 8.0 mm, the extended length of eaves (a_k) calculated using Eq-1 for closing moment, is 123.1 mm. Consequently, the total length of the eaves (l_k) will be 973.1 mm. In contrast, the minimum length stipulated for opening moments is 802.1 mm.

5.7. Summary

This chapter employs validated modelling techniques, based on previously reported experimental tests, to develop design equations for predicting the moment capacity of bolted-side plates. The reliability of these proposed equations was assessed, yielding a reliability index greater than 2.5, which confirms their robustness. A sensitivity analysis was conducted on the eaves joints, considering factors such as the yield stress of the NTB members, the thickness of the bolted-side plate, and the geometric parameters commonly used in practice. The ultimate load capacity of the eaves joints is primarily influenced by the strength of the bolted-side plates, provided the NTB members have sufficient capacity to resist buckling. Finally, a design recommendation is presented for calculating the optimal length of the bolted-side plate for eaves joints in NTB portal frames, based on the outcomes of the parametric study.

Table 5-4 Minimum length of bolted side-plates (in millimeters) from Eq-5.1 to 5.3

a) Pitch of frame, $\theta = 0^0$

NTB Section	l_k (mm)									
	Closing moment					Opening moment				
	t_s = 8.0	t_s = 10.0	t_s = 12.0	t_s = 14.0	t_s = 16.0	t_s = 8.0	t_s = 10.0	t_s = 12.0	t_s = 14.0	t_s = 16.0
	(mm)					(mm)				
700 x 125 x 5	880.1	825.5	793.4	766.2	749.9	727.8	712.7	706.7	703.8	702.5
750 x 150 x 6	970.0	903.3	864.1	828.6	809.3	798.8	772.2	761.7	756.8	754.2
800 x 150 x 8	1057.4	979.3	933.5	889.1	867.2	879.2	836.1	819.0	811.0	806.9

b) Pitch of frame, $\theta = 5^0$

NTB Section	l_k (mm)									
	Closing moment					Opening moment				
	t_s = 8.0	t_s = 10.0	t_s = 12.0	t_s = 14.0	t_s = 16.0	t_s = 8.0	t_s = 10.0	t_s = 12.0	t_s = 14.0	t_s = 16.0
	(mm)					(mm)				
700 x 125 x 5	882.5	827.2	794.7	766.1	749.9	729.7	713.5	707.1	704.1	702.5
750 x 150 x 6	973.1	905.4	865.7	828.5	809.2	802.1	773.7	762.5	757.2	754.5
800 x 150 x 8	1061.0	981.8	935.4	889.0	867.1	884.5	838.5	820.2	811.7	807.3

c) Pitch of frame, $\theta = 10^0$

NTB Section	l_k (mm)									
	Closing moment					Opening moment				
	t_s = 8.0	t_s = 10.0	t_s = 12.0	t_s = 14.0	t_s = 16.0	t_s = 8.0	t_s = 10.0	t_s = 12.0	t_s = 14.0	t_s = 16.0
	(mm)					(mm)				
700 x 125 x 5	890.3	832.6	798.7	766.0	749.8	736.0	716.4	708.6	705.0	703.1
750 x 150 x 6	982.6	912.0	870.6	828.3	809.1	813.2	778.8	765.1	758.8	755.5
800 x 150 x 8	1072.0	989.6	941.1	888.8	866.9	902.6	846.7	824.5	814.2	808.9

Chapter 6 Method of predicting vertical load for portal frames with back-to-back channel sections-a case study

6.1. Introduction

In New Zealand and Australasia, CFS portal frames with back-to-back channel sections are widely used in warehouses, shelters, garages, and agricultural buildings (see Figure 6-1). The eaves and apex joints of these portal frames are typically semi-rigid, formed using brackets bolted to the channel webs. While an eaves brace (see Figure 2-6a) can enhance stability, it is often avoided due to its impact on clear column height. In practice, designers often assume these joints to be rigid without accounting for shear lag effects, which can lead to unsafe designs due to sudden failures in the columns near the bolt-group. While the current design guidelines (e.g. Australian and New Zealand design guidelines AS/NZ 4600, 2018) for portal frames generally specify that joints must not fail before the members, they do not provide any clear guidance for designers on predicting the load-carrying capacity of such systems.

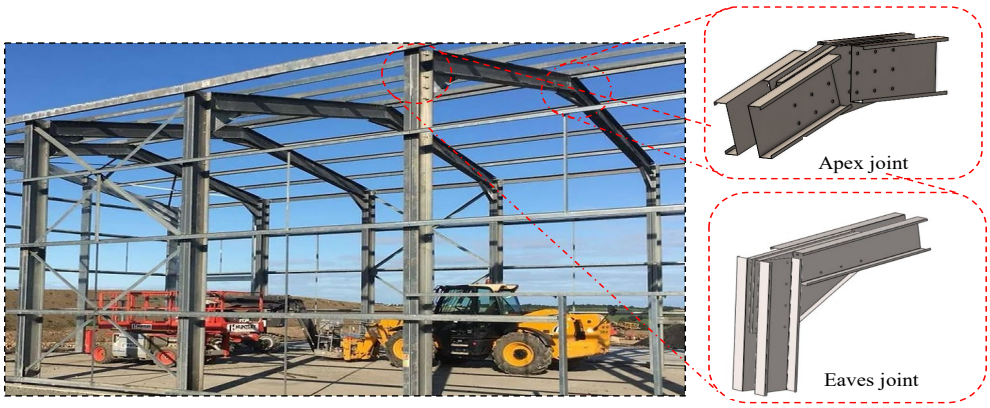

a) Photograph of portal frame with back-to-back channel section

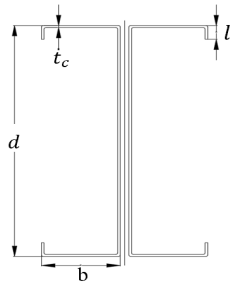

b) Back-to-back channel section

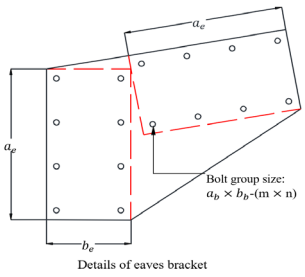

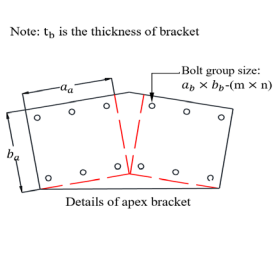

c) Bracket details

Figure 6-1 Photograph of a CFS portal frame building with back-to-back channel section and its joints

In terms of full-scale tests, several studies in the literature have reported on CFS portal frames with back-to-back channel sections for the columns and rafter members. These are described here in chronological order. Kirk (1986) conducted full-scale tests on a back-to-back portal framing system, known as the Swagebeam system. The novelty of the system was that rigid joints could be formed as a result of interconnecting swages. It was found that the Swagebeam channel-sections failed with a reduced moment capacity (see Figure 6-2), as a result of being adjacent to moment-resisting bolted connections, combined with shear lag effects (Mojtabaei et al. 2020, 2021; McCrum et al. 2019). Lim and Nethercot (2004) described full-scale tests on a more general portal frame, with back-to-back channel sections that used back-to-back brackets bolted to the web of channel-sections for the joints. Figure 6-3 shows an ‘‘aerial’’ view of the test. It was found that the joints were semi-rigid due to bolt-hole elongation. Wrzesien et al. (2015) conducted experimental tests on full-scale portal frames, one having roof sheeting and the other without roof sheeting. It was shown that while stressed-skin action reduced frame deflections by 90% under horizontal load, there was almost no effect from stressed-skin action under vertical load. Zhang et al. (2016) conducted full-scale portal frame tests with eaves braces (see Figure 2-6a). In this case, the focus of the research was not the joints but, on the lateral-torsional buckling of the columns. Blum and Rasmussen (2019a) described similar tests to Zhang et al., again with the back-to-back channel sections failing through lateral-torsional buckling of the column member. One of these tests was conducted with braced columns, which comprised girts on the columns between the frames. Failure was initiated by buckling of the apex bracket which caused large vertical displacements at the apex, and subsequent frame failure occurred at both the apex joint and the rafter at the knee-brace connection locations. Mojtabaei et al. (2018) investigated the seismic performance of an innovative CFS moment-resisting frame through both experimental and analytical methods. The study concluded that a 50% increase in the axial load ratio of the columns led to reductions

of 26%, 62%, and 50% in the ultimate lateral load, energy dissipation capacity, and ductility ratio of the studied CFS frame, respectively. McCrum et al. (2019, 2021) conducted portal frame tests under both monotonic and cyclic loading. Their tests demonstrated that ignoring the reduced moment capacity of the channel-sections, due to shear lag effects near the moment-resisting bolted connections, could lead to overestimating the frame capacity by as much as 40%.

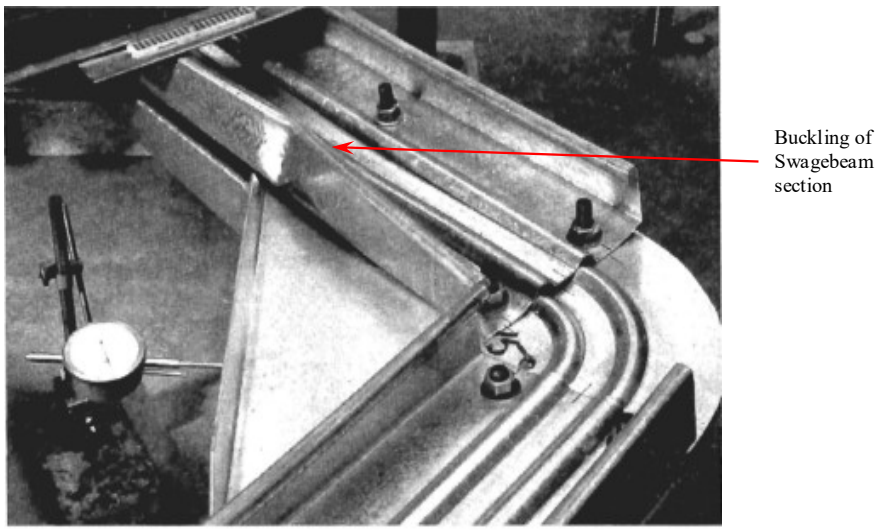

Figure 6-2 Failure of Swagebeam portal frame joint due to joint arrangement after Kirk (1986)

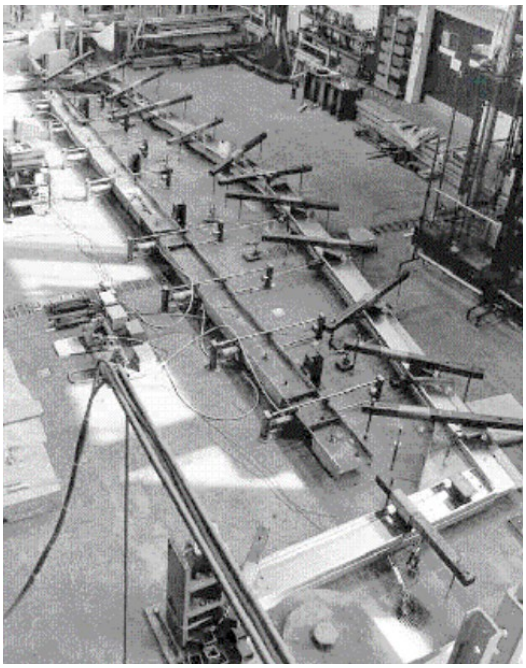

Figure 6-3 Full-scale portal frame test (Frame B) after Lim and Nethercot (2004)

Experimental component tests on the moment-capacity of cold-formed steel apex brackets have also been reported in the literature (Öztürk and Pul, 2015; Peng et al., 2018; Blum and Rasmussen, 2019b). It should be noted that all these experimental tests relate to the apex bracket being tested under opening moment (see Figure 2-17a). Figure 4-6 shows the typical buckling failure. None of these tests, however, proposed design recommendations for the moment capacity of the apex brackets. Such design recommendations for opening moment, were proposed by Chen et al. (2021), using the result of a validated nonlinear elasto-plastic FE model; this model assumed full lateral restraint. More recently, Chen et al. (2023a) proposed a revised set of equations for partially restrained brackets, this time under both opening and closing moment, consistent with New Zealand practice in terms of bracket size and restraints.

In terms of the eaves joint, while experimental component tests have been described (Zhang et al., 2016a; Dubina et al., 2006; Kwon et al., 2006; Chung and Lau, 1999; Lim and Nethercot; 2002b), only Lim and Nethercot (2002b) conducted tests to determine the strength of the eaves brackets. More recently, Chen et al. (2023b), validated a nonlinear elasto-plastic FE model against the test results of Lim and Nethercot (2002b), and proposed design equations under both opening and closing moment, again consistent with New Zealand practice.

As can be seen from Figure 6-2, if the brackets are detailed and designed to have a higher moment capacity than the sections then, as mentioned previously, there may be a reduced moment capacity of the channel-sections due to their nearness to the moment-resisting bolted connections , combined with important shear lag effects (Kirk, 1986; Mojtabaei et al., 2020; McCrum et al., 2019, 2021; Lim and Nethercot, 2003; Lim et al., 2016; Phan et al., 2020). These are described here in chronological order. Lim and Nethercot (2003) investigated the effect of different length of bolt groups and proposed design equations. Later, Lim et al. (2016) showed that the DSM can be applied to predict the reduced moment capacity for practical sizes

of bracket (and therefore joint) i.e. the equations did not include bolt-group length as a parameter. Phan et al. (2020) developed an analytical method to determine the reduced moment capacity of back-to-back channel sections due to joint effects; Phan et al. used the results to optimize the geometry of the channel sections. Mojtabaei et al. (2020) proposed strength reduction equations from the results of non-linear elasto plastic FE models concluding, as mentioned before, that the reduction in strength is attributed to their close positioning near moment-resisting bolted connections, combined with shear lag effects.

With respect to joint flexibility, early work by Zadanfarrokh and Bryan (1992) and Zaharia and Dubina (2006) both proposed equations for determining the bolt-hole elongation stiffness; that leads to the flexibility of the joints. However, these equations were for joints in single shear, with a modification applied for double shear. More recently, in 2019 Ahmed and Teh (2019) proposed an equation, based on FEA validated against the experimental test results, for predicting the bolt-hole elongation stiffness of double shear connections.

Few studies have been carried out on CFS portal frames without knee braces and their components through both experimental and numerical investigations. However, the previous studies have primarily focused on isolated aspects, with limited consideration of joint flexibility and combined actions including shear lag effects. Therefore, these effects are not generally incorporated into design practices or used for predicting the load-carrying capacity of portal frames. This paper aims to address this research gap by providing a better understanding of the complex behaviour of these connections leading to more efficient assessment and, for the first time, a simplified design method that can be used by practicing engineers. To this end, a non-linear elasto-plastic FE model of a CFS portal frame is first presented. The results of this model are validated against the experimental test results of Lim and Nethercot (2004) (see Figure 6-3 for an ‘‘aerial’’ view of the frame test setup). As mentioned previously, while other vertical frame test setups have been reported in the literature (Kirk, 1986; McCrum et al., 2019, 2021;

Wrzesien et al., 2015; Zhang et al., 2016a; Blum and Rasmussen, 2019b), this test setup comprises a single frame tested horizontally on the laboratory floor, and so all the load applied is all resisted by the test frame. It should be noted, however, that as full lateral restraint is provided, this test setup is not representative of practical frames consistent with New Zealand practice. Nevertheless, it is the only frame test result in the literature suitable for validating a FE model where joint failure occurs.

The validated FE model is then used to investigate the influence of important factors discussed above. A beam idealization of the portal frames was also presented, incorporating joint flexibility along with component test results. It is also shown that the model can closely predict the gravity load for all the above cases Using the validated FE model, a parametric study was conducted for practical frames using the parameters shown in Figure 6-4, and the results were then compared with different design equations from the literature. For apex and eaves bracket failure, vertical loads were predicted using the equation from Chen et al. (2023a, 2023b), respectively combined with beam idealization. For member failure near column joint, the design equations from Lim and Nethercot (2003), Phan et al. (2020) and Mojtabaei et al. (2021) were also used to predict the vertical loads.

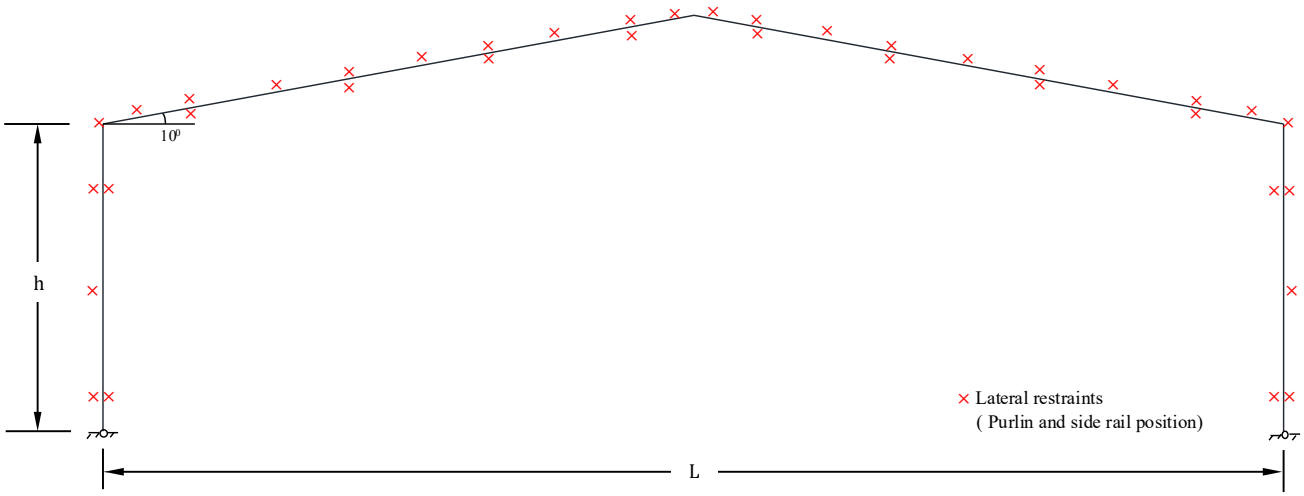

Figure 6-4 Geometric parameters of portal frame with lateral restraints

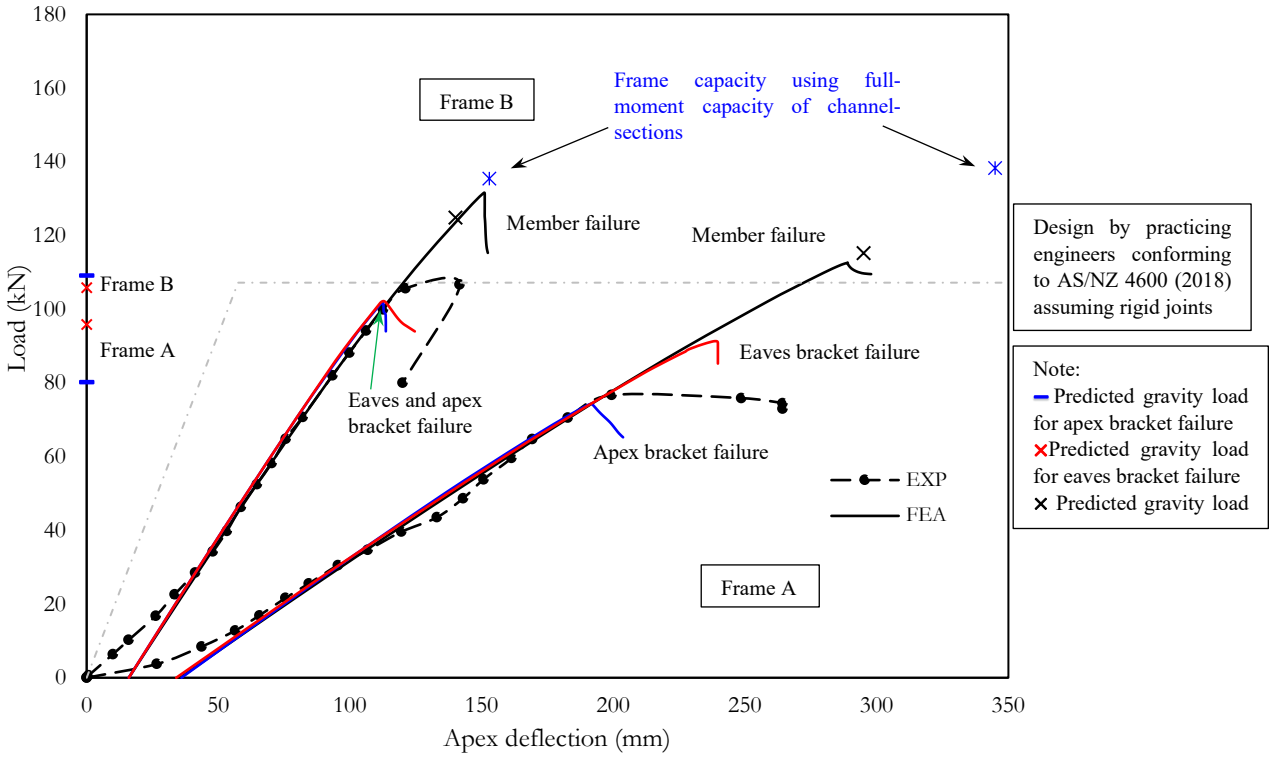

(a) Component test model (k_{1b1c} is 6.21 kN/mm)

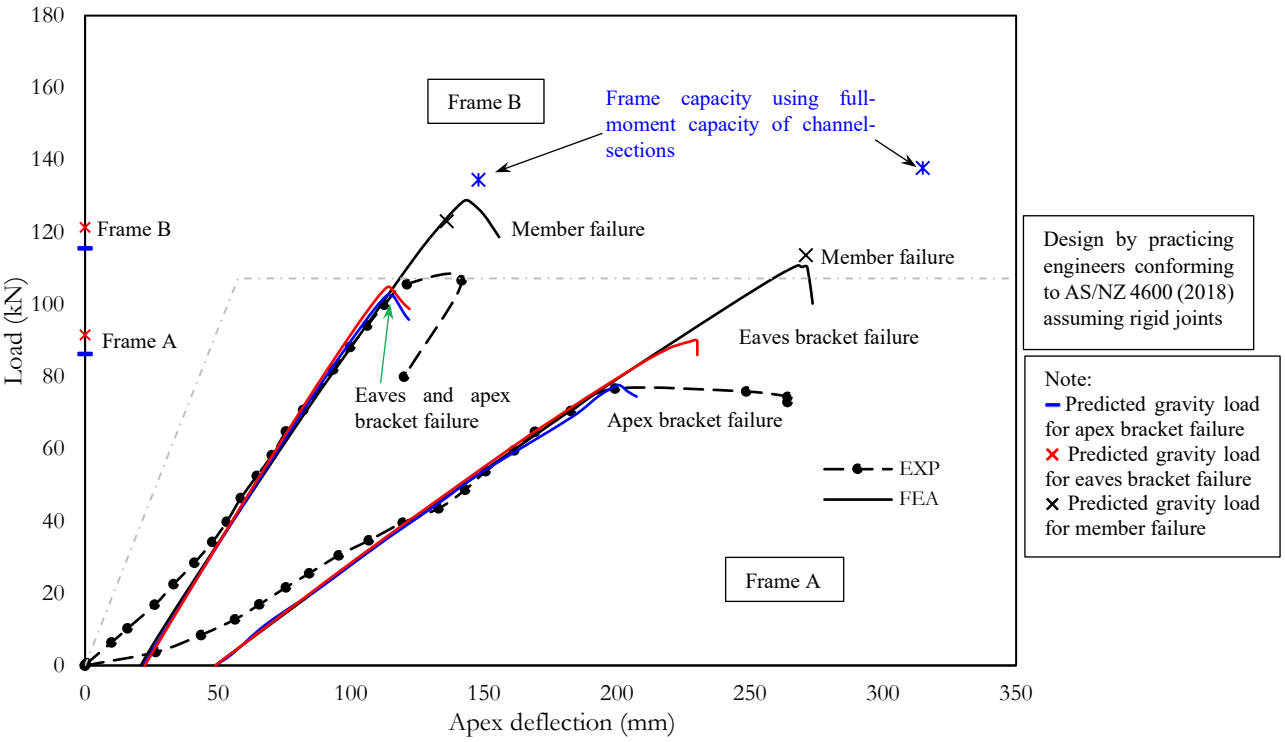

(b) Design procedure (k_{1b1c} is 7.42 kN/mm)

Figure 6-5 Description of the reference frame and validated shell FE model

In Section 3.3.2, the experimental test details have been thoroughly discussed, along with the validated modelling technique in Section 3.4. However, for the reader's clarity, the load-displacement relationship is reiterated and presented in Figure 6-5.

6.2. Bolt-hole elongation stiffness in double shear

In the FE results shown in Figure 6-5a, a value of k_{1b1c} of 6.21 kN/mm was used for the bolt-hole elongation stiffness for one bracket and one channel. In the absence of an experimental test to determine the bolt-hole elongation stiffness for one bracket or channel (k_{1b_AT} or k_{1c_AT}), its value can be predicted from an equation proposed by Ahmed and Teh (2019) (see Eq 6.1). From Eq 6.2, bolt-hole elongation stiffness (k_{1b1c_AT}) for a pair of one bracket and one channel can be determined. This equation leads to a value of k_{1b1c_AT} of 7.42 kN/mm. Figure 6-5b shows the load-apex deflection curve for Frames A and B having a value of k_{1b1c_AT} of 7.42 kN/mm. For detailed calculation see Appendix A (see section A.4).

$$k_{AT} = 0.015t \left(\frac{d_{minor_{M16}}}{d_{minor_{M20}}}\right)^{0.3} f_u \qquad 6.1$$

where 't' is the thickness of the bracket or channel, '$d_{minor_{M16}}$' and '$d_{minor_{M16}}$' are minor diameter for M16 and M20 bolts, respectively and 'f_u' is the ultimate stress of the bracket or channel, and k_{AT} is the bolt-hole elongation stiffness of any plate from Eq 6.1.

$$k_{1b1c\_AT} = \frac{1}{\frac{1}{k_{1b\_AT}} + \frac{1}{k_{1c\_AT}}} \qquad 6.2$$

where k_{1b1c_AT} is the bolt-hole elongation stiffness presented as the force required to cause a unit displacement for two plates, representing the channel section and the bracket, which are arranged in series (see Figure 6-6). k_{1b_AT} and k_{1c_AT} are the bolt-hole elongation stiffness for bracket and channel from Eq 6.1, respectively.

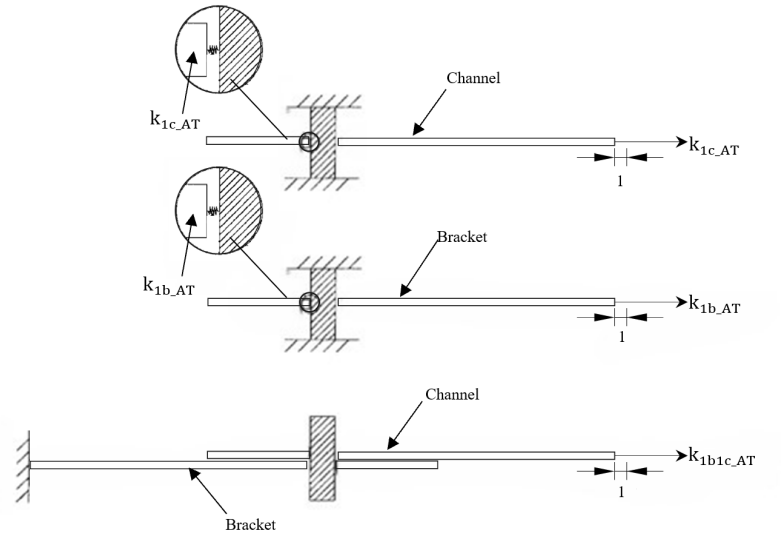

Figure 6-6 Diagram showing bolt-hole elongation stiffness as the force required to cause a unit displacement for a system of plates

6.3. Rotational stiffness of semi-rigid joints

From Figure 3-5, it can be seen that the eaves and apex joints are formed through bolt-groups comprising arrays of 3 x 3 bolts. The bolt group sizes for Frames A (315 mm × 230 mm) and B (615 mm × 230 mm) are different. Figure 2-46 shows the rotational stiffness of such a bolt-group and the position of its center of rotation. As can be seen, the force (F_i) in each bolt hole is proportional to its distance (d_i) from the center of rotation, and from this the rotational stiffness of the bolt group can be calculated. The equation is as follows:

$$K_{2b2c} = k_{2b2c} \sum d_i^2 \qquad 6.3$$

Lim and Nethercot (2002b) showed that for a 3 ×3 bolt group this is:

$$K_{2b2c} = 3/2 \times (a_b^2 + b_d^2) \times k_{2b2c} \qquad 6.4$$

where K_{2b2c} is the rotational stiffness of joints, a_b and b_b are the length and breadth of the bolt group (see Figure 2-46), and k_{2b2c} =2 × k_{1b1c} . A more detailed calculation could be found in Appendix A (see section A.5).

6.4. Moment capacity of the apex brackets

As can be seen from Figure 3-5, in the frames tested by Lim and Nethercot (2004), the joints were formed through back-to-back apex brackets having 3×3 bolt groups. In the absence of experimental test results for the moment capacity of the apex brackets, the strength can be predicted accurately using a component test or validated non-linear FE model as described by Chen et al. (2021) and Blum and Li (2019).

In Chapter 3, the FE modelling techniques for modelling the whole portal frame were described, which showed good agreement with the experimental test results and predicted failure of the apex bracket at the same load. The same model can be used to predict the vertical load to the apex bracket. Figure 6-7a shows the FE model for the component test for the apex bracket; as can be seen, only the brackets and channel-sections are modelled, with pure bending applied.

Table 6-1 shows the moment-capacity of the apex bracket determined from the FE model of the component test of the apex bracket. The moment-capacity of the apex bracket for Frame A and Frame B are 44.1 kNm and 50.2 kNm, respectively. From this, the failure load for Frame A and Frame B can be predicted to be 80.2 kN and 109.1 kN, respectively. This is shown in Figure 6-5a (blue dash on the y-axis) and corresponds to the moment capacity at which the apex bracket fails. Detailed calculation could be found from section A.7.1.

In terms of design recommendations for the moment capacity of the apex bracket, Chen et al. (2021) proposed an equation for determining the moment capacity for fully restrained apex brackets. It should be noted that Chen et al. (2023a) proposed another set of equations for partially restrained brackets consistent with New Zealand practice. However, in this case, in the experimental test conducted by Lim and Nethercot (2004), the apex bracket can be considered as being fully restrained. For detailed calculation see Appendix A (see section A.3).

In accordance with Chen et al. (2021), for a single apex bracket

$$M_{1ab} = f_y b_a^2 t_b [\alpha' \left(\frac{b_a}{a_a}\right)^2 - \beta' \left(\frac{b_a}{a_a}\right) + \gamma'] \quad 6.5$$

Thus, for double brackets, the moment capacity would be

$$M_{2ab} = 2 \times M_{1ab} \quad 6.6$$

However, in accordance with Chen et al. (2023a) for partially restrained double brackets, the moment capacity would be

$$M_{2ab} = 5.3415\, a_a^{0.4652} b_a^{0.9519} f_y^{0.6412} t_b^{1.7447} 10^{-5} \quad 6.7$$

where α', β' and γ' are constant coefficients that can be found in Chen et al. (2021). In the above equation, a_a is the width of the triangular area of an apex bracket, b_a is the edge width of the apex bracket, and t_b represents the thickness of the bracket (see Figure 6-1c). M_{1ab} and M_{2ab} are the moment capacities of a single and double apex bracket, respectively, while f_y is the yield stress of bracket.

Table 6-1 Moment capacity of back-to-back apex bracket used in the portal frame test after Lim and Nethercot (2004)

Frame	Component test model	Eq 6.6
	M_{2ab}	
	kNm	kNm
A	44.1	45.8
B	50.2	52.0

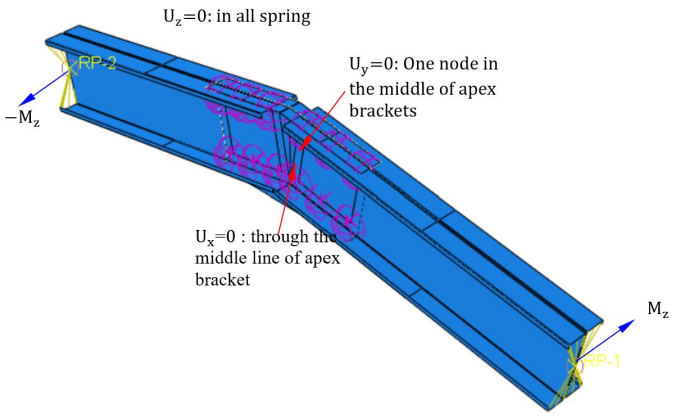

(a) Apex joint

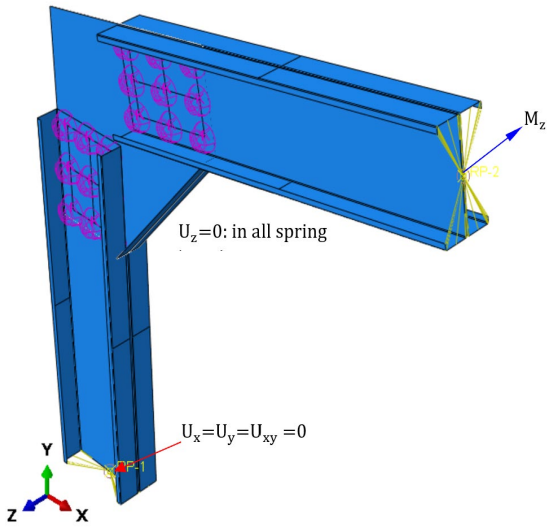

(b) Eaves joints

Figure 6-7 Details of component tests model of brackets

6.5. Moment capacity of the eaves brackets

Similarly, the moment capacity of the eaves brackets can also be determined using non-linear elasto-plastic FEA, in absence from the component test results from the experiments. Figure 6-7b shows the FE model for the component tests; as in the case of the apex brackets, only the brackets and channel-sections are modelled, with pure bending applied. Consistent with the frame tested by Lim and Nethercot (2002b), full lateral restraint is provided. Chen et al. (2023b) also described a component test for the moment capacity of eaves brackets using non-linear elasto-plastic FEA, albeit for partially restrained brackets consistent with New Zealand practice.

Table 6-2 presents the moment-capacity of the eaves bracket determined from the FE model of the component test of the eaves bracket. The moment capacities of the eaves bracket for Frame A and Frame B are 59.4 kNm and 67.7 kNm, respectively. From this, the failure load for Frame A and Frame B can be predicted to be 95.8 kN and 105.8 kN, respectively. This is shown in Figure 6-4a (red dash on the y-axis) and corresponds to the moment capacity at which the eaves

bracket fails. Again, this load is also predicted from the bending moment diagrams shown in Figure A-11. For detailed calculation see Appendix A (see section A.3).

In accordance with Chen et al. (2023b), for a partially restrained eaves bracket

$$M_{1eb} = 1.0177\, a_e^{0.9364} b_e^{0.3450} f_y^{0.4134} t_b^{1.9766} 10^{-4} \quad 6.8$$

Thus, for double brackets, the moment capacity would be

$$M_{2eb} = 2 \times M_{1eb} \quad 6.9$$

Another approach for calculating the moment capacity of partially restrained double brackets would be (Chen et al. 2023b)

$$M_{2eb} = 2.4022\, a_e^{1.2674} b_e^{-0.0503} f_y^{0.4401} t_b^{2.1270} 10^{-4} \quad 6.10$$

where a_e is the width of the triangular area of an eaves bracket, b_e is the edge width of the eaves bracket, and $t_b$is the thickness of the bracket (see Figure 6-1c). M_{1eb} and M_{2eb} are the moment capacities of a single and double eaves bracket, respectively.

Table 6-2 Moment capacity of back-to-back eaves bracket used in the portal frame test after Lim and Nethercot (2004)

Frame	Component test model	Eq 6.9
	M_{2eb}	
	kNm	kNm
A	59.4	57.7
B	67.7	78.9

6.6. Effects of reduced moment capacity of the channel-sections

As mentioned in Section 6.4 and Section 6.5, non-linear elasto-plastic FEA can also be used to predict the failure load of Frames A and B. However, in this case, the failure loads were predicted by assuming the back-to-back eaves and apex brackets do not fail. As shown in Figure 6-5a for both frames, failure occurs in the vicinity of the column joint, and the moment capacity of the channel-section is reduced due to the shear lag effects, which is directly influenced by the size of the bolt group (Lim and Nethercot 2003; Phan et al. 2020; Mojtabaei et al. 2021).

Figure 6-8 shows the mode of failure. For more information, Table 3 compares the reduced moment capacity of the channel section with those obtained from FEA and those calculated using the design equations proposed by Lim and Nethercot (2003), Phan et al. (2020) and Mojtabaei et al. (2021) for such systems.

From Figure 6-5a, Frames A and B fail at 112.2 kN and 131.6 kN, respectively, representing a 46% and 21% increase over the experimental failure loads. For Frame A, at the centre of rotation, this corresponds to a rotational moment of 71.5 kNm, which is close to the bending moment of 69.4 kNm at the failure location. This occurs in combination with a shear force of 125.1 kN and an axial force of 36.1 kN. Notably, the axial load is reduced from 56.1 kN at the column base to 36.1 kN at the failure location, likely due to the joint effect influenced by shear lag (Mojtabaei et al. 2021). However, the overall effect due to the reduction of axial force can be neglected, as the primary interaction in this case is governed by bending and shear. Similarly, for Frame B, this corresponds to a bending moment of 79.8 kNm in combination with an axial force of 65.8 kN. It is worth mentioning that the above values are extracted from the FEA of the full frame, referred to as Frame A and Frame B.

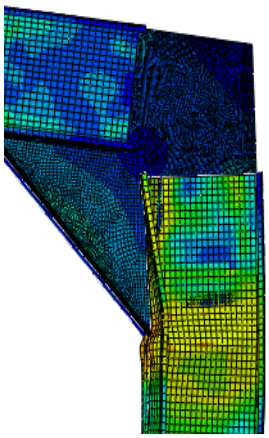

Figure 6-8 Buckling failure of column near eaves joint of Frame B (both eaves and apex brackets idealised as elastic)

Table 6-3 Reduced moment capacity of channel sections used in the portal frame test after Lim and Nethercot (2004)

Joint	M_{2c}^{R}			
	Component test model	Lim and Nethercot (2003)	Phan et al. (2020)	Mojtabaei et al. (2021)
	kNm	kNm	kNm	kNm
A	78.3	79.6	63.6	67.9
B	87.9	87.3	87.1	92.8

Details of the component test model (FE idealization) used to investigate the ultimate moment capacity of the joints of the portal frame, are shown in Figure 6-9. From the component test model, back-to-back channel sections fail at 78.3 kNm for Frame A and 87.9 kNm for Frame B (see Table 6-3). To compare these with the bending moments of 69.4 kNm and 79.1 kNm extracted from FEA for Frame A and Frame B, the values should be reduced to take into account the shear force and axial force. The predicted bending moments at the failure point (i.e. centre of rotation of bolt group) using beam idealisations are 70.3 kNm and 78.5 kNm, respectively. These lead to the predicted failure load of Frames A and B equal to 115.3 kN and 124.5 kN, respectively (see Figure 6-5a).

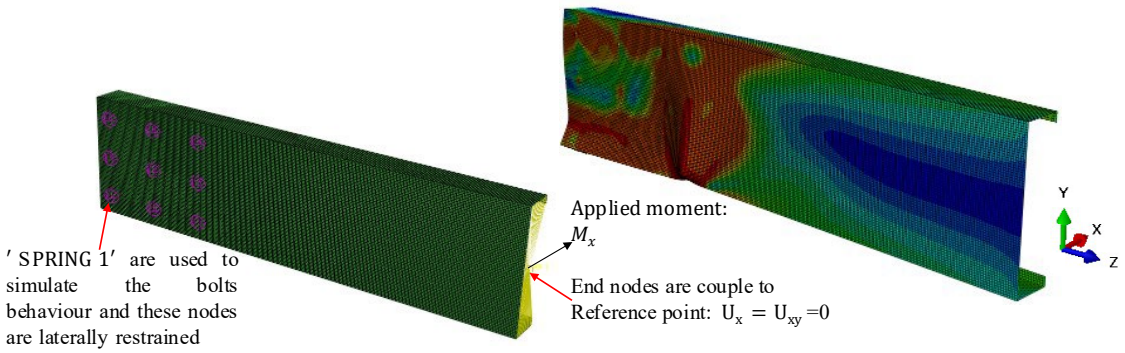

Figure 6-9 Details of the finite element idealization for bolted joints

Figure 6-5b also shows the failure load predicted for failure at column joints due to premature buckling. In this case, the moment capacity of the channel-section under the influence of the bolt-group is predicted using the equations of Lim and Nethercot (2003) to be 79.6 kNm and 87.3 kNm for Frames A and B, respectively. This leads to a predicted frame load of 115.3 kN and 122.0 kN.

Table 6-3 also shows the values for reduced moment capacity of channel sections calculated from Lim and Nethercot (2003), Phan et al. (2020) and Mojtabaei et al. (2021) (For more details see Table 6-4). It is to be noted that the design equation proposed by Mojtabaei et al. (2021) (Eq-6.11) is adjusted using the interaction Eq-6.12 to take into account the axial-bending-shear interaction effects.

$$M_{2c}^{R} = \left[1 - 0.42e^{-13.8\left(\frac{a_b}{d}\right)\left(\frac{t_c}{X_c}\right)}\right] M_{2c}^{**} \quad (6.11)$$

$$\left(\frac{P_{2c}^{**}}{P_{2c}}\right)^2 + \left(\frac{M_{2c}^{**}}{M_{2c}}\right)^2 + \left(\frac{V_{2c}^{**}}{V_{2c}}\right)^2 \leq 1.0 \quad (6.12)$$

where M_{2c}^{R} = Reduced moment capacity of channel section

a_b and d are the length of the bolt group and the depth of the channel section, respectively. t_c and X_c are the thickness of the channel section and the centroidal distance from the channel's web respectively. P_{2c} , M_{2c} and V_{2c} are the pure axial capacity, pure moment capacity and pure shear capacity of the back-to-back channel section, respectively. P_{2c}^{**} , M_{2c}^{**} and V_{2c}^{**} are the axial force, bending moment and shear force in the bolted joint due to the interactions, respectively.

Table 6-4 Comparison of reduced moment capacity of channel sections from the equations proposed in the literature

(a) Equations after Lim and Nethercot (2003)

Frame	$\frac{M_{2c}^{R}}{M_{2c}^{BS\ 5950\ (1998)}}$	M_{2c}^{R} kNm
A	0.81	79.6
B	0.91	87.3

(b) Equations after Phan et al. (2020)

Frame	a_b	b_b	X_s	M_b	V	T	ω	B	σ_b	σ_m	M_{2c}^{R}
	mm	mm	mm	kN-m	kN	kN-m	mm^2	kN-m2	MPa	MPa	kNm
A	315.0	230.0	32.8	75.0	78.7	2.58	4657.6	929.1	146.6	211.3	63.6
B	615.0	230.0		87.5	62.8	2.06	4657.6	433.5	68.4	289.6	87.1

(c) Equation after Mojtabaei et al. (2021)

Frame	a_b	t_c	a_b/d	t_c/X_c	P_{2c}	V_{2c}	M_{2c}	M_{2c}^{**}	M_{2c}^{R}
	mm	mm	mm	mm	kN	kN	kNm	kNm	kNm
A	315.0	2.95	0.94	0.16	665.2	165.8	118.2	71.1	67.9
B	615.0	2.95	1.83	0.16	665.2	165.8	118.2	93.3	92.8

M_{2c}^{**} is the moment capacity determined from Eq 6.12

6.7. Beam idealization

The FEA method described in Chapter 3 is very complex and computationally expensive. Herein, a design method is described to predict the load carrying capacity of portal frames incorporating the joint flexibility. Figure 6-10 shows a beam idealization for Frames A and B. As can be seen, rotational spring elements are modelled at the centre of rotation of each bolt-group. The brackets can be assumed to function as rigid (Lim and Nethercot, 2002b). Figure A-10 represents the details of the node and element connectivity.

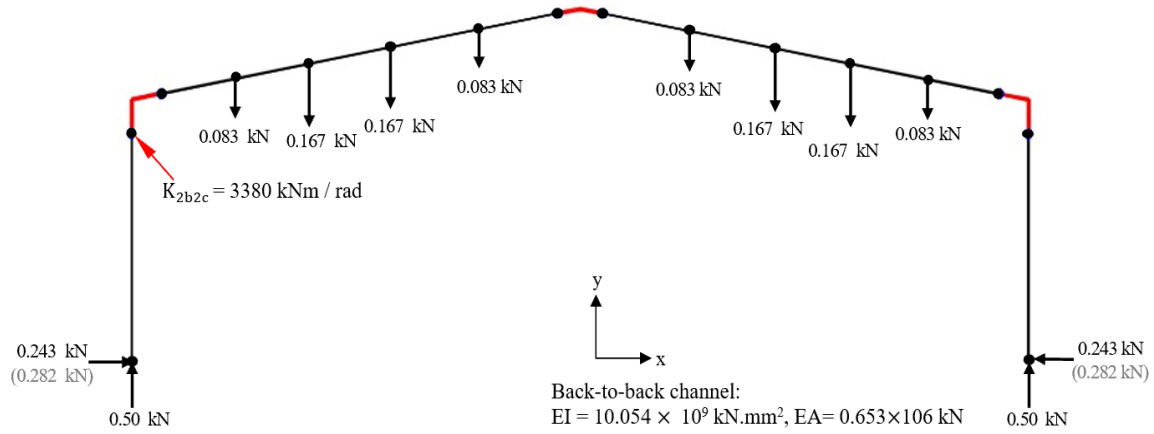

(a) Frame A

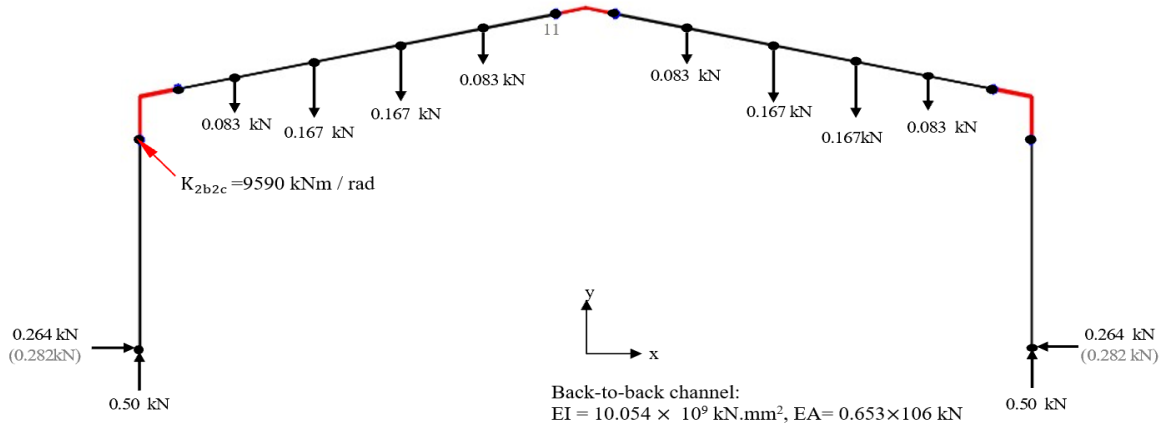

(b) Frame B

Figure 6-10 Beam idealization portal frame with semi-rigid joint

The load-carrying capacity of the portal frame can be predicted using the bending moment determined from the beam idealization described above, provided the strength of the components (apex bracket, eaves bracket, or channel section) is known. The following equations can be used to predict the load carrying capacity for the different failure modes of the portal frame.

Load carrying capacity for apex bracket failure,

$$F_{beam} = \frac{M_{2ab}}{\alpha} \quad 6.13$$

Load carrying capacity for eaves bracket failure,

$$F_{beam} = \frac{M_{2eb}}{\beta} \quad 6.14$$

Load carrying capacity for member failure,

$$F_{beam} = \frac{1}{\left[\frac{\beta}{M_{2c}^{R}} + \frac{0.5}{P_{2c}}\right]} \quad 6.15$$

where α is the bending moment at the center of rotation of the apex joint and β is the bending moment at the center of rotation of the eaves joint of either the column or the rafter (whichever is greater) from beam idealization for a total load of 1 kN applied to the portal frame; M_{2ab} and M_{2eb} are the moment capacities of back-to-back apex bracket and eaves bracket, respectively. P_{2c} is the axial capacity of back-to-back channel section, and F_{beam} is the predicted failure load from the beam idealization.

Using the above simplified approach, the capacity of the frames under gravity loads was predicted and presented in Figure 6-4a and 6-4b. In general, the results show a good agreement with both the experimental test and FEA. Therefore, this method can be used for predicting the gravity load capacity of portal frames.

6.8. Parametric study

A parametric study was conducted using the validated FE model, considering a range of frame geometries, as shown in Figure 6-4. Specifically, three different frame geometries were analysed, with eave heights (h) ranging from 3.0 to 6.0 m and span lengths (L') from 12.0 to 20.0 m. For both bracket and back-to-back channel sections (see Figure 1b and 1c), the same G450 grade of CFS was used. Details of channel section and brackets are presented in Table 6-5a, b and c. Lateral restraints were applied at 950 mm intervals for all frames, which is smaller than the typical spacing used in practice consistent with New Zealand.

All frames were designed to carry only vertical loads, consisting of a dead load of 0.25 kPa and a live load of 0.25 kPa, in accordance with AS/NZ 1170: part 1(2002). The results of this section were used to investigate the gravity load carrying capacity of the frames for three different failure modes, i.e., apex bracket failure, eaves bracket failure, and member failure. Subsequently, the outcomes were compared with those obtained from beam idealization. The findings from the parametric study are presented in Table 6-5b.

Table 4a presents the component test results for apex brackets and compares them with the strength predicted by Chen et al. (2023a). As shown in Table 6-5a, their equation is conservative by around 5%. The corresponding gravity load predicted using the component test results from beam idealization was 12% higher compared to the FEA results for all the selected frames (see Table 6-6). A similar trend is observed in Table 6-6 when the equation from Chen et al. (2023a) is used instead of the component test results for comparison with the FEA results.

For eaves brackets, the equation from Chen et al. (2023b) was found to overestimate the strength by an average of 20% when compared to the results from the component test model, as presented in Table 6-5b. As expected, the corresponding gravity load overestimates the results by 17% in comparison to the FEA results when the equation from Chen et al. (2023b)

is used. However, the gravity load predicted from the results of component test models for eaves brackets was found to be conservative by only 3% for all frames, as shown in Table 6-6. This discrepancy is likely due to the b_e/a_e ratio for the eaves bracket being close to the lower limit of the equations proposed by Chen et al. (2023b).

The reduced moment capacity of the back-to-back channel section, considering the significant shear lag effect near bolted joints for frames 1 to 4, is determined using the design equations proposed by proposed by Lim and Nethercot (2003), Phan et al. (2020), and Mojtabaei et al. (2021) along with FEA. As can be seen from Table 6-4c, the component test results from FEA, the results from the equations proposed by Lim and Nethercot (2003), and those from Mojtabaei et al. (2021) accurately predict the gravity load using the beam idealization at member failure. The prediction from component test model is only 3% lower, while predictions from the equation by Lim and Nethercot (2003) are accurate, and those by Mojtabaei et al. (2021) differ by 3% (on average) compared to the full-scale FEA results for the practical frames (see Table 6-7). Although the design approach commonly adopted by practicing engineers assumes rigid joints, close agreement with the gravity load predicted from beam idealization was observed in a few cases. However, the results remain inconsistent overall. It should be noted that the equation from Lim and Nethercot (2003) cannot be applied to Frame 1 and Frame 3, as their d/t ratios are below 84.0 which is the lower limit of the equation. However, for Frame 2 and Frame 4 the equation demonstrates good agreement with the FEA results.

In general, the results indicate that the equation from Phan et al. (2020) is conservative by 25% compared to the FEA predictions for all the selected frames, as it is based on an analytical solution and does not account for the shear lag effect when determining the reduced moment capacity of the back-to-back channel section. On the other hand, the equation from Mojtabaei

Table 6-5 Strength of channel section and brackets used for practical frames from component test and equations

a) Geometric details and strength of apex brackets

Frames	Dimension	Bracket details					Component test model	$\frac{M_{2ab}^{Eq\ 6.7}}{M_{2ab}}$
	(h×L)	a_a	b_a	t_b	$a_b \times b_b$	No of bolts	M_{2ab}	
	m×m		mm		mm×mm	m ×n	kNm	
Frame 1	3.0 × 12.0	200.0	150.0	3.0	120×70	2×2	26.1	0.96
Frame 2	3.0 × 12.0	360.0	336.0	3.0	280×256	3×2	76.5	0.93
Frame 2	6.0 × 14.0	320.0	200.0	2.7	240×120	3×2	37.7	0.92
Frame 4	6.0 × 20.0	360.0	300.0	2.7	280×220	3×2	53.3	1.00
							Mean	0.95
							COV	0.05

Geometric details and strength of eaves brackets

Frames	Dimension	Bracket details					Component test model	$\frac{M_{2eb}^{Eq\ 6.9}}{M_{2eb}}$
	(h×L)	a_e	b_e	t_b	$a_b \times b_b$	No of bolts	M_{2eb}	
	m×m		mm		mm×mm	m × n	kNm	
Frame 1	3.0 × 12.0	300.0	150.0	2.98	220×70	3×2	29.9	1.29
Frame 2	3.0 × 12.0	630.0	336.0	2.98	550×256	4×2	83.3	1.14
Frame 3	6.0 × 14.0	390.0	200.0	2.70	310×120	4×2	37.7	1.14
Frame 4	6.0 × 20.0	660.0	300.0	2.70	580×220	4×2	67.4	1.23
							Mean	1.20
							COV	0.06

b) Geometric details and strength of back-to-back channels

Frames	Dimension	Channel section				Component test model				Lim and Nethercot (2003)	Phan et al. (2020)	Mojtabaei et al. (2021)
	(h×L)	d	b	l	t_c	P_{2c}	V_{2c}	M_{2c}	M_{2c}^R		M_{2c}^R	
	m×m		mm			kN	kN	kNm	kNm		kNm	
Frame 1	3.0 × 12.0	150.0	65.0	15.0	3.0	581.8	122.9	43.7	32.5	-	23.1	31.0
Frame 2	3.0 × 12.0	336.0	88.0	20.0	3.0	715.0	198.2	139.8	110.3	106.2	90.1	127.6
Frame 3	6.0 × 14.0	200.0	75.0	15.0	2.7	573.7	130.0	59.2	42.6	-	30.3	47.0
Frame 4	6.0 × 20.0	300.0	100.0	20.0	2.7	726.7	166.7	107.0	86.6	92.6	67.4	97.0

et al. (2021) is not applicable directly to the failure mode shown in Figure 6-8, as it was developed for pure moment capacity and local buckling failure. However, when the ultimate moment capacity of the back-to-back channel section was reduced to account for the interaction of flexure, shear and axial load, the equation accurately predicted the gravity load using the proposed approach. On the other hand, the equation from Mojtabaei et al. (2021) is not applicable directly to the failure mode shown in Figure 6-8, as it was specifically developed for pure moment capacity and local buckling failure. However, when the ultimate moment capacity of the back-to-back channel section was reduced to account for the interaction of flexure, shear and axial load, the equation accurately predicted the gravity load using the proposed approach. This reduction is logical and justified, as this failure mode results from the combined effects of axial, bending and shear force. It should also be noted that the reduced moment capacity, determined from the equation by Lim and Nethercot (2003) and the component FEA, accounts for these effects by assuming the semi-rigid behaviour of joints. This reduced moment capacity is then combined with axial load to predict the gravity load for member failure of the frames.

6.9. Summary and Conclusions

This study investigates the gravity load capacity of back-to-back channel section CFS portal frames using a beam idealization model that accounts for semi-rigidity of joints and, for the first time, the reduced strength of the channel sections due to shear-lag effects. Detailed non-linear FE models validated against experimental test results were used to investigate the influence of key design parameters on the structural performance and failure mode of CFS portal frames. Using the beam idealization model, the proposed simplified design approach could significantly reduce the computational costs of analyses, while the simulated responses compared very well with those obtained from detailed validated FEA. The key conclusions drawn from this study are as follows:

- It was shown that the beam idealization model provides a simplified yet effective method for analysing portal frame behaviour, capturing joint flexibility and shear lag effects. It predicts load capacity with an average accuracy of 1% compared to detailed FEA results.
- Under the rigid-jointed assumption, the predicted loads exhibit inconsistency, and can lead to inaccurate prediction by up to 19% error. It was shown that the semi-rigid joint flexibility incorporated in the model, reflecting the realistic behaviour of the connections compared to fully rigid assumptions, could significantly enhance the accuracy of the analysis leading to always less than 5% error (on average 3% error).
- The Mojtabaei et al. equations (2021) can be used to estimate the gravity load capacity, incorporating shear and axial load effects. It provides accurate predictions, with results on average within 3% of FEA outcomes for all frames, making it a reliable method for assessing channel section strength.
- The Lim and Nethercot equations (2003) can be used to predict the gravity load in CFS portal frames. However, their validity is limited to sections d/t ratio in the range of 84.0 to 168.0.
- The Phan et al. (2020) equation was also used to predict capacity for gravity load and found to be on average 25% conservative compared to FEA results, highlighting the importance of considering the reduced strength of channel sections due to shear-lag effects.
- In terms of strength, the equation proposed by Chen et al. (2023a) on average is found to be conservative by 5% compared to the component test results for the apex bracket.

Table 6-6 Predicted gravity loads for apex and eaves bracket failure using the beam model, component tests, and equations from literature

Frames	Dimension (h×L)	k_{1b1c_AT}	α	β	F_{FEA} (kN)		$\frac{F_{beam}^{Eq\ 6.13}}{F_{FEA}}$	$\frac{F_{beam}^{Eq\ 6.14}}{F_{FEA}}$	$\frac{F_{beam}^{Eq\ 6.13}}{F_{FEA}}$	$\frac{F_{beam}^{Eq\ 6.14}}{F_{FEA}}$
	m×m	kN/mm	kN.m/kN		Apex	Eaves	Component test model		Chen et al. (2023a)	Chen et al. (2023b)
Frame 1	3.0 × 12.0	11.01	0.491	0.809	47.7	37.6	1.11	0.98	1.07	1.27
Frame 2	3.0 × 12.0	11.01	0.803	0.475	146.8	106.8	1.10	0.97	1.02	1.11
Frame 3	6.0 × 14.0	10.06	0.723	0.904	46.4	41.7	1.13	1.00	1.08	1.14
Frame 4	6.0 × 20.0	10.06	0.767	1.390	61.4	51.3	1.13	0.94	1.14	1.15
						Mean	1.12	0.97	1.09	1.17
						COV	0.02	0.03	0.05	0.06

Table 6-7 Predicted gravity loads for member failure using the beam model, component tests, and equations from literature

Frames	Dimension (h×L)	k_{1b1c_AT}	β	F_{FEA} (kN)	$\frac{F_{beam}^{Eq\ 6.15}}{F_{FEA}}$				
	m×m	kN/mm	kN.m/kN	Member	Component test model	Lim and Nethercot (2003)	Phan et al. (2020)	Mojtabaei et al. (2021)	Rigid joint [1]
Frame 1	3.0 × 12.0	11.01	0.809	38.7	1.00	-	0.73	0.96	1.19
Frame 2	3.0 × 12.0	11.01	0.803	131.0	0.96	0.92	0.81	1.09	1.09
Frame 3	6.0 × 14.0	10.06	0.904	48.2	0.95	-	0.68	1.04	0.98
Frame 4	6.0 × 20.0	10.06	1.390	62.5	0.96	1.02	0.75	1.03	0.97
				Mean	0.97	0.97	0.75	1.03	1.06
				COV	0.02	0.07	0.07	0.05	0.10

Chapter 7 Conclusion and future studies

7.1. Conclusion

The primary focus of this study is to investigate the behaviour of NTB portal frames and to develop a connection system utilizing bolted-side plates for these frames. Additionally, the study aims to assess the moment capacity of bolted-side plates for both apex and eaves joints through numerical analysis. Parametric studies were conducted to comprehensively examine the strength characteristics of the apex and eaves joints under both opening and closing moments. Based on these studies, unified design equations were formulated to accurately predict the moment capacity of these joints.

7.1.1. Numerical investigation

The shell FE model of NTB portal frames was validated against previously reported full-scale experimental tests. Following this validation, the study explored the feasibility of using a bolted-side plate connection system for NTB portal frames. The findings indicated that the ultimate capacity of NTB portal frames could be increased by up to 17.5% with the bolted-side plate connection compared to a bolted-end plate system, if 16 mm thick bolted-side plates is used to form the joints at eaves of NTB portal frame. The enhanced load-carrying capacity of the NTB portal frame is due to the confinement provided by the bolted-side plates at the eaves joint. As a result, the design of these bolted-side plates is crucial to the overall structural performance and efficiency of the portal framing system.

Additionally, a FE model for the apex joint was developed and validated against experimental tests from the literature. Sensitivity analysis revealed that the moment capacity of the apex joint primarily depends on the strength of the bolted-side plate. Both types of bolted side plates, i.e., those without stiffeners and those with top and bottom stiffeners, were examined under both opening and closing moments.

A similar analysis was conducted for eave joints. The sensitivity study for eave joints took into account parameters such as the yield stress of NTB members, the thickness of the bolted-side plate, and various features of the bolted-side plates. It was observed that when the NTB has adequate capacity to resist buckling, the strength of the bolted-side plate becomes critical in determining the moment capacity of the joints.

7.1.2. Prediction of the moment capacity of bolted-side plates

The FE model of the apex joints was utilized for parametric studies to assess the moment capacity of bolted-side plates in apex joints. This study considered two types of bolted-side plates: those with no stiffeners and those with top and bottom stiffeners. Based on the analysis, unified equations were developed to predict the moment capacities for both opening and closing moments of bolted-side plates.

Similarly, unified equations were proposed for bolted-side plates in eave joints of NTB portal frames, applicable for both opening and closing moments. It is important to note that these equations are valid for plate thicknesses greater than 8 mm and do not account for the presence of stiffeners.

7.1.3. Design recommendations for bolted-side plates

Design recommendations were also provided for the bolted-side plates at both the apex and eaves joints, with a focus on the design thickness and length of the side plates, respectively. These recommendations were based on the proposed equations and the moment capacity of the NTB member.

7.1.4. Design methodology for portal frames

A comprehensive design methodology was developed for portal frames with back-to-back channel section. It was observed that predicted vertical loads from proposed methodology are within 1% (on average) of the FEA results. A worked example is also shown in Appendix A.

The same methodology was applied to the NTB portal frames covering both bolted end plate and bolted-side plate systems. This methodology is illustrated through detailed design examples in Appendix B to Appendix C. A comparative analysis with FEA results validated the accuracy of the proposed approach, confirming its reliability and practical applicability for industrial use.

Key contribution of the research are as follows:

- Develop a detailed FE model for the full-scale NTB portal frame
- Develop a robust component test model (FE idealization) for both the apex and eaves joints of NTB portal frames
- Propose new design equation for predicting the moment capacity of apex and eaves joints in NTB portal frames
- Development of a simplified beam idealization for portal frames that can accurately predict the vertical load capacity for any failure mode, provided the joint strength is known either from component test model or the proposed design equation

7.2. Recommendations for future work

As an extension of this research, the following areas warrant further investigation:

1. The current research focuses primarily on the development of the portal framing system. However, for successful commercialization, additional research is required to optimize the joints, improving strength while reducing costs.
2. The effects of residual stress in NTB sections on the ultimate capacity of full-scale NTB portal frames could be investigated.
3. The equations proposed for determining the strength of bolted-side plates are valid when the bolted-side plates are subjected to pure bending. However, the combined effect of bending, axial, and shear forces may reduce the strength of the bolted-side plates, which presents a research gap for future studies.

4. Since the research is based entirely on numerical analysis, once the portal framing system is fully optimized, physical tests could be conducted on both the entire system and individual joints to verify its overall performance.
5. Existing equations from literature (Lim and Nethercot 2003; Phan et al. 2020; Mojtabaei et al. 2021) for predicting the vertical load of portal frames when failure occurs due to shear lag effects have also shown inconsistencies. A new equation should be proposed to accurately predict the vertical load capacity of portal frames under such failure conditions.

Appendix A

Example of a cold-formed steel portal frame back-to-back channel section portal frame after Lim and Nethercot (2004)

Table of contents

Notation	
a_a	Width of triangular area of an apex bracket
a_b	Length of bolt-group
a_{ab}	Distance from the outline of the bolt group to the edge of an apex bracket
a_e	Width of triangular area of an eaves bracket
a_{eb}	Distance from the outline of the bolt group to the edge of an eaves bracket
α	Bending moment at the center of bolt group at apex bracket for unit applied load on the frame
b_a	Edge width of the apex bracket
b_d	Breadth of bolt-group
b_e	Edge width of an eaves bracket
β	Bending moment at the center of bolt group at apex bracket for unit applied load on the frame
d	Nmoinal diameter of bolt (mm)
$d_{minor_{M16}}$	Minor diameter of M16 bolt
$d_{minor_{M20}}$	Minor diameter of M20 bolt
EI	Axial rigidity of column and rafter members
EA	Flexural rigidity of column and rafter members
f_y	Yeild stress (N/mm^2)
f_u	Ultimate strength (N/mm^2)
M_{2c}	Moment capacity of back-to-back channel section
M_{2c}^R	Reduced moment capacity of back-to-back section due to the bolt group effect
M_{1ab}	Strength of single apex bracket
M_{2ab}	Strength of back-to-back apex bracket
M_{2ab}^A	Strength of back-to-back apex bracket from Frame A
M_{2ab}^B	Strength of back-to-back apex bracket from Frame B
M_{1eb}	Strength of back-to-back eaves bracket
M_{2eb}	Strength of back-to-back eaves bracket from Frame A
M_{2eb}^A	Strength of back-to-back apex bracket from Frame A
M_{2eb}^B	Strength of back-to-back eaves bracket from Frame B
M_{2eb}	Strength of back-to-back eaves bracket from Frame A
k_{AT}	Bolt-hole elongation stiffness of a plate under double shear using thread bolts from Ahmed and Teh (2019)
k_{1b_AT}	Bolt-hole elongation stiffness of one bracket
k_{1c_AT}	Bolt-hole elongation stiffness of one channel
k_{1b1c_AT}	Bolt-hole stiffness of the interconnected plates system for joints comprised one bracket with one channel
k_{2b2c_AT}	Bolt-hole stiffness of the interconnected plates system for joints comprised two brackets with two channels
F_{beam}	Predicted failure load from beam idealization
P_{2c}	Axial capacity of back-to-back channel sections
t_b	Thickness of bracket
t_c	Thickness of channel section

A.1 Introduction

Lim and Nethercot (2004) tested two portal frames (referred to as Frame A and Frame B) (see Figure A-1a). Details of the eaves and apex joints are shown in Figure A-2. Both frames had a span of 12 m, column height of 3 m, and pitch of 10°; the difference between the two frames was the size of the eaves and apex brackets. As can be seen from Figure A-1b, the frame was loaded through a loading rig consisting of eight jacks and pinned supports at the column bases. Lateral restraints were provided at the loading position (on the rafter) and at the joints to prevent the premature failure of the back-to-back channel sections due to lateral buckling. Figure A-3 shows the load-displacement curves for the tested frames. Fully threaded M16 bolts are used to connect the back-to-back channels to the back-to-back brackets. Geometric details of cross-section and brackets are shown in Figure A-4.

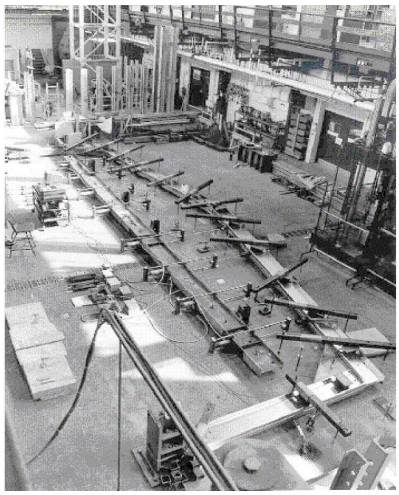

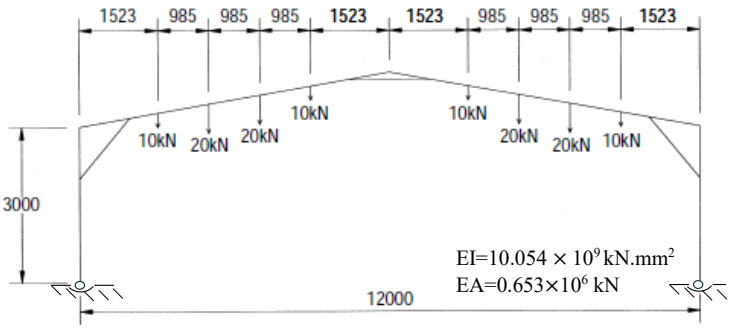

All dimensions are in millimeters

(a) Full-scale portal frame test (frame B) (b) Details of point loads applied to standard frame

Figure A- 1 Details of general arrangements for the test frame after Lim and Nethercot (2004)

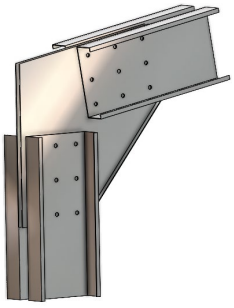

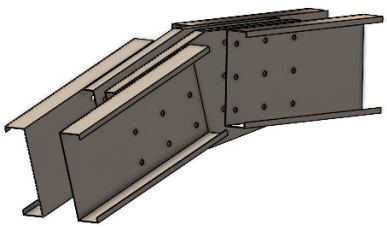

(a) Eaves joint (b) Apex joint

Figure A- 2 Joints of portal frame

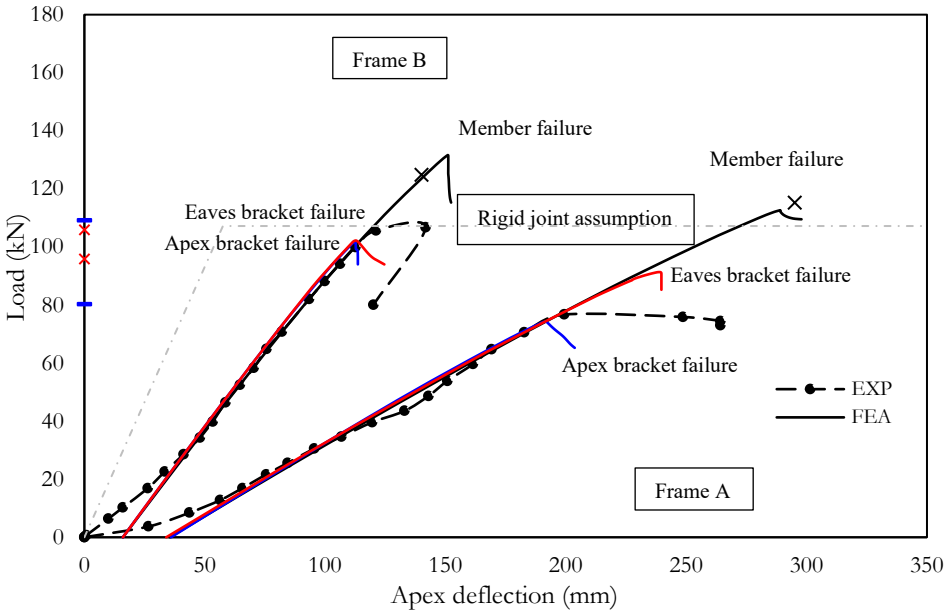

(a) k_{1b1c} is 6.21 kN/mm

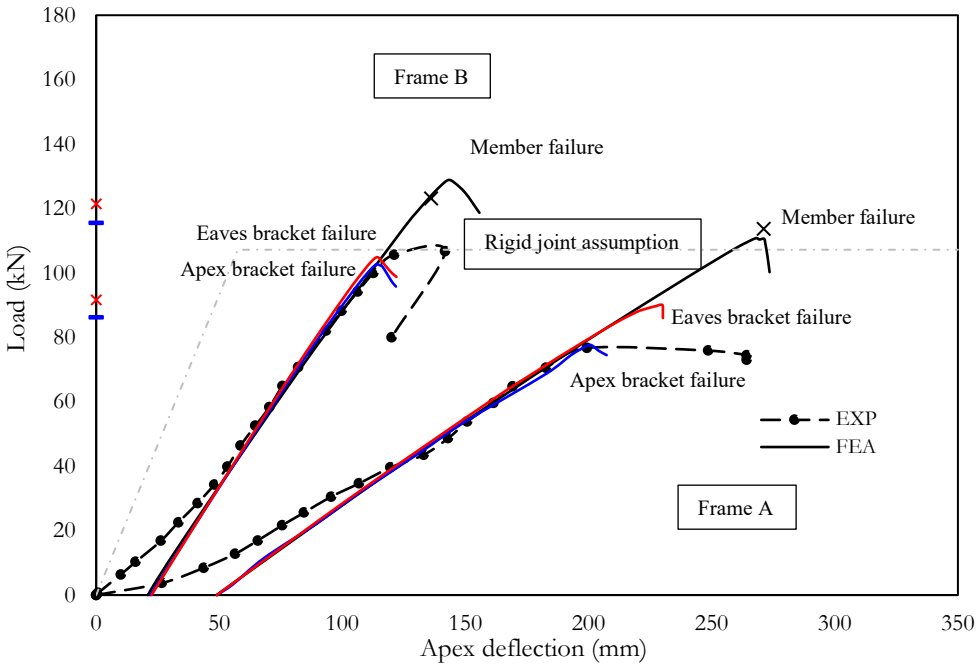

(b) k_{1b1c} is 7.42 kN/mm

Figure A- 3 Load-displacement curves for test frame

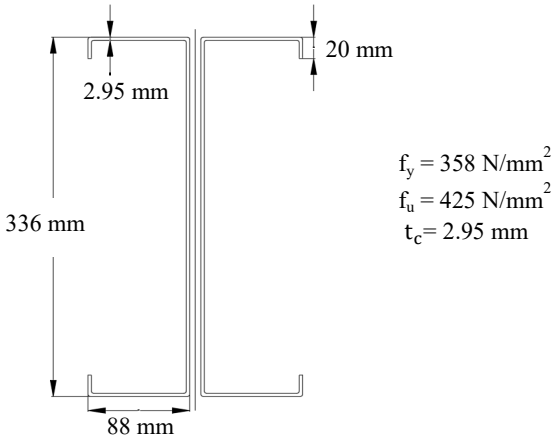

(a) Cross section details of back-to-back channel

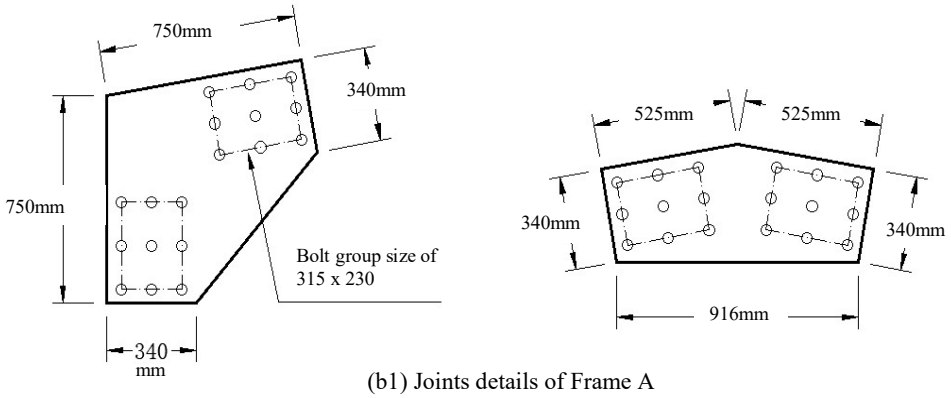

(b1) Joints details of Frame A

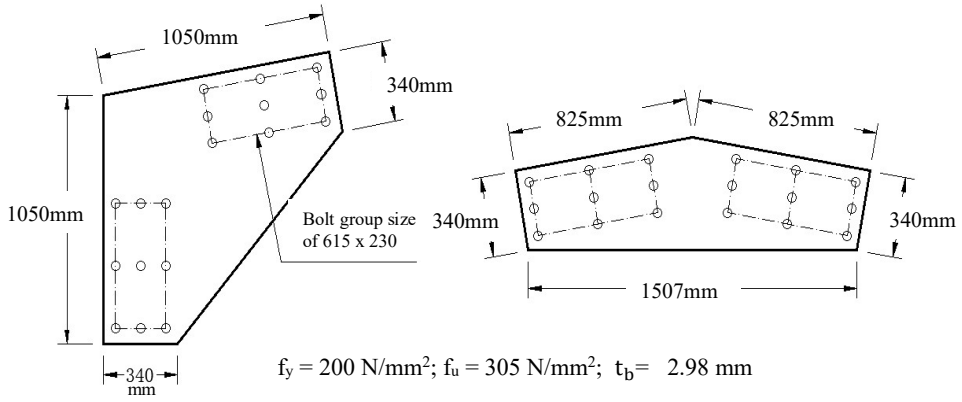

f_y = 200 N/mm^2; f_u = 305 N/mm^2; t_b= 2.98 mm

(b2) Joints details of Frame B

Figure A- 4 Dimensions of back-to-back channel section and brackets used for column and rafter members (Lim and Nethercot 2004)

A.2 Section strength using AS/NZ 4600 (2018)

In this section, the section strength under bending and compression has been determined using the DSM in accordance with AS/NZ 4600 (2018). Lim and Nethercot (2003) previously discussed the effect of semi-rigid bolted joints, which primarily leads to the premature buckling of the channel section. The author believes that the premature buckling of the channel section affects the ultimate load capacity of the portal frame, possibly due to shear lag effects (Mojtabaei et al. 2021). Since AS/NZ 4600 (2018) does not provide specific guidelines for calculating the bimoment strength of bolted joints, FEA was employed to evaluate its effect on the portal frame joints.

A.2.1 Moment capacity of back-to-back channel section

As can be seen from Figure A-5, a signature curve for single channel section under bending was generated from Thin-Walled 2 software. From Figure A-5, local buckling stress (f_{ol}) and distortional buckling (f_{od}) for the test channel are 450.1 MPa and 369.1 MPa, respectively.

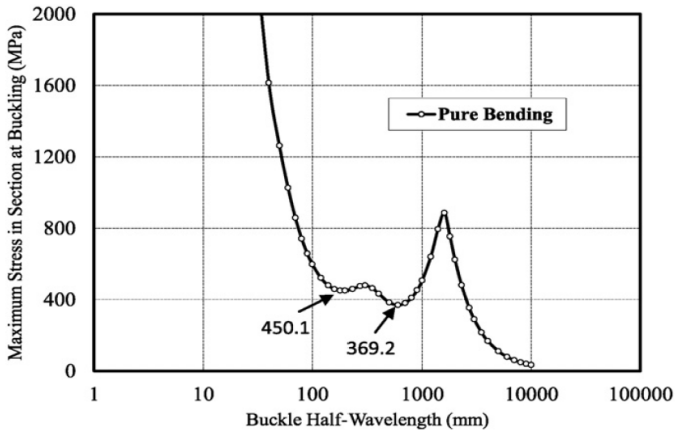

Figure A- 5 Signature curve for the test channel under pure bending

Herein, as the frame was fully restrained against lateral-torsional buckling, therefore, only yield moment capacity (M_y) of the section was considered for both local and distortional buckling strength calculation of the channel subjected to pure bending.

Yield moment capacity for single channel

$M_y = f_y Z_f = [358 \times (25703021/ 118)]/10^6 = 54.77$ kNm [Cl.7.2.2.2]

Non-dimensional slenderness ratio for local buckling

$\lambda_l = \sqrt{\frac{f_y}{f_{ol}}} = \sqrt{\frac{358}{450.1}} = 0.896 > 0.776$ [Cl.7.2.2.3 (1) and Cl.7.2.2.3 (3)]

$M_l = \left[1 - 0.15 \left(\frac{f_{ol}}{f_y}\right)^{0.4}\right] \left(\frac{f_{ol}}{f_y}\right)^{0.4} \times M_y$ [Cl.7.2.2.3 (2)]

$= \left[1 - 0.15 \left(\frac{450.1}{358}\right)^{0.4}\right] \left(\frac{450.1}{358}\right)^{0.4} \times 54.77$

$= 48.27$ kNm

Non-dimensional slenderness ratio for distortional buckling

$\lambda_d = \sqrt{\frac{f_y}{f_{od}}} = \sqrt{\frac{358}{369.2}} = 0.989 > 0.673$ [Cl.7.2.2.4(1) and Cl.7.2.2.4 (3)]

$M_d = \left[1 - 0.22\left(\frac{f_{od}}{f_y}\right)^{0.5}\right]\left(\frac{f_{od}}{f_y}\right)^{0.5} \times M_y$ [Cl.7.2.2.4 (2)]

$= \left[1 - 0.22\left(\frac{369.2}{358}\right)^{0.5}\right]\left(\frac{369.2}{358}\right)^{0.5} \times 54.77$

$= 42.89$ kNm

Nominal moment capacity for test channel = min (M_l, M_d) =42.89 kNm

Nominal moment capacity for back-to-back channels = 2×42.89 = 85.78 kNm

A.2.2 Axial capacity of back-to-back section

Figure A-6 depicts the signature curve for the test channel generated using Thin-wall-2 software when subjected to axial compression. As can be seen from the figure, local buckling (f_{ol}) and distortional buckling (f_{od}) stresses for the test channel are 83.9 MPa and 113.2 MPa, respectively.

Nominal yield capacity of single channel section in compression

$P_y = f_y A_g = [358 \times 1593.59]/10^3 = 570.5$ kN [Cl. 7.2.1.2 (5)]

Non-dimensional slenderness ratio for local buckling

$\lambda_l = \sqrt{\frac{f_y}{f_{ol}}} = \sqrt{\frac{358}{83.9}} = 2.06 > 0.776$ [Cl. 7.2.1.3 (1)]

$P_l = \left[1 - 0.15\left(\frac{f_{ol}}{f_y}\right)^{0.4}\right]\left(\frac{f_{ol}}{f_y}\right)^{0.4} \times P_y =$ $= 378.9$ kN [Cl. 7.2.1.3 (2)]

Non-dimensional slenderness ratio for local buckling

$\lambda_d = \sqrt{\frac{f_y}{f_{od}}} = \sqrt{\frac{358}{113.7}} = 1.77 > 0.561$ [Cl. 7.2.1.4 (1) and Cl. 7.2.1.4 (3)]]

$P_d = \left[1 - 0.25\left(\frac{f_{od}}{f_y}\right)^{0.6}\right]\left(\frac{f_{od}}{f_y}\right)^{0.6} \times P_y$ [Cl. 7.2.1.4 (2)]

$= \left[1 - 0.25\left(\frac{113.7}{358}\right)^{0.6}\right]\left(\frac{113.7}{358}\right)^{0.6} \times 570.5$

$= 332.7$ kN

Nominal axial capacity for test channel = min (P_l, P_d) =332.7 kN

Nominal axial capacity for back-to-back channels = 2×332.7 = 665.5 kN

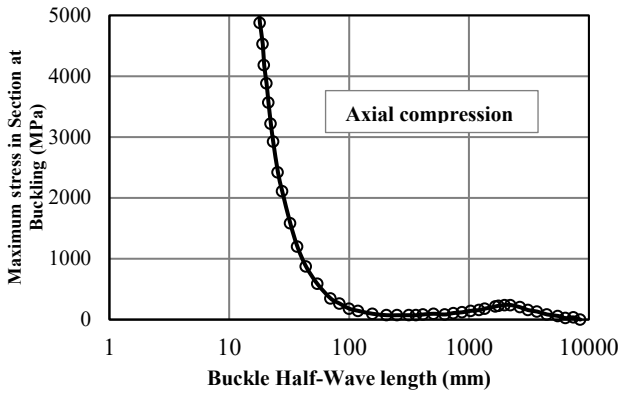

Figure A- 6 Signature curve for the test channel under axial compression

A.2.3 Ultimate capacity of joint using FEA

As there is no guideline available in AS/NZ 4600 (2018) for the calculation of bimoment effect for the bolted joints, a FE idealisation used to investigate the ultimate moment capacity of the joints A and B of the portal frame (see Figure A-7). From the FE model the back-to-back channel-sections fail at 78.3 kNm and 87.9 kNm, respectively.

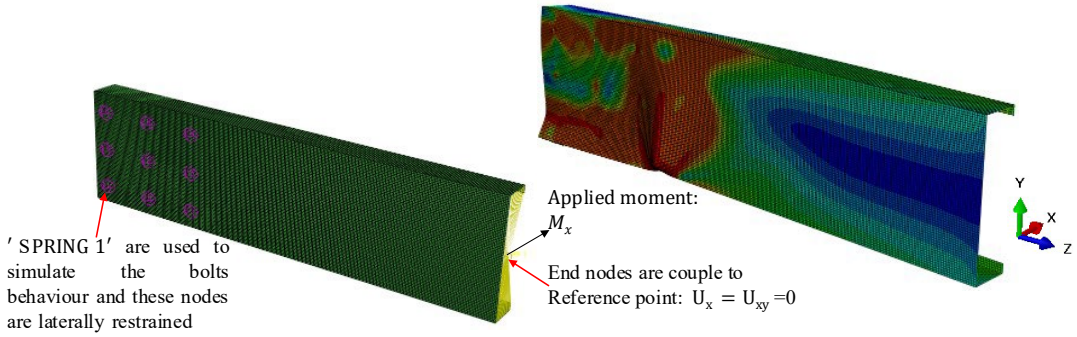

Figure A- 7 Details of the FE idealization for bolted joints

A.3 Brackets strength

The strength of the eaves and apex brackets can be as follows:

Single apex brackets (Chen et al. 2021)

$$M_{1ab} = f_y b_a^2 t_b \left[\alpha \left(\frac{b_a}{a_a}\right)^2 - \beta \left(\frac{b_a}{a_a}\right) + \gamma\right] \quad \text{Eq. a1}$$

Where α, β and γ are from Chen et al. [3]

Thus, for double brackets, the strength would be

$$M_{2ab} = 2 \times M_{1ab} \quad \text{Eq. a2}$$

Joint A: $M_{2ab}^A = 2 \times M_{1ab}^A = 2 \times 200 \times 3402 \times 2.98 \left[0.13 \left(\frac{340}{463.6}\right)^2 - 0.31 \left(\frac{340}{463.6}\right) + 0.49\right] 10^{-6}$

=45.82 kNm

Joint B: $M_{2ab}^B = 2 \times M_{1ab}^B = 2 \times 200 \times 3402 \times 2.98 \left[0.13 \left(\frac{340}{762.6}\right)^2 - 0.31 \left(\frac{340}{4762.6}\right) + 0.49\right] 10^{-6}$

= 52.04 kNm

Single eaves brackets (Chen et al. 2023b)

$$M_{1eb} = 1.0177\, a_e^{0.9364} b_e^{0.3450} f_y^{0.4134} t_b^{1.9766} 10^{-4} \quad \text{Eq. a3}$$

Thus, for double brackets, the strength would be

$$M_{2eb} = 2 \times M_{1eb} \quad \text{Eq. a4}$$

Joint A: $M_{2eb}^A = 2 \times M_{1eb}^A = 2 \times 1.0177 \times 750^{1.2674} \times 340^{0.3450} \times 200^{0.4134} \times 2.98^{1.9766} \times 10^{-4}$

= 57.57 kNm

Joint B: $M_{2eb}^B = 2 \times M_{1eb}^B = 2 \times 1.0177 \times 750^{1.2674} \times 340^{0.3450} \times 200^{0.4134} \times 2.98^{1.9766} \times 10^{-4}$

= 78.90 kNm

It should be noted that the eaves bracket strength predicted by equation does not accurately predict the load capacity for portal frames in the case of eaves bracket failure. Therefore, nodal forces from the nodes at the spring locations were used to determine the moment capacity of the bolt group, which was found to be 59.04 kNm and 66.6 kNm for Frames A and B, respectively.

A.4 Bolt-hole elongation stiffness

Figure A-8 defines the bolt-hole elongation stiffness for two plates representing the channel-section and bracket. The bolt-hole elongation can be calculated from (in series):

$$k_{1b1c\_AT} = \frac{1}{\frac{1}{k_{1b\_AT}}+\frac{1}{k_{1c\_AT}}} \qquad \text{Eq.a5}$$

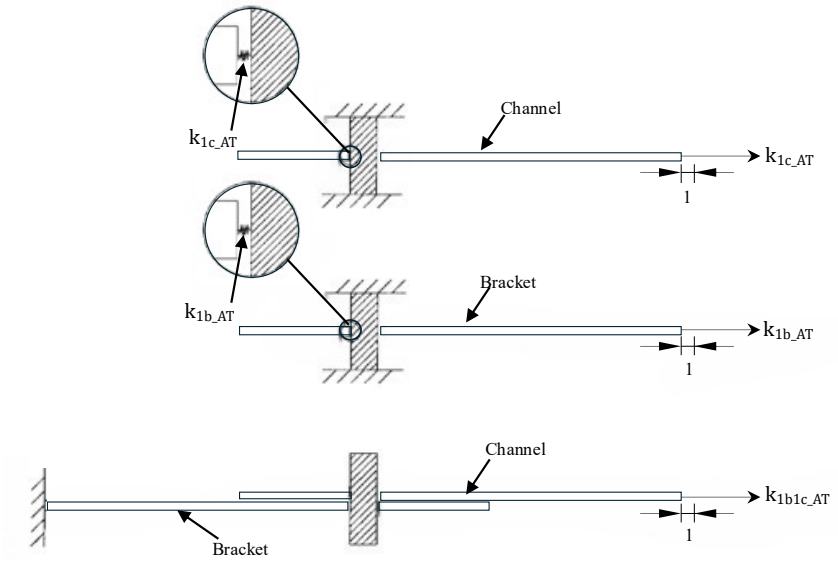

Figure A- 8 Diagram showing bolt-hole elongation stiffness as the force required to cause a unit displacement for a system of plates

From Ahmed and Teh (2019):

$$k_{1b\_AT} = 0.015 t_b \left(\frac{d_{minor_{M16}}}{d_{minor_{M20}}}\right)^{0.3} f_u = 0.015 \times 2.98 \times \left(\frac{13.4}{16.54}\right)^{0.3} \times 305 = 12.80 \text{ kN/mm} \quad \text{[see Figure A-9]}$$

$$k_{1c\_AT} = 0.015 t_c \left(\frac{d_{minor_{M16}}}{d_{minor_{M20}}}\right)^{0.3} f_u = 0.015 \times 2.95 \times \left(\frac{13.4}{16.54}\right)^{0.3} \times 425 = 17.66 \text{ kN/mm} \quad \text{[see Figure A-9]}$$

Thus,

$$k_{1b1c\_AT} = \frac{1}{\frac{1}{12.80}+\frac{1}{17.66}} = 7.42 \text{ kN/mm}$$

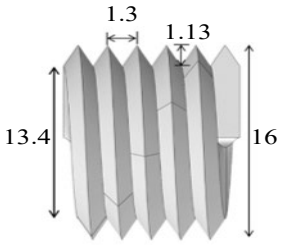

Figure A- 9 Dimensions of shank and threaded M16 bolts

A.5 Rotational stiffness of the joints

Rotational stiffness can be determined from Lim and Nethercot (2004) as follows:

For 3×3 bolts group

$K_{2b2c} = 3/2 \times (a_b^2 + b_d^2) \times k_{2b2c\_AT}$ Eq. a6

It should be noted that the rotational stiffness is propositional to the bolt-hole elongation stiffness. From Figure A-2, it can be seen that the joint arrangement comprises back-to-back brackets sandwiched between back-to-back channel-sections, as opposed to a single bracket bolted to a single channel-section. The value of the bolt-hole elongation stiffness is thus twice that of k_{1b1cAT} calculated in Section A.4.

$k_{2b2c\_AT} = 2\times k_{1b1c\_AT}$

$=14.84$ kN/mm

For the bolt-group of Frame A, the value of K is:

$K^A_{2b2c} = 3/2 \times (a_b^2 + b_d^2) \times k_{2b2c\_AT}$

$= \frac{3}{2} \times (315^2 + 230^2) \times 14.84 \times 10^{-3} = 3380$ kN. m/rad

For the bolt-group of Frame B, the value of K is:

$K^B_{2b2c} = 3/2 \times (a_b^2 + b_d^2) \times k_{2b2c\_AT}$

$= \frac{3}{2} \times (615^2 + 230^2) \times 14.84 \times 10^{-3} = 9590$ kN. m/rad

A.6 Beam idealization

Figure A-10 shows beam idealisations for Frames A and B. As can be seen, rotational spring elements are modelled at the centre of rotation of each bolt-group. The brackets can be assumed to function as rigid (Lim and Nethercot (2002a). Bending moment diagrams for both the frames are shown in Figure A-11.

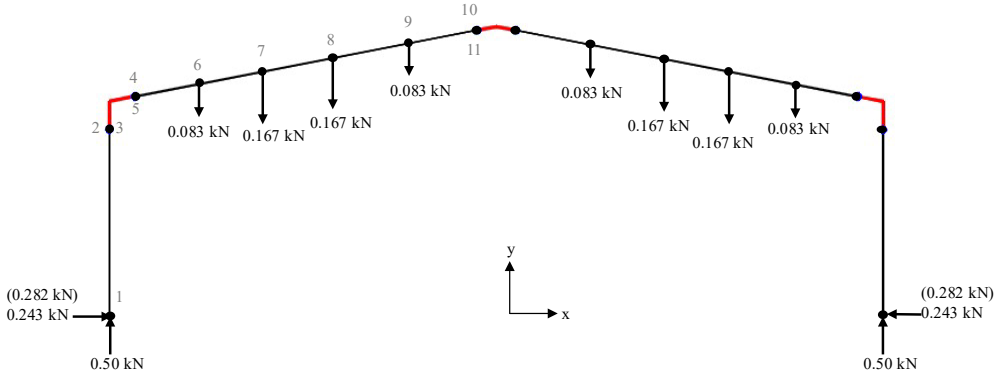

Nodes	Coordinates (m)		
	x	y	z
1	-6.00	0.00	0.00
2	-6.00	2.60	0.00
3	-6.00	2.60	0.00
4	-5.61	3.06	0.00
5	-5.61	3.06	0.00
6	-4.78	3.27	0.00
7	-3.49	3.44	0.00
8	-2.51	3.62	0.00
9	-1.52	3.79	0.00
10	-0.39	3.99	0.00
11	-0.39	3.99	0.00
-	-	-	-

Element	Node connectivity
1	1-2[1]
2	2- 3[3]
3	2-4[2]
4	4-5[3]
6	6-7[1]
7	7-8[1]
8	8-9[1]
9	9-10[1]
10	10-11[3]

Note:
1. Back-to-back channel, EI = 10.054 × 10^9 kN.mm^2, EA= 0.653×10^6 kN
2. Bracket, EI =∞ ; EA =∞
3. Rotation spring stiffness, K_{2b2c} = 3380 kNm / rad

(a) Frame A

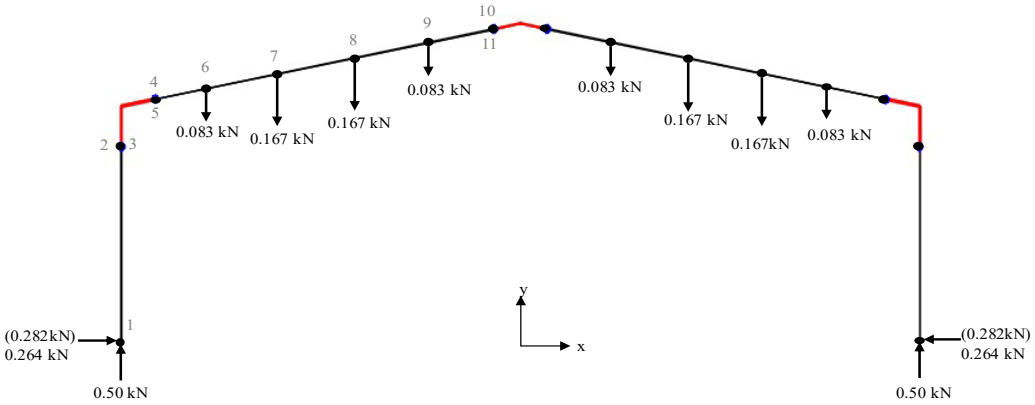

Nodes	Coordinates (m)		
	x	y	z
1	-6.00	0.00	0.00
2	-6.00	2.45	0.00
3	-6.00	2.45	0.00
4	-5.49	3.10	0.00
5	-5.61	3.06	0.00
6	-4.78	3.27	0.00
7	-3.49	3.44	0.00
8	-2.51	3.62	0.00
9	-1.52	3.79	0.00
10	-0.54	3.96	0.00
11	-0.54	3.96	0.00
-	-	-	-

Element	Node connectivity
1	1-2[1]
2	2- 3[3]
3	2-4[2]
4	4-5[3]
6	6-7[1]
7	7-8[1]
8	8-9[1]
9	9-10[1]
10	10-11[3]

Note:
1. Back-to-back channel, EI = 10.054 × 10^9 kN.mm^2, EA= 0.653×10^6 kN
2. Bracket, EI =∞ ; EA =∞
3. Rotation spring stiffness, K_{2b2c} = 9590 kNm / rad

(b) Frame B

Figure A- 10 Beam model for the portal frame

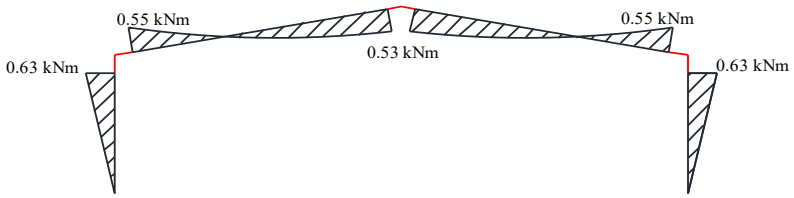

(a) Frame A

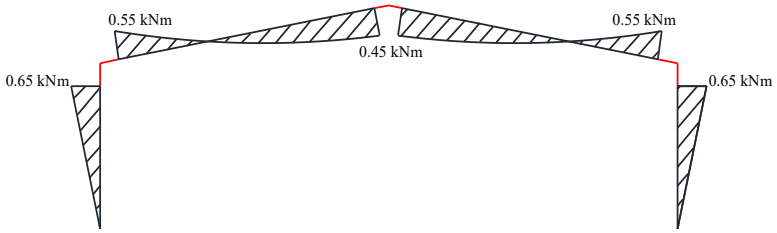

(b) Frame B

Figure A- 11 Bending moment diagram from beam model (Unit load and $k_{1B1C} = 7.42$ kN/mm)

A.7 Prediction of the ultimate load capacity

In this section, the prediction of ultimate load failure for the eaves, apex, and member has been discussed. The predicted ultimate loads are based on the section strength and the bracket strength, determined either from the FE model or equations. The results for section strength and bracket strength are summarized in Table 1.

Table A- 1 Section capacity and bracket strength from FEA and equations

	Section capacity				Bracket strength				Bolt-hole elongation stiffness
	Full Section capacity	Reduced moment capacity		Axial capacity	Apex		Eaves		
	M_{2c}	M_{2c}^{R}		P_{2c}	M_{2ab}		M_{2eb}		
		A	B		A	B	A	B	
	kNm	kNm	kNm	kN	kNm	kNm	kNm	kNm	kN/mm
Finite element	96.8	78.3	87.9	665.6	44.1	50.2	59.4	67.8	6.21
Equation	85.7	79.6	87.3	665.6	45.2	52.4	57.7	78.8	7.42

A.7.1 Bracket failure

As discussed in Section A.1, both frames failed due to the buckling of the apex bracket in the experiment, at 76.7 kN and 106.6 kN for Frames A and B, respectively. As shown in Figure A-3a, these failure loads are also captured by the FE model, which predicts them as 74.7 kN and 101.7 kN for Frames A and B, respectively. Additionally, Figure A-3a shows that the FE model captures the failure load of the eaves bracket, which is 90.1 kN for Frame A and 102.3 kN for Frame B. A similar prediction of failure load can also be made using the beam model if the strength of the brackets is known from the experiment/ FE model. From the FE models, the strength of the apex brackets was determined to be 44.1 kNm and 50.2 kNm for Frame A and Frame B, respectively, with corresponding failure loads of 80.2 kN and 109.1 kN, respectively. Similarly, for the eaves brackets, the strength determined from FEA was 59.4 kNm for Frame A and 67.8 kNm for Frame B, respectively, with corresponding failure loads of 95.8 kN for Frame A and 105.8 kN for Frame B. The following are the detailed calculations:

For Frame A,

Predicted failure load due to failure of apex bracket

$F_{beam} = \frac{M_{2ab}}{\alpha} = \frac{44.1}{0.55}$=80.2 kN

Predicted failure load due to failure of eaves bracket

$F_{beam} = \frac{M_{2eb}}{\beta} = \frac{59.4}{0.62}$=95.8kN

Similarly, for Frame B

Predicted failure load due to failure of apex bracket

$F_{beam} = \frac{M_{2ab}}{\alpha} = \frac{50.2}{0.46}$=109.1kN

Predicted failure load due to failure of eaves bracket

$F_{beam} = \frac{M_{2eb}}{\beta} = \frac{67.7}{0.64}$=105.8 kN

Where F_{beam} is the predicted load, M_{2ab} and M_{2eb} are the strength of the apex and eaves brackets, respectively. α and β represent the bending moments at the center of the bolt group at the apex and eaves brackets, respectively, for a unit load ($k_{1B1c} = 6.21$ kN/mm).

A.7.2 Premature buckling of channel section

From Figure A-3a, Frames A and B fail at 112.2 kN and 131.6 kN, respectively, representing a 46% and 21% increase over the experimental failure loads. For Frame A, at the center of rotation, this corresponds to a bending moment of 71.5 kNm in combination with an axial force of 56.1 kN. Similarly, for Frame B, this corresponds to a bending moment of 79.8 kNm in combination with an axial force of 65.8 kN.

Figure A-3b also shows the failure load predicted for failure at column joints due to premature buckling. In this case, the reduced moment capacity of the channel section under the influence of the bolt group can be predicted either from FEA or using the equation by Lim and Nethercot (2003). From the FE model, the reduced moment capacity of the channel section was determined to be 78.3 kNm for Frame A and 87.3 kNm for Frame B, respectively. The corresponding failure loads for Frame A and Frame B are 115.3 kN and 124.5 kN, respectively. The following are the detailed calculations:

For Frame A

Predicted load due to the failure of member

$$F_{beam} = \frac{1}{\left[\frac{\beta}{M_{2c}^{R}} + \frac{0.5}{P_{2c}}\right]} = \frac{1}{\left[\frac{0.62}{78.3} + \frac{0.5}{665.6}\right]} = 115.3 \text{ kN}$$

Similarly, for Frame B

Predicted load due to the failure of member

$$F_{beam} = \frac{1}{\left[\frac{\beta}{M_{2c}^{R}} + \frac{0.5}{P_{2c}}\right]} = \frac{1}{\left[\frac{0.64}{87.9} + \frac{0.5}{665.6}\right]} = 124.5 \text{ kN}$$

Where F_{beam} is the predicted load, M_{2c}^{R} is the reduced moment capacity of back-to-back channel section, respectively. β represents the bending moments at the center of the bolt group at the eaves brackets for a unit load ($k_{1B1c} = 6.21$ kN/mm). P_{2c} is the axial capacity of back-to-back channel section.

As shown in Figure A-3, assuming the joints as rigid would predict a failure load of 107.3 kN, which would be conservative for the design of a portal frame with semi-rigid joints.

Appendix-B

Example of a cold-formed steel Portal frame with nested tapered box (NTB) section having bolted end plate joints after Shahmohammadi (2019)

Table of contents

Notation	
A_g	Gross cross sectional area of NTB section
A_w	Web area of NTB section
α_1	Slenderness for flange
α_2	Slenderness for web
D	Depth of NTB section
D_s	Shallower depth of NTB section
E	Modulus of elasticity
EA	Axial rigidity of column/ rafter members
EI	Flexural rigidity of column/rafter members
f_y	Yeild stress
f_{ya}	Average yeild stress in compression/ flexural
f_u	Ultimate strength
f_{oc}	Critical buckling stress for global buckling for NTB section under compression
f_{ol}	Critial elastic buckling stress for local buckling due to compression or bending
f_{od}	Critial elastic buckling stress for distorsional buckling due to compression or bending
G	Modulus of rigidity
I_x, I_y	Moment of inertia about major and minor axis, respectively
J	Torsional constant
l_{ez}	Effective length of member
λ_l	Non-dimensional slenderness ratio for local buckling
λ_d	Non-dimensional slenderness ratio for distortional buckling
λ_v	Non-dimensional slenderness ratio for shear
M_{be}	Nominal moment capacity of NTB section for lateral-torsional buckling
M_d	Nominal moment capacity of NTB section for distortional buckling
M_l	Nominal moment capacity of NTB section for local buckling
M_{ol}	Nominal moment capacity of NTB section for distortional buckling
M_o	Nominal moment capacity of NTB section for overall buckling
M_{oa}	Reduced moment capacity of NTB section for overall buckling
M_{od}	Critical elastic moment capacity of NTB section for distortional buckling
M_{ol}	Critical elastic moment capacity of NTB section for local buckling
M_y	Nominal yield moment capacity
P_{ce}	Nominal axial capacity of NTB section for flexural, torsional, or lateral-torsional buckling
P_d	Nominal axial capacity of NTB section for distortional buckling
P_l	Nominal axial capacity of NTB section for local buckling
P_{ol}	Critical elastic moment capacity of NTB section for distortional buckling
P_{od}	Critical elastic moment capacity of NTB section for local buckling
P_y	Nominal yield moment capacity
r	Corner radius
r_x, r_y	Radius of gyration about major and minor axis, respectively
k_v	Shear buckling co-efficient
t	Thickness of NTB section
V_{cr}	Critical buckling in shear
V_y	Yeild capacity in shear
V_v	Nominal shear capacity
Z_f	Section modulus of NTB section

B.1 Introduction

Shahmohammadi (2019) tested a full-scale test NTB portal frame under gravity load (See Figure B-1). Frame had a span of 18.16 m, column height of 4.27 m, and pitch of 5°. As can be seen from Figure B-1a, the frame was loaded through the four set water tanks and the pinned supports at the column bases. Minimum no of lateral restraints was employed to take the advantage of the tapered box member. As can be seen, the frame was loaded using the four set water tanks and the pinned supports were at the column bases. Figure B-2 shows the load displacement curve. M16 bolts are used to connect the bolted end plates at each joint. Geometric details of cross-section and brackets are shown in Figure B-3.

(a) Photograph of the portal frame test

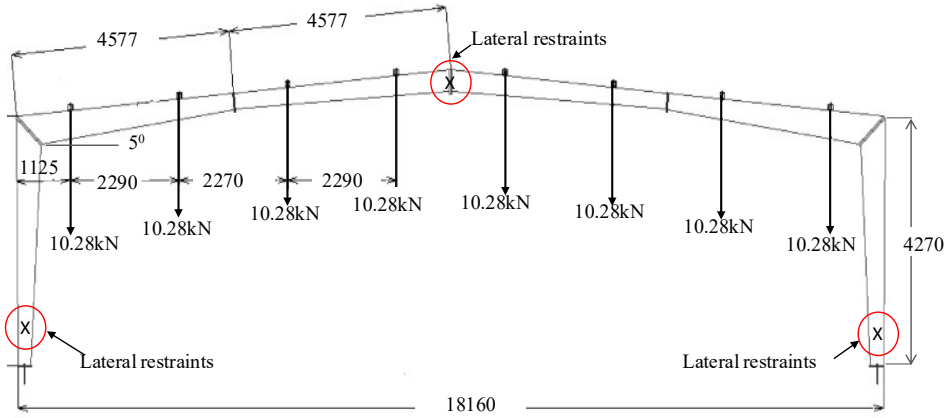

(b) Point loads applied to standard frame

Figure B-1 Details of the general arrangement of the test frame after Shahmohammadi (2019)

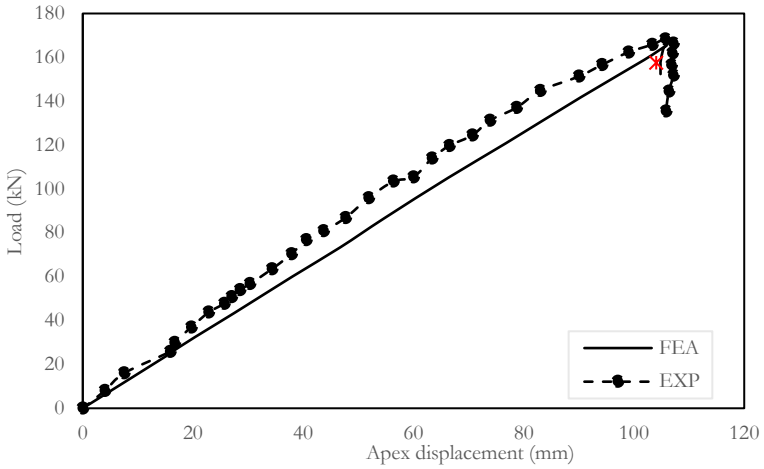

Figure B-2 Load-displacement curve for test frame

f_y = 258 N/mm^2
f_u = 386 N/mm^2
t = 4.2 mm

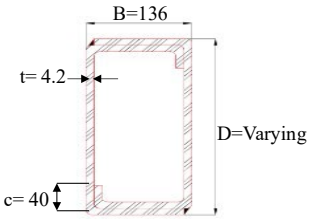

Joints	D (mm)
Column base	282
Eaves	513
Mid rafter	282
Apex	369

(a) Cross section details of NTB section

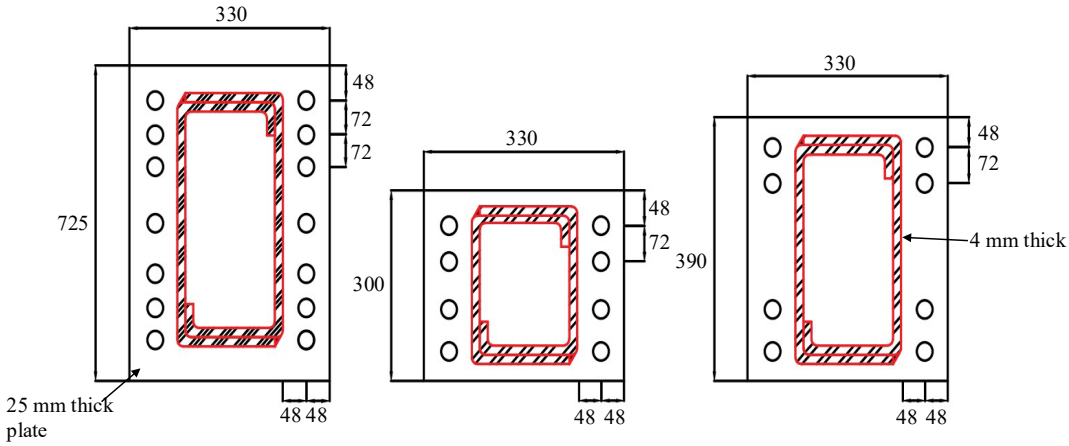

(b) Eaves joint (c) Mid rafter joint (d) Apex joint

All dimensions are in millimetres

Figure B- 3 Dimensions of NTB section and bolted end plate joint used for column and rafter members (Shahmohammadi, 2019)

B.2 Section strength using AS/NZ 4600 (2018)

In this section, the section strength under bending and compression has been determined using the DSM in accordance with AS/NZ 4600 (2018). Since the cross-section is tapered, calculation for the only eaves was carried out to demonstrate the design procedure. It should be noted that the effect of bimoment was not considered as the cross-section being a nested box section with rigid joints.

B.2.1 Elastic buckling analysis

The local and distortional buckling stress f_{ol}, f_{od} under bending and compression can be determined by implementing elastic buckling analysis. The buckling stress can be obtained via equations proposed by Shahmohammadi (2019). The equations are as follows:

$$\alpha_1 = \frac{(B-3t-2r)}{t}\sqrt{\frac{f_y}{250}} = \frac{(136-3\times4.2-2\times6)}{4.2}\sqrt{\frac{258}{250}} = 26.94$$

$$\alpha_2 = \frac{(D-3t-2r)}{t}\sqrt{\frac{f_y}{250}} = \frac{(513-3\times4.2-2\times6)}{4.2}\sqrt{\frac{258}{250}} = 118.13$$

For bending,

$$f_{ol} = \alpha_1 + \frac{5673175\alpha_2-\alpha_2 1.33^{\alpha_1}-6.06{\alpha_2}^3}{29490+880\alpha_2+{\alpha_2}^3+397{\alpha_2}^2-5906\alpha_1} = 26.94 + \frac{5673175-3\times118.13-118.13\times1.33^{26.94}-6.06\times118.13^3}{29490+880\times118.13+118.13^3+397\times118.13^2-5906\times26.94}$$

$=372.23$ N/mm^2

$$f_{od} = 3.54\alpha_2 + \frac{31533}{\alpha_1} + \frac{14896}{\alpha_2} - \frac{20.3{\alpha_2}^2}{{\alpha_1}^2} - 338 - 8.93{\alpha_1}^2$$

$$= 3.54\times118.13 + \frac{31533}{26.94} + \frac{14896}{118.13} - \frac{20.3\times118.13^2}{26.94^2} - 338 - 8.93\times26.94^2 = 769.96 \text{ N/mm}^2$$

For compression,

$$f_{ol} = \frac{1127777}{(18.7\alpha_2+9.05\alpha_1+\alpha_2^2)} = \frac{1127777}{(18.7\times118.13+9.05\times26.94+118.13^2)} = 68.74 \text{ N/mm}^2$$

$$f_{od} = 0.0441\alpha_1\alpha_2 - 6.83\alpha_1 + \frac{13196494\alpha_1}{(20424+{\alpha_2}^3+621{\alpha_1}^2-153\alpha_1\alpha_2)}$$

$$= 0.0441\times26.94\times118.13 - 6.83\times26.94 + \frac{13196494\times26.94}{(20424+118.13^3+621\times26.94^2-153\times26.94\times118.13)} = 174 \text{ N/mm}^2$$

B.2.2 Moment capacity

Yield moment capacity (M_y) for NTB section,

$M_y = Z_f f_{ya}$ [Cl.7.2.2.2]

$= 992805\times 277.28 = 2.75\times10^8$ Nmm

$$M_o = \frac{0.36c_b\pi}{l}\sqrt{EGJI_y} = \frac{0.36\times1.67\times\pi}{4270}\sqrt{(2\times10^5)\times80000\times(6.3\times10^7)\times25436757}$$ [Cl. D.1]

$= 2.22\times10^9$ N.mm

$$M_{oa} = \left[1-0.25\times\left(1-\frac{D_{end}}{D}\right)\right]\times M_o = \left[1-0.25\times\left(1-\frac{282}{513}\right)\right]\times2.22\times10^9$$ [NZS3404, Cl.5.6.1.1.1]

$= 1.97\times10^9$ N.mm $>2.78M_y$

The nominal moment capacity of the member (M_{be}) for lateral-torsional buckling is then determined via the following equations:

$M_{be} = M_y = 2.75\times10^8$ N.mm [Cl. 7.2.2.2(3)]

Non-dimensional slenderness ratio for local buckling

$\lambda_l = \sqrt{\frac{M_y}{M_{ol}}} = \sqrt{\frac{2.75\times10^8}{992805\times372.23}} = 0.863 > 0.776$ [Cl.7.2.2.3 (1) and Cl.7.2.2.3 (3)]

The nominal moment capacity of the member (M_l) for local buckling,

$M_l = \left[1 - 0.15\left(\frac{M_{ol}}{M_y}\right)^{0.4}\right]\left(\frac{M_{ol}}{M_y}\right)^{0.4} \times M_{be}$ [Cl.7.2.2.3 (2)]

$= \left[1 - 0.15\left(\frac{1}{0.863}\right)^{0.4}\right]\left(\frac{1}{0.863}\right)^{0.4} \times 2.75\times10^8 = 2.574\times10^8$ N.mm

Non-dimensional slenderness ratio for distortional buckling

$\lambda_d = \sqrt{\frac{M_y}{M_{od}}} = \sqrt{\frac{2.75\times10^8}{992805\times769.69}} = 0.60 < 0.673$ [Cl.7.2.2.4 (3)]

The nominal moment capacity of the member (M_d) for distortional buckling,

$M_d = M_{be} = 2.75\times10^8$ N.mm [Cl.7.2.2.4(1)]

Nominal moment capacity for NTB section (M_b) = min (M_l, M_d, M_{be}) $= 2.574\times10^8$ N.mm =257.4 kNm

B.2.3 Axial capacity

Nominal yield capacity (P_y) for NTB section in compression,

$P_y = A_g f_{ya} = 6536.85\times277.28 = 1.73\times10^6$ N [Cl. 7.2.1.2 (5)]

$\lambda_c = \sqrt{\frac{P_y}{P_{oc}}} = \sqrt{\frac{1.73\times10^6}{2.72\times10^6}} = 0.799 < 1.5$ [Cl. 7.2.1.2 (3)]

$P_{oc} = A_g f_{oc} = 6536.85\times415.42 = 2.72\times10^6$N [Cl. 7.2.1.2 (4)]

$f_{oc} = \min(f_{ox}, f_{oy}, f_{oz}) = 415.42$ N/mm^2

$f_{ox} = \frac{\pi^2 E}{(l_{ex}/r_x^2)} = \frac{\pi^2\times2\times10^5}{(4270/197^2)} = 4158.85$ N/mm^2

$f_{oy} = \frac{\pi^2 E}{(l_{ey}/r_y^2)} = \frac{\pi^2\times2\times10^5}{(4270/62^2)} = 415.42$ N/mm^2

$f_{oz} = \frac{GJ}{A_g r_{o1}^2}\left(1 + \frac{\pi^2 EI_W}{GJl_{ez}^2}\right) = \frac{80000\times6.37\times10^7}{6536.85\times207^2}\left(1 + \frac{\pi^2\times2\times10^5\times1.52\times10^{14}}{80000\times6.37\times10^7\times4300^2}\right) = 76271.88$ N/mm^2

$r_{o1} = \sqrt{r_x^2 + r_y^2} = \sqrt{197^2 + 62^2} = 207.0$ mm

The nominal capacity of the member (N_{ce}) in compression for flexural, torsional or flexural-torsional buckling is determined by using equations:

$P_{ce} = \left(0.658^{\lambda_c{}^2}\right)P_y = \left(0.658^{0.799^2}\right)\times1.73\times10^6 = 1.32\times10^6$ N [Cl. 7.2.1.2 (1)]

Non-dimensional slenderness ratio for local buckling

$\lambda_l = \sqrt{\frac{P_y}{P_{ol}}} = \sqrt{\frac{1.73\times10^6}{4.93\times10^5}} = 1.718 > 0.776$ [Cl. 7.2.1.3 (1)]

$P_{ol} = A_g f_{ol} = 6536.85\times68.74 = 4.93\times10^5$ N [Cl. 7.2.1.3 (4)]

Local buckling capacity of NTB section

$P_l = \left[1 - 0.15\left(\frac{P_{ol}}{P_{ce}}\right)^{0.4}\right]\left(\frac{P_{ol}}{P_{ce}}\right)^{0.4} \times P_{ce}$

$= \left[1 - 0.15\left(\frac{4.93\times10^5}{1.32\times10^6}\right)^{0.4}\right]\left(\frac{4.93\times10^5}{1.32\times10^6}\right)^{0.4} \times 1.32\times10^6$

$= 7.764\times10^5$ N [Cl. 7.2.1.3 (2)]

Non-dimensional slenderness ratio for distortional buckling

$\lambda_d = \sqrt{\frac{P_y}{P_{od}}} = \sqrt{\frac{1.73\times10^6}{1.136\times10^6}} = 1.235 > 0.776$ [Cl. 7.2.1.4 (3)]

$P_{od} = A_g f_{od} = 6536.85\times174 = 1.136\times10^6$ N [Cl. 7.2.1.4 (4)]

Distortional buckling capacity of NTB section

$$P_d = \left[1 - 0.25\left(\frac{P_{od}}{P_y}\right)^{0.6}\right]\left(\frac{P_{od}}{P_y}\right)^{0.6} \times P_y \qquad \text{[Cl. 7.2.1.4 (2)]}$$

$$= \left[1 - 0.25\left(\frac{1.136\times10^6}{1.72\times10^6}\right)^{0.6}\right]\left(\frac{1.136\times10^6}{1.72\times10^6}\right)^{0.6} \times 1.72 \times 10^6$$

$$= 1.15 \times 10^6 \text{ N}$$

Nominal axial capacity for NTB section (P_b) = min (P_l, P_d, P_{ce}) =7.764×10^5 N= 776.4 kN

B.2.4 Shear capacity

Yield capacity in shear,

$V_y = 0.6A_w f_y$ =$0.6\times 2 \times 513 \times 4.2 \times 258 = 6.67 \times 10^5$ N [Cl. 7.2.3(5)]

Critical buckling capacity in shear

$V_{cr} = \frac{\pi^2 E A_W K_v}{12(1-\mu^2)(d_1/t_w)^2} = \frac{\pi^2\times2\times10^5\times2\times513\times4.2\times5.34}{12(1-0.3^2)(513/4.2)^2} = 1.41\times 10^5$ N [Cl. D3(1)]

Non-dimensional slenderness ratio for shear

$\lambda_v = \sqrt{\frac{V_y}{V_{cr}}} = \sqrt{\frac{6.67\times10^5}{1.41\times10^5}} = 2.175 > 1.227$ [Cl. 7.2.3(4)]

Nominal shear capacity of the section (V_v) is determined by the equations below:

$V_v = V_{cr} = 1.41 \times 10^5$ N =141 kN [Cl. 7.2.3(3)]

B.3 Beam Idealization

Figure B-4 shows a beam model for NTB portal frame where joints were considered as rigid. Herein, FE software was used for the analysis. As NTB section is not present in the section templates of FE software, design section option was used with the same width, depth and thickness; however, modification factors are applied to the moment of inertia, cross-section area and section weight to reach to the same properties as the equivalent NTB section. The factors modify the section bending stiffness, section axial stiffness and self-weight of the frame. For tapering of NTB section, non-prismatic option was employed in FE software (see Figure B-4). A rotational spring with the stiffness 2370 kNm/rad is assigned to the column bases as suggested by Shahmohammadi et al. (2022) in his paper. Bending moment diagram has been shown in Figures B-5.

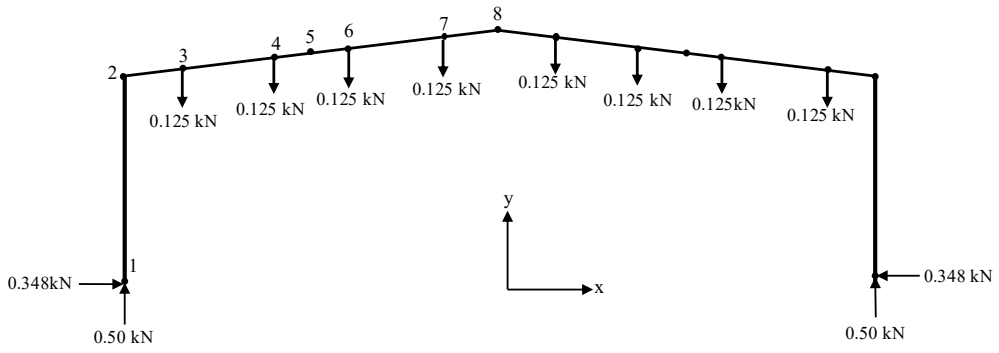

Nodes	Coordinates (m)		
	x	y	z
1	-9.08	0.00	0.00
2	-9.08	4.27	0.00
3	-7.96	4.37	0.00
4	-5.67	4.57	0.00
5	-4.59	4.67	0.00
6	-3.40	4.78	0.00
7	-1.11	4.95	0.00
8	0	5.06	0.00
-	-	-	-

Element	Node connectivity
1	1-2[1,2]
2	2- 3[1]
3	3-4[1]
4	4-5[1]
5	5-6[1]
7	6-7[1]
8	7-8[1]

Note:
1. NTB section, EI and EA = varying
2. Rotational stiffness of 2370 kNm/rad

Figure B-4 Beam model for the NTB portal frame

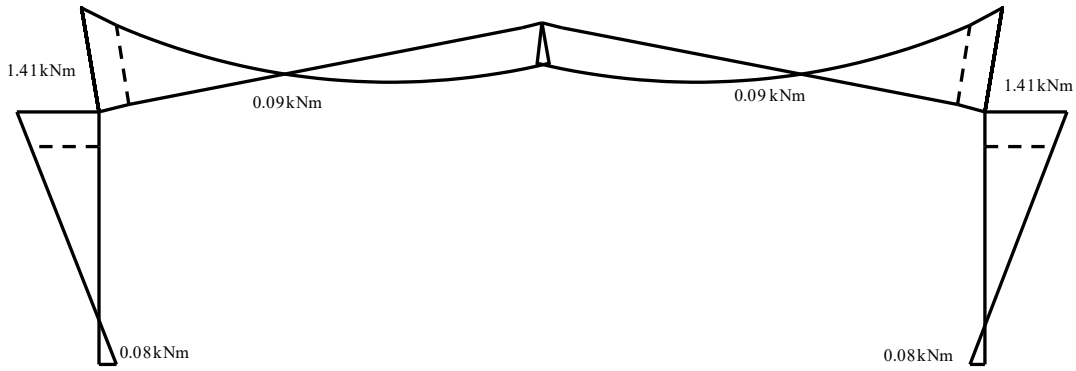

Figure B-5 Bending moment diagram from beam model (unit load)

B.4 Prediction of the ultimate load capacity

From Figure B-2, it can be seen that NTB portal frame with bolted end joint failed at 163.98 kN due to the failure of NTB member near eaves, which is close to the experimental test. A similar prediction could also be made from the beam model (see Figure B-4), which shows a failure load of 157.8 kN at eaves. This corresponds to a bending moment of 217.9 kNm, combined with an axial force of 60.2 kN and a shear force of 69.7 kN.

B.5 Detailed calculation

The followings steps are shown for the design of portal frame:

Calculate cross-sectional capacities and check for combined actions

Description	Parameter	Column base	Column eaves	Rafter eaves	Rafter mid	Rafter apex
Actual section thickness (mm)	**t**	4.2	4.2	4.2	4.2	4.2
Section width (mm)	**B**	136	136	136	136	136
Depth (mm)	**D**	282	513	513	282	369
Member length about x axis in bending (mm)	**L major-M**	4270	4270	9100	9100	9100
Member length about y axis in bending (mm)	**L minor-M**	4270	4270	9100	9100	9100
Member length about x axis in compression (mm)	**L major-P**	4270	4270	9100	9100	9100
Member length about y axis in compression (mm)	**L minor-P**	4270	4270	9100	9100	9100
Yield stress (MPa)	f_y	258	258	258	258	258
Tensile stress (MPa)	f_u	386	386	386	386	386
Depth at the other end	D_{end}	513	282	282	513	282
Design bending moment (kN.m)	**M***	12.1	217.9	217.9	14.2	82.3
Design axial force (kN)	**P***	78.5	78.5	60.2	56.9	56.9
Design shear force (kN)	**V***	53.9	53.9	69.7	32.3	4.7
Average yield stress (MPa) in compression	$f_{ya\text{-}comp}$	268.1	265.1	265.1	268.1	266.7
Average yield stress (MPa) in flexural	$f_{ya\text{-}flex}$	277.3	277.3	277.3	277.3	277.3
Area of the bend to the area of the full section	C_{comp}	0.1	0.0	0.0	0.1	0.0
Area of the bend to the area of the flange	C_{flex}	0.1	0.1	0.1	0.1	0.1
Bent yield stress (MPa)	f_{yc}	452.7	452.7	452.7	452.7	452.7
constant	B_c	1.9	1.9	1.9	1.9	1.9
constant	**m**	0.2	0.2	0.2	0.2	0.2
Shallower end to deeper end depth ratio for tapered members	D_s/D_j	0.55	0.55	0.550	0.55	0.76

Description	Parameter	Column base	Column eaves	Rafter eaves	Rafter mid	Rafter apex
Radius	r	6.0	6.0	6.0	6.0	6.0
Lip	c	40.0	40.0	40.0	40.0	40.0
Moment of inertia about x (mm^4)	I_x	6.28E+07	2.55E+08	2.55E+08	6.28E+07	1.17E+08
Moment of inertia about y (mm^4)	I_y	1.58E+07	2.54E+07	2.54E+07	1.58E+07	1.95E+07
Elastic section modulus	Z	4.45E+05	9.93E+05	9.93E+05	4.45E+05	6.32E+05
Section area (mm^2)	A_g	4.60E+03	6.54E+03	6.54E+03	4.60E+03	5.33E+03
Torsion constant (mm^4)	J	2.96E+07	6.30E+07	6.30E+07	2.96E+07	4.19E+07
Warping constant (mm^6)	I_w	1.53E+14	1.53E+14	1.53E+14	1.53E+14	1.53E+14
Radius of gyration about the x axes (mm)	r_x	1.17E+02	1.97E+02	1.97E+02	1.17E+02	1.48E+02
Radius of gyration about the y axes (mm)	r_y	5.87E+01	6.24E+01	6.24E+01	5.87E+01	6.04E+01
Young's modulus of elasticity (MPa)	E	2.00E+05	2.00E+05	2.00E+05	2.00E+05	2.00E+05
Shear modulus of elasticity (MPa)	G	8.27E+04	8.00E+04	8.00E+04	8.00E+04	8.00E+04
Coefficient depending on moment distribution	c_b	1.67	1.67	1.67	1.67	1.67
Polar radius of gyration (mm)	r_{o1}	130.8	207.0	207.0	130.8	159.8
Strength reduction factor for moment and shear	$ø_b$, $ø_v$	1.0	1.0	1.0	1.0	1.0
Strength reduction factor for moment and axial	$ø_c$	1.0	1.0	1.0	1.0	1.0
Elastic lateral-torsional buckling moment (N.mm)	M_o	1.24E+09	2.22E+09	1.05E+09	5.68E+08	7.49E+08
Reduction factor applied to Mo for tapered members (NZS3404, cl-5.6.1.1.1)	a_s	0.89	0.89	0.89	0.89	0.94
Reduced elastic lateral-torsional buckling moment because of being tapered (N.mm)	m_{oa}	1.10E+09	1.97E+09	9.33E+08	5.04E+08	7.05E+08
Flange slenderness	λ_{ef}	26.9	26.9	26.9	26.9	26.9
Web slenderness	λ_{ew}	62.3	118.1	118.1	62.3	83.3
Elastic local buckling stress under bending moment (MPa)	f_{ol}	800.2	372.2	372.2	800.2	605.9
Elastic distortional buckling stress under bending moment (MPa)	f_{od}	943.7	746.6	746.6	943.7	872.2
Elastic local buckling stress including depth and moment variation and contact between flanges effects (MPa)	$f_{ol,mod}$	800.2	372.2	372.2	800.2	605.9
Elastic distortional buckling stress including depth and moment variation and contact between flanges effects (MPa)	$f_{od,mod}$	972.1	769.0	769.0	972.1	898.3
Elastic local buckling moment (N.mm)	M_{ol}	3.56E+08	3.70E+08	3.70E+08	3.56E+08	3.83E+08
Elastic distortional buckling moment (N.mm)	M_{od}	4.33E+08	7.63E+08	7.63E+08	4.33E+08	5.68E+08
Local buckling non-dimensional slenderness	λ_l	0.59	0.86	0.86	0.59	0.68

Description	Parameter	Column base	Column eaves	Rafter eaves	Rafter mid	Rafter apex
Distortional buckling slenderness	λ_d	0.53	0.60	0.60	0.53	0.56
Yield moment (N.mm)	M_y	1.23E+08	2.75E+08	2.75E+08	1.23E+08	1.75E+08
Nominal member moment capacity for lateral-torsional buckling (N.mm)	M_{be}	1.23E+08	2.75E+08	2.75E+08	1.23E+08	1.75E+08
Nominal member moment capacity for local buckling (N.mm)	M_{bl}	1.23E+08	2.57E+08	2.57E+08	1.23E+08	1.75E+08
Nominal member moment capacity for distortional buckling (N.mm)	M_{bd}	1.23E+08	2.75E+08	2.75E+08	1.23E+08	1.75E+08
Moment capacity (N.mm)	M	1.23E+08	2.57E+08	2.57E+08	1.23E+08	1.75E+08
Section moment capacity equal to M_{bl} (N.mm)	M_s	1.23E+08	2.57E+08	2.57E+08	1.23E+08	1.75E+08
Nominal capacity of the member in compression for flexural (N)	P_{ce}	9.17E+05	1.33E+06	5.32E+05	3.31E+05	4.07E+05
Euler axial force (N)	P_{ex}	6.92E+06	2.72E+07	6.07E+06	1.50E+06	2.78E+06
Section capacity of member in compression equal to P_{cl}	P_s	9.71E+05	9.22E+05	9.22E+05	1.23E+06	1.42E+06
Non-dimensional slenderness for N_{ce}	λ_c	0.84	0.80	1.69	1.81	1.75
Nominal yield capacity of the member in compression (N)	N_y	1.23E+06	1.73E+06	1.73E+06	1.23E+06	1.42E+06
Least of the elastic compression member buckling load in flexural, torsional and flexural-torsional buckling (N)	P_{oc}	1.75E+06	2.72E+06	6.06E+05	3.78E+05	4.64E+05
Elastic buckling stress in an axially loaded compression member for flexural buckling about the y-axis (MPa)	f_{oy}	380.2	415.4	92.8	82.1	87.0
Elastic buckling stress in an axially loaded compression member for flexural buckling about the x-axis (MPa)	f_{ox}	1506.3	4158.9	928.6	325.4	521.7
Elastic buckling stress in an axially loaded compression member for torsional buckling (MPa)	f_{oz}	245743.8	76271.9	31006.7	76461.1	51419.1
Elastic flexural, torsional and flexural-torsional buckling stress (MPa)	f_{oc}	380.2	415.4	92.8	82.1	87.0
Elastic local buckling stress under compression (MPa)	f_{ol}	213.5	68.7	68.7	213.5	129.0
Elastic distortional buckling load under compression (MPa)	f_{od}	669.7	173.8	173.8	669.7	418.4
Elastic local buckling load under compression (N)	P_{ol}	9.81E+05	4.49E+05	4.49E+05	9.81E+05	6.87E+05
Elastic distortional buckling compression load (N)	P_{od}	3.08E+06	1.14E+06	1.14E+06	3.08E+06	2.23E+06

Description	Parameter	Column base	Column eaves	Rafter eaves	Rafter mid	Rafter apex
Non-dimensional slenderness for local buckling under compression	λ_l	0.97	1.72	1.09	0.58	0.77
Non-dimensional slenderness for distortional buckling under compression	λ_d	0.63	1.24	1.24	0.63	0.80
Nominal member capacity for elastic buckling (N)	P_{cl}	7.97E+05	7.77E+05	4.27E+05	3.31E+05	4.07E+05
Nominal member capacity for distortional buckling (N)	P_{cd}	1.14E+06	1.15E+06	1.15E+06	1.14E+06	1.19E+06
Axial compression capacity (N)	P	7.97E+05	7.77E+05	4.27E+05	3.31E+05	4.07E+05
Nominal shear capacity (N)	V_v	2.54E+05	1.41E+05	1.41E+05	2.50E+05	1.96E+05
Non-dimensional slenderness under shear	λ_v	1.18	2.18	2.18	1.20	1.56
Elastic shear buckling force (N)	V_{cr}	2.65E+05	1.41E+05	1.41E+05	2.56E+05	1.96E+05
Yield shear force of the section (N)	V_y	3.67E+05	6.67E+05	6.67E+05	3.67E+05	4.80E+05
Shear capacity (N)	V	2.54E+05	1.41E+05	1.41E+05	2.50E+05	1.96E+05
Moment amplification factors due to the axial load	α_n	0.99	1.00	0.99	0.95	0.98
Moment D/C ratio	M check	0.10	0.85	0.85	0.11	0.47
Axial D/C ratio	P check	0.10	0.10	0.14	0.17	0.14
Shear D/C ratio	V check	0.21	0.38	0.49	0.13	0.02
$\frac{P^*}{P}+\frac{M^*}{M}<1$	M-P	0.18	0.93	0.91	0.16	0.51
$\frac{P^*}{P}+\frac{C_m M^*}{\alpha_n M}<1$	M-P	0.20	0.95	**1.00**	0.29	0.62
$\left(\frac{M^*}{M}\right)^2+\left(\frac{V^*}{V}\right)^2<1$	M-V	0.05	0.86	0.96	0.03	0.22
$0.46\frac{M^*}{M}+\frac{V^*}{1.3V}<1$	M-V	0.21	0.68	0.77	0.15	0.23

Appendix-C

Example of a cold-formed steel Portal frame with nested tapered box (NTB) section having bolted-side plate joints

Table of contents

Notation	
A_g	Gross cross sectional area of NTB section
A_w	Web area of NTB section
α_1	Slenderness for flange
α_2	Slenderness for web
D	Depth of NTB section
D_s	Shallower depth of NTB section
d	Nominal diameter of bolt
$d_{minor_{M16}}$	Minor diameter of M16 bolt
$d_{minor_{M20}}$	Minor diameter of M20 bolt
E	Modulus of elasticity
EA	Axial rigidity of column/ rafter members
EI	Flexural rigidity of column/rafter members
f_y	Yield stress
f_u	Ultimate strength
f_{oc}	Critical buckling stress for global buckling for NTB section under compression
f_{ol}	Critical elastic buckling stress for local buckling due to compression or bending
f_{od}	Critical elastic buckling stress for distortional buckling due to compression or bending
G	Modulus of rigidity
I_x, I_y	Moment of inertia about major and minor axis, respectively
J	Torsional constant
l_{ez}	Effective length of member
λ_l	Non-dimensional slenderness ratio for local buckling
λ_d	Non-dimensional slenderness ratio for distortional buckling
λ_v	Non-dimensional slenderness ratio for shear
M_{be}	Nominal moment capacity of NTB section for lateral-torsional buckling
M_d	Nominal moment capacity of NTB section for distortional buckling
M_l	Nominal moment capacity of NTB section for local buckling
M_{ol}	Nominal moment capacity of NTB section for distortional buckling
M_o	Nominal moment capacity of NTB section for overall buckling
M_{oa}	Reduced moment capacity of NTB section for overall buckling
M_{od}	Critical elastic moment capacity of NTB section for distortional buckling
M_{ol}	Critical elastic moment capacity of NTB section for local buckling
M_y	Nominal yield moment capacity
P_{ce}	Nominal axial capacity of NTB section for flexural, torsional, or lateral-torsional buckling
P_d	Nominal axial capacity of NTB section for distortional buckling
P_l	Nominal axial capacity of NTB section for local buckling
P_{ol}	Critical elastic moment capacity of NTB section for distortional buckling
P_{od}	Critical elastic moment capacity of NTB section for local buckling
P_y	Nominal yield moment capacity
r	Corner radius
r_x, r_y	Radius of gyration about major and minor axis, respectively
k_v	Shear buckling co-efficient
k_{1p_AT}	Bolt-hole elongation stiffness of one NTB plate
k_{1b_AT}	Bolt-hole elongation stiffness of one bolted-side plate

k_{1b1p_AT}	Bolt-hole stiffness of the interconnected plates system for joints comprised one bolted-side plate with one NTB plate
k_{2b2p}	Bolt-hole stiffness of the interconnected plates system for joints comprised two bolted-side plate with two NTB plate
K	Rotational stiffness of joints
K_a	Rotational stiffness of apex joints
K_e	Rotational stiffness of eaves joints
t_s	Thickness of bolted-side plate
t	Thickness of NTB section
V_{cr}	Critical buckling in shear
V_y	Yield capacity in shear
V_v	Nominal shear capacity
Z_f	Section modulus of NTB section

C.1 Introduction

The frame shown in Figure C-1a is a NTB portal frame with bolted-side plate joints. Details of the eaves and apex joints are shown in Figure C-2. This frame also has a same span (18.16m), eaves heights (4.27m), pitch of 5^0 as the test described in Appendix B. As can be seen from Figure C-1b, the point loads were applied to the frame and pinned supports at the column bases, albeit partially restrained in lateral direction. Lateral restraints were provided to the loading position and near the joints to prevent the possibility lateral buckling. Figure C-3 shows the load-displacement curves for the tested frames. Fully threaded M16 bolts (See Figure C-1a) are used to connect the NTB section with the bolted-side plates. Geometric details of NTB cross-section and bolted-side plates are shown in Figure C-4.

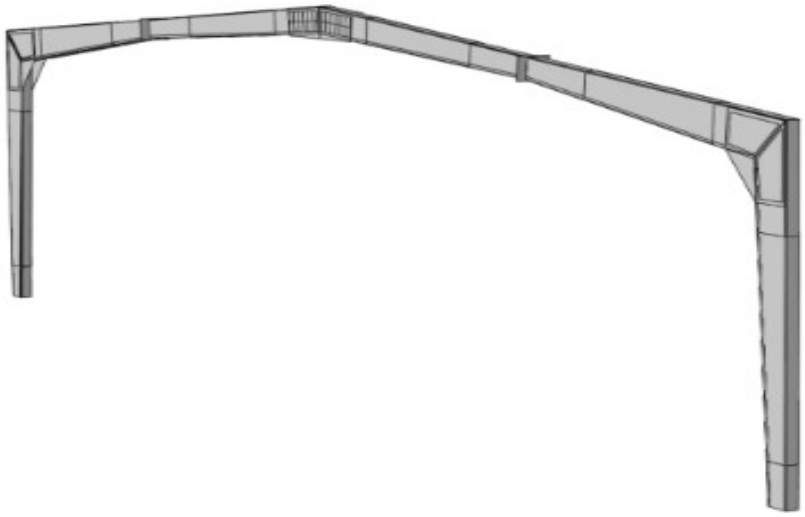

(a) A schematic diagram of NTB portal frame with bolted-side plate joints considered for this study

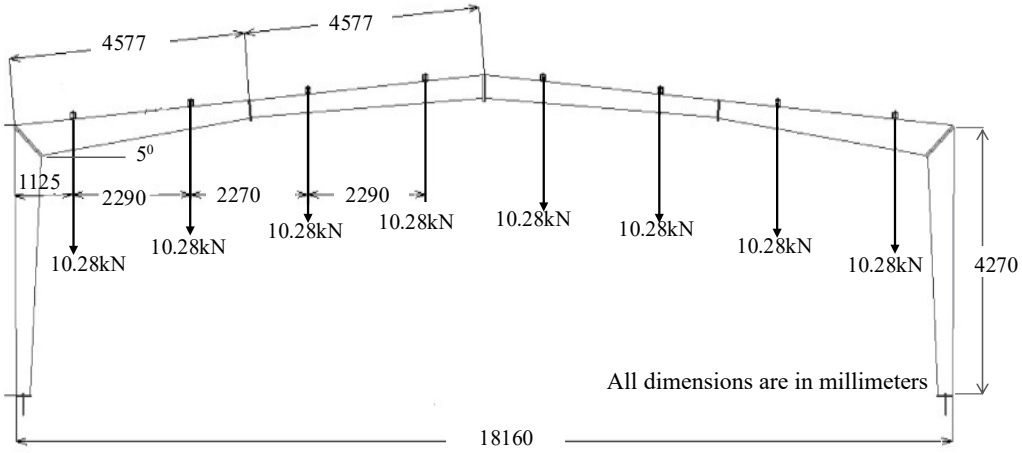

(b) Details of point loads applied to standard frame

Figure C- 1 Details of the general arrangement for the NTB portal frame with bolted-side plate joints

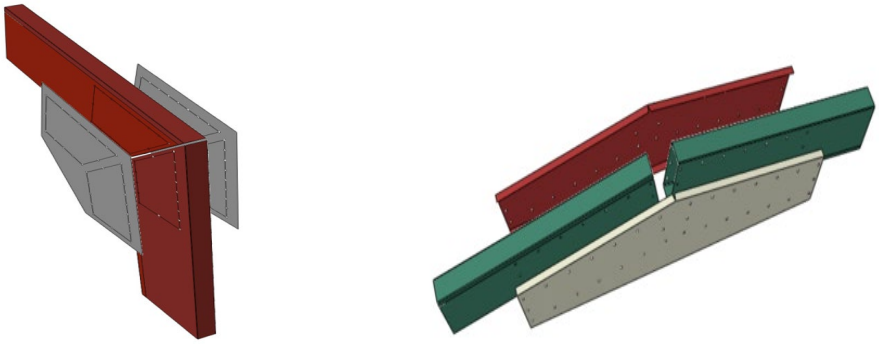

(a) Eaves joint (b) Apex joint

Figure C- 2 Joints of NTB portal frame

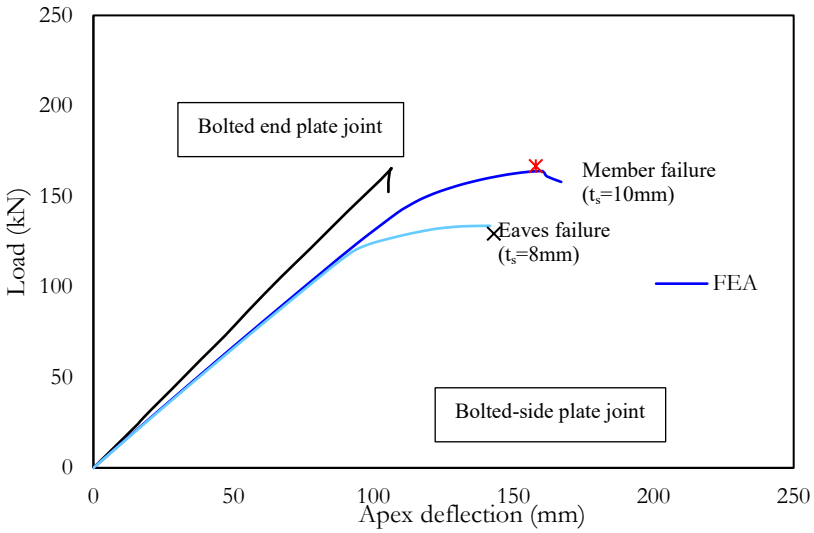

Figure C- 3 Load-displacement curve for the NTB portal frame from FEA

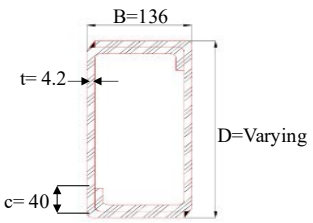

Joints	D (mm)
Column base	282
Eaves	513
Mid rafter	282
Apex	369

f_y = 258 N/mm^2; f_u = 386 N/mm^2; t= 4.2 mm

(a) Cross section details of back-to-back channel section

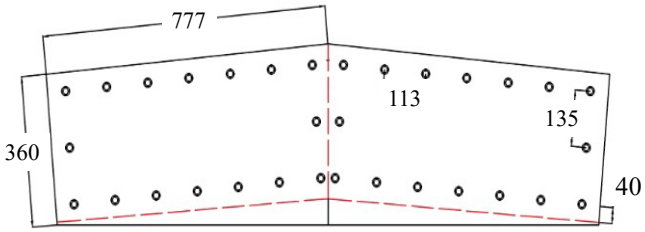

f_y = 350 N/mm^2; f_u = 425 N/mm^2 ; t_s= 8 mm

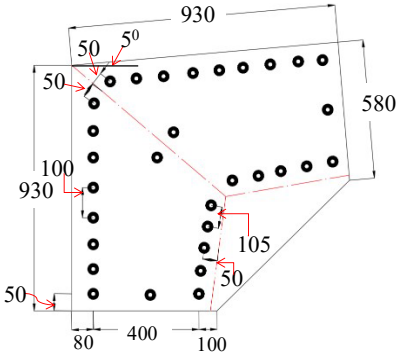

(c) Joints details

All dimensions are in millimeters

Figure C- 4 Dimensions of NTB section used for column and rafter members and details of bolted-side plate used at eaves and apex joint

C.2 Section strength using AS/NZ 4600 (2018)

In this section, the section strength under bending and compression has been determined using the DSM in accordance with AS/NZ 4600 (2018). Since the cross-section is tapered, calculation for the only eaves was carried out to demonstrate the design procedure. It should be noted that the effect of bimoment was not considered as the cross-section being a nested box section with rigid joints.

C.2.1 Elastic buckling analysis

The local and distortional buckling stress f_{ol}, f_{od} under bending and compression can be determined by implementing elastic buckling analysis. The buckling stress can be obtained via equations proposed by Shahmohammadi (2019). The equations are as follows:

$$\alpha_1 = \frac{(B-3t-2r)}{t}\sqrt{\frac{f_y}{250}} = \frac{(136-3\times4.2-2\times6)}{4.2}\sqrt{\frac{258}{250}} = 26.94$$

$$\alpha_2 = \frac{(D-3t-2r)}{t}\sqrt{\frac{f_y}{250}} = \frac{(513-3\times4.2-2\times6)}{4.2}\sqrt{\frac{258}{250}} = 118.13$$

For bending,

$$f_{ol} = \alpha_1 + \frac{5673175\alpha_2-\alpha_2 1.33^{\alpha_1}-6.06{\alpha_2}^3}{29490+880\alpha_2+{\alpha_2}^3+397{\alpha_2}^2-5906\alpha_1} = 26.94 + \frac{5673175-3\times118.13-118.13\times1.33^{26.94}-6.06\times118.13^3}{29490+880\times118.13+118.13^3+397\times118.13^2-5906\times26.94}$$

=372.23 N/mm^2

$$f_{od} = 3.54\alpha_2 + \frac{31533}{\alpha_1} + \frac{14896}{\alpha_2} - \frac{20.3{\alpha_2}^2}{{\alpha_1}^2} - 338 - 8.93{\alpha_1}^2$$

$$= 3.54\times118.13 + \frac{31533}{26.94} + \frac{14896}{118.13} - \frac{20.3\times118.13^2}{26.94^2} - 338 - 8.93\times26.94^2 = 769.96 \text{ N/mm}^2$$

For compression,

$$f_{ol} = \frac{1127777}{(18.7\alpha_2+9.05\alpha_1+\alpha_2^2)} = \frac{1127777}{(18.7\times118.13+9.05\times26.94+118.13^2)} = 68.74 \text{ N/mm}^2$$

$$f_{od} = 0.0441\alpha_1\alpha_2 - 6.83\alpha_1 + \frac{13196494\alpha_1}{(20424+{\alpha_2}^3+621{\alpha_1}^2-153\alpha_1\alpha_2)}$$

$$= 0.0441\times26.94\times118.13 - 6.83\times26.94 + \frac{13196494\times26.94}{(20424+118.13^3+621\times26.94^2-153\times26.94\times118.13)} = 174 \text{ N/mm}^2$$

C.2.2 Moment capacity

Yield moment capacity (M_y) for NTB section,

$M_y = Z_f f_y$ [Cl.7.2.2.2]

$= 992805 \times 277.28 = 2.75 \times 10^8$ Nmm

$M_o = \frac{0.36 c_b \pi}{l}\sqrt{EGJI_y} = \frac{0.36\times1.67\times\pi}{4270}\sqrt{(2\times10^5)\times80000\times(6.3\times10^7)\times25436757}$ [Cl. D.1]

$= 2.22 \times 10^9$ N.mm

$M_{oa} = \left[1 - 0.25 \times \left(1 - \frac{D_s}{D}\right)\right] \times M_o = \left[1 - 0.25 \times \left(1 - \frac{282}{513}\right)\right] \times 2.22 \times 10^9$ [AS/NZ 3404, Cl.5.6.1.1.1]

$= 1.97 \times 10^9$ N.mm >2.78M_y

The nominal moment capacity of the member (M_{be}) for lateral-torsional buckling is then determined via the following equations:

$M_{be} = M_y = 2.75 \times 10^8$ N.mm [Cl. 7.2.2.2(3)]

Non-dimensional slenderness ratio for local buckling

$\lambda_l = \sqrt{\frac{M_y}{M_{ol}}} = \sqrt{\frac{2.75\times10^8}{992805\times372.23}} = 0.863 > 0.776$ [Cl.7.2.2.3 (1) and Cl.7.2.2.3 (3)]

The nominal moment capacity of the member (M_l) for local buckling,

$M_l = \left[1 - 0.15\left(\frac{M_{ol}}{M_y}\right)^{0.4}\right]\left(\frac{M_{ol}}{M_y}\right)^{0.4} \times M_{be}$ [Cl.7.2.2.3 (2)]

$= \left[1 - 0.15\left(\frac{1}{0.863}\right)^{0.4}\right]\left(\frac{1}{0.863}\right)^{0.4} \times 2.75 \times 10^8 = 2.574 \times 10^8$ N.mm

Non-dimensional slenderness ratio for distortional buckling

$\lambda_d = \sqrt{\frac{M_y}{M_{od}}} = \sqrt{\frac{2.75\times10^8}{992805\times769.69}} = 0.60 < 0.673$ [Cl.7.2.2.4 (3)]

The nominal moment capacity of the member (M_d) for distortional buckling,

$M_d = M_{be} = 2.75 \times 10^8$ N.mm [Cl.7.2.2.4(1)]

Nominal moment capacity for NTB section = min (M_l, M_d, M_{be}) $= 2.574 \times 10^8$ N.mm =257.4 kNm

C.2.3 Axial capacity

Nominal yield capacity (P_y) for NTB section in compression,

$P_y = A_g f_y = 6536.85 \times 277.28 = 1.73 \times 10^6$ N [Cl. 7.2.1.2 (5)]

$\lambda_c = \sqrt{\frac{P_y}{P_{oc}}} = \sqrt{\frac{1.73\times10^6}{2.72\times10^6}} = 0.799 < 1.5$ [Cl. 7.2.1.2 (3)]

$P_{oc} = A_g f_{oc} = 6536.85 \times 415.42 = 2.72 \times 10^6$N [Cl. 7.2.1.2 (4)]

$f_{oc} = \min(f_{ox}, f_{oy}, f_{oz}) = 415.42$ N/mm^2

$f_{ox} = \frac{\pi^2 E}{(l_{ex}/r_x^2)} = \frac{\pi^2\times2\times10^5}{(4270/197^2)} = 4158.85$ N/mm^2

$f_{oy} = \frac{\pi^2 E}{(l_{ey}/r_y^2)} = \frac{\pi^2\times2\times10^5}{(4270/62^2)} = 415.42$ N/mm^2

$f_{oz} = \frac{GJ}{A_g r_{o1}^2}\left(1 + \frac{\pi^2 EI_W}{GJl_{ez}^2}\right) = \frac{80000\times6.37\times10^7}{6536.85\times207^2}\left(1 + \frac{\pi^2\times2\times10^5\times1.52\times10^{14}}{80000\times6.37\times10^7\times4300^2}\right) = 76271.88$ N/mm^2

$r_{o1} = \sqrt{r_x^2 + r_y^2} = \sqrt{197^2 + 62^2}$= 207.0 mm

The nominal capacity of the member (P_{ce}) in compression for flexural, torsional or flexural-torsional buckling is determined by using equations:

$P_{ce} = \left(0.658^{\lambda_c{}^2}\right)P_y = \left(0.658^{0.799^2}\right) \times 1.73 \times 10^6 = 1.32 \times 10^6$ N [Cl. 7.2.1.2 (1)]

Non-dimensional slenderness ratio for local buckling

$\lambda_l = \sqrt{\frac{P_y}{P_{ol}}} = \sqrt{\frac{1.73\times10^6}{4.93\times10^5}} = 1.718 > 0.776$ [Cl. 7.2.1.3 (1)]

$P_{ol} = A_g f_{ol} = 6536.85 \times 68.74 = 4.93 \times 10^5$ N [Cl. 7.2.1.3 (4)]

Axial Local buckling capacity of NTB section

$$P_l = \left[1 - 0.15\left(\frac{P_{ol}}{P_{ce}}\right)^{0.4}\right]\left(\frac{P_{ol}}{P_{ce}}\right)^{0.4} \times P_{ce}$$

$$= \left[1 - 0.15\left(\frac{4.93\times10^5}{1.32\times10^6}\right)^{0.4}\right]\left(\frac{4.93\times10^5}{1.32\times10^6}\right)^{0.4} \times 1.32 \times 10^6$$

$= 7.764\times 10^5$ N [Cl. 7.2.1.3 (2)]

Non-dimensional slenderness ratio for distortional buckling

$\lambda_d = \sqrt{\frac{P_y}{P_{od}}} = \sqrt{\frac{1.73\times10^6}{1.136\times10^6}} = 1.235 > 0.776$ [Cl. 7.2.1.4 (3)]

$P_{od} = A_g f_{od} = 6536.85 \times 174 = 1.136 \times 10^6$ N

The nominal axial capacity of the member (P_d) for distortional buckling,

$$P_d = \left[1 - 0.25\left(\frac{P_{od}}{P_y}\right)^{0.6}\right]\left(\frac{P_{od}}{P_y}\right)^{0.6} \times P_y$$ [Cl. 7.2.1.4 (2)]

$$= \left[1 - 0.25\left(\frac{1.136\times10^6}{1.72\times10^6}\right)^{0.6}\right]\left(\frac{1.136\times10^6}{1.72\times10^6}\right)^{0.6} \times 1.72 \times 10^6$$

$= 1.15 \times 10^6$ N

Nominal axial capacity for NTB section = min (P_l, P_d, P_{ce}) =7.764×10^5 N= 776.4 kN

C.2.4 Shear capacity

Yield capacity in shear,

$V_y = 0.6A_w f_y = 0.6\times 2 \times 513 \times 4.2 \times 258 = 6.67 \times 10^5$ N [Cl. 7.2.3(5)]

Critical buckling capacity in shear

$V_{cr} = \frac{\pi^2 E A_W K_v}{12(1-\mu^2)(D/t)^2} = \frac{\pi^2\times2\times10^5\times2\times513\times4.2\times5.34}{12(1-0.3^2)(513/4.2)^2} = 1.41\times 10^5$ N [Cl. D3(1)]

Non-dimensional slenderness ratio for shear

$\lambda_v = \sqrt{\frac{V_y}{V_{cr}}} = \sqrt{\frac{6.67\times10^5}{1.41\times10^5}} = 2.175 > 1.227$ [Cl. 7.2.3(4)]

Nominal shear capacity of the section (V_v) is determined by the equations below:

$V_v = V_{cr} = 1.41 \times 10^5$ N =141 kN [Cl. 7.2.3(3)]

C.3 Bolted-side plates strength

The strength of the eaves and apex brackets can be as follows:

Bolted-side plate at apex joint (Paul et al. 2023)

$$M_{ba}^{s} = 0.001 \times a_s^{0.006} \times b_s^{1.793} \times f_y \times (\sin\theta)^{0.093} \times t_s^{1.201} \quad \text{Eq. c1}$$

For one bolted-side plate

$$M_{ba}^{s} = 0.001 \times 780^{0.006} \times 350^{1.793} \times 0.35 \times (\sin 5^0)^{0.093} \times 8^{1.201}$$

=135.23 kNm

For two bolted-side plate

$M_{2ba}^{s} = 2 \times 135.23 = 270.46$ kNm

Bolted-side plate at eaves joint (Eq.5.2)

$$M_{be}^{s} = 2.77 \times a_k^{0.47} \times b_k^{4.80} \times f_y \times (\cos\theta)^{1.70} \times t_s^{0.761} \times 10^{-13} \quad \text{Eq. c2}$$

$$= 2.77 \times 350^{0.47} \times 580^{4.80} \times 0.35 \times (\cos 5^0)^{1.70} \times 8^{0.761} \times 10^{-13}$$

=135.49 kNm

For two bolted-side plate

$M_{2be}^{s} = 2 \times 135.23 = 270.98$ kNm

It is important to note that the above equations are valid when the bolted-side plates are subjected to pure bending. However, in the NTB portal frames, the bolted-side plates experience a combination of bending, shear, and axial forces. Consequently, the moment capacities of the bolt groups at both the eaves and apex joints (as shown in Figure C-4b) are determined using the FE model of the NTB portal frame. The calculated moment capacities for the eaves and apex joints are 160.2 kNm and 157.8 kNm, respectively.

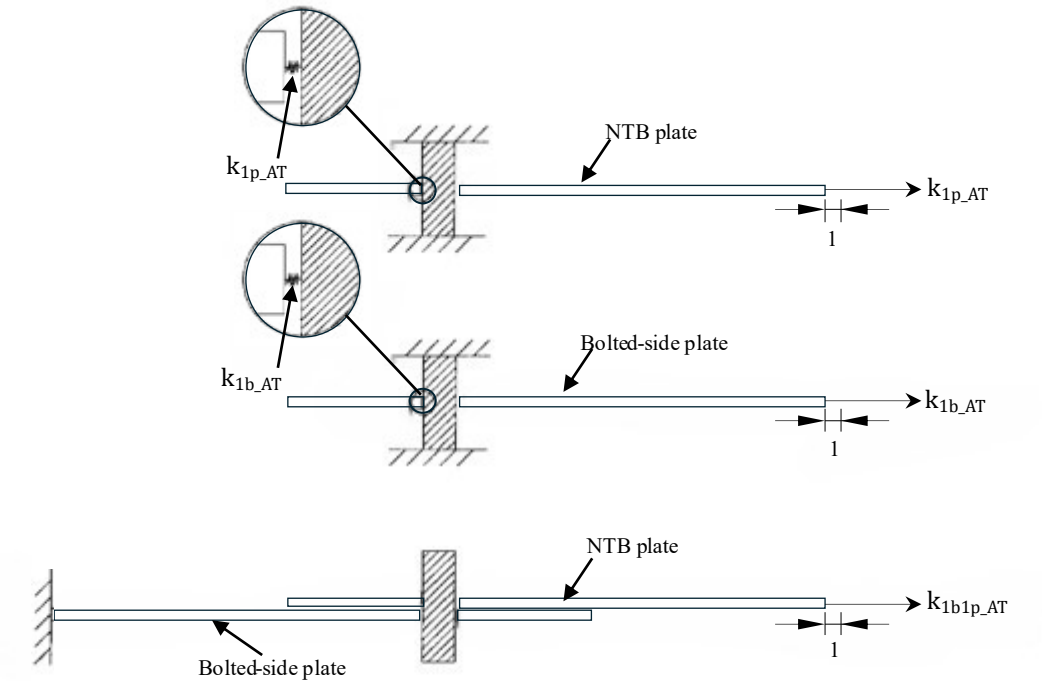

Figure C- 5 Diagram showing bolt-hole elongation stiffness as the force required to cause a unit displacement for a system of plates

C.3 Bolt-hole elongation stiffness

Figure C-5 defines the bolt-hole elongation stiffness for two plates representing the channel-section and bracket. The bolt-hole elongation can be calculated from (in series):

$$k_{1b1p\_AT} = \frac{1}{\frac{1}{k_b}+\frac{1}{k_{1c\_AT}}} \qquad \text{Eq.c3}$$

From Ahmed and Teh (2019):

Bolt hole elongation stiffness for the NTB plate,

$$k_b = 0.015\, t_b \left(\frac{d_{minor_{M16}}}{d_{minor_{M20}}}\right)^{0.3} f_u = 0.015 \times 4.2 \times \left(\frac{13.4}{16.54}\right)^{0.3} \times 425 = 22.83\,\text{kN/mm} \quad \text{[See Figure C-6]}$$

Bolt hole elongation stiffness for the bolted-side plate,

$$k_p = 0.015\, t_s \left(\frac{d_{minor_{M16}}}{d_{minor_{M20}}}\right)^{0.3} f_u = 0.015 \times 8 \times \left(\frac{13.4}{16.54}\right)^{0.3} \times 386 = 47.88\,\text{kN/mm} \quad \text{[See Figure C-6]}$$

$$k_p = 0.015\, t_s \left(\frac{d_{minor_{M16}}}{d_{minor_{M20}}}\right)^{0.3} f_u = 0.015 \times 10 \times \left(\frac{13.4}{16.54}\right)^{0.3} \times 386 = 59.84\,\text{kN/mm} \quad \text{[See Figure C-6]}$$

Thus,

$$k_{1b1p\_AT} = \frac{1}{\frac{1}{k_{1b}}+\frac{1}{k_{1p}}} = \frac{1}{\frac{1}{22.83}+\frac{1}{47.88}} = 15.5\,\text{kN/mm}$$ (16.53 kN/mm)

Bolt-hole stiffness for each plate

$k_{2b2p} = 2 \times k_{1b1p\_AT} = 2 \times 15.5 = 31.0\,\text{kN/mm}$ (33.05 kN/mm)

C.4 Rotational stiffness of the joints

Rotational stiffness can be determined from Lim and Nethercot (2004) as follows:

$$K = \sum r_i^2 \times k_{1b1p\_AT} \qquad \text{Eq. c4}$$

Apex joint

$K_a = (0.365^2 + 0.263^2 + 0.176^2 + 0.135^2 + 0.176^2 + 0.263^2 + 0.365^2 + 0.339^2 + 0.365^2 + 0.339^2 + 0.263^2 + 0.176^2 + 0.135^2 + 0.176^2 + 0.263^2 + 0.365^2 + 0.339^2) \times 31.0 \times 1000 = 37201.74\,\text{kNm/rad}$

Eaves joint

$K_e = (0.504^2 + 0.411^2 + 0.323^2 + 0.244^2 + 0.186^2 + 0.173^2 + 0.212^2 + 0.283^2 + 0.368^2 + 0.326^2 + 0.326^2 + 0.290^2 + 0.231^2 + 0.215^2 + 0.253^2 + 0.295^2) \times 31 \times 1000 = 45230.74\,\text{kNm/rad}$

(33.05 kN/m) (48223.94 kNm/rad)

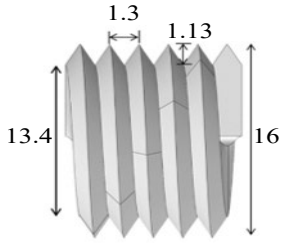

Figure C- 6 Fully threaded M16 bolt

C.5 Beam idealization

Figure C-7 shows beam idealisations for NTB portal frames with bolted-side plate joints. As can be seen, rotational spring elements are modelled at the centre of rotation of each bolt-group. The bolted-side plates can be assumed to function as rigid. Figure C-8 shows the bending moment for unit applied load.

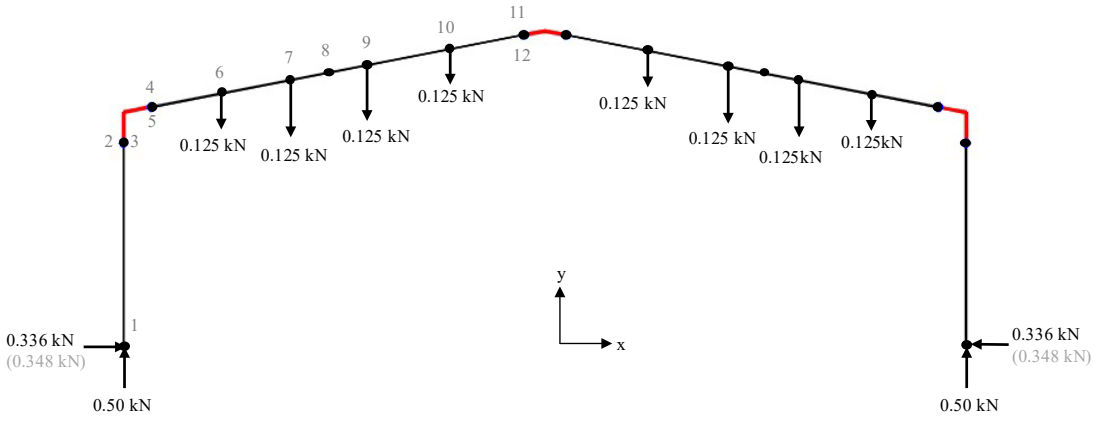

Nodes	Coordinates (m)		
n	x	y	z
1	-9.08	0.00	0.00
2	-9.08	3.93	0.00
3	-9.08	3.93	0.00
4	-8.75	4.30	0.00
5	-8.75	4.30	0.00
6	-7.96	4.97	0.00
7	-5.67	4.77	0.00
8	-4.54	4.67	0.00
9	-3.40	4.57	0.00
10	-1.11	4.37	0.00
11	-0.39	5.03	0.00
12	-0.39	5.03	0.00
-	-	-	-

Element	Node connectivity
1	1-2[1]
2	2- 3[3]
3	2-4[2]
4	4-5[3]
6	6-7[1]
7	7-8[1]
8	8-9[1]
9	9-10[1]
10	10-11[2]
11	11-12[4]

Note:
1. NTB section, EI = varying, EA= Varying
2. Bolted-side plate, EI =∞ ; EA =∞
3. Rotation spring stiffness, K_e = 45230.74/ 48223.94kNm / rad
4. Rotation spring stiffness, K_a = 37201.74kNm / rad

Figure C- 7 Beam model for the NTB portal frame with bolted-side plate joints

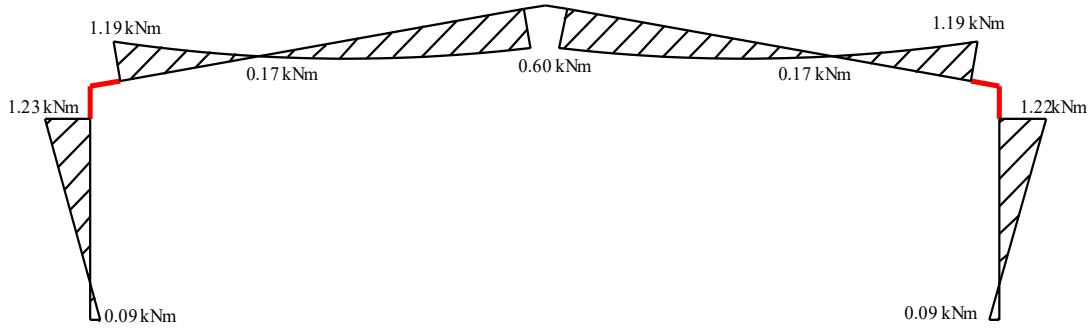

Figure C- 8 Bending moment diagram from beam model NTB portal frame bolted-side plate joints (unit load)

C.6 Prediction of the ultimate load capacity

In this section, the prediction of ultimate failure load for the eaves and NTB member has been discussed. The predicted ultimate loads are based on the section strength and the strength of bolted-side plate, determined either from the FE model or equations. As shown in Figure C-3, the load carrying capacity of NTB portal frame with bolted end plate joints were compared with the bolted-side plates joints.

C.6.1 Bolted-side plate failure

When the thickness of the bolted-side plates at both eaves and apex joints is 8mm, failure of the NTB portal frame was due to the failure of the bolted-side plate at eaves, at 133.5 kN, which is 17% less than the load carrying capacity NTB portal frame with bolted end plate joints. Similarly, a prediction of the failure load can also be made using the beam model (see Figure C-7) if the strength of the bolted-side plate is known from the FE model. From the FE models, the strength of the bolted-side plate was determined to be 160.2 kNm for the eaves joint. The corresponding failure loads for NTB portal frame with bolted-side plates were at 134.62 kN.

C.6.2 Member failure

From Figure C-3, it can be also seen that increasing the thickness of bolted-side plates from 8mm to 10mm at eaves joints, NTB portal frame failed at 163.98 kN due to the failure of NTB member near eaves, which is close to the NTB portal frame with bolted end plate. A similar prediction could also be made from the beam model, which shows a failure load of 167.8 kN at the center of rotation. This corresponds to a bending moment of 200.0 kNm, combined with an axial force of 83.9 kN and a shear force of 56.4 kN.

C.7 Detailed calculations:

Description	Parameter	Column base	Column eaves	Rafter eaves	Rafter mid	Rafter apex
Actual section thickness (mm)	**t**	4.2	4.2	4.2	4.2	4.2
Section width (mm)	**B**	136	136	136	136	136
Depth (mm)	**D**	282	495	483	282	362
Member length about x axis in bending (mm)	**L major-M**	4270	4270	9100	9100	9100
Member length about y axis in bending (mm)	**L minor-M**	4270	4270	9100	9100	9100
Member length about x axis in compression (mm)	**L major-P**	4270	4270	9100	9100	9100
Member length about y axis in compression (mm)	**L minor-P**	4270	4270	9100	9100	9100
Yield stress (MPa)	f_y	258.0	258	258	258	258
Tensile stress (MPa)	f_u	386.0	386	386	386	386
Depth at the other end	D_{end}	513.0	282.0	282.0	513.0	282.0
Design bending moment (kN.m)	**M***	15.4	206.6	200.0	27.8	99.2
Design axial force (kN)	**P***	83.9	81.5	63.3	59.7	56.2
Design shear force (kN)	**V***	56.4	56.4	75.8	35.4	4.7
Average yield stress (MPa) in compression	$f_{ya\text{-}comp}$	268.1	265.1	265.1	268.1	266.7
Average yield stress (MPa) in flexural	$f_{ya\text{-}flex}$	277.3	277.3	277.3	277.3	277.3
Area of the bend to the area of the full section	C_{comp}	0.1	0.0	0.0	0.1	0.0
Area of the bend to the area of the flange	C_{flex}	0.1	0.1	0.1	0.1	0.1
Bent yield stress (MPa)	f_{yc}	452.7	452.7	452.7	452.7	452.7
constant	B_c	1.9	1.9	1.9	1.9	1.9
constant	**m**	0.2	0.2	0.2	0.2	0.2
Shallower end to deeper end depth ratio for tapered members	D_s/D	0.55	0.57	0.58	0.55	0.77
Radius	**r**	6.0	6.0	6.0	6.0	6.0
Lip	**c**	40.0	40.0	40.0	40.0	40.0
Moment of inertia about x (mm^4)	I_x	6.28E+07	2.34E+08	2.20E+08	6.28E+07	1.12E+08
Moment of inertia about y (mm^4)	I_y	1.58E+07	2.47E+07	2.42E+07	1.58E+07	1.92E+07
Elastic section modulus	Z_f	4.45E+05	9.44E+05	9.12E+05	4.45E+05	6.16E+05
Section area (mm^2)	A_g	4.60E+03	6.39E+03	6.28E+03	4.60E+03	5.27E+03
Torsion constant (mm^4)	**J**	2.96E+07	6.03E+07	5.86E+07	2.96E+07	4.09E+07
Warping constant (mm^6)	I_w	1.53E+14	1.53E+14	1.53E+14	1.53E+14	1.53E+14
Radius of gyration about the x axes (mm)	r_x	1.17E+02	1.91E+02	1.87E+02	1.17E+02	1.45E+02

Description	Parameter	Column base	Column eaves	Rafter eaves	Rafter mid	Rafter apex
Radius of gyration about the y axes (mm)	r_y	5.9E+01	6.2E+01	6.2E+01	5.8E+01	6.0E+01
Young's modulus of elasticity (MPa)	E	2.07E+05	2.00E+05	2.00E+05	2.00E+05	2.00E+05
Shear modulus of elasticity (MPa)	G	8.27E+04	8.00E+04	8.00E+04	8.00E+04	8.00E+04
Coefficient depending on moment distribution	c_b	1.67	1.67	1.67	1.67	1.67
Polar radius of gyration (mm)	r_{o1}	130.8	207.0	207.0	130.8	159.8
Strength reduction factor for moment and shear	$ø_b$, $ø_v$	1.0	1.0	1.0	1.0	1.0
Strength reduction factor for moment and axial	$ø_c$	1.0	1.0	1.0	1.0	1.0
Elastic lateral-torsional buckling moment (N.mm)	M_o	1.25E+09	2.16E+09	9.88E+08	5.68E+08	7.35E+08
Reduction factor applied to Mo for tapered members (NZS3404, cl-5.6.1.1.1)	a_s	0.89	0.89	0.90	0.89	0.94
Reduced elastic lateral-torsional buckling moment because of being tapered (N.mm)	m_{oa}	1.1E+09	1.9E+09	8.8E+08	5.0E+08	6.9E+08
Flange slenderness	λ_{ef}	26.9	26.9	26.9	26.9	26.9
Web slenderness	λ_{ew}	62.3	113.8	110.9	62.3	81.6
Elastic local buckling stress under bending moment (MPa)	f_{ol}	800.2	394.4	410.1	800.2	620.7
Elastic distortional buckling stress under bending moment (MPa)	f_{od}	943.7	764.2	775.6	943.7	877.7
Elastic local buckling stress including depth and moment variation and contact between flanges effects (MPa)	$f_{ol,mod}$	800.2	394.4	410.1	800.2	620.7
Elastic distortional buckling stress including depth and moment variation and contact between flanges effects (MPa)	$f_{od,mod}$	972.1	787.1	798.9	972.1	904.0
Elastic local buckling moment (N.mm)	M_{ol}	3.56E+08	3.72E+08	3.74E+08	3.56E+08	3.82E+08
Elastic distortional buckling moment (N.mm)	M_{od}	4.33E+08	7.43E+08	7.29E+08	4.33E+08	5.57E+08
Local buckling non-dimensional slenderness	λ_l	0.59	0.82	0.81	0.59	0.66
Distortional buckling slenderness	λ_d	0.53	0.58	0.58	0.53	0.54
Yield moment (N.mm)	M_y	1.2E+08	2.5E+08	2.4E+08	1.2E+08	1.7E+08
Nominal member moment capacity for lateral-torsional buckling (N.mm)	M_{be}	1.2E+08	2.5E+08	2.4E+08	1.2E+08	1.7E+08
Nominal member moment capacity for local buckling (N.mm)	M_l	1.2E+08	2.4E+08	2.4E+08	1.2E+08	1.7E+08
Nominal member moment capacity for distortional buckling (N.mm)	M_d	1.2E+08	2.5E+08	2.4E+08	1.2E+08	1.7E+08
Moment capacity (N.mm)	M	1.2E+08	2.4E+08	2.4E+08	1.2E+08	1.7E+08
Section moment capacity equal to M_{bl} (N.mm)	M_s	1.2E+08	2.4E+08	2.4E+08	1.2E+08	1.7E+08
Nominal capacity of the member in compression for flexural buckling (N)	P_{ce}	9.2E+05	1.29E+06	5.1E+05	3.3E+05	4.01E+05

Description	Parameter	Column base	Column eaves	Rafter eaves	Rafter mid	Rafter apex
Euler axial force (N)	P_{ex}	7.0E+06	2.5E+07	5.3E+06	1.5E+06	2.7E+06
Section capacity of member in compression equal to N_{cl}	P_s	9.7E+05	9.2E+05	9.1E+05	1.2E+06	1.4E+06
Non-dimensional slenderness for N_{ce}	λ_c	0.83	0.79	1.68	1.81	1.74
Nominal yield capacity of the member in compression (N)	P_y	1.2E+06	1.7E+06	1.6E+06	1.3E+06	1.4E+06
Least of the elastic compression member buckling load in flexural, torsional and flexural-torsional buckling (N)	P_{oc}	1.8E+06	2.7E+06	5.7E+05	3.8E+05	4.6E+05
Elastic buckling stress in an axially loaded compression member for flexural buckling about the y-axis (MPa)	f_{oy}	385.5	418.6	91.7	82.1	86.7
Elastic buckling stress in an axially loaded compression member for flexural buckling about the x-axis (MPa)	f_{ox}	1527.6	3961.9	835.7	325.4	504.5
Elastic buckling stress in an axially loaded compression member for torsional buckling (MPa)	f_{oz}	248770.5	82745.6	34062.3	76461.1	52919.9
Elastic flexural, torsional and flexural-torsional buckling stress (MPa)	f_{oc}	385.5	418.6	91.7	82.1	86.7
Elastic local buckling stress under compression (MPa)	f_{ol}	213.5	73.6	77.2	213.5	133.8
Elastic distortional buckling load under compression (MPa)	f_{od}	669.7	191.9	205.6	669.7	436.9
Elastic local buckling load under compression (N)	P_{ol}	9.8E+05	4.7E+05	4.8E+05	9.8E+05	7.1E+05
Elastic distortional buckling compression load (N)	P_{od}	3.1E+06	1.2E+06	1.3E+06	3.1E+06	2.3E+06
Non-dimensional slenderness for local buckling under compression	λ_l	0.97	1.65	1.02	0.58	0.75
Non-dimensional slenderness for distortional buckling under compression	λ_d	0.63	1.17	1.12	0.63	0.77
Nominal member capacity for elastic buckling (N)	P_l	8.0E+05	7.7E+05	4.2E+05	3.3E+05	4.1E+05
Nominal member capacity for distortional buckling (N)	P_d	1.14E+06	1.15E+06	1.14E+06	1.14E+06	1.17E+06
Axial compression capacity (N)	P	7.99E+05	7.73E+05	4.24E+05	3.31E+05	4.01E+05
Nominal shear capacity (N)	V_v	2.54E+05	1.46E+05	1.50E+05	2.50E+05	2.00E+05
Non-dimensional slenderness under shear	λ_V	1.18E+00	2.10E+00	2.05E+00	1.20E+00	1.54E+00
Elastic shear buckling force (N)	V_{cr}	2.65E+05	1.46E+05	1.50E+05	2.56E+05	2.00E+05
Yield shear force of the section (N)	V_y	3.67E+05	6.44E+05	6.28E+05	3.67E+05	4.71E+05
Shear capacity (N)	V	2.54E+05	1.46E+05	1.50E+05	2.50E+05	2.00E+05
Moment amplification factors due to the axial load	α_n	0.99	1.00	0.99	0.96	0.98

THE UNIVERSITY OF
WAIKATO
Te Whare Wānanga o Waikato

Project no: 3/2022
Project Name: Design of nested tapered box section portal frame with bolted-side plate joints
Date:21/6/24 Rev:
Designer: Bikram Paul Checked by: Prof. James Lim Date:

Description	Parameter	Column base	Column eaves	Rafter eaves	Rafter mid	Rafter apex
Moment D/C ratio	**M check**	0.12	0.85	0.84	0.23	0.60
Axial D/C ratio	**P check**	0.07	0.11	0.15	0.18	0.14
Shear D/C ratio	**V check**	0.22	0.39	0.51	0.14	0.02
$\frac{P^*}{P}+\frac{\mathbf{M}^*}{M}<1$	**M-P**	0.18	0.94	0.91	0.27	0.64
$\frac{P^*}{P}+\frac{C_m\mathbf{M}^*}{\alpha_n M}<1$	**M-P**	0.20	0.96	**1.00**	0.42	0.76
$\left(\frac{\mathbf{M}^*}{M}\right)^2+\left(\frac{\mathrm{V}^*}{\mathrm{V}}\right)^2<1$	**M-V**	0.06	0.87	0.96	0.07	0.36
$0.46\frac{\mathbf{M}^*}{M}+\frac{\mathrm{V}^*}{1.3\mathrm{V}}<1$	**M-V**	0.23	0.69	0.78	0.21	0.30

Above design calculation is for the applied load of 167.8 kN on the NTB Portal frame. Bending moment, shear force and axial force used in this calculation can be used found from the Figure C-6 and C-7, respectively. As can be seen form Figure C-3, failure load is close to the FEA which is occuurred at rafter near the eaves joints.

References

ABAQUS. (2021). ABAQUS/CAE User's Guide v6.21.

AISI S-16 (2016). North American Specification for the Design of Cold-Formed Steel Structural Members. American Iron and Steel Institute.

Arrayago, I., González-de-León, I., Real, E., & Mirambell, E. (2020a). Tests on stainless steel frames. Part I: Preliminary tests and experimental set-up. *Thin-Walled Structures*, 157. https://doi.org/10.1016/j.tws.2020.107005

Arrayago, I., González-de-León, I., Real, E., & Mirambell, E. (2020b). Tests on stainless steel frames. Part II: Results and analysis. *Thin-Walled Structures*, 157. https://doi.org/10.1016/j.tws.2020.107006

AS/NZ 4600 (2018). Cold-Formed Steel Structures, AS/NZ 4600. Standards Australia/Standards New Zealand.

AS/NZ 3404: Part 1 and Part 2 (1997). Cold-Formed Steel Structures. Standards Australia/Standards New Zealand.

AS/NZ 1170: Part 1(2002), Structural design actions—Part 1: Permanent, imposed and other actions, Australian/New Zealand Standard

Ahmed, A., & Teh, L. H. (2019). Thread effects on the stiffness of bolted shear connections. *Journal of Constructional Steel Research*, 160, 77-88.

Blum, H. B., Li, Z. (2019). Stability of apex connections in cold-formed steel portal frames. *Structural Stability Research Council Annual Stability Conference*.

Blum, H. B., Rasmussen, K. J. R. (2019a). Experimental investigation of long-span cold-formed steel double channel portal frames. *Journal of Constructional Steel Research*, 155, 316-330.

Blum, H. B., Rasmussen, K. J. R. (2019b). Experimental and numerical study of connection effects in long-span cold-formed steel double channel portal frames. *Journal of Constructional Steel Research*, 155, 480-491.

BS 5950 (1998): Structural use of steelworks in building. Part 5. Code of practice for design of cold-formed thin gauge sections, British Standards.

Chen, X., Blum, H. B., Roy, K., Pouladi, P., Uzzaman, A., & Lim, J. B. (2021). Cold-formed steel portal frame moment-resisting joints: Behaviour, capacity and design. *Journal of Constructional Steel Research*, 183, 106718.

Chen, X., Boston, M., Bell, D., Mares, J., Roy, K., & Lim, J. B. (2023a). Moment capacity of apex brackets of cold-formed steel portal frames. *Thin-Walled Structures*, 185, 110574.

Chen, X., Boston, M., Bell, D., Roy, K., Mares, J., & Lim, J. B. (2023b). Moment capacity of eaves brackets of cold-formed steel portal frames. *Thin-Walled Structures*, 189, 110947.

Chung, K. F., and Lau, L. (1999). Experimental investigation on bolted moment connections among cold formed steel members. *Engineering Structures*, *21*(10), 898-911.

Donovan Group Ltd. Takapuna, Auckland,0622.

Dowling, P. J., TF, M., GW, O., & GK, R. (1982). A development in the automated design and fabrication of portal framed industrial buildings.

Dubina, D., Stratan, A., Ciutina, A., Nagy, Z. (2006). Performance of ridge and eaves joints in cold-formed steel portal frames. *International Specialty Conference on Cold-Formed Steel Structures*.

Dubina, D. (2008). Structural analysis and design assisted by testing of cold-formed steel structures. *Thin-Walled Structures*, 46(7-9), 741-764.

Dubina, D., Ungureanu, V., Nagy, Z., Nunes, L., Pernes, P. (2010). Imperfections sensitivity analysis of pitched roof cold–formed steel portal frames. *SDSS'rio*, 8, 929-936.

EN1993-1-1. (2005). Eurocode 3: Design of steel structures. In Part 1-1: General rules and rules for buildings. Brussels: European Committee for Standardization.

EN 1993-1-4(2006). European Committee for Standardization. Eurocode 3. Design of Steel Structures. Part 1–4: General Rules. Supplementary Rules for Stainless Steels, 2015. Brussels, Belgium.

Gardner, L., Yun, X., Fieber, A., Macorini, L. (2019). Steel design by advanced analysis: material modeling and strain limits. *Engineering*, 5(2), 243-249.

Hancock, G. J., Murray, T., & Ellifrit, D. S. (2001). Cold-formed steel structures to the AISI specification. CRC Press.

Hayalioglu, M. S., & Degertekin, S. O. (2005). Minimum cost design of steel frames with semi-rigid connections and column bases via genetic optimization. *Computers & Structures*, 83(21-22), 1849-1863.

Hwang, J. S., Chang, K. C., & Lee, G. C. (1991). Seismic behaviour of gable frame consisting of tapered members. *Journal of Structural Engineering, 117(3),* 808-821.

Jackson, C., Wrzesien, A., Johnston, R. P., Uzzaman, A., Lim, J. (2012). Effect of reduced joint strength and semi-rigid joints on cold-formed steel portal frames. *In 6th International Conference on Coupled Instabilities in Metal Structures*, CIMS 2012.

Junid, S. M. B. S. (1992). Lateral-torsional buckling of haunched members in portal frames: An assessment of BS 5950; part 1 [Doctoral dissertation], University of Salford, UK.

Jůza, J., and Jandera, M. (2022). Stainless Steel Portal Frame Tests. *ce/papers*, *5*(4), 500-505.

Kirk. P. (1986) "Design of a Cold Formed Section Portal Frame Building System," [Online]. Available: https://scholarsmine.mst.edu/isccss/8iccfss/8iccfss-session4/1

Kwon, Y. B., Chung, H. S., & Kim, G. D. (2006). Experiments of cold-formed steel connections and portal frames. Journal of structural engineering, 132(4), 600-607.

Lacey, A. W., Chen, W., Hao, H., Bi, K., & Tallowin, F. J. (2019). Shear behaviour of post-tensioned inter-module connection for modular steel buildings. *Journal of Constructional Steel Research*, 162, 105707.

Lim, J. B. (2001). Joint effects in cold-formed steel portal frames (Doctoral dissertation, University of Nottingham).

Lim, J. B., and Nethercot, D. A. (2002a). Design and development of a general cold-formed steel portal framing system. *Structural Engineer*, 80(21), 31-39.

Lim, J. B., and Nethercot, D. A. (2002b). F. E.-Assisted design of the eaves bracket of a cold-formed steel portal frame. *Steel and Composite Structures*, 2(6), 411-428.

Lim, J. B., and Nethercot, D. A. (2003). Ultimate strength of bolted moment-connections between cold-formed steel members. *Thin-Walled Structures*, 41(11), 1019-1039.

Lim, J. B., and Nethercot, D. A. (2004). Finite element idealization of a cold-formed steel portal frame. *Journal of Structural Engineering*, 130(1), 78-94.

Lim, J. B., and Young, B. (2007). Effects of elevated temperatures on bolted moment-connections between cold-formed steel members. *Engineering Structures*, 29(10), 2419-2427.

Li, J. J., & Li, G. Q. (2002). Large-scale testing of steel portal frames comprising tapered beams and columns. *Advances in Structural Engineering*, *5*(4), 259-269.

Lukačević, I., Ungureanu, V., Valčić, A., & Ćurković, I. (2021). Numerical study on bending resistance of cold-formed steel back-to-back built-up elements. *ce/papers*, 4(2-4), 487-494.

McCrum, D. P., Simon, J., Grimes, M., Broderick, B. M., Lim, J. B., & Wrzesien, A. M. (2019). Experimental cyclic performance of cold-formed steel bolted moment resisting frames. *Engineering Structures*, *181*, 1-14.

McCrum, D. P., Wrzesien, A. M., Simon, J., Grimes, M., Broderick, B., & Lim, J. B. (2021). Cyclic Performance of Cold-formed Steel Moment Resisting Frames. *ce/papers*, *4*(2-4), 1837-1843.

Meck, H. R. (1977). Experimental evaluation of lateral buckling loads. *Journal of the Engineering Mechanics Division*, 103(2), 331–337.

Mojtabaei, S. M., Kabir, M. Z., Hajirasouliha, I., Kargar, M. (2018). Analytical and experimental study on the seismic performance of cold-formed steel frames. *Journal of Constructional Steel Research*, *143*, 18-31.

Mojtabaei, S. M., Becque, J., Hajirasouliha, I. (2020). Local buckling in cold-formed steel moment-resisting bolted connections: behavior, capacity and design. *Journal of Structural Engineering,* 146(9), 04020167.

Mojtabaei, S. M., Becque, J., Hajirasouliha, I. (2021). Behavior and Design of Cold-Formed Steel Bolted Connections Subjected to Combined Actions. *Journal of Structural Engineering*, 147(4), p.04021013.

Msabawy, A., & Mohammad, F. (2019). Practical analysis procedures of steel portal frames having different connections rigidities using modified stiffness matrix and end-fixity factor concept In IOP Conference Series: Materials Science and Engineering.

New Zealand Steel Ltd., Glenbrook 2681, New Zealand.

Nguyen, H. C., Pham, C. H., & Rasmussen, K. J. (2024) Experimental investigation of long-span cold-rolled aluminium built-up section portal frames: Unbraced columns and flexural-torsional buckling. *Engineering Structures*, 306, 117778.

Öztürk, F., and Pul, S. (2015). Experimental and numerical study on a full scale apex connection of cold-formed steel portal frames. *Thin-Walled Structures*, 94, 79-88.

Paul, B., Roy, K., Lim, J. B., Fang, Z., McCollum, K., & Bell, D. (2023). Moment-capacity of bolted side-plates for apex joint of nested tapered box beam portal frames. *Journal of Building Engineering*, 107011.

Peng, J., Bendit, J., & Blum, H. B. (2018). Experimental study of apex connection stiffness and strength of cold-formed steel double channel portal frames CCFSS *Proceedings of International Specialty Conference on Cold-Formed Steel Structures*.

Phan, D. T., Mojtabaei, S. M., Hajirasouliha, I., Lau, T. L., & Lim, J. B. (2020). Design and optimization of cold-formed steel sections in bolted moment connections considering bimoment. *Journal of structural engineering*, 146(8), 04020153.

Pouladi, P., Ronaldson, J., Clifton, G. C., Ingham, J. M., Wrzesien, A. M., & Lim, J. B. (2019). Finite-element assisted design of eaves joint of cold-formed steel portal frames having single channel-sections. *Structures*, 20, 452-464.

Qin, J., & Tan, P. (2022). Design method of innovative box connections for modular steel constructions. *Journal of Building Engineering*, *57*, 104820.

Rainchen, Rasmussen, Kim. J. R, and Hao Zhang. Design of cold-formed steel single C-section portal frames. Journal of constructional steel research 162 (2019): 105722.

Rinchen, & Rasmussen, K. J. R. (2019a). Behaviour and modelling of connections in cold-formed steel single C-section portal frames. *Thin-Walled Structures*, 143, 106233.

Rinchen, & Rasmussen, K. J. R. (2019b). Numerical modelling of cold-formed steel single C-section portal frames. *Journal Of Constructional Steel Research*, 158, 143-155.

Rinchen, & Rasmussen, K. J. R. (2020). Experiments on long-span cold-formed steel single C-section portal frames. *Journal of Structural Engineering*, 146(1), 04019187.

SCI_P358. (2014). Joints in steel construction: Simple Joints to Eurocode 3.

Shahmohammadi, A. (2019). A Novel Tapered Box Cold-formed Steel Portal Framing System: Full-Scale Testing, Simulation and Design Optimisation (Doctoral dissertation, ResearchSpace@ Auckland).

Shahmohammadi, A., Lim, J. B., Clifton, C., & Hajsadeghi, M. (2022). Full-scale experimental tests on portal frames comprising novel cold-formed tapered box sections. *Journal of Structural Engineering*, *148*(9), 04022133.

Southwell, R. V. (1932). On the Analysis of Experimental Observations in Problems of Elastic Stability. *Proceedings of the Royal Society of London. Series A, Containing Papers of a Mathematical and Physical Character*, 135(828), 601–616.

Tekieh, S. M. R., Zandi, A. P., & Pashaei, M. H. (2022). Numerical and experimental study of the BUEEP connection using an inner box. *Journal of Constructional Steel Research*, 193, 107264.

Toma`, A., Sedlacek, G., & Weynand, & K. (1993). Connections in Cold-Formed Steel. *Thin-Walled Structures*, *16*, 219–237.

Wilkinson, T., & Hancock, G. J. (1998). Tests of portal frames in cold-formed RHS. In *Tubular Structures-International Symposium-* (Vol. 8, pp. 521-530). E & FN SPON.

Wilkinson, T., & Hancock, G. J. (2000). Tests to examine plastic behavior of knee joints in cold-formed RHS. *Journal of Structural Engineering*, 126(3), 297-305.

Wrzesien, A. M., Lim, J. B., Xu, Y., MacLeod, I. A., & Lawson, R. M. (2015). Effect of stressed skin action on the behaviour of cold-formed steel portal frames. *Engineering Structures*, 105, 123-136.

Coresteel. Coresteel Buildings – Customised steel building solutions. Coresteel. https://www.coresteel.co.nz

Zaharia, R., & Dubina, D. (2006). Stiffness of joints in bolted connected cold-formed steel trusses. *Journal of Constructional Steel Research*, 62(3), 240-249.

F. Zadanfarrokh and E. R. Bryan (1992). Testing and Design of Bolted Connections in Cold Formed Steel Sections.

Zhang, X. (2014). Steel portal frames with locally unstable members (Doctoral dissertation, The University of Sydney)].

Zhang, X., Rasmussen, K. J., & Zhang, H. (2015). Structural modeling of cold-formed steel portal frames. *Structures*, 4, 58-68.

Zhang, X., Rasmussen, K. J., & Zhang, H. (2016a). Experimental investigation of locally and distortionally buckled portal frames. *Journal of Constructional Steel Research*, 122, 571-583.

Zhang, X., Rasmussen, K. J., & Zhang, H. (2016b). Second-order effects in locally and/or distortionally buckled frames and design based on beam element analysis. *Journal of Constructional Steel Research*, 122, 57-69.